Transactions of the ASME®

Transactions of the ASME, Journal of Engineering for Gas Turbines and Power (ISSN 0022-0825) is published quarterly (Jan., Apr., July, Oct.,) for $95 per year by The American Society of Mechanical Engineers, 345 East 47th Street, New York, NY 10017. Second class postage paid at New York, NY and additional mailing offices. POSTMASTER: Send address change to The Journal of Engineering for Gas Turbines and Power, c/o The AMERICAN SOCIETY OF MECHANICAL ENGINEERS, 22 Law Drive, Box 2300, Fairfield, NJ 07007-2300.
CHANGES OF ADDRESS must be received at Society headquarters seven weeks before they are to be effective. Please send old label and new address.
PRICES: To members, $27.00, annually; to nonmembers, $95.00.
Add $12.00 for postage to countries outside the United States and Canada.
STATEMENT from By-Laws. The Society shall not be responsible for statements or opinions advanced in papers or ... printed in its publications (B 7.1, para. 3).

INDEXED by Applied Mechanics Reviews and Engineering Information, Inc.

Journal of Engineering for Gas Turbines and Power

Published Quarterly by The American Society of Mechanical Engineers
VOLUME 110 • NUMBER 1 • JANUARY 1988

TECHNICAL PAPERS

ANNOUNCEMENTS

An Equation of State for Steam for Turbomachinery and Other Flow Calculations

J. B. Young
Whittle Laboratory,
Cambridge University Engineering Department,
Cambridge, CB3 0DY, England

Large-scale equations of state for steam used for generating tables are unsuitable for inclusion in finite difference flow calculation computer codes. Such codes, which are in common use in the turbomachinery industry, may require 10^6 property evaluations before convergence is achieved. This paper describes a simple equation of state for superheated and two-phase property calculations for use in these circumstances. Computational efficiency is excellent and accuracy over the range of application is comparable to that of the large-scale equations. Further advantages are that complete thermodynamic consistency is maintained and the equation can be differentiated analytically for direct substitution into the gas dynamic equations where required. A truncated virial form is used to represent superheated properties and a new empirical correlation for the third virial coefficient of steam is presented.

Introduction

The properties of water and steam are known to a greater accuracy than those of any other substance and there have been many attempts to represent them by empirical equations of state designed to combine accuracy with thermodynamic consistency. The equations of the precomputer era were designed for hand calculation and their necessary simplicity was incompatible with high accuracy. Furthermore, a large quantity of experimental data has become available in recent years, which has significantly increased the precision with which property values are known and which has rendered redundant these early equations.

At present, five empirical equations describing the properties of steam are in common use. These are: the IFC Formulation for Industrial Use [1], the IFC Formulation for Scientific Use [2], the M.I.T. equation [3], the Pollak equation [4] and the NBS/NRC equation [5]. Virtually all modern steam tables are based on one or another of these forms.

The authors of the five master equations of state were concerned primarily with accuracy and thermodynamic consistency rather than computational speed or ease of coding. For the production of steam tables or power cycle calculations, the equations serve their purposes well, because relatively few property evaluations are required and computational speed is not a controlling influence. This is not true, however, in the context of modern finite difference flow calculation methods. As an example, a three-dimensional calculation on a typical grid of $100 \times 20 \times 10$ nodes using a time-marching method converging in 500 time steps would require 10^7 property evaluations, assuming these were performed at every grid node once every time step. Relaxing this rather stringent criterion and updating properties every 10 time steps would still require 10^6 evaluations. Even the M.I.T. equation, computationally the most efficient, proves far too cumbersome for this type of duty.

Because of this difficulty, industries involved with steam flow calculations often make sweeping approximations when modeling the behavior of steam. Steam turbine manufacturers, for example, usually approximate the equation of state by the perfect gas equation with an "equivalent" gas constant and isentropic exponent. This is common practice even at high pressure and in the two-phase region where the approximation is far from valid.

This paper describes a very simple equation of state that combines ease of coding, computational efficiency, and thermodynamic consistency with accuracy comparable to that of modern steam tables. The equation was formulated with turbomachinery calculations in mind, and, with the possible exception of supercritical machines, is valid over the range of operation of all modern steam turbines. It may also prove of value to other industries involved with steam flow calculations of a similar type.

Equations of State for Steam

The five equations cited above are all in *characteristic form*, that is, they all express the specific Helmholtz function ($\psi = u - Ts$) as a function of temperature T and specific volume v. This formulation is generally preferred for modern, large-scale equations of state because all the thermodynamic properties can then be obtained by differentiation as opposed to integration, a process requiring the specification of arbitrary constants and functions.

Contributed by the Power Division for publication in the JOURNAL OF ENGINEERING FOR GAS TURBINES AND POWER. Manuscript received by the Power Division September 29, 1986.

Before obtaining the seal of respectability, all equations of state must pass a severe test of comparison with experimental data. The quantity of data available for water and steam is now very large indeed and much work has been done to assess the accuracy and consistency of the measurements and to present the data in easily accessible standard form. Measurable properties are the pressure, temperature, specific volume, specific enthalpy, isobaric specific heat capacity, the two Joule-Thomson coefficients, and the speed of sound. Specific volume and enthalpy data have been collated in the form of the 1963 Skeleton Tables (see [6] for example) and, although improvements to the tables have been suggested since, they still adequately represent the precision with which these properties are known in the regions of engineering interest. Other property data have not been similarly collated and this is quite a serious drawback, because comparison with specific heat and Joule-Thomson coefficient data in particular is a far greater test of accuracy for an equation of state than comparison with specific volume and enthalpy data.

It is not widely known by engineers that, despite propaganda to the contrary, most steam tables are not completely thermodynamically consistent and sometimes do not even represent all the properties with acceptable engineering accuracy. The two IFC Formulations [1, 2] are quite seriously deficient in both these respects. The earlier Formulation for Industrial Use [1] generates values of the isobaric specific heat capacity which deviate considerably from reliable experimental data. (In other words, the equation can accept one differentiation to obtain specific volumes and enthalpies, but not two to obtain the specific heat capacities.) The later Formulation for Scientific Use [2] corrected this inadequacy, but at the expense of simplicity: The equations are so complex they are simply never used! Three sets of tables [6-8] based on the IFC Industrial Formulation are in common use. The author of the V.D.I. Tables [7] accepted the inaccuracy of the specific heat capacity without comment, but the authors of the U.K. Tables [6] took the unprecedented step of using a totally unrelated equation from a different source for calculating this property, thus destroying the thermodynamic consistency of the tables in one fell swoop!

A more serious criticism of the IFC Formulations is that different equations are used to represent the Helmholtz function in different regions of the chart and this results in discontinuities in properties when crossing the dividing boundaries. The M.I.T., Pollack, and NBS/NRC equations are free of this deficiency, because they use a single equation covering the whole region of interest. They are also much easier to code, are probably more accurate, and are therefore to be preferred.

In formulating an equation of state for use with flow calculations, however, it was decided not to work in terms of the Helmholtz function, but instead to adopt an equation in virial form for the pressure in terms of temperature and density

$$p = \rho RT(1 + B\rho + C\rho^2 + \ldots) \tag{1}$$

This approach has two major advantages. Firstly, it can be shown theoretically that the virial coefficients B, C, etc., are functions of temperature only. Secondly, the equation can be terminated at any term depending on the region of interest, the accuracy required, and the computational effort considered acceptable. In practice only the second and third virial coefficients B and C are ever employed, the resulting equation being perfectly adequate for all steam turbine calculations. In any case, the errors involved in deducing the fourth virial coefficient from experimental data are so great as to preclude its usefulness. It is not realistic, therefore, to suppose that equation (1) could be extended to include the critical region or the liquid state.

Thermodynamic Properties

The equation of state for the vapor phase is of truncated virial form with temperature and density (or specific volume) as the independent variables

$$p = \rho_g RT_g(1 + B\rho_g + C\rho_g^2) \tag{2}$$

The second and third virial coefficients are represented by empirical functions of temperature as described in the next section. If temperature and pressure are the prescribed independent variables, then the density must be calculated from equation (2) iteratively. A Newton-Raphson technique is easily implemented and convergence is attained in three to five iterations. Computational efficiency is good because the virial coefficients need to be evaluated only once.

The calculation of the other properties of state requires the evaluation of the first and second derivatives of the virial coefficients. The following parameters are therefore defined:

$$B_1 = T_g \frac{dB}{dT_g}, \qquad B_2 = T_g^2 \frac{d^2B}{dT_g^2}$$

$$C_1 = T_g \frac{dC}{dT_g}, \qquad C_2 = T_g^2 \frac{d^2C}{dT_g^2} \tag{3}$$

The isobaric coefficient of expansion α_g is given by

$$\alpha_g T_g = -\frac{T_g}{\rho_g}\left(\frac{\partial \rho_g}{\partial T_g}\right)_p = \frac{1 + (B + B_1)\rho_g + (C + C_1)\rho_g^2}{1 + 2B\rho_g + 3C\rho_g^2} \tag{4}$$

and the isothermal coefficient of compressibility β_g by

$$\beta_g p = \frac{p}{\rho_g}\left(\frac{\partial \rho_g}{\partial p}\right)_{T_g} = \frac{1 + B\rho_g + C\rho_g^2}{1 + 2B\rho_g + 3C\rho_g^2} \tag{5}$$

The specific enthalpy of the vapor is calculated from the thermodynamic relationship

$$\left(\frac{\partial h_g}{\partial \rho_g}\right)_{T_g} = \frac{(1 - \alpha_g T_g)}{\beta_g \rho_g^2} \tag{6}$$

Substituting equations (4) and (5) into (6) and integrating gives

$$h_g = h_0(T_g) + RT_g[(B - B_1)\rho_g + (C - C_1/2)\rho_g^2] \tag{7}$$

where $h_0(T_g)$ is a function of temperature only.

Nomenclature

B = second virial coefficient
B_1 = $T_g\, dB/dT_g$
B_2 = $T_g^2\, d^2B/dT_g^2$
C = third virial coefficient
C_1 = $T_g\, dC/dT_g$
C_2 = $T_g^2\, d^2C/dT_g^2$
c_p = specific heat capacity at constant pressure
c_v = specific heat capacity at constant volume
h = specific enthalpy
k = isentropic exponent
p = pressure
R = specific gas constant
s = specific entropy
T = thermodynamic temperature
u = specific internal energy
v = specific volume
α = coefficient of expansion $= (1/v)(\partial v/\partial T)_p$
β = coefficient of compressibility $= -(1/v)(\partial v/\partial p)_T$
ρ = density
ψ = specific Helmholtz function

Subscripts

f = liquid phase (not necessarily saturated)
g = vapor phase (not necessarily saturated)
s = saturated
0 = zero pressure limit

The specific entropy is obtained from the relationship

$$\left(\frac{\partial s_g}{\partial \rho_g}\right)_{T_g} = \frac{\alpha_g}{\beta_g \rho_g^2} \tag{8}$$

Substituting equations (4) and (5) into (8) and integrating gives

$$s_g = s_0(T_g) - R\left[\ln \rho_g + (B+B_1)\rho_g + \frac{(C+C_1)}{2}\rho_g^2\right] \tag{9}$$

where $s_0(T_g)$ is a function of temperature only.

The isobaric specific heat capacity is obtained from the definition

$$c_{pg} = \left(\frac{\partial h_g}{\partial T_g}\right)_p = c_{p0}(T_g) + R\{[(1-\alpha_g T_g)(B-B_1) - B_2]\rho_g + [(1-2\alpha_g T_g)C + (\alpha_g T_g)C_1 - C_2/2]\rho_g^2\} \tag{10}$$

where $c_{p0}(T_g)$ is a function of temperature.

The functions of temperature h_0, s_0, and c_{p0} are related by the expressions

$$h_0(T_g) = \int c_{p0}(T_g)\,dT_g + h_c \tag{11}$$

and

$$s_0(T_g) = \int \frac{c_{p0}(T_g)}{T_g}\,dT_g + s_c \tag{12}$$

where h_c and s_c are arbitrary constants. An empirical expression for $c_{p0}(T_g)$ is given in the next section.

The isochoric specific heat capacity can be obtained from the relationship

$$c_{pg} - c_{vg} = \frac{\alpha_g^2 T_g}{\beta_g \rho_g} \tag{13}$$

with the result

$$c_{vg} = c_{p0}(T_g) - R[1 + (2B_1 + B_2)\rho_g + (C_1 + C_2/2)\rho_g^2] \tag{14}$$

Finally the isentropic exponent is given by

$$k = \frac{\rho_g}{p}\left(\frac{\partial p}{\partial \rho_g}\right)_s = \frac{1}{\beta_g p}\frac{c_{pg}}{c_{vg}} \tag{15}$$

In specifying the properties of the liquid phase, it is difficult to maintain thermodynamic consistency between the two saturation states. Even the large-scale equations (with the exception of the Pollak and NBS/NRC equations) fail in this respect. The problem arises because, having specified an equation of state for both vapor and liquid properties, then ideally the saturation states are defined by those states having identical values of pressure and Gibbs function. In practice, however, tedious numerical computation is required to obtain the saturation states, which may then display significant inaccuracy compared with experimental data. For practical calculations, it is preferable to specify an empirical pressure-temperature relationship for the saturation line, together with an equation for the liquid specific volume. Although the problem is now overspecified, the thermodynamic inconsistencies can be kept to a minimum and be virtually undetectable in numerical calculation by following the procedure described below.

For the purposes of nonequilibrium two-phase flow calculations, where the liquid temperature deviates at most by only a few degrees from the saturation value, it is acceptable to negelct the effect of pressure on liquid density. Thus

$$\rho_f = \rho_f(T_f) \tag{16}$$

An accurate empirical equation giving the saturated liquid density as a function of temperature is presented in the following section. The saturated vapor pressure as a function of temperature is also given by a suitable empirical relationship

$$p_s = p_s(T_s) \tag{17}$$

The specific enthalpy of saturated liquid is calculated from the Clausius-Clapeyron equation

$$h_{fs} = h_{gs} - v_{fg} T_s \frac{dp_s}{dT_s} \tag{18}$$

where the term dp_s/dT_s is obtained by differentiating equation (17). The specific entropy of saturated liquid is likewise given by the thermodynamic relationship

$$s_{fs} = s_{gs} - \frac{(h_{gs} - h_{fs})}{T_s} \tag{19}$$

If the liquid is subcooled or superheated, then the specific enthalpy and entropy are obtained from

$$h_f = h_{fs} + \int_{T_s}^{T_f} c_{pf}\,dT_f \tag{20}$$

and

$$s_f = s_{fs} + \int_{T_s}^{T_f} \frac{c_{pf}}{T_f}\,dT_f \tag{21}$$

In equations (20) and (21), c_{pf} must not be chosen arbitrarily, but must be compatible with the vapor specific heat capacity and equation (17). It is best obtained by differentiating the Clausius-Clapeyron equation to give

$$c_{pf} = c_{pg} - v_{fg} T_s \frac{d^2 p_s}{dT_s^2} - 2T_s\left(\frac{dp_s}{dT_s}\right)(\alpha_g v_g - \alpha_f v_f) + T_s\left(\frac{dp_s}{dT_s}\right)^2 (\beta_g v_g - \beta_f v_f) \tag{22}$$

where α_f and β_f are the liquid coefficients of expansion and compressibility, respectively. α_f is obtained by differentiating equation (16) and β_f, under the present assumptions, is zero. Equation (22) is rarely considered when assessing the thermodynamic consistency and accuracy of steam property formulations. Because the second derivative of equation (17) enters as a dominant term, it is necessary to represent saturation data with high accuracy in order to give reliable values of c_{pf}. Failure to use a compatible value of c_{pf} in equations (20) and (21) results in significant error when calculating the entropy of two-phase states. This can become serious, for example, when computing losses in nonequilibrium two-phase expansions.

To appreciate the inconsistency due to overspecification in the above procedure, note that the thermodynamic relationship

$$\left(\frac{\partial c_{pf}}{\partial p}\right)_{T_f} = -T_f\left(\frac{\partial^2 v_f}{\partial T_f^2}\right) \tag{23}$$

is not satisfied. However, at the pressures and temperatures of engineering interest, the error involved in the pressure dependence of c_{pf} is quite negligible.

Empirical Equations and Constants

In order to calculate the thermodynamic properties of steam by the method described above, five empirical equations are required. These represent the second and third virial coefficients, the isobaric specific heat capacity at zero pressure, the saturated vapor pressure, and the specific volume of saturated liquid, all expressed as functions of temperature.

The problem in fitting empirical equations to the second and third virial coefficients is to maintain accuracy to the second derivative. The terms involving B_2 and C_2 in equation (10) are not minor and, although it is comparatively straightforward to devise equations which generate accurate values of specific volume, it is the specific heat capacity that is the property most sensitive to inaccurate representation.

Initially an attempt was made to obtain values of B and C

by differentiation of the M.I.T. equation [3]. Values of B obtained in this way appeared at first sight to be acceptable, but the second derivative behaved anomalously at low temperatures and this was reflected in calculations of c_{pg} by equation (10). Values of C were poor and the first and second derivatives displayed behavior that was obviously inconsistent with reality. It therefore appears that differentiation of even the highly accurate large-scale equations of state must be undertaken with great caution.

Three equations for the second virial coefficient have appeared in the literature [3, 9, 10]. The equation due to Keyes quoted in the appendix of [3] generates acceptable values of specific volume, but specific heat capacities show comparatively large deviations from experimental values in regions where the effect of the third virial coefficient is negligible. A later equation due to Kell et al. [9] is superior in this respect, but only correlates data from 150°–450°C. The most recent equation by LeFevre et al. [10] covers the required range of 0°–800°C and was therefore adopted for the present work.

Thus

$$B = a_1(1 + T/\alpha)^{-1} + a_2 e^{\tau}(1 - e^{-\tau})^{5/2}\tau^{-1/2} + a_3\tau \qquad (24)$$

where $\tau = 1500/T$. With T in K, the values of the constants to give B in m^3/kg are

$$\alpha = 10000.0 \qquad a_1 = 0.0015$$
$$a_2 = -0.000942 \qquad a_3 = -0.0004882$$

Figure 1 shows the variation of B with temperature and Fig. 2 the variation of the compressibility factor correction $B\rho_g$ with pressure and temperature.

Data for the third virial coefficient are sparse [11] and exhibit considerable scatter. An empirical correlation is given in [9] but only extends to 450°C. It was therefore decided to formulate a new correlation valid to 800°C. The equation was based on values of specific volume and enthalpy from the 1963 Skeleton Tables, together with values of isobaric specific heat capacity from the IFC Scientific Formulation [2]. The latter are almost identical to values generated by an equation due to Juza which was used to calculate values of c_p for the U.K. Steam Tables [6]. These are in good accord with experimental data.

Initially an estimate of the third virial coefficient was made at each point of the Skeleton Table based on the tabulated value of specific volume and equation (24) for B. High-pressure values obviously affected by the fourth and higher virial terms were discarded as also were values at low pressure where the effect of the third virial term was slight. The remaining data proved to be remarkably consistent and could be represented by a simple equation with just four constants. Subsequently the constants were adjusted by a process of successive approximation in order to represent the specific enthalpy and heat capacity data as accurately as possible. As with the second virial coefficient, it was the specific heat data, especially on the saturation line at higher pressure, which proved the most sensitive to small changes in the equation.

The final expression for the third virial coefficient was

$$C = a(\tau - \tau_0)e^{-\alpha\tau} + b \qquad (25)$$

where $\tau = T/647.286$. With T in K, the values of the constants to give C in m^6/kg^2 are

$$\tau_0 = 0.8978 \qquad \alpha = 11.16$$
$$a = 1.772 \qquad b = 1.5 \times 10^{-6}$$

Figure 3 shows the variation of C with temperature and Fig. 4 the variation of the compressibility factor correction $C\rho_g^2$ with pressure and temperature.

An empirical equation for the isobaric specific heat capacity at zero pressure is given in [3] and was adopted without change for the present work. Thus,

$$c_{p0} = \sum_{i=1}^{6} a_i T^{i-2} \qquad (26)$$

With T in K and c_{p0} in kJ/kg K, the constants are

$$a_1 = 46.0 \quad a_2 = 1.47276 \quad a_3 = 8.3893 \times 10^{-4}$$
$$a_4 = -2.19989 \times 10^{-7} \quad a_5 = 2.46619 \times 10^{-10}$$
$$a_6 = -9.70466 \times 10^{-14}$$

The constants h_c and s_c in equations (11) and (12) are given by

$$h_c = 1811.06 \text{ kJ/kg}, \qquad s_c = 0.97012 \text{ kJ/kg K}$$

These values are also taken from [3] and represent the arbitrary conditions that the specific internal energy and entropy should be zero at the triple point. Note that with s_c as defined above, the density in the logarithmic term of equation (9) must be expressed in kg/m^3.

An equation for the saturation pressure is also taken directly from [3]

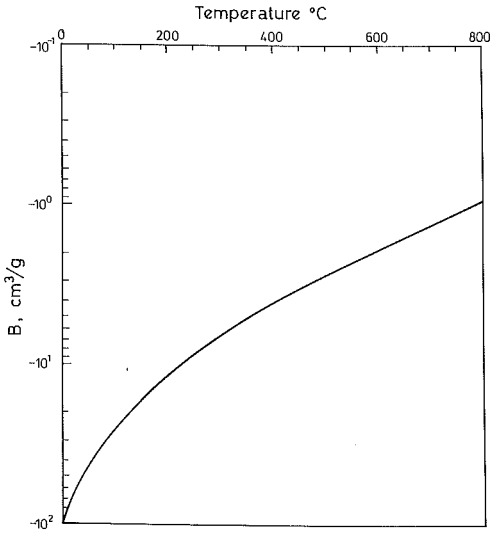

Fig. 1 The second virial coefficient as a function of temperature

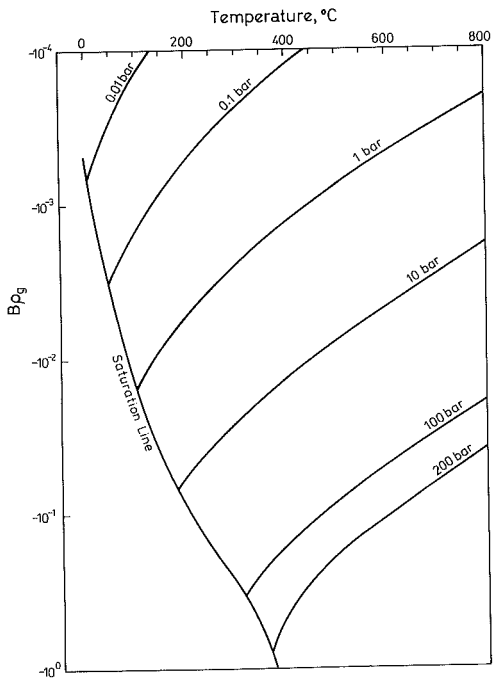

Fig. 2 Graph of $B\rho_g$ as a function of temperature and pressure

$$\frac{p_s}{p_c} = \exp\left[0.01(T_c/T - 1)\sum_{i=1}^{8} a_i(3.3815 - T)^{i-1}\right] \tag{27}$$

where $T_c = 647.286$ K, $p_c = 220.98$ bar, and the constants a_i are given by

$a_1 = -741.9242$ $a_2 = -29.72100$ $a_3 = -11.55286$

$a_4 = -0.8685635$ $a_5 = 0.1094098$ $a_6 = 0.439993$

$a_7 = 0.2520658$ $a_8 = 0.05218684$

The liquid density is approximated by a cubic polynomial obtained by a least-squares minimization procedure,

$$\rho_f = \sum_{i=0}^{3} a_i \tau^i \tag{28}$$

where $\tau = T/647.286$. With T in K and ρ_f in kg/m^3, the constants are

$a_0 = 928.08$ $a_1 = 464.63$ $a_2 = -568.46$

$a_3 = -255.17$

Finally, the specific gas constant takes the standard value $R = 0.46151$ kJ/kg K.

Superfast Property Evaluation

The equations described in the previous sections can be used as they stand to calculate superheated or saturated properties of steam and, as such, prove adequate for many applications. Should it be necessary to reduce computational expense even further, however, a large saving can be made with virtually no loss of accuracy while still maintaining complete thermodynamic consistency.

A study of the equations reveals that most of the computational effort is expended in evaluating the expressions for B, C, c_{p0}, and p_s, together with the first and second derivatives where these are required. The expressions are all functions of the single variable temperature and a large saving may be made by approximating them with one-dimensional cubic spline equations. The coefficients of the splines are evaluated once only at the start of the main calculation and stored for future use. Calculation of the functions then involves the evaluation of cubic polynomials only and the derivatives can be obtained by differentiating the spline equations analytically. The advantage of the cubic spline is that continuity of the second derivative is guaranteed and so thermodynamic consistency of the properties is maintained. This is in contrast to most methods of interpolation, where derivatives cannot be obtained by differentiating the interpolating formulae and thermodynamic consistency is consequently lost.

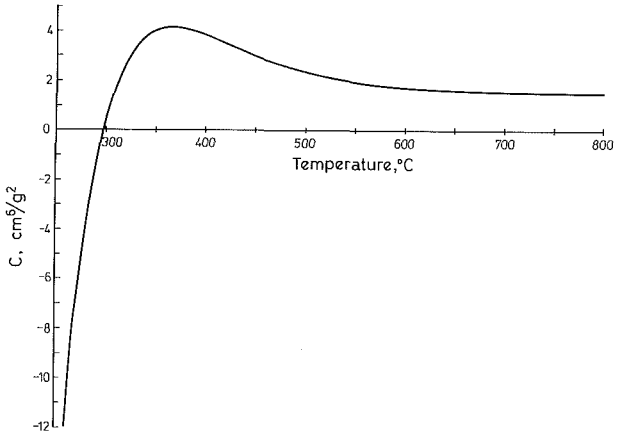

Fig. 3 The third virial coefficient as a function of temperature

Cubic spline equations were obtained for the second and third virial coefficients in the range 0°–800°C and for the saturation pressure in the range 0°–340°C. A cubic spline approximation was also obtained for c_{p0}, but calculations showed that higher accuracy was realized by fitting a spline equation to the zero pressure Helmholtz function

$$\psi = h_0 - RT_g - T_g s_0 \tag{29}$$

and obtaining h_0, s_0, and c_{p0} by differentiating as follows:

$$h_0 = \psi_0 - T_g \frac{d\psi_0}{dT_g} + RT_g$$

$$s_0 = -\frac{d\psi_0}{dT_g} \tag{30}$$

$$c_{p0} = R - T_g^2 \frac{d^2\psi_0}{dT_g^2}$$

In calculating the spline coefficients, knots were deployed at intervals of 10°C and the spline equations made to agree exactly with the master equations at these points. Values of the first derivative were specified at both ends of the range in order uniquely to determine the spline. A comparison of steam properties calculated first from the master equations and then from the spline approximations showed agreement to five significant figures in specific volume and enthalpy. Specific heat capacities agreed to within 2 parts in 1000.

Range of Application and Accuracy

The range of application of the equations for superheated properties is illustrated in the (T–s) diagram of Fig. 5. Within the area bounded by the saturation line from 0°–310°C, the isochore $v = 18$ cm^3/g, and the isotherm $T = 800$°C, values of the specific volume and enthalpy calculated from the equations fall within the tolerances set by the 1963 Skeleton Tables, with the exception of the following three points:

Point	T, °C	p, bar	V, cm^3/g	v (skeleton)
1	300	75.0	26.785	26.71 ± 0.05
2	310	sat.	18.212	18.316 ± 0.035
3	425	25.0	125.11	125.0 ± 0.1

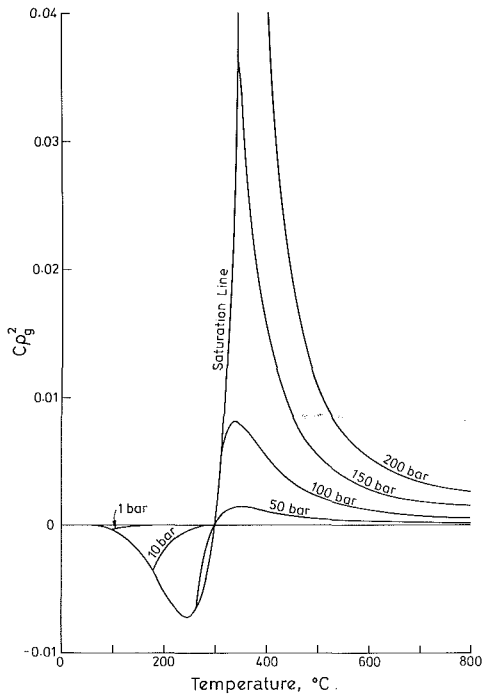

Fig. 4 Graph of $C\rho_g^2$ as a function of temperature and pressure

Table 1 Standard deviations of specific volume and enthalpy from the 1963 Skeleton Tables

	Standard deviation from Skeleton Table in percent			
	v (present)	v (M.I.T.)	h (present)	h (M.I.T.)
Saturation line	0.057	0.032	0.067	0.018
1 bar	0.014	0.012	0.013	0.013
10 bar	0.030	0.026	0.030	0.021
50 bar	0.072	0.079	0.017	0.026
100 bar	0.095	0.076	0.045	0.043
150 bar	0.090	0.072	0.048	0.065
200 bar	0.094	0.086	0.073	0.098

In the appendix of [3], it is noted that the M.I.T. equation also fails to satisfy the Skeleton Table tolerance requirement for point No. 3. The present work confirms that this value may indeed be in need of revision.

The standard deviations of predicted values of specific volume and enthalpy from those of the Skeleton Tables are presented in Table 1, together with the results of similar calculations using the M.I.T. equation. A comparison of the two sets of figures shows that, over the range of application, the accuracy of the present equation is comparable to that of the M.I.T. equation.

Figure 6 shows a comparison of computed values of the isobaric specific heat capacity with values taken from [6]. The latter were calculated from an equation formulated by Juza that correlates experimental data very accurately. Over the range of application, the discrepancy between the two sets of data is generally less than 1 percent, with the exception of a small region on the saturation line where the error rises from 1 percent at 250°C to 8 percent at 300°C. This is probably due to the increasing influence of the fourth virial term which has not been included in the analysis. In general it is found that, with increasing pressure, errors in specific heat capacity become noticeable before errors in specific volume or enthalpy. This is the reason why it is essential to correlate all equations of state with heat capacity data to ensure good accuracy and is also the reason why a Skeleton Table of collated experimental values is long overdue.

Other properties that are very sensitive to the derivatives of the virial coefficients are the two Joule-Thomson coefficients. Figure 7 shows a comparison between recent measurements [12] of the isenthalpic Joule-Thomson coefficient $(\partial T/\partial p)_h$ and values calculated from the present equation. The increasing systematic discrepancy detectable at higher temperatures (4 percent at 700°C) may indicate a slight error in the second virial coefficient above 400°C, the influence of the third virial term being negligible at pressures below 25 bar. In general, however, the agreement is very good.

For many flow calculations, accuracy of such a high order is not essential and if errors of a few percent are acceptable, then the range of application can be considerably extended to that bounded by the isentrope $s = 5.7$ kJ/kg K and the isochore $v = 8$ cm^3/g as shown in Fig. 5. Within this range, errors in specific volume do not exceed 4 percent, in specific enthalpy 1 percent, and in specific heat capacity 10 percent. The range now includes the steam inlet conditions for the most extreme supercritical turbogenerators presently operating or under construction (345 bar, 652°C; 320 bar, 535°C). Further extrapolation of the equations should be undertaken with caution, especially near the saturation line where accuracy deteriorates rapidly.

For low-pressure turbine calculations, the third virial coefficient usually has a negligible effect and can be dispensed with in the equation of state to considerable computational advantage. From equation (1), the density can now be ex-

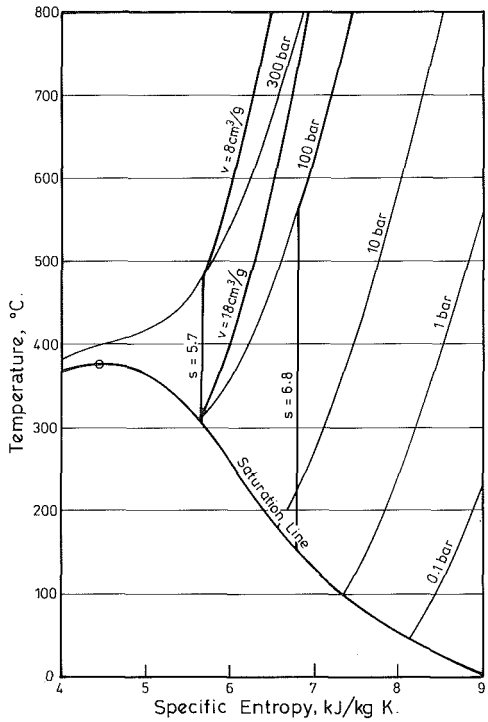

Fig. 5 (T-s) diagram showing the range of application of the equation of state

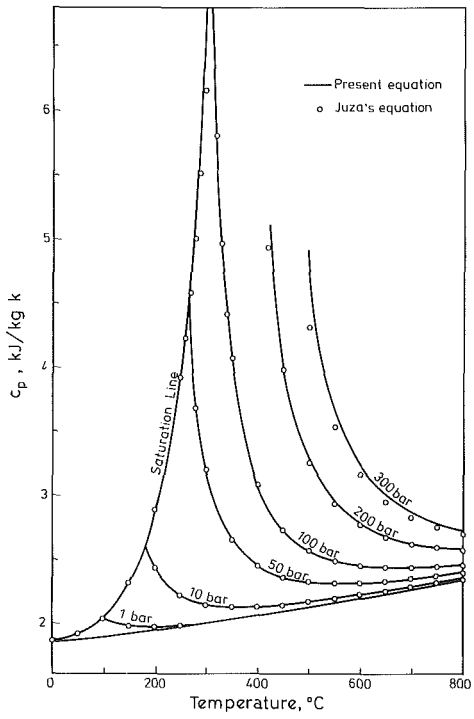

Fig. 6 Comparison of isobaric specific heat capacity with the results of Juza

Table 2 CPU times in seconds for 10^4 superheated property evaluations

	Prescribed (T_g, ρ_g)	Prescribed (T_g, p)
Master equations (B and C)	14.3 s	16.3 s
Spline equations (B and C)	7.3 s	9.3 s
Master equations (B only)	11.5 s	13.1 s
Spline equations (B only)	5.8 s	7.4 s
M.I.T. equation	114.0 s	508.0 s

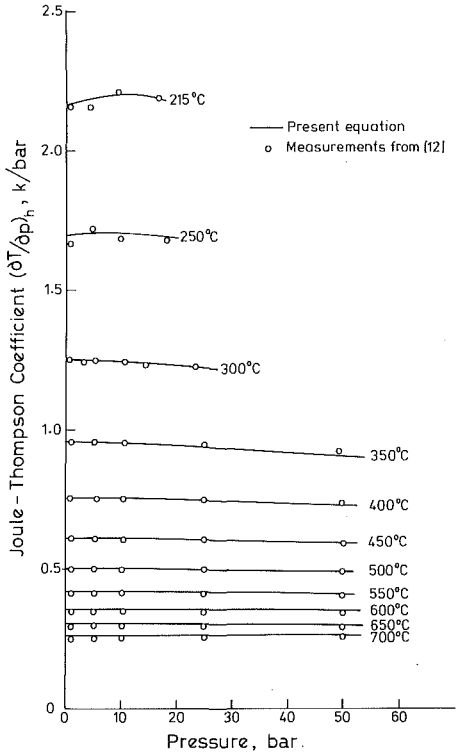

Fig. 7 Comparison of isenthalpic Joule-Thomson coefficient with experimental measurements of [12]

pressed in terms of the pressure and temperature explicitly by the equation

$$\rho_g = \frac{2p/RT_g}{1+(1+4pB/RT_g)^{1/2}} \tag{31}$$

All other thermodynamic properties are calculated as before, except that the third virial coefficient C and its derivatives are set equal to zero.

Figure 5 also shows the range of application for the equation involving the second virial term only. Within the area bounded by the saturation line from 0°–150°C, the isentrope s = 6.8 kJ/kg K, the isobar p = 100 bar, and the isotherm T = 800°C, virtually all specific volumes and enthalpies satisfy the Skeleton Table tolerances and all specific heat capacities agree with Juza's equation to within 1 percent. The only exceptions are the three points on the saturation line

Point	T°C	p	v, cm^3/g	v (skeleton)
1	120.0	Sat.	892.66	891.71 ± 0.89
2	140.0	Sat.	509.23	508.66 ± 0.51
3	150.0	Sat.	393.19	392.57 ± 0.39

These points also display errors in specific heat capacity up to 2.5 percent.

Metastable States

For nonequilibrium two-phase steam flow calculations it is necessary to extrapolate the equation of state for superheated steam below the saturation line in order to represent the properties of subcooled vapor. Theory and experiment indicate that the maximum subcooling attainable before the onset of nucleation is between 20° and 40°C depending on the pressure and rate of expansion. (Higher subcoolings are achieved at low pressure and high rates of expansion.) Within this range, the equations are well behaved and do not display any unexpected anomalies. However, due to the complete lack of experimental measurements in this important region, there can be no guarantee of the accuracy of the extrapolations. Judging by the behavior of the equations in the vicinity of the saturation line, it would appear that accuracy is likely to deteriorate as the pressure increases (note the slopes of the isobars near the saturation line in Figs. 4 and 6). The author feels that extrapolations above a few bars pressure should be treated with caution and that it would be unwise to rely on subcooled data for specific entropies less than 5.8 kJ/kg K.

Computational Efficiency

Evaluation of a complete set of superheated properties (p, h_g, s_g, α_g, β_g, c_{pg}, c_{vg}, k) from prescribed temperature and density using the spline curve fit approximations requires 125 floating point operations and the evaluation of one logarithmic function. (Using the master equations requires 160 floating point operations and the evaluation of two logarithms and two exponentials.) It is therefore unlikely that significant improvements in the computational efficiency of steam property calculations will be forthcoming in the future.

Benchmark calculations were performed on a Perkin-Elmer 3230 minicomputer (rated at approximately 0.6 Whetstone MFLOPS) for 10^4 complete superheated property evaluations using single precision arithmetic. Properties were evaluated both from prescribed temperature and density, and from prescribed temperature and pressure. The CPU times recorded appear in Table 2.

References

1 *1967 IFC Formulation for Industrial Use of the Thermodynamic Properties of Ordinary Water Substance*, ASME, New York, 1967.

2 *1968 IFC Formulation for Scientific and General Use of the Thermodynamic Properties of Ordinary Water Substance*, ASME, New York, 1968.

3 Keenan, J. H., Keyes, F. G., Hill, P. G., and Moore, J. G., *Steam Tables*, Wiley Interscience, New York, 1978.

4 Pollak, R., "The Thermodynamic Properties of Water and Steam up to 1200 K and 3000 bars," Translation No. PC/T14, IUPAC Thermodynamic Tables Project Centre, Imperial College, London; translated from Pollak, R., Dr. Ing. Dissertation, University of Ruhr, Bochum, West Germany, 1974.

5 Haar, L., Gallagher, J. S., and Kell, G. S., *NBS/NRC Steam Tables*, Hemisphere, 1984.

6 *U.K. Steam Tables in SI Units 1970*, Edward Arnold, London, 1970.

7 Schmidt, E., *Properties of Water and Steam in SI Units*, Springer-Verlag, New York, 1979.

8 Meyer, C. A., McClintock, R. B., Silvestri, G. J., and Spencer, R. C., *ASME Steam Tables*, ASME, New York, 1977.

9 Kell, G. S., McLaurin, G. E., and Whalley, E., "PVT Properties of Water II, Virial Coefficients in the Range 150°C–450°C Without Independent Measurement of Vapour Volumes," *J. Chem. Phys.*, Vol. 48, 1968, pp. 3805–3813.

10 LeFevre, E. J., Nightingale, M. R., and Rose, J. W., "The Second Virial Coefficient of Ordinary Water Substances: A New Correlation," *J. Mech. Eng. Sci.*, Vol. 17, 1975, pp. 243–251.

11 Dymond, J. H., and Smith, E. B., *The Virial Coefficients of Gases: A Critical Compilation*, OUP, 1969.

12 Ertle, S., Grigull, U., and Straub, J., "Measurements of the Adiabatic and Isothermal Joule-Thomson Coefficients for Water Vapour," *Proc. 9th Conf. on the Properties of Steam*, Tech. Univ. Munich, 1979, pp. 191–196.

Steam-Injected Gas Turbine Integrated With a Self-Production Demineralized Water Thermal Plant

G. Cerri
Professor.
Assoc. Mem. ASME

G. Arsuffi
Engineer.

Dipartimento di Meccanica e Aeronautica,
Università di Roma,
"La Sapienza," Italy

A simple steam-injected gas turbine cycle equipped with an exhaust heat recovery section is analyzed. The heat recovery section consists of a waste heat boiler, which produces the steam to be injected into the combustion chamber, and a self-production demineralized water plant based on a distillation process. This plant supplies the pure water needed in the mixed steam-gas cycle. Desalination plant requirements are investigated and heat consumption for producing distilled water is given. Overall steam-gas turbine cycle performance and feasibility of desalting plants are investigated in a firing temperature range from 1000.°C to 1400.°C for various compressor pressure and steam-to-air injection ratios. An example is reported.

Introduction

Injecting steam or water into a gas turbine combustion chamber has often been regarded as a means of increasing gas turbine output—especially during hot weather operations. Efficiency improvement has frequently resulted when steam is produced by exhaust gas thermal energy [1-6]. Sometimes steam injection has been used to reduce gas turbine firing temperature and lengthen the life of the turbine. NO_x emission reduction has also been obtained through steam injection [7-9].

Usually the steam injection ratio has been maintained below 5-8 percent following the compressor surge margin safety of heavy-duty or aero-derived gas turbines already on the market.

Further output improvement could have been obtained by adopting a steam-to-air injection ratio higher than 10 percent depending on firing temperature and pressure ratio.

Several analyses have been published during the last decade. In [10] steam injection was compared with two other kinds of plants. Water consumption and cost analyses were emphasized; lower limits of 125°C for the stack temperature and 28°C for the pinch-point temperature difference were considered. A gas turbine firing temperature of 1427°C was accounted for. The conclusions were that the water consumption was about 0.42-0.44 kg/MJ (1.15-1.60 kg/kWh), which was less than other plants. Therefore economic convenience exists when the water cost (WC) is lower than \$3.9-4.7/m^3 (\$15-18/1000 gal) and the fuel cost (FC) is \$1.9/GJ (\$2/10^6 Btu). Economically convenient water cost is also WC=\$6.0-7.0/m^3 (\$23-27/1000 gal) when FC=\$2.8/GJ (\$3/10^6 Btu).

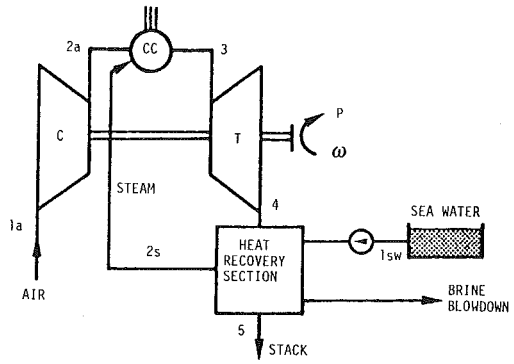

Fig. 1 Scheme of the gas turbine with steam-injection plant equipped with a heat recovery section fed by sea water

Lewis and Kinney [11] investigated steam injection for restoring maximal power when the gas turbine was operating on medium-Btu fuels during hot days. They concluded that there was no substantial change in water consumption for the whole plant (STAG type) because reduction of cooling tower makeup requirements tends to offset the water lost by steam injection.

In a previous paper [12] a thermodynamic analysis of steam-injected gas turbine cycles was given. Steam injection into the gas turbine combustion chamber improves the fuel consumption (efficiency) if the steam is produced in a waste heat boiler by the exhaust gas. Improvement of efficiency can go up by 27 percent when the pressure ratio is 10, the firing temperature 1000°C, and the steam injection ratio S=14 percent. Specific work, referred to by the compressed air taking part in the combustion, increases by about 50 percent.

The opinion of the authors is that the problem arising with steam injection is not connected with the water consumption but with the quality of the injected water that has to be demineralized. No suspended solids and few ppm of salts should be in the boiler feed water and hot turbine gas.

Contributed by the Gas Turbine Division of THE AMERICAN SOCIETY OF MECHANICAL ENGINEERS and presented at the 31st International Gas Turbine Conference and Exhibit, Düsseldorf, Federal Republic of Germany, June 8-12, 1986. Manuscript received at ASME Headquarters Janaury 9, 1986. Paper No. 86-GT-49.

As suggested in [12], if the salinity of the raw water is not high it is possible to use special indirect boilers such as the Schmidt–Hartman. If a high-salinity water source like the sea is available, a water treatment plant to get desalted water is required.

The aim of this paper is to investigate the performance achieved by a steam-injected gas turbine equipped with self-producing demineralized water that uses a fraction of the thermal power in the exhaust. The scheme is shown in Fig. 1.

After a brief description of some desalting thermal plants, a multistage flash distillation plant is considered. Specific heat consumption is derived as a function of stage number and heat exchanger surface extension parameter.

Steam-injected gas turbine plants are studied in the firing temperature range 1000°C–1400°C, pressure ratio range of 3–30, and steam injection ratios up to 0.30. Practicability of desalting plants that supply water for injected steam is also considered.

An example of an aero-derived gas turbine plant typical for marine use is reported.

Finally, comments on costs and plant operation and complexity are also made.

Typical Desalting Plant as Reference Point

Water desalination treatment (total dissolved solids < 10 ppm) is based on many processes, among which the most important are:

- distillation by thermal energy
- ion exchange
- freezing
- electrodialysis
- reverse osmosis
- solvent extraction

The two processes of interest for the present application are: (*i*) distillation by thermal energy; (*ii*) ion exchange.

In the second method cation and anion exchange resins are used to remove salts. The exhausted resins are regenerated with acids, ammonia, or lime depending upon the specifics of the process. This kind of plant is well developed for other industrial uses. Foreign matter can foul ion exchange resins so pretreatment of some saline waters may be needed. Production costs are about proportional to total dissolved solids removed and depend on the load factor. Research carried out on a steam-injected gas turbine plant whose power is 100 MW and firing temperature 1000°C showed that if the hours of operation exceed a thousand the water cost is lower than 2.8 percent of the fuel cost. The ratio between the unit mass of fuel and water costs was at least 200; in this case the water source was a river.

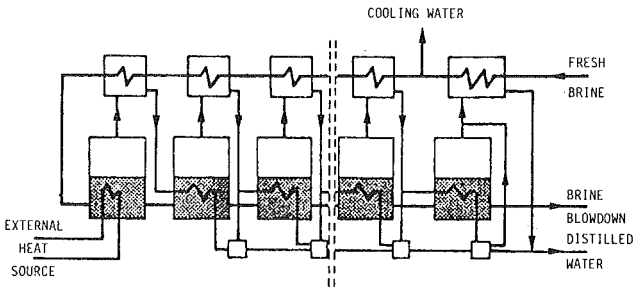

Fig. 2 Mulitiple effect evaporation plant scheme

Water treatment plants based on distillation processes are more suitable for the present application since they can use the heat in the exhaust gas stream directly. This is particularly important when the primary water source is the sea.

In these kinds of plant a saline solution is vaporized and pure water is obtained by condensation (a final salt content less than 10 ppm can be obtained by these processes).

Water from the sea (or from a river) is pumped into the plant, deaerated, treated with chemicals, and combined with a stream of recycled brine (if a recycle loop exists). The saline

Nomenclature

ADT = approach temperature difference, °C
At = specific total desalting plant heat transfer surface, m^2
B = gas turbine pressure ratio
BH = brine heater
BHA = brine heater surface, m^2
CA = condenser surface, m^2
Cb = brine specific heater, J/kg K
Cp = specific heat at constant pressure, J/kg K
D = difference
E = envelope curve
EA = economizer surface, m^2
FAR = fuel–air ratio
FC = fuel cost
L = curve of limits
LHV = fuel low heating value, J/kg
m = mass, kg
O = maximum specific output work curve
P = power, W
p = pressure, Pa
Q = heat, J
Qd = specific heat consumption of the distillation plant, J/kg
S = steam air injection ratio
SHA = superheater surface, m^2
SN = distillation plant stage number
SR = distillation plant heat transfer area parameter
T, t = temperature, K, °C
U = heat transfer coefficient, W/m^2K
VA = vaporizer surface, m^2
WB = waste heat recovery boiler
WC = water cost
WF = water flow, kg/s
Wo = plant specific output work, J/kg
ϵ = effectiveness
η = efficiency
η_m = mechanical efficiency
σ = ratio between the steam feeding the distillation plant brine heater and the compressed air

Subscripts

a = air, exhaust
av = available
b = brine
bb = brine blowdown
bc = cold brine
bh = hot brine
c = compressor
cc = combustion chamber
dw = demineralized water
i = inlet
l = lower, minimum
m = mixture
o = outlet
p = polytropic
pp = pinch-point
s = steam
ss = saturated steam
sw = sea water
t = turbine
u = upper, maximum
ut = utilized
w = water
1, 2, 3, . . . = initial and end points of transformations

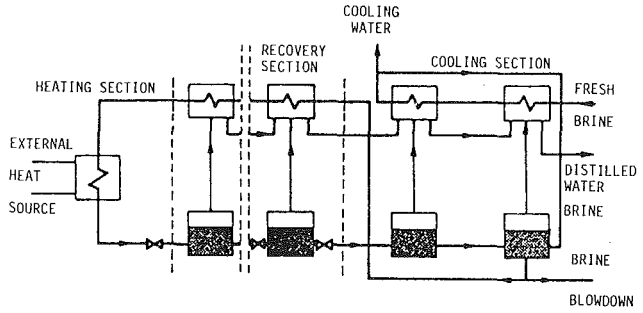

Fig. 3 Multistage flash distillation plant scheme

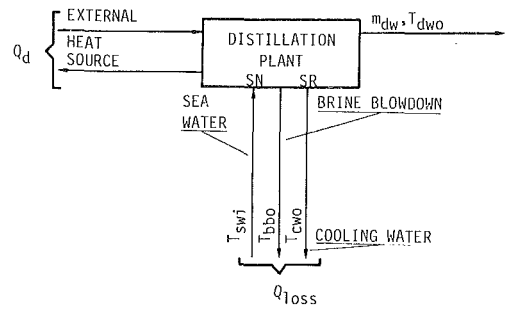

Fig. 4 Reference distillation plant scheme seen as a black box for energy and mass conservation point of view

solution is usually heated progressively up to a maximal temperature with chemical treatment dependent on this temperature [acid treatment allows higher temperatures (> 120°C) than polyphosphate or similar]. The peak temperature is reached by means of an external heat source; in the present situation the heat is from the gas turbine exhaust gas. The heat available in the brine and condensed pure water is partially saved in some recovery stages [13-16].

Due to the pure water separation the brine salinity rises. Then one fraction is drained out of the plant while sea water is added.

A fraction of fresh sea water is usually used as cooling water and then discharged without taking part in the distillation process.

Fundamentally two kinds of distillation processes are used: (*a*) multiple-effect evaporation (MEE); (*b*) multistage flash distillation (MSF).

In the MEE plant, shown in Fig. 2, once the brine has been heated up to the peak temperature it enters the first evaporator (first effect) where the steam is distilled by external heat. Distilled steam goes into the first brine preheater where it partially condenses and then goes into the second evaporator where it totally condenses causing the distillation of other steam from the brine. The second evaporator pressure is lower than the first, so the temperature is also lower. The process is repeated for each stage. The final brine preheater condenses all the distilled vapor from the last stage with a certain amount of brine discharged as surplus. The brine exiting from the last stage at the minimum pressure and temperature is blown off. A fraction of the heat available in the blowdown brine can be recovered by a freshwater-brine heat exchanger. This can assume a certain importance for a small stage number.

The process can operate at higher blowdown concentrations than the MSF.

Capital investment is higher than for the MSF; it may be quite competitive for very high pure water production (exceeding 1600 m^3/h corresponding to about 500 L/s).

A multistage flash distillation (MSF) plant having three sections is schematically represented in Fig. 3. The first section is where the brine is heated up to the maximal temperature by an external source. The second (central) section is for recovery and the third one is for cooling. One stage consists of a chamber where the vapor distills at the bottom and condenses at the top in a brine preheater. A drop separator divides the upper from the lower part of the chamber. In the cooling section the distilled steam is condensed by the feedwater, which is partially discharged from the plant. Brine from the last stage can be recycled to lower heat consumption.

Both the above processes can be schemed from the energetic point of view as a black box where heat from the outside enters together with the feedwater that is at its inlet temperature T_{bci}. The brine blowdown, at temperature T_{bho}, exits the plant as well as the cooling water at temperature T_{cwo} and the demineralized water at temperature T_{dwo} (see Fig. 4).

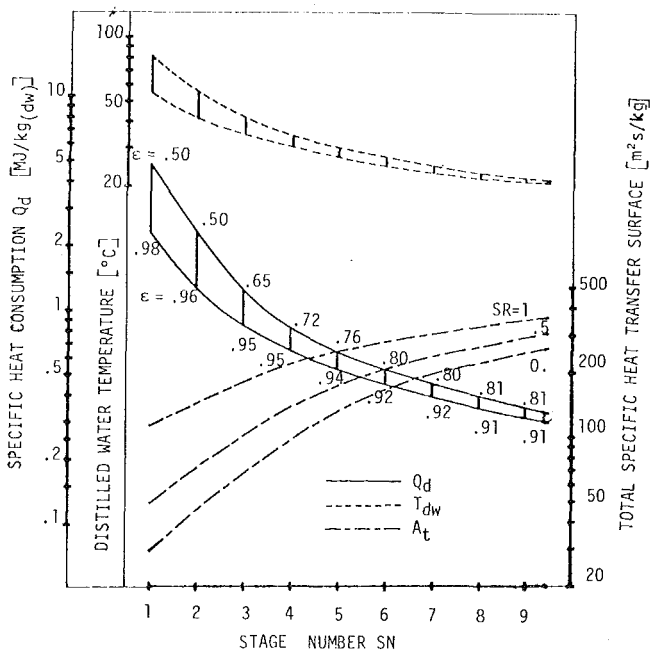

Fig. 5 MSF plant specific heat consumption, outlet water temperature, and total heat transfer area versus stage number and *SR* parameter

A multistage flash distillation plant is considered here, although a multiple-effect evaporation plant can be treated in the same way.

The question arising in the present study regards the feasibility of a distillation plant able to give the required amount of pure water by using a fraction of exhaust heat.

To answer this question it is necessary to determine for a certain number of stages *SN* what the maximum and the minimum amount of heat consumption (*Qd*) for the unit mass of demineralized water is. Moreover, for such a specific heat consumption range, a parameter has to give the heat transfer surface extension. This parameter, *SR*, varies from zero to one with the minimum and maximum surface. The distilled water final temperature is also in relation to the number of stages and *SR*. The following relationships can be found:

Specific heat consumption

$$Qd = Qd(SN, SR) \tag{1}$$

Specific total heat transfer area

$$At = At(SN, SR) \tag{2}$$

Distillate temperature

$$T_{dwo} = T(SN, SR) \tag{3}$$

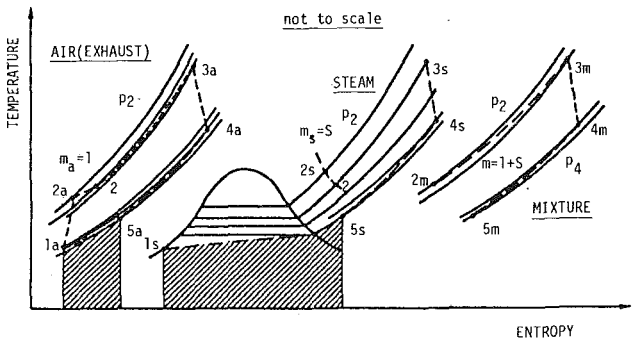

Fig. 6 Temperature-entropy diagram of steam-injected gas turbine cycle

The above are shown in Fig. 5. How these relationships are found is reported in [17].

Data assumed for plots in Fig. 5 are

$$T_{bci} = 15°C$$

$$T_{bhu} = 120.°C$$

$$DT_{db} = 1.75°C$$

$$Cb = 4.2 \text{ kJ/kg°C}$$

$$U = 1.63 \text{ kW/m}^2\text{°C}$$

$$ADT_1 = 1.5°C$$

Figure 5 plots do not account for the possible heat recovery from the blowdown brine that lowers Qd_1 and can be really important for $SN = 1$–4. Instead of using the blowdown brine recovery system brine recycling could be adopted.

Figure 5 also gives the corresponding condenser effectiveness for $SR = 0$ and $SR = 1$. The latter value is related to the minimum approach, which corresponds to the maximum heat transfer area.

The maximum heat consumption for SN stages is assumed equal to the minimum value for $SN - 1$ stages [17].

Specific heat consumption for desalting water decreases by increasing the stage number as well as the heat transfer surface, therefore increasing initial capital investment.

Cycle Analysis

Performance of steam-injected gas turbines is analyzed with reference to the Fig. 1 plant scheme showing a traditional gas turbine plant (compressor, combustion chamber, and turbine) equipped with a waste heat recovery section that produces the injected steam by using sea water as the primary water source.

The thermodynamic analysis has been carried out taking the mixed gas steam cycle, shown in Fig. 6, and the heat recovery section into consideration.

Air and steam can be considered separately for the mixed gas-steam cycle thermodynamic analysis. The air is compressed up to pressure $2a$, then mixed with steam. The air (combustion gas) is then heated up to the firing temperature, expanding from its upper partial pressure to the lower partial pressure $p4a$. The environment produces the steam-air (exhaust gas) separation.

The steam is produced at a pressure just higher than $p2$ (ideally $p2s = p2$) and is injected into the combustion chamber. It then goes with the air at its partial pressure, into the combustion, expansion, and heat recovery processes. Finally it goes out into the environment separating in a dew temperature range that has a lower boundary value approximately close to feed water temperature T_{dwo}.

Specific work refers to the compressed air unit mass taking part in the combustion, and cycle efficiency can be evaluated according to [12, 17] as functions of five quantities:

Specific work

$$Wo = W(T_3, B, S, SN, SR) \tag{4}$$

Efficiency

$$\eta = \eta(T_3, B, S, SN, SR) \tag{5}$$

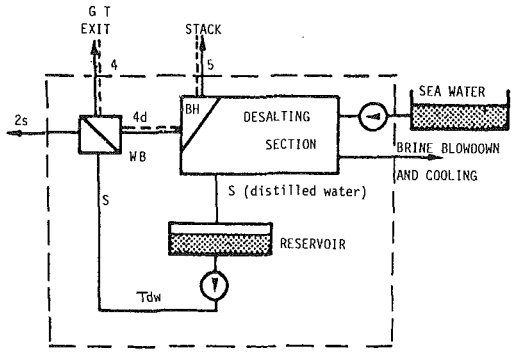

Fig. 7(a) Brine heater fed by exhaust gas

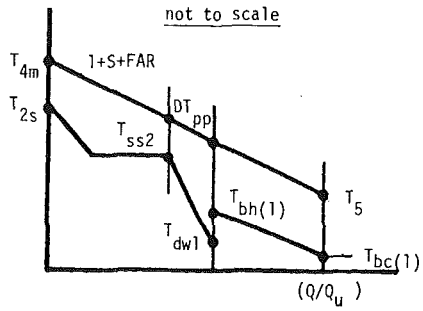

Fig. 7(b) Temperature profile for scheme 7(a)

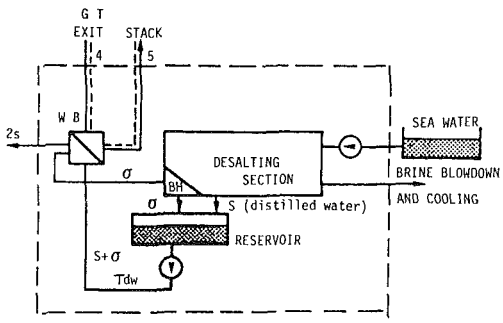

Fig. 7(c) Brine heater fed by dry steam from the boiler

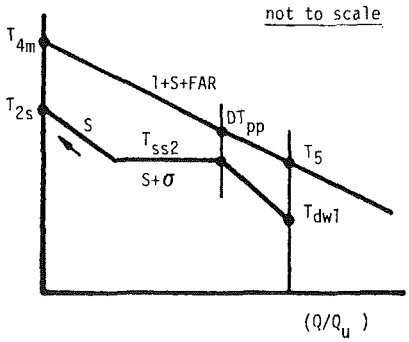

Fig. 7(d) Temperature profile for scheme 7(c)

Fig. 7 Two possible schemes for the heat recovery section (*HRS*) and typical temperature profiles

It is worth pointing out that the above two functions can be calculated with the condition that the efficiency is maximum for each pair (B, S). Once T_3 has been assumed this condition leads to the steam temperature calculation by taking the heat transfer process in the heat recovery section into account.

According to Figs. 7(a, c), the heat recovery section can be arranged in two ways.

In the first scheme (Fig. 7a) there are the waste heat boiler (WB), which produces the injected steam, and the desalting plant brine heater, where the brine is heated directly by the exhaust gas.

In the second scheme (Fig. 7c) the waste heat boiler produces the steam to be injected as well as the steam condensing in the desalination plant brine heater. The exhaust gas in the heat recovery section must supply the heat needed for the injected steam,

$$Q_s = Q(S, B, T_{dwo}, T_{2_s}) \tag{6}$$

and for desalting the right amount of pure water

$$Q_{dw} = Q(S, SN, SR) \tag{7}$$

where the heat required by the desalting point depends on its specific heat consumption and steam-to-air injection ratio

$$Q_{dw} = Q_d(SN, SR)S \tag{8}$$

The heat recovery section introduces further conditions:

1 steam and exhaust temperature difference must be higher than a lower limit

$$T_{4m} - T_{2s} \geq DT_{sml} \tag{9}$$

2 the pinch-point temperature difference has to be higher than a lower limit

$$DT_{pp} \geq DT_{ppl} \tag{10}$$

3 Another condition regards the steam quality; owing to combustion stability [4] it must be at least dry steam. Due to technological reasons [even if condition (9) is satisfied] maximum steam temperature must not exceed an upper limit of

$$T_{ss2} \leq T_{2s} \leq T_{2su} \tag{11}$$

To avoid low temperature sulfur corrosions stack exhaust temperature can't become lower than a limit connected with the fuel quality

$$T_5 \geq T_{5l} \tag{12}$$

Typical exhaust gas and water-steam temperature distribution profiles for both heat recovery section schemes are represented in Figs. 7(b, d).

The calculation scheme follows this procedure:

1 the gas turbine firing temperature T_3 is assumed known, in addition to the GT pressure ratio B, and the injection ratio S;

2 the exhaust temperature is then calculated in addition to the turbine work and the maximum value available heat in the exhaust

$$Q_{avm} = (1 + FAR + S)C_{pm}(T_{4m} - T_{5l}) \tag{13}$$

3 since feedwater temperature T_{dwo} is not known a priori it is assumed as being tentative. Then the heat required for producing the injected steam is calculated assuming T_{2s} in the range established by conditions (9) and (11). The positive difference of heat

$$DQ = Q_{avm} - Q_s \tag{14}$$

available in the exhaust is compared with the heat needed to desalt the sea water. If this difference is higher than the maximum value of heat for distilling the sea water with a one-stage desalting plant

$$DQ \geq SQ_d(1, 0) \tag{15}$$

the desalination plant is assumed to have one stage and the minimum heat transfer surface.

If inequality (15) is not satisifed, the minimum number of stages is calculated as well as the heat transfer surface parameter that satisfies

$$Qd(SN, SR) = DQ/S \tag{16}$$

Of course conditions (9), (10), and (11) are verified. Iterations are needed for the variable T_{dwo} to evaluate Qd, the difference DQ, and to get the maximum efficiency for the pair (B, S).

Once the heat recovery section quantities, i.e., injected steam temperature T_{2s}, desalting plant stage number SN, desalting plant heat transfer surface parameter SR, feedwater temperature T_{dwo}, and all the temperature differences (pinch-point, etc.), have been found, the feasibility of the heat recovery section is possible;

4 the compressor requirements are then calculated as well as combustion process; the specific work and efficiency are found. Next a new set of variables (T_3, B, S) is assumed and calculation is repeated.

A typical plot of heat balance in the heat recovery section is given in Fig. 8. Gas turbine firing temperature $T_3 = 1000°C$ and pressure ratio $B = 7$; the heat required for the injected steam Q_s, the desalting plant Q_{dw}, and overall utilized heat

$$Q_{ut} = Q_s + Q_{dw} \tag{17}$$

divided by the available exhaust heat are given versus the steam-to-air injection ratio. On the desalting heat curve (Q_{dw}) the number of flash stages SN is given. The injected steam temperature (T_{2s}) is reported on the Q_s curve.

Only a fraction of the available exhaust heat is utilized when steam-to-air injection ratios are lower than $S \simeq 6$ percent (see Fig. 8). In this case 1 or 2 flashing stages are needed and the

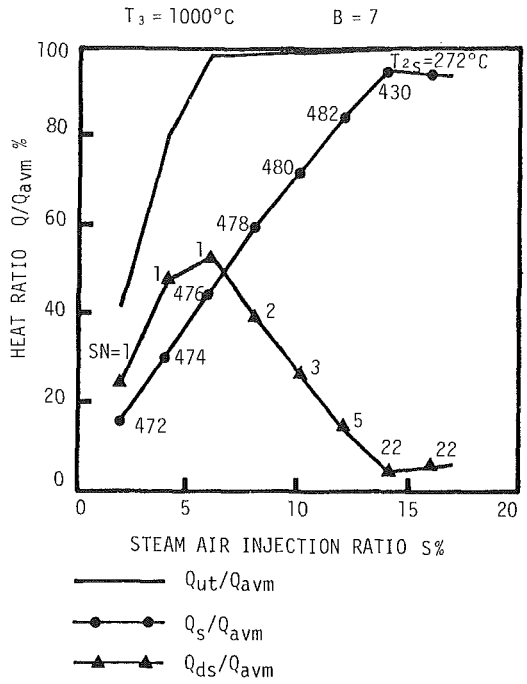

Fig. 8 Heat balance in the heat recovery section versus steam-air injection ratio: desalting stage number and steam temperature are indicated

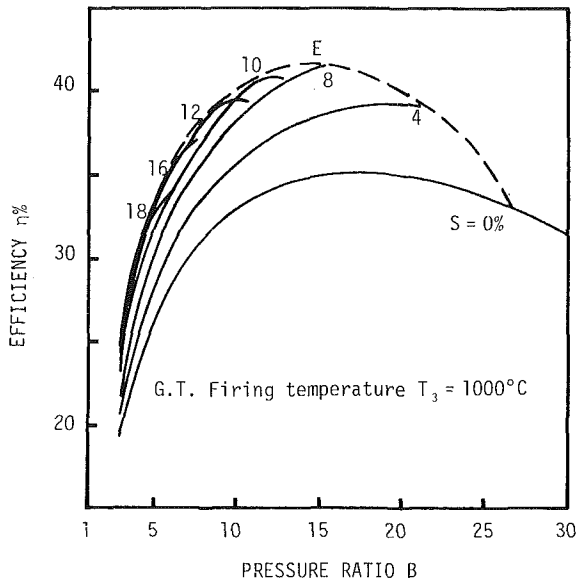

Fig. 9(a)

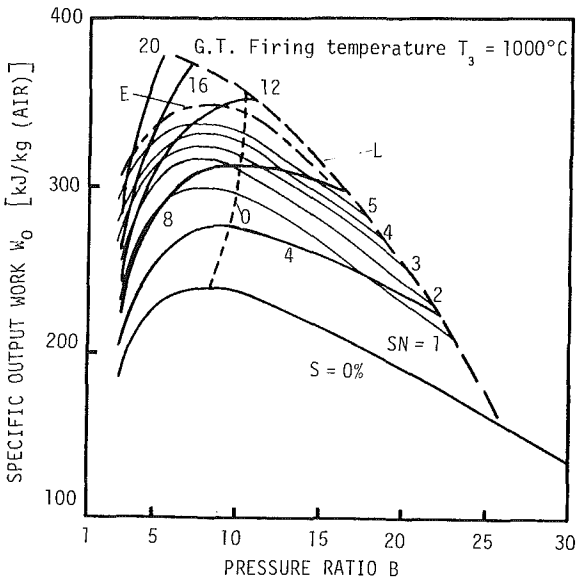

Fig. 9(b)

Fig. 9 Efficiency (*a*) and specific work (*b*) versus pressure ratio; parameter is steam-air injection ratio; *E* = locus of max efficiency; *L* = locus of limits; O = locus of maximum specific work

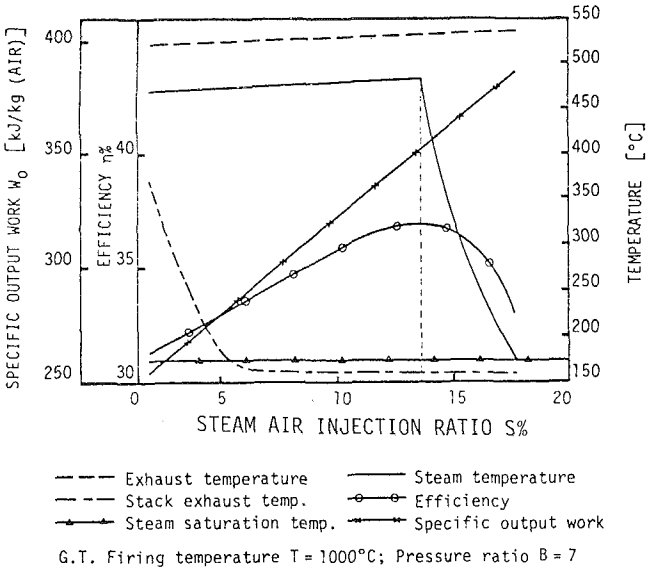

Fig. 10 Some plant parameters versus steam-air injection ratio

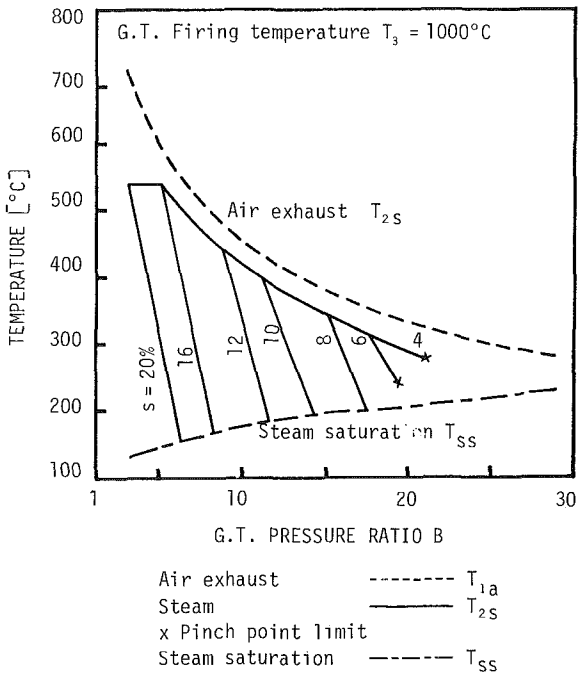

Fig. 11 Exhaust and steam temperature curves versus gas turbine pressure ratio

steam is produced at the highest temperature possible. For steam-to-air injection ratios higher than 6 percent the stage number of the desalting plant increases while the corresponding heat is reduced, and the steam temperature remains at the maximum. This solution is of course the most convenient from an energy saving point of view (maximum efficiency).

For steam-to-air injection ratios exceeding approximately 13 percent, steam temperature decreases until the saturation temperature is reached.

The pinch-point temperature difference is always higher than 80°C for the scheme in Figs. 7(*a*, *c*). The steam-injected gas turbine maximum efficiency is reached when the steam-air ratio corresponds to all available exhaust heat used as well as to the highest possible steam temperature ($S \simeq 13$ percent, in Fig. 8).

Discussion of Results

The main outcome of the present analysis is calculation of overall cycle efficiency, specific work output (referring to the unit mass of compressed air taking part in the combustion), and the feasibility of a sea water desalting plant using heat from exhaust gas.

A multistage flash distillation plant is considered even if, conceptually, a multiple-effect evaporation plant can be utilized.

Major assumptions which underlie the analysis are:

- compressor inlet temperature and sea water temperature $t_1 = t_{sw} = 15°C$.
- compressor inlet pressure and stack back pressure $p_1 = p_6 = 100$ kPa.
- pressure loss in the combustion chamber $Dp_2/p_2 = 3$ percent.

Table 1 Comparison between steam-injected gas turbine and conventional combined gas-steam plants

	Steam-injected gas turbines			Conventional combined gas-steam plants		
Firing temperature, °C	1000	1200	1400	1000	1200	1400
Efficiency, percent	42	46	51	44	50	55
Pressure ratio	15	17	23	6–10	10	14
Steam-to-air ratio, percent	8	11	14	16–12	16	20
Specific work, kJ/kg	300	450	630	420–360	550	720

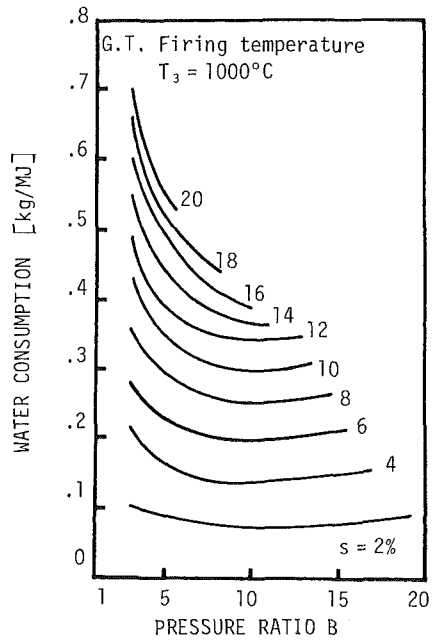

Fig. 12 Water consumption versus pressure ratio

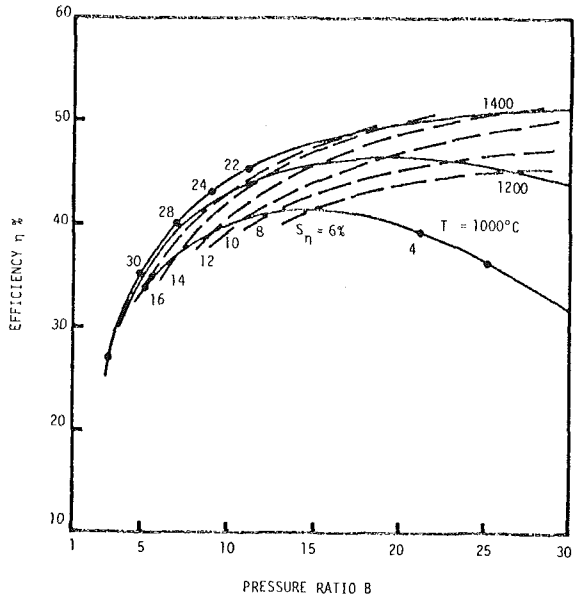

Fig. 13 Maximum efficiency for T = const and iso-$S\eta$ curves versus pressure ratio

• back pressure at the gas turbine exit $p_4 = 105$ kPa when there is an exhaust heat recovery section; $p_4 = 101.5$ kPa without heat recovery section.
• polytropic efficiency: compressor $\eta_{pc} = 0.89$; turbine $\eta_{tc} = 0.90$.
• mechanical efficiency of compressor and turbine $\eta_{m,c,t} = 0.98$.
• combustion chamber efficiency $\eta_{cc} = 0.96$.
• heat exchanger external losses 4 percent.
• fuel low heating value $LHV = 42$ MJ/kg.
• steam upper temperature limit $t_{2su} = 538$°C.
• boiler steam-gas temperature difference lower limit $DT_{sal} = 50$°C.
• pinch-point temperature difference lower limit $DT_{ppl} = 30$°C.
• minimum stack exhaust temperature $t_{5l} = 160$°C.
• auxiliary power requirements as well as steam loop losses have not been accounted for due to their negligible effects.
• gas turbine firing temperature has been investigated in the range $t_3 = 1000$–1400°C.
• gas turbine pressure ratio B, and steam-to-air injection ratio variable in proper ranges according to present application.
• desalination plant performance shown in Fig. 5 is considered.

The analysis has been carried out according to [12, 17].

Results given in Fig. 9 show typical efficiency and specific work curves versus gas turbine pressure ratio, the parameter being steam-to-air injection ratio S. Figures are for a gas turbine firing temperature equal to 1000°C. For each value of B there is a particular $S\eta$ that makes for maximum efficiency.

Curve E is the envelope line $[E = E(B, S\eta)]$ of curves $\eta = \eta(B)S = \text{const}$ and the locus of maximum efficiency.

Specific work curves are given in Fig. 9(b) where curve L represents a boundary that is related to low steam temperature (saturation point) at low pressure ratio. For high pressure ratios (low steam-to-air injection ratios), the limit is the pinch point. This condition is not interesting for the applications. In Fig. 9(b) the locus of maximum efficiency, curve E (which corresponds to the Fig. 9(a) envelope curve) is also given together with the maximum specific work curve O. Minimum stage number of the desalting plant is also given in the figure.

Figure 10 gives some plant parameters: exhaust, steam, stack exhaust, steam saturation temperatures as well as efficiency and specific work versus steam-to-air injection ratio. Gas turbine firing temperature is $t_3 = 1000$°C and pressure ratio $B = 7$. Specific work increases with S. Efficiency rises too when S is lower than S_η while steam temperature rises slightly or remains constant and stack exhaust temperature is reduced. Peak efficiency is achieved when $T_5 = T_{5l}$ and steam temperature is maximum.

In Fig. 11 some cycle temperatures are given versus gas turbine pressure ratio.

Water consumption versus pressure ratio is given in Fig. 12; the parameter is steam-to-air injection ratio. Near the maximum efficiency ($B = 12$ and $S = 10$ percent for $t_3 = 1000$°C) water consumption is about 0.3 kg/MJ; that means a 100 MW plant would consume about 111 m^3/h of pure water.

Figure 8, already discussed, gives an idea of the heat recovered for steam injection and the heat used in the desalination plant besides the desalting stage number.

Steam-injected gas turbine performance has been investigated in the firing temperature range 1000–1400°C. The

envelope curves which represent maximum efficiency [$\eta = \eta(B, S\eta) T_3 = \text{const}$] are given in Fig. 13 where iso-$S\eta$ curves are also shown.

Overall plant efficiencies between 40 and 50 percent can be obtained for pressure ratios between 10 and 20, and steam-to-air injection ratios from 8 to 14 percent.

In the same firing temperature range, conventional combined cycles of performances [18–20] – when afterburning is not considered – are compared with injected gas turbine plant performance in Table 1.

Data reported in Table 1 are close to maximum efficiency conditions and are for plants designed "ad hoc." Conventional combined gas-steam plants present better performances (n and Wo) than steam-injected gas turbines and their compressors are less expensive. However, in steam-injected plants only one turbine exists; there are no steam turbine, condenser, and cooling water system.

Figures 14(a, b) give efficiency and specific work versus steam-to-air injection ratio (parameters are firing temperature and pressure ratio). Curves show that for low pressure ratios it is not convenient to raise the firing temperature and the highest steam injection ratio would be about 22–25 percent (small gas turbine plants), while for medium-high pressure ratios the higher the firing temperature the higher the efficiency and the maximum efficiency steam-to-air injection ratio is.

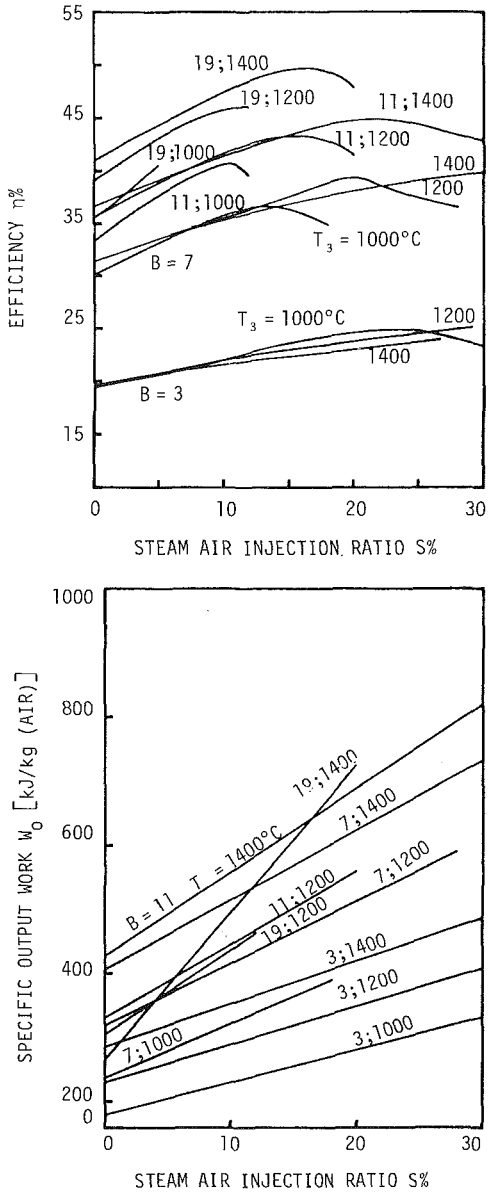

Fig. 14 Efficiency (a) and specific work (b) versus steam air injection ratio; parameters: firing temperature and pressure ratio

Example

As an example a gas turbine plant is considered with main characteristics

- firing temperature 1250°C
- compressor pressure ratio $B = 18$
- compressed air flow $ma = 65$ kg/s

Without steam injection, mechanical power is $P = 20.0$ MW. Exhaust temperature is $t_a = 532.$ °C, and overall plant efficiency $\eta = 34.8$ percent.

Table 2 gives plant performance for the steam-injection case. The assumption is that the same compressor is used while the turbine would be designed ad hoc, as well as the combustion chamber secondary flow.

A maximum of three distillation stages is assumed.

The most convenient steam-injected gas turbine plant would be No. 4 with a steam-to-air injection ratio $S = 12$ percent; since the enthalpy drop in this turbine is about 7 percent greater than one without steam, it would have the same stage number as a dry gas turbine, while the blade height would be greater.

Adopting a direct steam production boiler that produces the steam for the injection and the dry steam to feed the desalting plant, the heat transfer boiler surfaces would be:

- economizer $EA = 2900.$ m^2
- vaporizer $VA = 7700.$ m^2
- superheater $SHA = 1400.$ m^2

The desalting plant consists of a brine heater fed by 3.2 kg/s of dry steam with pressure reduced to 350 kPa. The brine heater surface is

$$BHA = 150. \text{ m}^2$$

Three flash stages must be adopted without brine recycling. There must be a brine-to-distilled water ratio of about 7.5. The brine temperature rise is 26°C in each stage, and each condenser is made up of a heat transfer surface

$$CA = 400. \text{ m}^2$$

Conclusions

The present analysis has pointed out that a steam-injected gas turbine can be equipped with a desalting plant that produces the required pure water from the sea by using exhaust heat.

Table 2 Steam-injected gas turbine main parameters

Plant No.	S, percent	AFR	η, percent	P, MW	t_4, °C	t_{2s}, °C	WF, kg/s	SN No.	SR
1	0	48.3	34.8	20.0	532	—	—	—	—
2	10	41.0	41.6	28.2	546	496	6.5	2	0.90
3	11	40.4	42.2	29.0	548	498	7.2	3	0.55
4	12	39.2	42.1	29.8	549	427	7.8	3	0.80
5	13	37.5	41.4	30.7	550	314	8.5	3	0.80

Main remarks are the following:

- desalting plants based on distillation methods may be employed integrated into steam-injected gas turbine power plants;
- a low number of stages (3–5, max 10) is enough for maximum efficiency;
- waste heat boiler pinch-point difference is not really a limit;
- by adopting a proper steam-to-air injection ratio, efficiency can be increased up to 40–50 percent and specific power output can increase more than 50–80 percent depending on the firing temperature and gas turbine pressure ratio.

The following points have to be considered by power plant designers when they compare traditional steam gas turbine combined plants and simple steam-injected gas turbine plants:

- both plants necessitate a waste heat recovery boiler. The steam-injected gas turbine boiler pressure is lower than that of the combined plant owing to the use of appropriate pressure ratios for steam-injected gas turbines. These pressures should be lower than those of high-pressure gas turbines (high firing temperature aero-derived gas turbines). Moreover, by lowering the steam injected gas turbine pressure ratio, high steam-to-air injection ratios can be adopted, therefore increasing the specific work;
- the steam injected plant does not require a condenser and the condensing water loop (possibly equipped with cooling towers);
- the steam turbine does not exist and then the electrical equipment is simplified. In fact, only one electrical generator is needed or, alternatively, the double coupling at both electric generator shaft ends is reduced to one coupling;
- steam-injected gas turbine plants should have a water treatment section that is a more sophisticated plant than the makeup system in the traditional combined steam and gas turbine plants;
- steam injection leads to improved pollution characteristics due to NO_x emission abatement.

All the above statements make for a low equipment cost for steam-injected gas turbine plants. In fact, comparing a steam-injected gas turbine plant and a conventional combined gas–steam plant having the same power, the latter should have an initial cost 25–50 percent higher than the former due to simplified cycle equipment.

For plants having main parameters according to Table 1, the steam-injected gas turbines have fuel costs 5–10 percent higher than conventional combined gas–steam plants with both plants using the same fuel.

However, high-quality fuel is required, especially for the highest firing temperatures. Steam-injected gas turbine plants can also use coal-derived gas fuel by integrating the plant with a gasification system.

Acknowledgments

This work was financially supported by the MPI (Ministry of Education) and CNR (National Research Council), Italy.

References

1 Hiniker,T. G., and Wilson, W. B., "Increase Gas Turbine Capability to Reduce Your Plant Cost," *Power,* Apr. 1966.

2 Bultzo, C., "Steam Injection a Source of Incremental Power," ASME Paper No. 69-GT-68, 1969.

3 Eddiss, B. G., "Steam Injection Can Improve Gas Turbines," *Power*, No. 6, 1970.

4 Featherston, C. H., "Retrofit Steam Injection for Increasing Output," *Gas Turbine International*, May–June 1975.

5 Digumarthi, R., and Chung-Nan Chang, "Cheng Cycle Implementation on a Small Gas Turbine Engine," ASME JOURNAL OF ENGINEERING FOR GAS TURBINES AND POWER, Vol. 106, 1984, pp. 699–702.

6 Mori, Y., Nakamura, H., Takahashi, T., and Yamamoto, K.., "A Highly Efficient Regenerative Gas Turbine System by New Method of Heat Recovery With Water Injection," 1983 Tokyo International Gas Turbine Congress, Oct. 1983, Paper No. 83-TOKYO-IGTC-38.

7 Roy, P., Schlader, A. F., and Odgers, J., "Premixed Combustion in a Baffle Combustor and the Effect of Steam Injection," ASME JOURNAL OF ENGINEERING FOR POWER, Vol. 96, 1974, pp. 387–393.

8 Bahr, D. W., and Lyon, T. F., "NO_x Abatement Via Water Injection in Aircraft-Derivative Turbine Engines," ASME Paper No. 84-GT-103, 1984.

9 Touchton, G. L., "An Experimentally Verified NO_x Prediction Algorithm Incorporating the Effects of Steam Injection," ASME JOURNAL OF ENGINEERING FOR GAS TURBINES AND POWER, Vol. 106, 1984, pp. 833–843.

10 Fraize, W. E., and Kinney, C. C., "Effect of Steam Injection on the Performance of Gas Turbine Power Cycles," ASME JOURNAL OF ENGINEERING FOR POWER, Vol. 101, 1979.

11 Lewis, J. P., and Kinney, C., "Steam Injection in Medium-Btu Gas-Fueled, High Temperature Combined Cycle Power Plants," ASME Paper No. 82-GT-274, 1982.

12 Cerri, G., "Turbina a gas a ciclo misto con iniezione di vapore in camera di combustione," *La Termotecnica*, Vol. XXXV, No. 1, 1981.

13 Maffei, E., "Deduzione delle relazioni intercorrenti tra i diversi parametri di un impianto di dissalazione tipo 'FLASH' ed ottimizzazione delle superfici di scambio termico," *Premio Italiano Worthington, Studi e Ricerche sul trattamento dei fluidi*, Vol. II, Hoepli, ed., 1970.

14 Biondi, L., and Vaudo, A., "Analisi dei vari processi di desalinizzazione delle acque salamstre mediante evaporazione e recuperi di calore," *La Termotecnica*, No. 5, 1965.

15 Magri, V., "Teoria ed aspetti caratteristici dei distillatori multiflash," *La Termotecnica*, No. 12, 1967.

16 Sideman, S., "Some Design Aspects of Thin Film Evaporators/Condensers," in: *Heat Exchangers Thermal-Hydraulic Fundamentals and Design*, S. Kakac, A. E. Bergles, and F. Mayinger, eds., Hemisphere, New York, 1981.

17 Cerri, G., and Arsuffi, G., "Calculation Procedure for Steam Injected Gas Turbine Cycle With Autonomous Distilled Water Production," ASME Paper No. 86-GT-297, 1986.

18 Cerri, G., "Parametric Analysis of Combined Gas Steam Cycles," ASME Paper No. 82-GT-95, 1982.

19 Lightbody, D. M. S., "Conserving Energy by the Efficient Use of the Industrial Gas Turbine," ASME Paper No. 82-GT-309, 1982.

20 Cerri, G., and Colagè, A., "Steam Cycle Regeneration Influence on Combined Gas-Steam Power Plant Performance," ASME JOURNAL OF ENGINEERING FOR GAS TURBINES AND POWER, Vol. 107, 1985.

The United Kingdom Engine Technology Demonstrator Program

W. J. Chrispin
United Kingdom Ministry
of Defence (PE),
London, United Kingdom

It is generally accepted that development time scales for civil and military aero-engines can exceed those of the airframe they will power. It is now essential to ensure that relevant engine technologies are conceived and proven ahead of commitment to full-scale engine development if future military and civil propulsion requirements are to be met in an affordable way. The scope and scale of UK demonstrator activity has been greatly expanded in recent years in recognition of this need, principally through increased government funding. This paper discusses the principles underlying technology demonstration including the circumstances pertaining in the UK, concluding that a comprehensive program of technology demonstration conducted in a step-by-step fashion and properly integrated with transition to full-scale engineering development will produce significant financial and operational benefits.

Introduction

The pressures on Western governments to reduce the burden of large defense budgets continue to grow. Procurement agencies must examine and implement more cost-effective means of providing equipment to their Armed Services to maintain and enhance their effectiveness in the face of diverse and uncertain threats.

The Gramm-Rudman legislation in the United States targets the elimination of the budget deficit by 1990, resulting in pressures to curtail defense budget growth. In the UK, government spending plans [1] announced in early 1986 project a real reduction in defense spending over the next 3 years. Meanwhile, there is every sign that the threats to be countered will continue to place severe demands on equipment technologies and upward pressures on their procurement costs. Equipment costs accounted for 51 percent of the 1985/86 UK defense budget, compared to 43 percent in 1976/77 [2, 3].

Similarly, in the commercial arena, competition in the worldwide aerospace market produces severe pressure on companies to reduce the R&D costs of their commercial products.

In Europe, collaboration has been widely cultivated as a politically attractive route to reducing the cost to a participating nation of expensive military equipment developments, without unacceptably compromising national objectives. Commercial aerospace continues to produce large-scale European collaborative programs, e.g., Concorde and Airbus, while severe competition in the commercial aero-engine market has produced some notable teaming arrangements between European and US manufacturers, e.g., on V2500, RTM322, CFM56, and CF6-80C2/RB211-535E4. While such arrangements may render full-scale development programs economically viable by broadening the participation and potential markets, they do not necessarily address the fundamental issue of reducing the inherent risk and cost of developing technologically ambitious equipment.

It is generally recognized that the evolution of a new military gas turbine aero-engine is a more protracted process than is allowed by normal project time scales. In the past, project commitment prior to the proven availability, even feasibility, of the appropriate technology has led to grossly inflated development costs through the whole multi-engine bench program pursuing unproductive test routes, propelled by the pressure generated by the needs of the aircraft flight and systems development programs and the in-service date. At entry into service, engines have typically failed to meet their required level of performance. Furthermore, very little attention has been paid to engine durability except to meet the limited level required for qualification. This combination of performance shortfall and inadequate durability has given rise to further large cost penalties and severe operational limitations following entry into service.

This problem is not confined to military engine programs. Nonderivative civil engines have also suffered from the effects of an inadequate technology base, exemplified in the spectacular demise of Rolls-Royce Ltd. in 1971, partly due to difficulties with the embryonic composite fan blade technology.

This paper postulates that a well-conceived and vigorously pursued program of prior engine technology demonstration is essential in ensuring that these past difficulties are not repeated. They will provide downstream cost benefits far outweighing the level of prior investment. In recognition of this, UK government and industry have joined to formulate programs and working arrangements within an overall demonstrator strategy, which seek to prepare engine technology for a wide range of future military and civil applications. The paper describes the scope and management of these engine technology demonstrator programs (TDPs), highlighting some achievements already secured.

Contributed by the Gas Turbine Division of THE AMERICAN SOCIETY OF MECHANICAL ENGINEERS and presented at the 32nd International Gas Turbine Conference and Exhibit, Anaheim, California, May 31-June 4, 1987. Manuscript received at ASME Headquarters February 19, 1987. Paper No. 87-GT-203.

Background to Technology Demonstration in the UK

In summary, the problem faced is one of ensuring that the relevant engine technologies are available ahead of entry into full-scale engineering development. What constitutes "availability" and how the launch of FSED based on emerging technologies is timed will be discussed later. First, the potential benefits of this approach must be identified and accepted as desirable and achievable.

The pressure to establish a comprehensive engine demonstrator program in the UK was largely based on an appreciation of long-standing practices applied in the United States. The UK has conducted a program of high-temperature technology demonstration since 1970 in the shape of the Rolls-Royce High Temperature Demonstrator Unit (HTDU). The MOD(PE) Engines Division believed that major benefits would accrue from extending this concept to all areas of engine technology by establishing an Engine Demonstrator strategy to evaluate concepts conceived through Research programs in component and engine environments. The potential benefits of this approach have been carefully assessed as part of a concerted effort to convince funding agencies within UK government that the required up-front investment will provide a significant return. They can be summarized as follows:

- Reduced risk at entry to full-scale development
- Lower development costs
- Reduced development time scales
- Economy of technology
- More mature product at entry into service

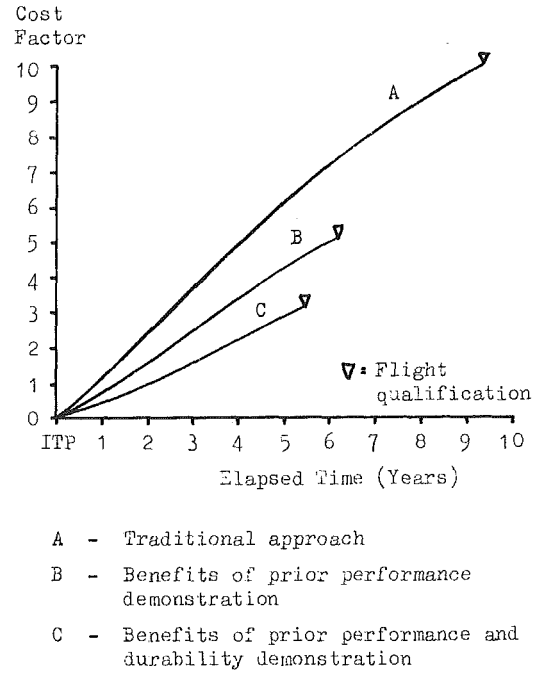

Fig. 1 Cost and time scale benefits of engine demonstration

Risk Reduction. The launch of the full-scale development phase in both military and civil arenas is contingent on obtaining assurance that the threat (or opportunity) identified can be met within an acceptable cost and time scale. The project definition phase of UK military programs is specifically aimed at continuous refinement of the technical, cost, and time scale assessments prior to contract negotiation, against a stated requirement and within resource and funding limitations. Clearly, the ability to provide cost and time scale estimates with tolerance bands reduced through the achievement of critical technology targets in associated demonstrator activity provides significant advantages to the decision-making process at this crucial stage of a project.

Lower Development Cost. Providing the development does not embody requirements significantly beyond those demonstrated in advanced engineering programs, the reduced risk inherent in entering development with proven technology should enable qualification and acceptance to be achieved at considerably reduced cost to that experienced in the past. Figure 1 illustrates the potential savings projected for a fighter engine developed with prior performance and durability demonstration, compared to the traditional 1970s "technology in development" approach.

These comparisons are based on analytical techniques developed within the MOD(PE) Engines Division as part of project time and cost analysis. The distinction between performance and durability demonstration will be discussed later.

Development Time Scales. Figure 1 shows a radically shorter development time scale for an engine based on proven technology. This gives the overall vehicle development program much needed flexibility in selecting the optimum point for full-scale engine development launch. Clearly, this decision can be delayed until critical aspects of the aircraft and flight systems have been settled, and the overall vehicle design is stable. Up to a point, it will be feasible to scale components between demonstration and development without compromising the confidence gained in the component technology.

Much attention has been devoted in the UK to this question of transition from engine demonstration to full-scale development. Decisions on project launch depend on an understanding of the objectives associated with progressive phases of the demonstrator program. This issue will be discussed in the next section of the paper, but in summary it is believed that some overlap between the later stages of an engine durability demonstrator and the early stages of full-scale development can be sustained without risk to the benefits projected.

Economy of Technology. Engine companies can no longer afford to mount separate and parallel developments to satisfy all areas of the volatile aircraft market. They must seek high degrees of commonality within families of engines which meet a broad span of requirements. There are many aspects of engine technology that are common to the diverse requirements of civil and military applications. In order to ensure that the return on the investment in advanced engineering is maximized, programs should be constructed on an integrated basis, thus providing a sound base for expanding product ranges for a reduced development effort. Common elements range from turbine blade cooling configurations to complete HP spools. In the UK for example, Rolls-Royce are actively studying low-risk applications of the military-based XG40 core as the basis for engines of diverse applications, ranging from EFA through advanced trainers to civil engine uses.

Product Maturity. Maturity means the ability of an engine to achieve its specified performance in the designated aircraft with acceptable levels of reliability and component life. Past military engine experience has seen the drive to restore inadequate engine performance following entry into service erode already deficient reliability levels and component lives. This results in continuing development in service, with cripplingly expensive support costs (parts and maintenance labor), and unacceptable operating penalties in the form of mission abort and unscheduled engine removals.

With appropriate prior demonstration and careful matching of the development engine specification to available technology, savings in in-service support costs of a similar order to those projected for the military engine development case shown in Fig. 1 are forecast.

Summary. It has now been accepted in the UK that the conduct of a properly funded and resourced engine demonstrator program is essential in supporting affordable civil and military engine developments. The direct financial savings attributable to the development and support phases of a military fighter engine life cycle procured for UK fleet purposes only, even on a discounted basis, are projected to be some nine times the demonstrator investment. This payback factor should increase for collaborative development effort soundly based on proven national technologies.

The key objectives of the demonstrator program can be summarized as follows:

- To explore and demonstrate the critical technologies under representative engine conditions but in small-scale, comparatively low-cost programs, so as to reduce the risks at project commitment to a low level. This will have highly beneficial effects on development program time scales, on development cost, and on the accuracy with which both these factors can be forecast.
- By addressing the question of durability from the earliest stage in the evolutionary process, to provide for a high degree of maturity at entry into service.

By definition, demonstrator program objectives must be set ahead of specific requirements being defined and covering a wide range of possible applications. This process calls for high-quality engineering study work involving role and mission projections, cycle study and selection, engine and airframe performance synthesis and preliminary design, to identify the most productive technology routes to be followed. Inevitably some initially promising concepts will fail to fulfill their potential, but better such difficulties are exposed at the demonstration stage rather than in the midst of a high-profile, high spending development program.

It must be stressed that an engine demonstrator must not be seen simply as a device for making an early start on a development program. If this were the aim the options available to the customer would be restricted to an unacceptable degree. In fact, the reverse is the case. By illuminating the options, by defining the limits of feasibility over a range of possible needs, a high degree of real flexibility is retained right up to the point of project commitment.

Scope of UK Engine Technology Demonstrator Program

The previous section outlined the overall objectives and potential benefits of engine technology demonstration. This section will describe the scope of the current program, how government and industry interfaces operate, including funding arrangements and program management, and present a model of demonstrator program structure from conception to transition into full-scale development.

Integrated Approach. The availability of limited funding and manpower and other resources makes it imperative that engine demonstrator programs have relevance to a wide range of potential applications. The core of the UK program is the grouping of *basic engine technology* activity. These programs generate the fundamental design concepts, using research findings or data from previous demonstrator phases, and evaluate them at rig and component level. While certain programs are seen as having particular relevance to certain types of engine usage, and indeed the work is conducted along notionally military and civil lines (with some work on a joint basis), especially when matching work to a funding source, the design concepts under assessment are relevant across the board. Allied to these programs is activity that while conducted at rig and component level and again building on research data or other demonstrator program findings, is application specific, for example Plenum Chamber Burning (PCB) for military ASTOVL.

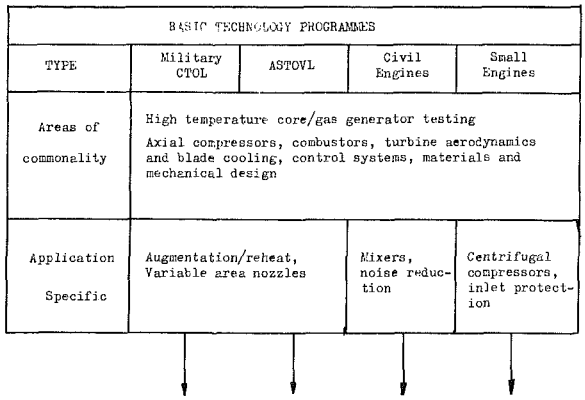

Fig. 2 The integrated basic technology program

Two examples graphically illustrate this interrelationship. Gas bearings are under evaluation in the Advanced Mechanical Engineering Demonstrator (AMED) at the helicopter engine group of Rolls-Royce. Gas bearings have SFC and maintainability benefits of particular interest to the small engine designer. But this technology could clearly benefit larger engine applications and is under active study for advanced military turbofans. Multipass turbine blade cooling was first demonstrated on the Adour-based High-Temperature Demonstrator Unit (HTDU) at the Rolls-Royce Derby facility. Since then adaptations of the multipass method have been applied in large civil engines – the RB211 success will be discussed later – and military HP turbines, and were actively considered for a cooled turbine in a small engine application.

This integrated approach is illustrated in Fig. 2. Four very diverse applications nevertheless have much that can be identified as common to each. Clearly, there will be special requirements within these broad areas of commonality, in addition to those specific items listed, e.g., fan and LP turbine configurations. All these aspects are now under active assessment within the UK program. Furthermore, this technology will be available not only as part of the drive toward new engine applications, but also for the enhancement of current in-service equipment. The RB199 engine in Tornado and the Pegasus in AV-8A, AV-8B, RAF Harrier, and the RN Sea Harrier could shortly benefit from work underway or completed in two demonstrator programs. XG20 (RB199) and XG15 (Pegasus) have both sought through fan pressure ratio and turbine temperature increases to provide thrust growth routes for their respective engines. The turbine technology programs comprise cooling improvements and the use of single crystal blade materials, and have contributed much to the rapid development of single crystal casting in the UK. In both cases, however, the operator will have the option of developing this technology to provide considerable improvements in hot end component life with much reduced in-service support costs.

Beyond the basic component technology programs, *HP spool and engine configuration demonstrators* seek to evaluate the proven components and system designs within an engine environment, enabling component matching, thermal and mechanical interractions, vibration, temperature and stresses to be measured at both steady-state and transient conditions. This highly instrumented phase provides the assurance that engine performance levels are achievable at temperatures and stresses that indicate that overall component life targets will be met.

To gain the necessary confidence in the potential of the engine design to meet reliability and life objectives prior to

commitment to full-scale engine development, a phase of *HP spool and engine durability* testing is advocated. This durability phase will subject HP spools and engines to cyclic endurance evaluation including accelerated mission testing.

Of all the components in a modern gas turbine engine, the HP turbine is the most critical. Development and in-service support costs are particularly sensitive to HP turbine problems. The fundamental difficulty is the sheer complexity of the evolution of a satisfactory cooled blade for a modern engine. The design is a difficult compromise between the conflicting demands of aerodynamics, cooling, and stressing. This is followed by a lengthy manufacturing development phase before testing can even commence. This was recognized in the UK as early as 1970 when the aforementioned HTDU program commenced. This was followed in 1974 by the launch of the Gem-based High-Temperature Small Turbine Unit (HTSTU) addressing the particular problems of a cooled HP turbine for small engine applications. Both programs aimed to evaluate advanced cooling designs at temperatures well in excess of current experience.

In order fully to represent the aerodynamic, temperature, and stress conditions a turbine blade sees in the engine, these high-temperature designs have been evaluated within highly instrumented HP spools. The testing includes a significant element of cyclic endurance running to expose potential thermal fatigue weaknesses as early as possible. Successful applications of HTDU and HTSTU blade cooling technology have shown that any scaling involved need not necessarily compromise the basic soundness of the design concept.

The successful demonstration of HP cooling air feed in the HTDU led to adoption of mixed HP/LP feed for the RB211-22 in 1973. In 1974, following successful evaluation of a multipass design in HTDU, a multipass cooling configuration was embodied into the RB211 long-life blade. This followed rejection of a so-called "multipinge" scheme first proposed for the RB211, after serious cracks developed on an HTDU evaluation of that concept. Straightforward development of the multipass blade followed, and by 1984 the lead set had completed over 10,000 h with no thermal fatigue failures. In early 1986, the HTSTU endurance vehicle embodying a single-pass pedestal HP turbine blade completed 4500 full thermal cycles. The RTM322 engine, now under development by Rolls-Royce and Turbomeca, has a similar cooling configuration, and confidence in the ability of that blade to meet its design life has been boosted by the demonstrator result.

In 1982, funding for the UK Engine TDP was greatly expanded in recognition that a more structured approach to prior demonstration had to be taken. The maximum benefits of programs like HTDU and HTSTU will be fully realized when new concepts are evaluated well in advance of full-scale development.

Government/Industry Relationship. The UK engine technology demonstrator program is wholly conducted through contracts placed on UK industrial concerns. Leading the industrial effort is Rolls-Royce, with Lucas and Dowty-Smiths playing a major role in digital engine control demonstrator programs. Certain programs have been linked to complementary activity carried out by European partners, notably the XG20 program with MTU and Fiat, and the demonstrator for RTM322, the RTM321 with Turbomeca. For the future, there will be scope for governmental and industrial collaboration with the United States on ASTOVL technology programs as part of the US/UK initiative on ASTOVL. However, there are clear signs that in the technology acquisition phase maintenance of a national capability in as broad a span of technologies as possible is preferable. This is a key objective of the UK Engine TDP.

Most demonstrator activity carried out by UK industry attracts government funding. Responsibility for this funding lies jointly with the UK Ministry of Defence and the Department of Trade and Industry. Work funded by these departments is on a cost-share basis with industry, the level of government contribution depending on the nature of the program. The DTI are involved principally in civil-oriented programs, while the MOD, in recognition of its interest in ensuring future trouble-free military developments, has a majority share in military-oriented demonstrator programs. All demonstrator contracts allow for the sponsoring department to exact levies on the companies concerned for future commercial exploitation of the ideas developed.

The integrated demonstrator program represents a major investment of government funding and industrial resources. It is imperative that objectives are clearly defined and programs for their achievement diligently managed if costs are to be controlled and time scales met. With a diverse and technically ambitious program, there are obvious dangers of attention wandering onto interesting diversions from the principal program objectives if these are not well defined and continually monitored against progress. The Engines Division of MOD(PE) is technically and financially/contractually responsible for the conduct of all engine demonstrator activity, and a detailed authorization and cost achievement management system has been developed with industry to ensure that divergence from the technical-cost, and time scale objectives is identified in time for corrective action to be taken.

Program Structure and Transition to Development. We have seen how the integrated Engine TDP is divided into discrete packages in order to formulate objectives and construct programs. At the heart of this packaging process is a philosophy of step-by-step demonstration from concept formulation through to the cyclic endurance testing of virtually flight standard hardware in the durability phase. This philosophy will now be examined and the associated time scales and the relationship to subsequent development activity discussed.

The flow chart in the Fig. 3 overleaf shows the steps involved for, say, a fighter engine program in reaching the final stage of durability demonstration. Ideally, at this stage the hardware should be fully representative of that proposed for subsequent full-scale development. In these circumstances, some overlap between the durability phase and the early stages of full-scale engine development will be acceptable without necessarily jeopardizing the success of the development program. The decisions made at the points shown following component and configuration (sometimes referred to as "performance") demonstration will benefit from extensive data on durability potential from highly instrumented rigs, spools, and engines to support the finalization of the design for durability and then to enable the risks associated with the proposed development engine program to be assessed.

The question of how far the development requirement can exceed the level of technology demonstrated ahead of project commitment will always arouse debate and speculation. There will be understandable pressures to maximize the projected capability of the engine entering development for commercial, political, and operational reasons. As prediction methods improve, the consequences of extrapolating from current experience may be better understood and therefore less risky. As is implied by Fig. 4 (discussed below), there should always be more advanced concepts in earlier stages of demonstration. Discipline must be exercised, to include only those technologies that will not risk the danger of unpredictable problems or failure modes arising to offset the benefits won through prior demonstration. In these circumstances the information generated in the demonstrator testing will permit the inherent risks associated with ambitious development targets to be assessed more objectively.

The chart at Fig. 4 matches the stages described above with

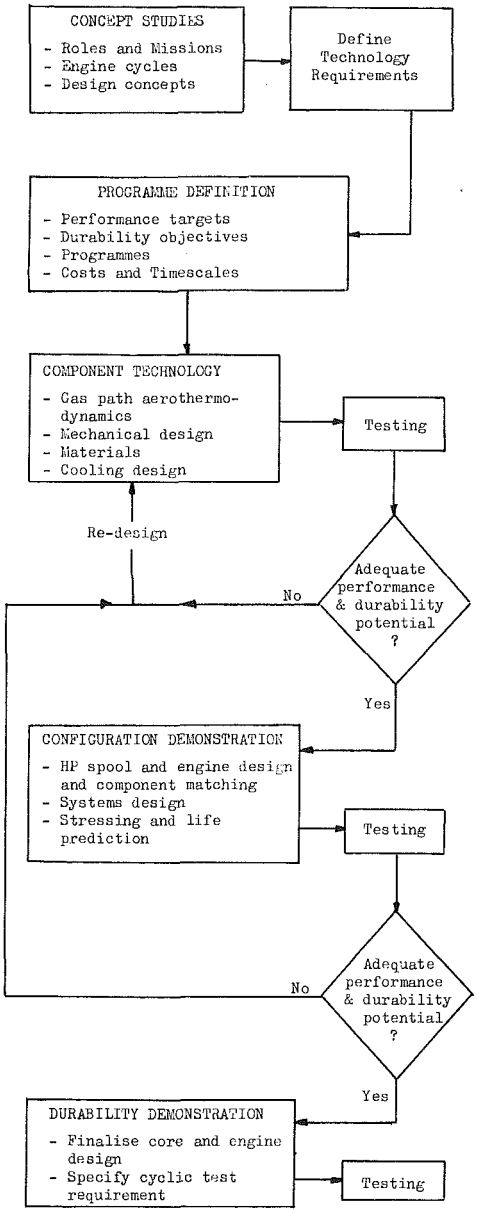

Fig. 3 Demonstrator life cycle

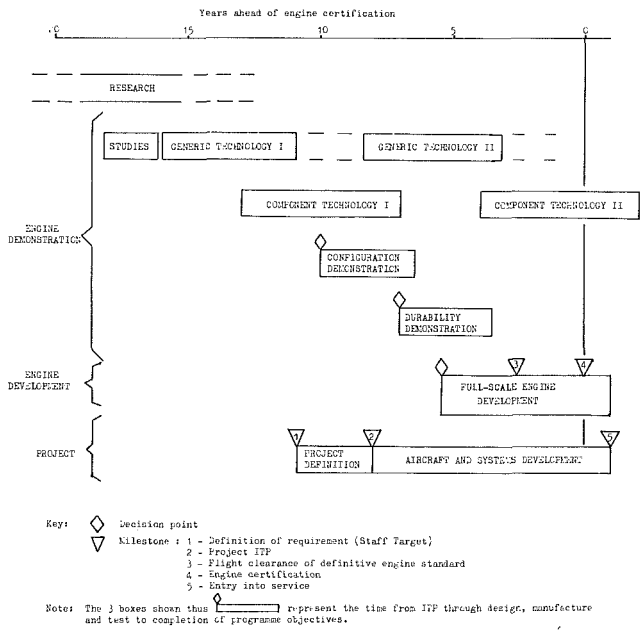

Fig. 4 Time scale of demonstrator stages and transition to development

an idealized time scale for the hypothetical fighter engine program, showing the decision points or "technology gates" that must be passed before the next phase of the program should proceed. The generic technology activity covers programs such as HTDU and HTSTU addressing particularly high risk components. It should be noted that together with the component technology programs, this basic technology activity is ongoing, with stages (shown as I, II, etc.) progressively aiming at more ambitious technical targets based on long-range concept studies. In this idealized model, the propulsion needs of the early aircraft and systems development stages can be served by established engine technology, where reliability will be more important than definitive performance.

Figure 4 demonstrates most graphically the importance and challenge of study work leading to program goal setting. These studies will take place some 6 years ahead of defining a project requirement and *17 years* ahead of certifying the engine utilizing the technology to be demonstrated. Clearly, if the customer is to have the support of well-proven engine technology without unacceptable constraint on his ability to define an operational requirement appropriate to the threat, the preceding generic and component technology programs must be based on structured and well-researched studies. The involvement of the customer, industry, and national centers of expertise such as RAE Pyestock at concept formulation and program definition is an integral part of the UK engine demonstrator strategy.

The Future. Engine demonstration in the UK is at something of a watershed at this time. Some notable successes have been achieved through HTDU, HTSTU, XG20 and XG15, and the XG40 program is now well underway, with good progress being made toward establishing a sound technology base for the mid-1990s fighter engine application and beyond. The next stage in the basic technology program is under active study. Designated the Advanced Core Military Engine (ACME), this program will build on progress already made on component technologies with technical targets in advance of XG40, to provide engine technology for a range of possible future applications. Enhancement and ultimately replacement of the mid-1990s fighter engine, ASTOVL, FIMA, future battlefield helicopters – all these post-2000AD military requirements, and continuing reductions in civil engine operation costs, will place severe demands on technology programs. Materials and innovative mechanical design will undoubtedly loom large in meeting these demanding targets, requiring long gestation periods within extensive component programs.

It is clear from Fig. 4 that at any point in time activities ranging from exploration of high-risk components targeted for EIS in 15 years time to durability demonstration of technology about to enter full-scale development will have to be sustained. This requires a disciplined balancing of activities to ensure that longer-term activities do not suffer at the expense of the exigencies of short-term considerations.

Finally, on the theme of commitment: Demonstrator activity needs the same commitment, by industry and government, given to projects. Vigorous pursuit of ambitious technology targets is vital to long-term commercial strength and an enhanced defense capability. As a set of carefully constructed intentions, the future UK Engine Technology Demonstrator Program now conforms to the model developed in this paper. With the right level of commitment, the considerable benefits

promised through the adoption of this approach will be realized.

Conclusions

Prior technology demonstration can confer considerable financial benefits on full-scale engineering development and subsequent service usage for gas turbine engines in both civil and military applications.

To maximize these benefits, it is important that the proposed development engine does not embody or require technology exceeding that demonstrated. The question of what technology enhancements can be introduced into development at low risk is extremely judgmental, but a more objective assessment is possible with the benefits of demonstrator experience.

Activities within the demonstrator program should be balanced between those addressing long-term objectives and those concerned with shorter-term and perhaps apparently more pressing requirements.

These programs need the same commitment from both government and industry as that afforded project activity. Their successful prosecution is vital to enhanced defense capability and long-term commercial strength.

In the UK, there has been established a balanced, integrated program of technology demonstration with a strategy of extensive government funding. Commitment to pursuing this program is vital if the projected benefits are to be fully achieved.

Acknowledgments

The author is indebted to his colleagues in the Engines Division of the MOD(PE) for their hard work in formulating the demonstrator strategy, which has been the basis of this paper.

References

1 UK Government White Paper "Government Expenditure Plans 1986/87 to 1988/89," Cmnd. 9702-I.

2 UK Government White Paper "Statement on the Defence Estimates, 1986," Cmnd. 9763-II.

3 UK Government White Paper "Statement on the Defence Estimates, 1980," Cmnd. 7826-II.

Introduction and Application of the General Electric Turbine Engine Monitoring Software Within KLM Royal Dutch Airlines

H. Lucas
Propulsion Systems Group,
Engineering & Maintenance Division,
Central Engineering Department,
KLM Royal Dutch Airlines,
Schiphol Airport, The Netherlands

J. E. Paas
Airline Support Performance Engineering,
Design Engineering Operation,
Aircraft Engine Business Group,
General Electric Company,
Cincinnati, OH

KLM Royal Dutch Airlines has been using the General Electric ground-based engine monitoring (GEM) system for the CF6-50 and CF6-80 engines for several years. During the last year, various additional elements of the monitoring system have been introduced to the maintenance departments and are currently operational. This paper describes the introduction and the application of the GEM system within KLM's organization. Also some attention is given to the (potential) benefits that are related to the use of this system, as well as to KLM's engine monitoring plans for the near future.

Introduction

Over the years, factors relating to the safe and profitable management of airline operators' aircraft engines have encouraged the development of effective monitoring systems. While such systems have always been important elements in efforts to provide safe operation of aircraft engines, utilization of such monitoring systems continues to be expanded for economic considerations in today's highly competitive environment. An effective monitoring system provides an airline with a valuable tool to manage its aircraft engines successfully relative to such concerns as availability, maintainability, operating costs, and improved performance.

An important aspect to commercial airline operators in maintaining high levels of on-time service to customers while, at the same time, controlling operating costs is the ability to determine the need and then schedule convenient engine maintenance. Every effort is made to minimize the need for unscheduled engine maintenance and removals, especially away from the airlines' home base. This is particularly important to an airline such as KLM Royal Dutch Airlines with its world-wide operations.

KLM has utilized engine monitoring techniques for a number of years. Such practice became necessary with the introduction of "on-condition" maintenance concepts for the high bypass turbofan engines installed on wide-body aircraft. KLM's B747 and DC-10 aircraft were equipped with aircraft integrated data systems (AIDS) to acquire data for monitoring purposes. This included cockpit monitoring of engine condition as well as further analysis and monitoring using ground-based computer systems.

The introduction in 1983 of the Airbus Industrie A310-200 aircraft powered by General Electric CF6-80A3 engines at KLM and Lufthansa German Airlines has led to an expanded engine monitoring approach. These airlines have participated, as part of a team, with the General Electric Company in the specification and development of an advanced engine monitoring computer system known as "GEM," the acronym for ground-based engine monitoring.

This airline monitoring system incorporates multiple engine performance and mechanical analysis functions into a single ground-based computer system. While the GEM system was initiated to provide extensive monitoring capabilities for the CF6-80A3 engine on the A310-200 aircraft, some of the functions were also extended to monitor KLM's CF6-50 engines (B747 and DC-10 aircraft). Further, the monitoring system has been recently expanded to include other General Electric and CFM International engine models.

This paper will describe the development, introduction, and actual use of the GEM system within KLM Royal Dutch Airlines through the autumn of 1986.

1 GEM Condition Monitoring Program

The ground-based engine monitoring (GEM) computer system provides the capability to monitor and analyze a wide range of engine thermodynamic and mechanical measurements within a single, flexible computer program. The multiple functions contained in GEM include analyses of engine performance (cruise, takeoff, and test cell), vibration signals (including fan rotor imbalance), engine control parameters, and performance simulation. While this system provides extensive monitoring capabilities, among the most important features are the automatic trend shift recognition and alert functions, which are built into the ground-based system. Equally important are the automatic data management capabilities, which provide versatile storage and display of analysis results.

The development of the GEM condition monitoring system

Contributed by the Gas Turbine Division of THE AMERICAN SOCIETY OF MECHANICAL ENGINEERS and presented at the 32nd International Gas Turbine Conference and Exhibit, Anaheim, California, May 31–June 4, 1987. Manuscript received at ASME Headquarters February 17, 1987. Paper No. 87-GT-167.

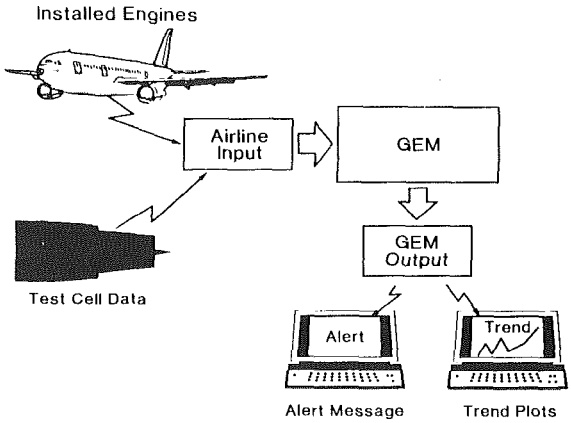

Fig. 1 Engine monitoring information flow

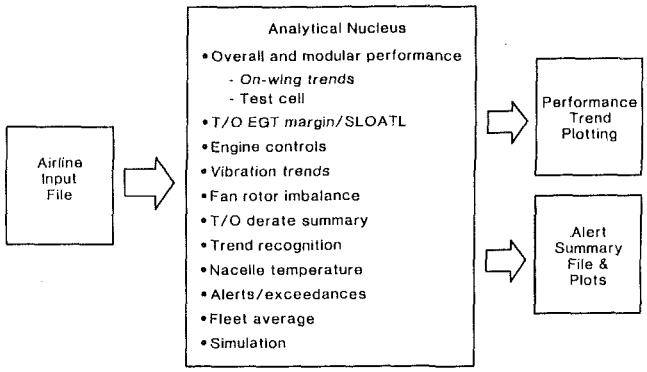

Fig. 2 GEM monitoring functions

has been a team effort. KLM, Lufthansa, and SAS (Scandinavian Airlines System), along with Airbus Industrie, have been working together with General Electric to define, develop, implement, and refine this monitoring system. Although all parties of the GEM team have made valuable contributions to the system development, some major responsibilities can be distinguished. The development of the analytical functions within an agreed software structure, which provides flexible data storage/retrieval capabilities, has been the responsibility of General Electric. The system users, on the other hand, have contributed significantly to the specification of the overall system design to meet their monitoring requirements in addition to the implementation and evaluation of the system at their sites.

The engine monitoring information flow is shown schematically in Fig. 1. Each airline has independently integrated the GEM monitoring system within its own operation. This includes acquiring the engine data and producing an input file in a specific format. At KLM, the installed engine data are retrieved from the on-board AIDS units using cassette tapes that contain data samples taken throughout the flight. Ground-based software developed by KLM is used to select and format desired data recordings from the cassette tapes for GEM processing. The resulting input file contains codes that automatically dictate the GEM analysis functions to be performed during batch computer processing (or interactively as an airline-provided option).

The available monitoring functions are shown in Fig. 2. The analysis results are automatically stored in GEM history files while any appropriate alert of a potential engine problem is provided in a summary report.

These GEM Alert summary reports are used by KLM to monitor their CF6-80A3 and CF6-50 engines. On a regular basis, the KLM trend analyst interrogates the alert summaries from his computer terminal to determine if the trends of the individual engine have changed significantly or if any trend limits are being approached. This contrasts with the more typical situation where the airline analyst must examine performance data for each individual engine, one at a time. When an alert message occurs, the analyst can investigate it further by obtaining supplemental information from the GEM history files using a menu of KLM defined plots and can then recommend appropriate actions if required.

More detailed descriptions of the GEM monitoring system can be found in papers by Dyson and Doel [1], Adamse [2], and Tykeson and Dienger [3].

Although the GEM trend monitoring system has been operational at KLM and Lufthansa for several years, the overall system is still in an evaluation stage at these and a limited number of other airline user sites. This monitoring system is a tool to support the total engine maintenance program at each airline. These airlines can make use of the GEM system versatility and flexibility to adapt the monitoring program to their own needs. As such, the extent of user-provided optional features and the related airline effort required to implement and integrate the GEM monitoring system vary at each airline. Refinement of the basic GEM program, as well as the airline implementation of this monitoring system, continues during this evaluation phase.

2 GEM Functions: From Requirements to Actual Use

The overall implementation process, beginning with the definition of a GEM function and proceeding to its final use, can be schematically divided into the subsequent stages as shown in Fig. 3.

The definition of the airline requirements is discussed during coordination meetings with General Electric and the other members of the GEM team. These requirements might, for example, relate to the desired parameters to be monitored, alert features to be incorporated, provisions to store processed data, or size of the computer program. General Electric has been primarily responsible for the development of monitoring functions resulting from this definition phase.

After the delivery of a function, it can be implemented within the airline's environment. At KLM, the start up of a GEM function takes place mainly within the engineering department. The analysis results of the initial data fed into the new function are discussed and evaluated with General Electric and KLM specialists. When this evaluation is successfully completed, the function can be introduced within the airline's organization. Introduction is done by means of a GEM pilot group, which includes members of KLM's central engineering department and maintenance control.

Nomenclature

AIDS = aircraft integrated data system
CSI = cycles since installation
EGT = exhaust gas temperature
FOD = foreign object damage
GEM = ground-based engine monitoring
GMT = Greenwich Mean Time
HP = high-pressure system
LP = low-pressure system
N2 = high-pressure spool speed
SLOATL = sea level outside air temperature limit
T/O = takeoff
TEMPER = turbine engine module performance estimation routine
VSV = variable stator vane

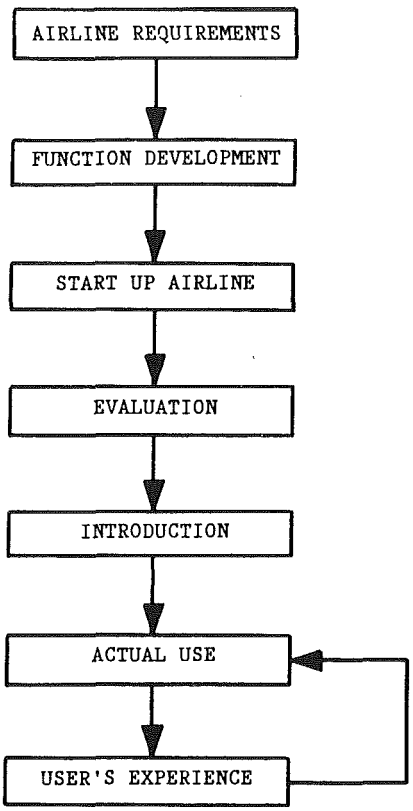

Fig. 3 Implementation process for a GEM function

After this introduction phase, the GEM function can become operational within the airline. Use of the GEM function results in experience, which is fed into the GEM pilot group. This feedback of information plays an important role in the overall evaluation of the function in particular and the GEM monitoring system in general.

The following paragraphs give a more detailed description of the GEM functions that were actually used and the functions that were being evaluated at KLM as of the autumn of 1986.

3 Functions in Use at KLM

As of that time period, the following GEM functions were used at KLM Royal Dutch Airlines:

- alert reporting for a limited number of parameters and
- trend reporting for the overall takeoff and cruise performance.

The abovementioned functions apply to both the General Electric CF6-50 and CF6-80 engines.

Alert Reporting. As was already mentioned in Section 1, a potentially useful feature of the GEM system is the availability of alerts generated during the analyses of the recorded engine data. Alert reporting was incorporated in the system to indicate to the user abnormal situations which, in general, should result in a corrective maintenance action (see Adamse [2]). These alerts can apply to either a single parameter as it is measured during engine operation (e.g., gas temperatures, engine speeds) or to a parameter which is computed (e.g., flow functions, efficiencies).

The KLM GEM pilot group defined which alerts should initially be made operational to maintenance control. As a result of this definition, alerts on the following parameters are in use at maintenance control:

- Exhaust gas temperature (EGT), the gas temperature measured at a location between the high-pressure turbine (HPT) and the low-pressure turbine (LPT).
- Vibration of the low-pressure and high-pressure spools. (Both the CF6-50 and CF6-80 are twin-spooled turbofan engines.)
- EGT margin, the parameter which is a projection of the difference that would exist between the certified redline (or limiting) EGT and the EGT that would be predicted to occur during a full-rated takeoff at sea level and hot-day corner point temperature conditions.
- EGT margin trend shift; when the parameter EGT margin is plotted as a function of time (e.g., engine cycles), it will result in an EGT margin trend. Sudden shifts in this trend can indicate a possible engine problem.

KLM's general philosophy on alert reporting is such that alerts on parameters should be generated before the aircraft crew is made aware of potential engine problems by means of their flight-deck instrumentation. These pre-warnings must provide the airline's engineering and maintenance control departments the opportunity to take corrective actions before the flight crew observes limit excesses. In fact, when the system is optimally tuned with respect to the alert levels, engine limit excesses reported by the flight crew should be limited to unforeseen occasions (e.g., foreign object damage (FOD), sudden failures).

Trend Reporting. Some trend reports, combined with the abovementioned alerts, are made available to the users of the GEM system. The trend reports consist of two parts (see Fig. 4):

- Takeoff engine performance: curves of the parameters T/O delta EGT and the LP/HP spool vibration plotted as a function of cycles since installation (CSI).
- Cruise engine performance: curves of the difference between the actual behavior and the nominal performance of the engine for the parameters EGT, fuel flow, and the high-pressure spool speed (N2) and, just as for takeoff, the LP/HP spool vibration. The time axis for this plot is also CSI.

The general layout of these plots is quite similar to the airborne trend charts which are in use by the flight engineer on the DC-10 and B747 aircraft. Based on these two plots of the GEM system, the trend analyst can get an impression of the overall condition of the engine.

The alerts and trend reports (Fig. 5) are available to the users of the GEM system by means of the information management system (IMS) data bases. Each night after the processing of the acquired engine data (the so-called production run) the most recently generated alerts and the corresponding trend reports are stored on these data bases. The data bases are interrogated on a regular basis by the users of the system. Based on the information stored in the data bases and the crew reports, the maintenance engineers can coordinate their actions.

4 GEM Functions Under Evaluation

Combined with the alert and trend reporting, which were mentioned in the previous section, the following functions are being investigated and evaluated within KLM's engineering department:

- Fan rotor imbalance (CF6-80)
- Test cell TEMPER (turbine engine module performance estimation routine) analysis (CF6-50/-80)
- Variable stator vane (VSV) tracking (CF6-80)

Fan Rotor Imbalance. The fan rotor imbalance function of the GEM system is designed to deduce from the CF6-80

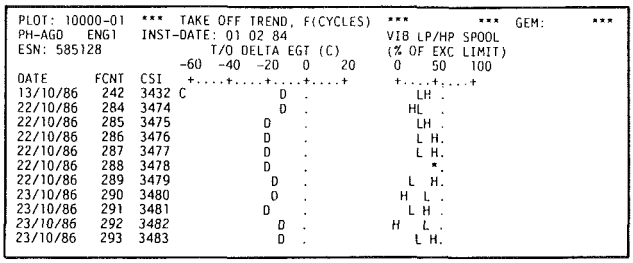

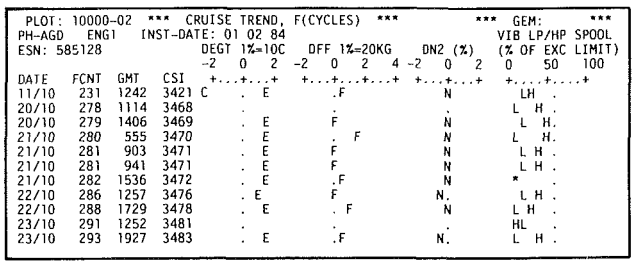

Fig. 4 Takeoff and cruise engine performance trends

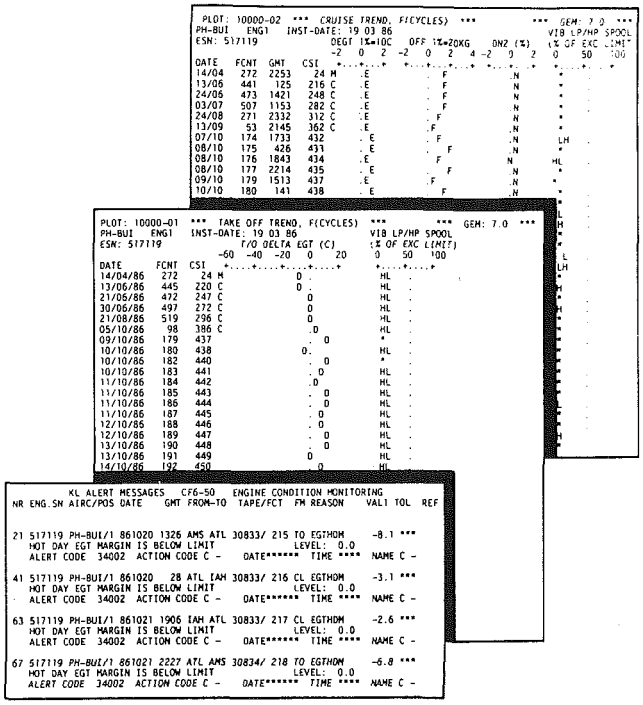

Fig. 5 Combined alert and trend reports

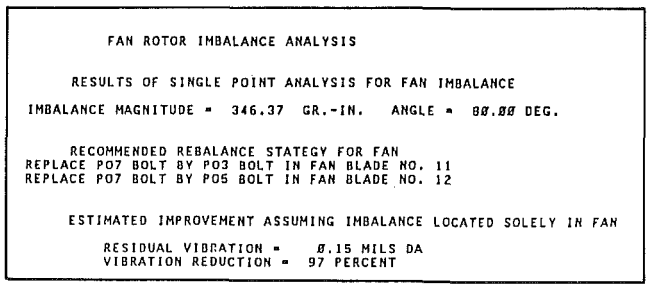

Fig. 6 CF6-80 GEM fan trim balance strategy

steady-state cruise vibration data (fan vibration magnitude/fan vibration phase angle), a fan trim balance strategy that should decrease the fan vibration to an acceptable level. Based on a known configuration of fan balance bolts, the GEM fan rotor imbalance function results will provide straightforward balancing advice (see Fig. 6). A detailed description of this fan rotor imbalance function can be found in Doel [4].

Within KLM, the practical application of this function has to face the following difficulties:

- in general, the fan balance bolt configuration is not readily available for the analysis function.
- the fan rotor imbalance analysis of individual cruise readings has not always been consistent.

Therefore, KLM has developed an application program that can be used in addition to the GEM fan rotor imbalance function. The user of this program can select a number of subsequent results from the fan rotor imbalance analysis. These individual readings are combined into one representative fan vibration magnitude and location of imbalance.

This application program is in the startup phase and the preliminary results will be evaluated by the airline's engineering group. If this program can be shown to produce reliable results it could contribute to a significant decrease in fan trim balance test runs.

Test Cell TEMPER. The GEM system is capable of analyzing the data acquired during a test cell run of an engine. The GEM function that can be used for this purpose is the test cell turbine engine module performance estimation routine (TEMPER). Based on the thermodynamic and mechanical measurements this function estimates the performance (defined by efficiencies and flow functions) of the individual modules of the CF6-50 and CF6-80 engines.

Recently, in cooperation with General Electric, a study has been made of the theoretical and practical backgrounds of the test cell TEMPER function (see Roelofs [5]). The results of this study have led to the decision to begin with a preliminary application of test cell TEMPER before the end of 1986.

Together with this application, a project was started within the propulsion systems group of KLM's central engineering to define and monitor the hardware conditions of the engines tested in the test cell. The combined results of the hardware conditions and the results of the test cell TEMPER function could give KLM a better indication of the correlation between shop output results and test cell data.

VSV Tracking. The GEM function for the variable stator vane (VSV) tracking compares, for the CF6-80 engines, the actual position of the VSV during stable cruise conditions to the nominal scheduled position. For the purpose of VSV monitoring within KLM, a plot has been specified to make the analysis results available to the user (see Fig. 7).

This figure shows some interesting features of the GEM data retrieval software. In essence, the user is completely free in choosing which parameters are to be printed on the output. In this VSV example the following parameters are plotted:

- On top of each plot some basic information is printed (plot title, GEM version number, aircraft registration, engine position, installation date, and the engine serial number).
- The four columns on the left indicate at which date, flightcount, GMT, and cycles since installation, the steady-state cruise data are taken.
- The three semi-graphic curves are the actual results of the VSV tracking function. From left to right, these are (1) the difference between the actual VSV position and the nominal position, (2) a long-term trend of this difference created by applying an exponential smoothing algorithm to the first curve, and (3) a curve which can be used to detect a sudden shift in the VSV tracking (i.e., the difference between the day-to-day VSV trend and the long-term VSV trend).

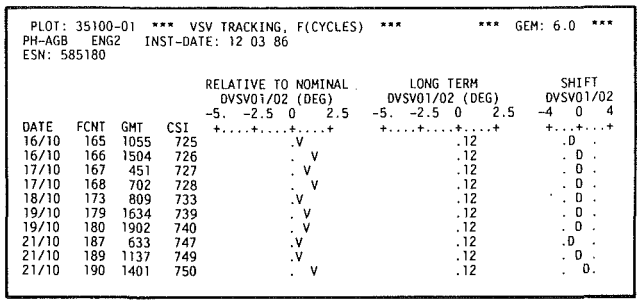

Fig. 7 CF6-80 GEM variable stator vane (VSV) tracking

• The semi-graphic curve for the long-term VSV trend also shows the split-up of the VSV analysis into speed bands (plot character 1 or 2). These speed bands can be used to detect VSV problems that are only apparent in one core spool speed regime.

Since the initiation of this plot, several A310 engines have been tested for VSV tracking. In general the results of this analysis, especially the use of the long term trend, show a good correlation with the established VSV rigging during ground runs.

The GEM function for VSV tracking also incorporates a feature that produces alerts when the actual VSV is not on its optimum schedule. However, in practice this alert reporting is too sensitive for use in daily airline operation and may have to be modified based on further experience.

5 KLM Experience

Using the results of the GEM system (i.e., alerts and trend reporting on a regular basis) for a one year period has shown encouraging results. However, the process of introduction of the system is still in progress. As was already stated in Section 2, a major part of this introduction is done by means of the GEM pilot group. Furthermore, the need was expressed by the users of the GEM system to get more information on the subject of data retrieval. Recently some GEM workshops were held in order to familiarize the users with the GEM concept of data retrieval.

During the last year, it also became clear that aspects of the overall management of such an advanced system as GEM cannot be neglected. Some questions involved in the system management are:

- Are the data properly acquired (sensors, recording)?
- Are the data properly processed?
- How are corrective actions incorporated on the above two subjects?

Based on the fact that KLM realized that good management of the system is of vital importance, a GEM management group was formed. This group will develop the guidelines and the tools which are thought to be necessary to "monitor the monitoring system." The basic discussions within this group have shown that an important point of attention for the good operation of the GEM system is the proper logistic management of the acquired data.

6 Future Developments

In the near future some changes will be made in the presentation of the GEM results (alerts/trend reports). Instead of the daily reporting of alerts and trends to the users, they will only receive the alerts that are triggered by the system. Based on these alerts, they can interrogate the system themselves, as was already mentioned in Section 2.

The major reason to implement the GEM system within KLM Royal Dutch Airlines was the potential cost saving that should be obtained by system use. Most of these cost reductions were summarized in Adamse [2]. During the next years, a thorough study must be made of actual benefits achieved by using the system. In this paper some of them were briefly mentioned (e.g., reduction of test runs for fan rotor imbalance and VSV tracking as well as more detailed and consistent information, which can result in more efficient trouble shooting).

Together with the evaluation of cost savings, the GEM system development will continue within KLM. Information has to be gathered regarding the good and weak points of the GEM system. This information has to be reported in the GEM coordination meetings where it can be discussed with the other users of the GEM system.

In a broader perspective, KLM has also stated their desire for some degree of industry-wide standardization in the field of engine monitoring for the future with regard to data acquisition as well as processing. This could ease the airline's task of setting up and managing monitoring systems for a fleet consisting of various aircraft and engine types.

The recently expanded GEM system will be implemented within KLM during 1987. This will at least provide a single, flexible ground-based program to monitor the current CF6 engines as well as the new CFM56-3 engines installed on the B737-300 aircraft and, in the future, CF6-80C2 engines on the B747-400 aircraft.

References

1 Dyson, R. J. E., and Doel, D. L., "CF6-80 Condition Monitoring—The Engine Manufacturer's Involvement in Data Acquisition and Analysis," AIAA Paper No. 84-1412, 1984.

2 Adamse, P. H. C., "Engine Condition Monitoring at KLM Royal Dutch Airlines," ASME Paper No. 86-GT-300, 1986.

3 Tykeson, T. N., and Dienger, G., "Engine Condition Monitoring Through AIDS—Two System Perspectives," Presented at the ATA E&M Forum, Kansas City, MO, 1985.

4 Doel, D. L., "GEM (Ground-based Engine Monitoring) Condition Monitoring Software CF6-80," Evendale, TM 85-308, 1985.

5 Roelofs, O., "TEMPER Evaluation," Final Study Report No. E113.10.5006, Schiphol-East, 1986.

W. J. Davies
Pratt & Whitney,
Engineering Division,
West Palm Beach, FL 33410

R. A. Baumbick
NASA Lewis Research Center,
Cleveland, OH 44135

R. W. Vizzini
Naval Air Propulsion Center,
Mechanical Components and
Controls Division,
Science and Technology Group,
Trenton, NJ 08628

Conceptual Design of an Optic-Based Engine Control System

Advanced integrated flight and propulsion control systems may require the use of optic technology to provide enhanced electromagnetic immunity and reduced weight. Immunity to electromagnetic interference and pulses is required for integrated systems where flight and propulsion control systems communicate with each other and diverse systems located throughout a composite aircraft. Weight reduction is crucial to the complex engine control systems required for advanced engines incorporating diagnostics, variable geometry and vectoring/reversing exhaust nozzles. A team of Pratt & Whitney, McDonnell Aircraft, Hamilton Standard, and United Technologies Research Center have developed the conceptual design of an optic engine control system, under a contract from NASA Lewis, entitled Fiber Optic Control System Integration (FOCSI). FOCSI is a triservice/NASA joint program designed to provide the optic technology requirements for advanced fighter/attack aircraft.

Introduction

The introduction of integrated flight and propulsion control systems provides operational benefits to the aircraft and engine. Communication between the control systems can provide reduced fuel consumption in cruise and rapid engine transients for increased maneuverability. The purpose of this paper is not to develop a case for integrated controls. These benefits have been established in recent government-sponsored studies, such as the Air Force "Design Methods for Integrated Controls" [1] and "Performance Seeking Control" [2]. Flight tests, such as the NASA "Highly Integrated Digital Electronic Controls" [3], have verified some of these benefits in actual operation. This paper will examine the implications of integrated controls for future engine control system designs.

The engine control hardware to implement this integrated system has become more complex due to the requirement that they become as reliable as flight control systems. This high mission reliability, a goal of one mission abort per million operating hours due to the engine control system, has led to the use of redundant components. The fault tolerant control components being introduced on modern engines approach this goal—but not without penalties. The principle drawbacks are increased mean time between failures, due to the redundant components required for mission reliability, and an associated weight increase.

Another factor in integrated control systems is the fact that they cannot be accomplished without using digital electronic controls. These controls must be made invulnerable to electromagnetic effects through the use of shielded cables. This shielding also increases the weight of the engine control system.

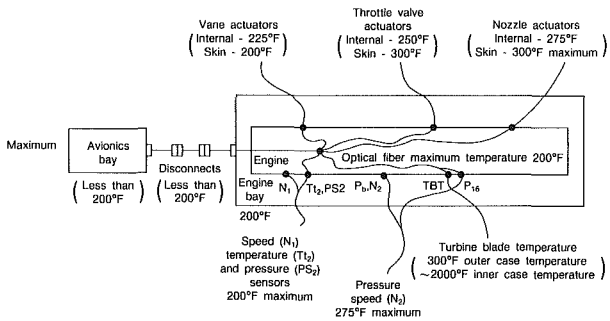

Fig. 1 FOCSI engine temperature profile

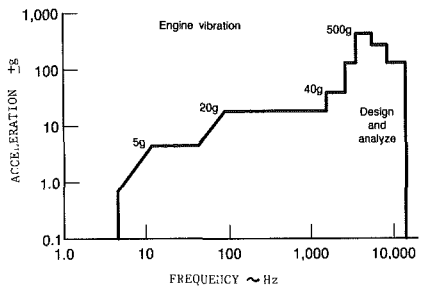

Fig. 2 FOCSI engine vibration profile

A solution to some of these problems may be the use of optics in the engine control systems. Fiber optics are lightweight and immune to all electromagnetic effects. In order to explore optic technology in the gas turbine engine environment NASA Lewis, in conjunction with the Navy, Air Force, and Army, sponsored the Fiber Optic Control System Integration (FOCSI) Program. Pratt & Whitney, McDonnell Aircraft, Hamilton Standard, and United Technologies Research

Contributed by the Gas Turbine Division of THE AMERICAN SOCIETY OF MECHANICAL ENGINEERS and presented at the 32nd International Gas Turbine Conference and Exhibit, Anaheim, California, May 31–June 4, 1987. Manuscript received at ASME Headquarters February 17, 1987. Paper No. 87-GT-168.

Center teamed on FOCSI to establish the state-of-the-art of optic technology as applied to gas turbine engines, produce a conceptual system design and develop a plan for development, and eventual flight test, of an optic-based engine control system. This paper will focus on the conceptual optic control system design.

Requirements

The introduction of optics to the engine means that two areas need to be addressed to establish a realistic optic conceptual design. The first requirement is to establish the operating environment for the optic components on the engine. The baseline aircraft is the Navy multimission fighter attack aircraft with a maximum speed of Mach 1.5. Pratt & Whitney (P&W) and McDonnell Aircraft reviewed the actual operating experience for the F100 engine and the F-15, F-18, and AV-8B aircraft to develop a composite temperature and vibration spectrum for a typical engine nacelle. For this application the maximum fiber optic cable/connector temperature was 200°F. The maximum temperature for the actuators and sensors varies between 200°F and 300°F, depending on the location on the engine. Figure 1 illustrates the temperature distribution around the engine. The minimum temperature is −65°F.

The vibration spectrum to be considered in the specification of all the optic components is shown in Fig. 2. As with the temperature this is a composite of actual operating experience.

The second requirement for the optic conceptual design is the sensor ranges and accuracies necessary to control and protect the engine. For FOCSI these are based on the requirements established by P&W in the Air Force Integrated Reliable Fault Tolerant Control For Engines (INTERFACE) and the Navy Advanced Fuel Management (AFM) programs. Both of these programs are structured to investigate control system hardware, digital electronic controls, sensors, actuators, pumps, and a data bus appropriate for advanced gas turbine engines. The selected sensors and their requirements are shown in Table 1. These INTERFACE and AFM components provide a realistic baseline for comparison with the optic devices selected for the FOCSI conceptual design.

Table 1 FOCSI sensor requirements

Sensor	Update	Total Required signal Accuracy (Whichever greater)	Signal resolution	Signal Range Low	Signal Range High
Frequency					
N1	10 ms	± 0.5% Point (PT) 7 rpm	2 rpm	500	15,000
N2	10 ms	± 0.5% Point (PT) 7 rpm	2 rpm	1500	20,000
WFAUG (4)	10 ms	± 2.0% Point (PT) or 20 pph	5 pph	100 pph	30,000 pph
WFGG	40 ms	± 2.0% Point (PT) or 40 pph	10 pph	200 pph	20,000 pph
EGT	20 ms	± 20°F	5 °F	0°F	3000°F
PS2	120 ms	± 1.0% Point (PT) or 0.03 psi	0.01 psi	1.5 psia	40 psia
PT6	10 ms	± 1.0% Point (PT) or 0.01 psi	0.025 psi	5 psia	120 psia
PB	10 ms	± 3.0% Point (PT) or 4 psi	0.2 psi	25 psia	700 psia
Analog					
TT2	120 ms	± 3° F	0.5°F	−65°F	500°F
Fuel temp	120 ms	± 5° F	2.5°F	−65°F	350°F
EGT	20 ms	± 5 °F	2.5 °F	500°F	3000°F
OPT pyro	20 ms	± 5 °F	2.5 °F	2 VDC	10 VDC
LOD	60 ms	± 5 % Full Scale	0.4%	0 VAC	50 VAC
Position					
PLA	10 ms	± 1.0 Degree (Deg)	±0.25 Deg	0 Deg	130 Deg
MVGG	3 ms	± 5% PT or 1% FS	10 pph	200 pph	20,000 pph
MVAUG	3 ms	± 5% PT or 1% FS	5 pph	100 pph	40,000 pph
Variable geometry	3 ms	± 1 Deg	0.25 Deg	-40 Deg	+ 5.0 Deg
Fuel bypass	3 ms	± 5 % PT or 1% FS	10 pph	200 pph	20,000 pph

Electronic Control Location

The use of optics in the engine control system requires a reevaluation of the implementation of the digital electronic control. The two issues considered are a combined flight and propulsion control or independent units and the location—on or off engine. The use of optics does not change the classical approach to implementation of the digital electronic controls. Development of the engine and control system precedes the aircraft and flight control by several years. This requires that the control logic and hardware be tested before an airframer, who would select a flight control system, has been selected. The multiplicity of possible system designs, dual, triplex, or quad, directly impacts the engine control designer's ability to develop and qualify both control logic and sensor redundancy levels. The result of an optic combined system would be program delays and added costs to develop multiple systems. Several other factors that influence implementation are the issues of fault propagation in a combined system and accountability in the event of a failure. Results of the DMICS program, by both General Dynamics and Northrop, indicate that the implementation of advanced integrated operating modes requires only a data bus for communication between flight

Nomenclature

A/C = aircraft
AFM = advanced fuel management
Aj = nozzle area
CIVV = compressor inlet variable vanes
Comp = compressor
deg = degree
EGT = exhaust gas temperature
EMS = engine monitoring system
F = Fahrenheit
FADEC = full authority digital electronic control
FMa = augmentor fuel flow
FMg = gas generator fuel flow
FOCSI = Fiber optic control system integration
FS = full-scale
g = force of gravity
GaAs = gallium arsenide
INTERFACE = integrated reliable fault tolerant control for engines
I/O = input/output
IOC = input/output controller
lb = pounds
Mbps = megabits per second
MIL-STD-1773 = fiber optics data bus
MIL-STD-38999 = connectors, electrical
ms = millisecond
MUX = multiplex
N/A = not applicable
NASA = National Aeronautics and Space Administration
N1 = low compressor speed
N2 = high compressor speed
Pb = burner pressure
PLA = power lever angle
pph = pounds per hour
psi = pounds per square inch
psia = pounds per square inch absolute
Ps2 = inlet pressure
PT = point
PT6 = exhaust pressure
P&W = Pratt & Whitney
PWM = pulse width modulated
Pyro = pyrometer
rpm = revolutions per minute
sq-in = square inches
TBT = turbine blade temperature
Tt2 = inlet temperature
VAC = volts alternating current
VDC = volts direct current
Wfa = augmentor fuel meter
Wfg = gas generator fuel meter
Wft = fuel temperature

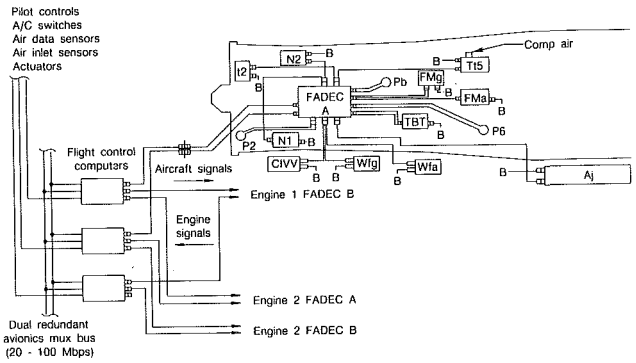

Fig. 3 FOCSI conceptual engine control system

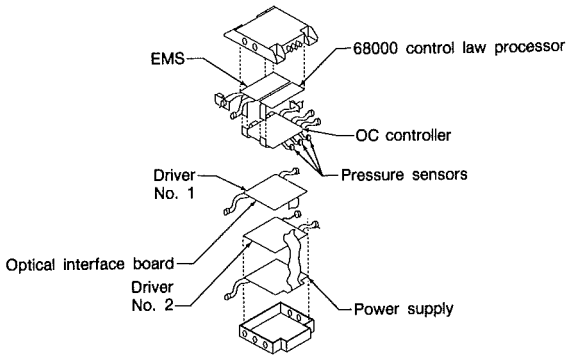

Fig. 4 Optic FADEC construction

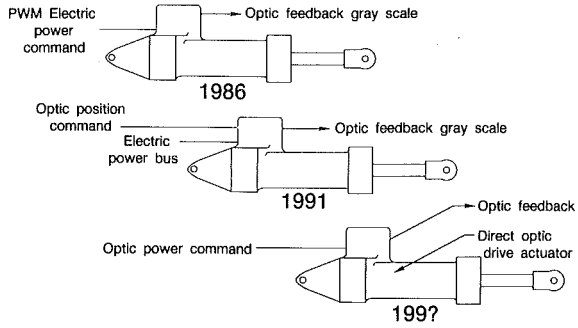

Fig. 5 Optic actuator evolution

and propulsion controls. This simple optic link and appropriate fault detection logic greatly reduce the possibility of common mode failures. In the event of a failure in a combined system accountability will always be an issue.

Combined flight and propulsion controls would result in the digital electronics being unified and the government, airframers, engine manufacturers, and control supplier being divided. For these reasons the digital electronic controls in the P&W FOCSI control system are independent of the flight control system, except for communication of an optic data bus.

The full authority digital electronic control (FADEC) in an optic-based system could be located on the engine or in an off-engine electronics bay in the aircraft. All current P&W military and commercial digital electronic controls are engine mounted. This implementation provides minimum weight, good hardware reliability, and easy maintenance. These factors may vary in degree for an optic system but the factors still favor an engine-mounted FADEC. In a wire-based system moving the FADEC to an off-engine bay can add up to 500 lb of electrical cables to a twin engine aircraft weight. With optics this weight will be reduced to approximately 60 lb—but it is still a penalty to the total aircraft system.

The second factor in favor of an on-engine FADEC is hardware reliability. Off-engine mounting introduces additional connectors, which tend to reduce system reliability. The engine-mounted FADEC is tank fuel cooled, with a maximum temperature of 165°F. The efficiency of this liquid cooling medium allows the heat sink temperature in the FADEC to reach a maximum temperature of 195°F. The heat sink temperature of an air-cooled FADEC in an avionics bay can reach a maximum temperature of 205°F with 105°F cooling air temperature. This difference in semiconductor heat sink temperature is due to the effectiveness of the liquid fuel as a heat transfer medium.

The third factor in the selection of an on-engine FADEC is improved maintenance. Currently the engine and FADEC are a self-contained unit, which can rapidly be removed and replaced in less than 15 min. An off-engine location increases the number of disconnects to be made and the number of modules to be removed. FADEC is designed to be a line replaceable unit so there is no benefit to an off-engine location where it can be opened and individual boards removed and replaced.

Conceptual Optic System Design

The optic system selected for evaluation in the FOCSI program has on-engine FADEC, optic sensors, optic-based actuators, and an optic data bus for communication with the aircraft flight control system. The conceptual optic system is shown in Fig. 3. The following paragraphs will describe the features inherent in each of these optic-based components.

FADEC. The basic design of the optic FADEC is derived from the advanced design being developed and tested in the INTERFACE program (Fig. 4). To implement an optic system the input/output (I/O) circuitry in this control must be changed. The basic computer architecture, processors, memory, internal data bus, power supply, etc., remain unchanged. To incorporate optics into FADEC the connectors must be changed to accommodate optical fibers. Optic sources, light emitting, and laser diodes must be installed at the I/O interfaces. Detectors to convert the optic to electric signals must be installed at the I/O interfaces. To compensate for these additions to the FADEC I/O, most of the electromagnetic protection devices currently in FADEC can be removed. These devices include tranzorbs, filter pins, filters, and protection diodes. The net result is no change in circuit board area (FADEC size and weight) and increased immunity to electromagnetic effects.

Three fast response, high accuracy engine pressure transducers are located in the FADEC. These are used for control of engine pressure ratio and engine protection. Since these pressure sensors are located in the engine-mounted FADEC they may be coupled, through pneumatic tubes, directly to the pressure source probe. This design eliminates the cost associated with the development of a new optic pressure transducer.

Optic Data Bus. An optic data bus will be used in the FOCSI system for communication between the engine and flight controls. This optic link is used to transmit operating signals, FADEC status, power lever angle, vector and reverse request, and Mach number. Integrated system operation, for maximum weapon effectiveness, will add signals, such as angle of attack and side slip angle, to this complement. The bus architecture selection is predicated on current and planned Military Standards for optic buses. Potential candidates include MIL-STD-1773, token passing ring, and linear token passing optic configurations. For the baseline optic system P&W and McDonnell Aircraft have selected a 100 MHz token passing ring. This selection may be revised in the future as the

Table 2 Fiber optic sensor technology summary

Engine/Aircraft Control System Component	Technology status: Flight ready now	Flight ready by 1990	Flight Ready beyond 1990
Engine/aircraft sensors			
o Speed			
1. Magnetic force		✓	
2. Reflective/absorbtive		✓	
3. Electromagnetic with optical interface			✓
o Temperature			
1. Black body		✓	
2. Photoelastic			✓
3. Fluidic (Optical I/O)		✓	
4. Fabry-Perot			✓
5. Pyrometer	✓		
o Pressure			
1. Microbend		✓	
2. Photoelastic			✓
3. Fabry-Perot cavity			✓
4. Capacitive		✓	
o Flowmeter			
1. Electromagnetic with optical I/O			✓
2. Fluidic with optical I/O		✓	
3. Acoustic			✓
4. Polarization			✓
o Actuator			
1. Gallium arsenide transistor			✓
Time division mux		✓	
Coherence multiplexer			✓
Wavelength division			✓
Opto-hydraulic servo			✓
Photo transitors	✓		
Optical fibers	✓		
Light emitting diode	✓		
Laser diode		✓	
Couplers		✓	

Table 3 Optic sensor selection

Control component	FOCSI approach	Fibers
N1 and N2 sensor	Reflective surface	2
Tt2 and Wtt sensor	Fluidic (air) oscillator with optical I/O	2
EGT sensor	Same as Tt2	2
Wfgg and Wf Aug	Fluidic (fuel) oscillator with optical I/O	2
Actuator position feedback	Time div mux'd gray code scale	2
Actuator servovalve drive	High temp (GaAs) phototransistor and high current torque motor driver in actuator	2
P s2, Pb and Pt6	Pneumatic lines to engine mounted FADEC	N/A

standards evolve and mature with little or no impact on the FOCSI system.

Optic Sensors. The optic sensors for the FOCSI system were selected based on the maturity of the technology and, therefore, the ability to be ready for flight test in the early 1990s. Further, these devices had to exhibit three additional characteristics: no compromise in current reliabilty levels, no weight increase, and the ability to be easily made redundant.

The sensor requirements for a modern gas turbine engine were defined in Table 1. Wire-based devices exist that can meet these high standards. After reviewing a variety of optic sensor concepts and their availability (Table 2), P&W reached two conclusions about optic engine control sensors. There are a variety of optic devices that have the potential to sense the parameters required for engine control and protection. However, almost all of these devices exist only in the commercial or laboratory environment and will require significant development before they can be considered for use on a gas turbine engine. For the FOCSI conceptual design the sensors listed in Table 3 were considered to have the most potential to be ready for flight test in the early 1990s. This selection was based on both the optic capability and vendor experience with similar, wire-based, engine sensors. This list must be considered as a preliminary selection. As optic technology develops and matures the FOCSI conceptual design is flexible enough to adapt to new devices.

Actuators. The actuator designs for the FOCSI engine control system are based on concepts developed as part of the Navy AFM program. The program established that direct drive actuators have significant benefits in terms of weight, reliability, and simplicity when compared to conventional low-power electro-hydraulic valves. For these reasons the direct drive concept was maintained in FOCSI. There is currently no way to transmit the 40 W of power required for each actuator optically. Therefore an evolutionary process for development of this optic drive actuator has been developed (Fig. 5).

The first step is to apply today's technology. That is, to maintain the direct electrical drive but change the feedback device to an optical encoder. This serves to introduce optics, reduce actuator weight, and increase electromagnetic immunity. This last benefit is achieved by replacement of low-level electrical feedback signals, which must be heavily shielded, with a simple multiplexed optic signal.

The second optic actuator design, which could be realized in about five years, with some development effort, is based on a NASA Lewis sponsored program for optic drive actuators [4]. This actuator maintains the optic encoder of the previous design. The drive mechanism is revised to connect the actuator directly to the aircraft 28 V power bus rather than provide electrical pulse width modulated (PWM) signals from the FADEC. The electrical power is then switched, in the actuator, by an optic signal from the FADEC. This system further enhances electromagnetic immunity as the bus power signal is less vulnerable to external interference than the PWM signal. However, this system requires the use of high-temperature, high-power semiconductors on the actuator. Materials, such as gallium arsenide, have the capability to operate in the projected environment but, currently, no high power switches are available.

The ultimate design for an optic direct drive actuator would eliminate all electrical connections to the actuator. Both drive and feedback would be totally optic. As previously described the feedback encoder exists today. Direct optic drive concepts are being investigated by several manufacturers. The final system, available for test sometime in the 1990s, may employ a combination of technologies, such as optic control of a fluidic amplifier, for the actuator drive mechanism.

Cables and Connectors. The final component required to bring together an optic-based engine control system is the optic harness. The optic cables and connectors must be designed to operate in the same thermal and vibration environment as the sensors, actuators, and FADEC. Optical fibers are available that can operate up to 392°F. This exceeds the temperatures projected for the FOCSI system. The effects of engine vibration are an unknown factor at this time. Early in the development of the optic system, sample cables must be fabricated and subjected to combined temperature and vibration tests to qualify the design.

Optic connectors are available in the engine MIL-STD-38999 configuration. A drawback of the current designs is that they require number 16 contacts for the optical fibers. This large contact size reduces the density of the connector when compared to the number 20 or 22 contacts used with wire systems. These smaller contacts for optical fibers are currently being developed for commercial applications and should transition to engine quality MIL-STD-38999 connectors in the next five years.

Optic Conceptual Design Benefits Summary

The immaturity of optics as an engine control technology makes it difficult, if not impossible, to quantify benefits. However two overriding trends are obvious.

An optic system will weigh less than a comparable wire-based system. This is due to the materials in the optic devices themselves and the elimination of wires and shielding from the engine harness. This combination of factors can reduce total control system weight by up to 25 lb for the engine-mounted FADEC configuration.

The second benefit of optics is immunity from electromagnetic effects such as lightning, radar, nuclear pulse, etc. This immunity is critical to insure the survivability of

future systems where the aircraft and engine will be required to operate routinely in severe electromagnetic environments. Increased survivability will increase weapon system effectiveness since the aircraft will not be inhibited for routine operations under severe electromagnetic conditions.

References

1 Clifton, J. V., Smith, K. L., Lehtomaki, N. A., and Langton, R., "Design Methods for Integrated Control Systems," AIAA Aircraft Design, Systems and Technology Meeting, Oct. 17–19, 1983, Paper No. AIAA-83-2562.

2 Shaw, P., Foxgrover, J., Berg, D. F., Swan, J., Adibhatla, S., and Skira, C. A., "A Design Approach to a Performance Seeking Control," AIAA/ASME/SAE/ASEE 22nd Joint Propulsion Conference, June 16–18, 1986, Paper No. AIAA-86-1474.

3 Yonke, W. A., "Integrated Flight/Propulsion Control: HIDEC Modes," NAECON 1984 Conference, McAir Number 84-011, May 21–25, 1984.

4 Berek, J. M., Grantham, D. H., and Eder, M., "Optical Switching of High-Temperature GaAs Devices for Digital Control of Aircraft Direct-Drive Actuators," NASA Publication, NASA CR-179456, June 1986.

R. A. Harrison

M. S. Yates

Dowty & Smiths
Industries Controls Ltd.,
Cheltenham, Glos. GL51 OTP,
United Kingdom

Gas Turbine Fuel Control Systems for Unmanned Applications

The technique of controlling engine acceleration has made possible gas turbine controls with simple hydromechanics and a minimal number of inputs into the electronics. This paper describes a control and electrical power generation system developed for an unmanned aircraft gas turbine, and the results obtained from the development engine running carried out with it.

Introduction

Unmanned aircraft are being used in an increasing number of applications such as reconnaissance, targets, and missiles. Target drones have to mimic the movements and attack formation of enemy aircraft and missiles must be capable of outmaneuvering enemy defenses. These two applications in particular require a propulsion system capable of high-speed and/or high-altitude flight. There is therefore an increasing number of small turbojets designed for such applications that require a low-cost automatic engine control system with a level of integrity to suit the unmanned role. The air vehicle also requires electrical power from the engine to drive its control surfaces, radar, telemetry, and flight control systems. An integrated digital engine control and power generation system intended for use in this field has been developed and is described below.

Although the system was initially intended as a single "bolt-on" unit, it can be repackaged into separate components and these mounted on the engine or airframe as the application demands. The system was first designed for the Hindustan Aeronautics Limited PTAE-7 engine and consisted of a 2-kW alternator, a 2-kW "burst firing" voltage regulator, a gear pump, a fuel metering unit (FMU), and a digital electronic control unit (DECU). All of the components were mounted in the engine nose cone.

The next application was the Alfa Romeo ARTJ-140 engine. The system components remained the same except the voltage regulator was not required and the alternator was designed to act as a starter motor. In this application the starter alternator and the fuel pump were mounted in the engine nose cone, the fuel metering unit on the engine compressor casing, and the DECU in the airframe.

This paper will concentrate on the development system designed for the Teledyne CAE 373-8 turbojet intended for use in target drones. The system configuration is similar to the HAL unit except that the regulator has been separated from the fuel control components and the alternator produces 4-kW. The majority of control development was carried out in the Teledyne CAE altitude test facility with the hydromechanics mounted in the engine nose cone and the DECU in the facility control room for ease of access.

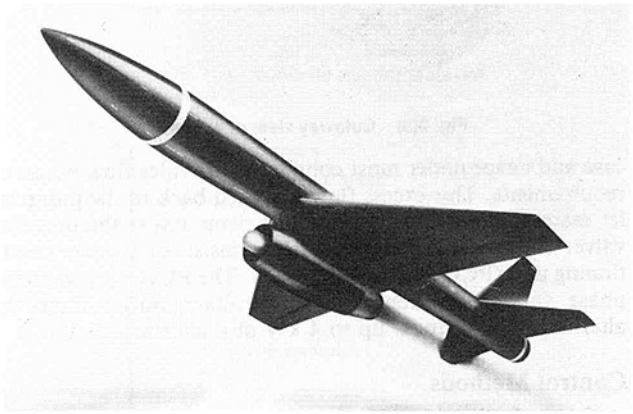

Fig. 1 Unmanned aircraft

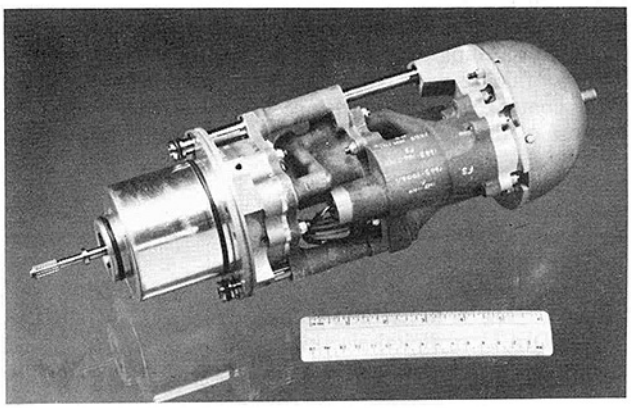

Fig. 2 Teledyne CAE 373-8 RPV engine control system

The system can be divided into two distinct sections, engine control and power generation. The engine control works in the following manner: The DECU compares engine speed obtained from the alternator with demanded speed from the airframe. The fuel metering unit (FMU) contains a valve driven by a stepper motor. In response to an error the DECU drives the stepper motor moving the valve and altering the quantity of fuel delivered to the engine. The pump is sized for the worst

Contributed by the Gas Turbine Division of THE AMERICAN SOCIETY OF MECHANICAL ENGINEERS and presented at the 32nd International Gas Turbine Conference and Exhibit, Anaheim, California, May 31–June 4, 1987. Manuscript received at ASME Headquarters February 5, 1987. Paper No. 87-GT-76.

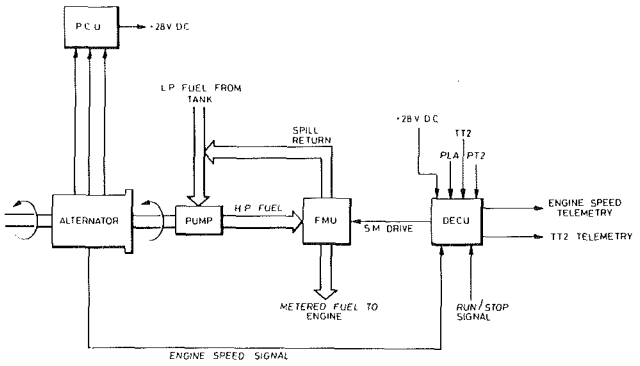

Fig. 3(*a*) System block diagram

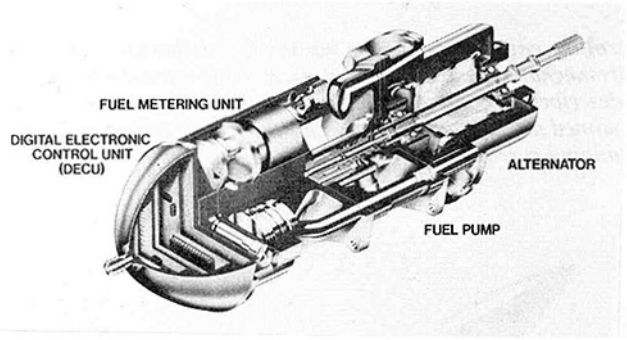

Fig. 3(*b*) Cutaway view of system

case and hence under most conditions provides flow excess to requirements. This excess flow is spilled back to the pump inlet maintaining a constant pressure drop across the metering valve. The power generating system consists of a power conditioning unit (PCU) and an alternator. The PCU extracts three-phase variable-frequency variable-voltage power from the alternator and outputs up to 4 kW at a constant 28 V d-c.

Control Methods

The control laws have been based on closed loop spool acceleration (Ndot). It was envisaged that this would be the primary control method for starting and power transients. T6 limiting was employed as a starting control but was removed once confidence with Ndot had been gained. Originally the Ndot control was configured as a slave datum system but because of difficulties in resetting the datum it was restructured to the form described in this paper. During lightup and starting the fuel valve is restricted in its movement by software schedules so the acceleration control loop is broken; with a slave datum system the datum must be reset so that it may resume control smoothly.

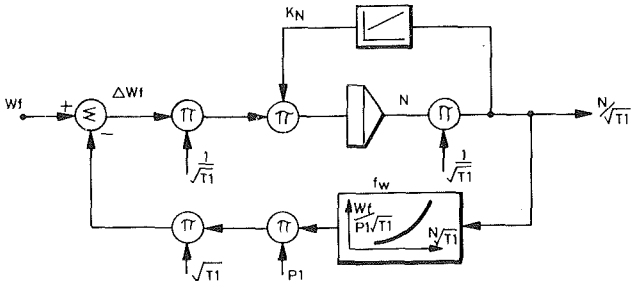

Fig. 4 Simple turbojet model

The introduction of a lightup fuel ramp improved ignition performance and this was made simpler by the restructuring of the control.

Design Considerations. Factors that have affected the design and development of the control software include air vehicle requirements, loop dynamics, engine limitations, and cost reduction.

(*a*) *Engine Dynamics.* To analyze the control loops, a model of a single-spool turbojet was defined that had representative steady-state and dynamic behavior yet was uncomplicated. By linearizing about steady state it was possible to assess the effect of operating conditions on control loop gains.

The model was obtained by simplifying a detailed thermodynamic representation of a single spool turbojet. It was assumed that mass air flow was the same at all points in the thermodynamic cycle, i.e., that there were no lags associated with pressurization of component volumes. This produced a first-order model that contained only the dominant time response due to the spool, combined with nonlinear component models determining the steady operating point. By linearizing about steady state (assuming a choked nozzle) it was shown that the parameters of interest, i.e., time constant, steady-state fuel flow, zero frequency gain, etc., are functions of three independent variables: $N/\sqrt{T1}$, $P1$, and $\sqrt{T1}$.

To calculate these functions much more data would have been needed, such as compressor characteristics, turbine characteristics, and efficiencies. Instead, as the structure of

Nomenclature

Ag = acceleration loop gain
DECU = digital electronic control unit
FMU = fuel metering unit
Ke = engine gain
Kf = control feedforward gain
Kve = combined valve and engine gain
N = engine speed
NDMAX = maximum allowable engine speed
NDMXT2 = table containing the temperature-limited maximum engine speed
Ndot = engine acceleration
NDREQ = demanded engine acceleration
$ND1$ = limited required engine speed
NENG = engine speed, control variable name
NH = engine speed, high-pressure spool
PATMOS = sea level atmospheric pressure
PCU = power conditioning unit
PLA = pilot lever angle, demanded engine speed input to control
$P1$ = compressor total inlet pressure
$P3$ = combustion chamber pressure
Sg = engine speed control loop gain
SGAIN = engine speed control loop gain within the control
TC = acceleration control loop filter time constant
Te = engine time constant
$TT2$ = compressor total inlet temperature within the control
$T1$ = compressor total inlet temperature
Wf = fuel flow
δ = $P1$/PATMOS

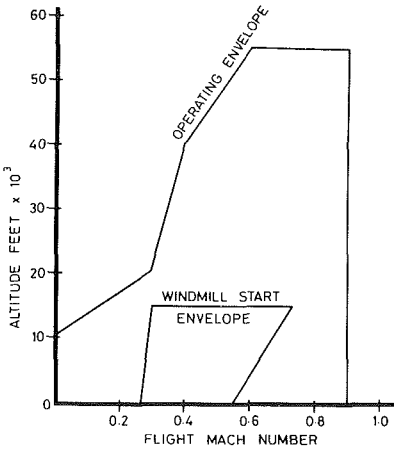

Fig. 5 Operating envelope

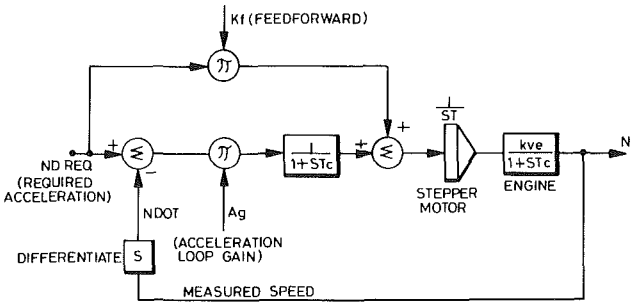

Fig. 6 Acceleration control loop

the model had been obtained, it was possible to extrapolate from known data for $P1$ and $T1$ variations. The model is shown in Fig. 4.

Linearization gives the following transfer function:

$$\frac{NH(s)}{Wf(s)} = Ke/(1+STe)$$

where $Ke = 1/fw'P1$; $Te = \sqrt{T1}/kNfw'P1$; $fw' = (F1NH/\sqrt{T1})$; $KN = F2(NH/\sqrt{T1})$. The model predicts that as $P1$ and $T1$ vary, both the steady-state fuel flow and dynamic response are affected. At a given $N/\sqrt{T1}$ fuel flow is proportional to $P1\sqrt{T1}$; the engine time constant Te is proportional to $rtT1/P1$, and its zero frequency gain Ke is inversely proportional to $P1$. $P1$ and $T1$ vary considerably over the flight envelope (see Fig. 5), such that the engine response is slower and it consumes less fuel at high altitudes than at sea level for the same $N/\sqrt{T1}$.

(*b*) *Fuel-Valve Profiling.* By careful profiling of the plate valve in the fuel metering unit it was possible to cancel the steady-state gain variations of the engine.

At all flight conditions and speeds a change in motor position of one step will now result in the same increment in speed. The combined valve and engine gain is therefore a constant.

(*c*) *Engine Surge.* If an engine is accelerated too quickly it may surge. The surge line is a compressor-related function and can, in theory, be mapped onto the compressor characteristic as a unique relationship between $P3/P1$ and $N/\sqrt{T1}$. It can be shown that $ecWf/P1\sqrt{T1}$ as a function of $N/\sqrt{T1}$ maps to the same line, and that for a choked engine, $Ndot/P1$ as a function of $N/\sqrt{T1}$ also maps to the line. Consequently, either fuel scheduling or closed-loop acceleration control can be used to maintain the surge margin.

(*d*) *Lightup/Starting.* An engine can be subject to a wide variation in lightup/starting conditions. RPV's can have an air launch requirement which might result in a windmill starting envelope as shown in Fig. 5, while compressor air im-

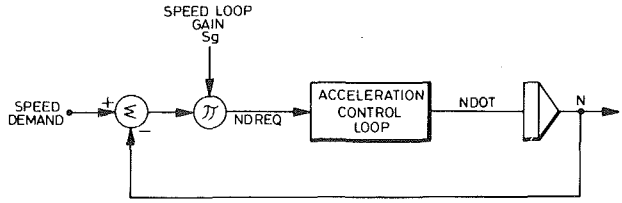

Fig. 7 Speed governing loop

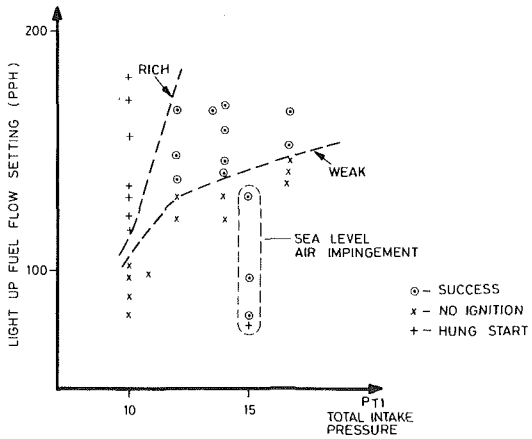

Fig. 7(*a*) Windmill lightup tests—A

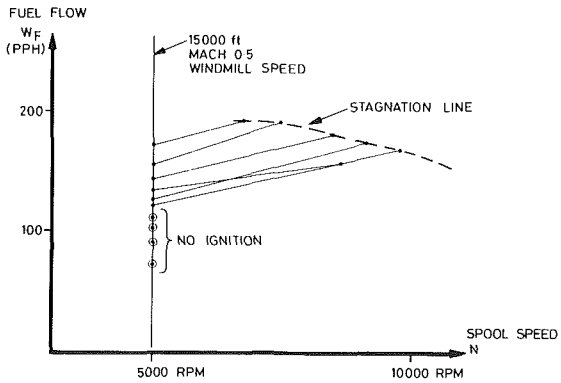

Fig. 7(*b*) Windmill lightup tests—B

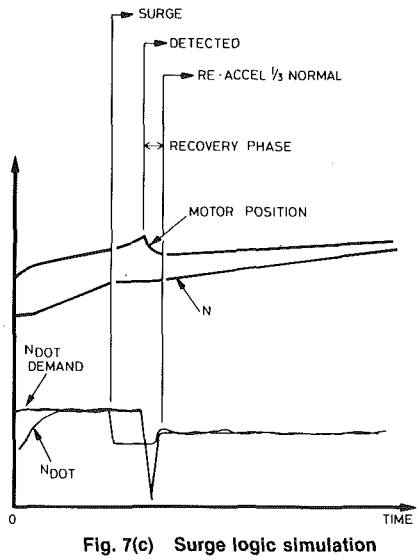

Fig. 7(c) Surge logic simulation

pingement is used for starting at sea level. This results in a big variation in starting air flow and combustion efficiency; consequently an optimum lightup flow is not easily defined. An automatic method of starting is required that can cater to these different operational modes.

(*e*) *Fuel Valve Position Feedback.* As a cost-saving feature the fuel metering system was designed without a valve position pick off. Therefore the controller has no fuel flow indication. The fuel valve is directly driven by a stepper motor so fuel flow can be reliably modeled for a short time after system initialization by dead reckoning. This is achieved by counting the step changes demanded by the controller. Redatum is performed during system initialization when 250 steps are output to ensure that the valve has closed against a mechanical endstop. This "dead reckoning" approach can only be used during the lightup to idle phase since there is not sufficient time for any significant errors to accrue.

(*f*) *EGT Measurement.* As a cost-saving feature Engine Gas Temperature measurement was dispensed with once the principle of starting with Engine Acceleration Control (Ndot) had been demonstrated.

Control Functions

Ndot Control. With no EGT measurement and no fuel flow signal, closed-loop control of spool acceleration (Ndot) was the only viable method of controlling transients. It provides surge margin control, which is probably more accurate than fuel valve scheduling since the inaccuracies of the metering valve and combustion system are not present. Moreover a high-quality speed signal is available from the alternator, which can be measured with quartz precision and differentiated by digital techniques.

The relationship between Ndot/$P1$ and $P3/P1$ (which defines the surge line) is unaffected by fuel system accuracy, fuel density, fuel calorific value, and combustion efficiency because it is determined by the balance of excess torque and spool inertia.

The acceleration schedule has been optimized and should provide surge and flame-out avoidance at all points in the flight envelope including the windmill start envelope. The same schedule has not yet been proven satisfactory for air impingement starts. At present a separate schedule is built into the control laws for these starts because they have less air flow and less cranking assistance and are therefore hotter and slower. It can be removed if tests show the windmill schedule is satisfactory for both. A single schedule will inevitably be a compromise to prevent hot impingement starts yet allow fast windmill starts.

Design of Ndot Control. To maintain the surge margin, the Ndot control objectives were that at a constant acceleration there would be no error and that in achieving the desired acceleration rate there would be no overshoot in fuel flow. These objectives, coupled with a closed-loop response that did not significantly vary for speed and altitude changes, would simplify the surge detection logic and speed control loop. In addition a consistent response would be presented to the flight control system/operator.

The ideal closed-loop transfer function would be a first-order lag with unity zero frequency gain. In practice a higher-order transfer function is obtained that should have real dominant poles. The time response of the loop is ultimately limited by the slewing rate of the fuel actuator. The loop should be designed such that in all positions within the flight envelope, the actuator slew rate is not exceeded. This ensures that the loop remains "closed," its performance predictable at all times. This is necessary for correct operation of the surge detection logic.

Figure 6 is a diagram of the acceleration control loop. The feed forward path provides the necessary step rate to achieve the demanded acceleration. The closed loop corrects this estimate and provides the desired dynamic response. If $Kf = 1/KveT$ then there will be zero error at constant acceleration. Kve is the combined gain of the engine and fuel valve and is nominally constant for all conditions. Therefore Kf is constant.

The time constant of the engine can be approximated by $Te = (9.2\sqrt{\theta}/8)\, e(N/24\sqrt{\theta})$. Sampled data theory was used to analyze the loop so that the cycle delay of the controller, its discrete algorithms, and the stepper motor could be better represented.

The acceleration loop gain Ag was calculated with the objective of maintaining critical damping for a range of speeds thus avoiding overshoot. A correction function to maintain critical damping with variations in $P1$ was computed at the nominal operating speed. This was to remove the need for carpet tables and simplify the task of the control processor. The controller now only has to multiply a function of N by a function of $P1$ to calculate Ag. Variations in the closed-loop pole positions occur because of this approach. If the engine time constant behaves exactly as assumed then the dominant closed-loop pole position has a ± 5 percent variation over the operating envelope.

Speed Governing. Maximum power at any condition is determined by the mechanical limitations of the engine. Speed governing was used as the means of controlling engine thrust so that the power demand signal would correspond to the fraction of power available at the prevailing flight condition.

Speed governing was easily implemented as an outer loop around the acceleration control. The variable gain terms employed in the Ndot control loop were then indirectly used for the speed loop thus avoiding duplication, and changes in speed demand provided a dynamic "feed forward" to the acceleration control.

The overall speed governing loop including the engine and fuel system can be modeled as shown in Fig. 7. Since the dynamic response of the acceleration loop is nominally constant, the speed gain Sg is fixed. Sg was chosen to give a damping ratio (zeta) of 0.7 for the dominant poles of this loop.

Lightup Fuel Ramp. Lightup was originally performed by scheduling fuel flow as a function of speed. After ignition the engine would accelerate and an Ndot limit take control.

The optimum lightup fuel flow is dependent upon air mass flow and fuel/air ratio. For windmill (air launch) starts air mass flow could be estimated from the available inputs since windmill speed is determined by the flight Mach number, which is related to the nozzle swallowing function. However the combustion chamber mixing ability can produce changes in the fuel/air ratio required for lightup at different operating points. There appear to be both rich and weak lightup limits, which meet at some altitude beyond which lightup cannot usually occur. At 15,000 ft only a small window exists, making fuel scheduling inaccuracies very significant. When starts are performed using compressed air impingement the engine air flow (and lightup fuel flow) is much reduced.

With the suite of inputs employed an air impingement start could look the same as a windmill start and yet the engine mass flow would be much less. A flow schedule that would enable lightup when windmilling would produce hot starts under air impingement. Indeed the original arrangement was characterized by high-temperature pulses after lightup because of the higher fuel flow schedule needed for windmill starts.

Near the 15,000 ft limit too much flow resulted in decreased combustion efficiency to the extent that with progressive increases in lightup flow, the engine stagnated at lower and

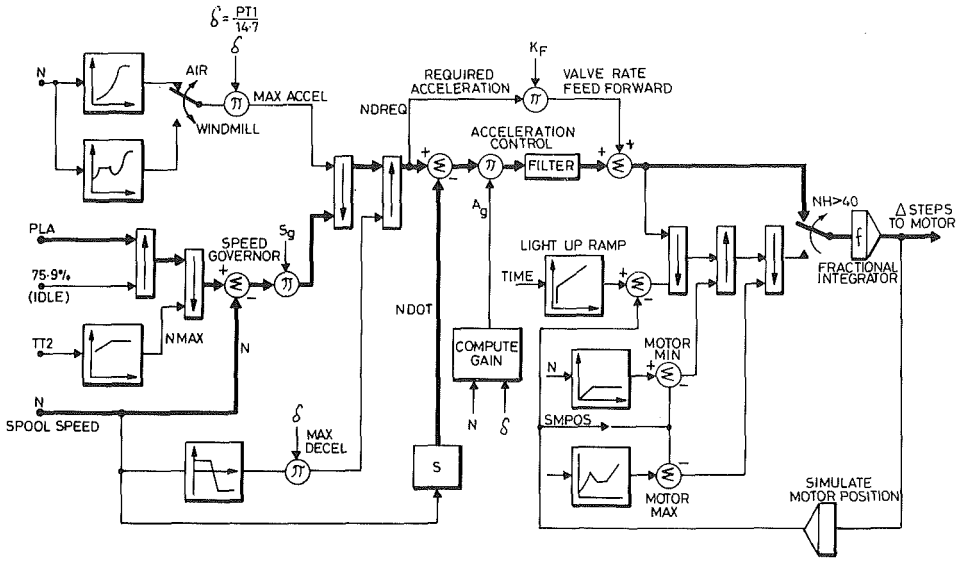

Fig. 8 Overall control schematic

lower speeds. Yet reduction in flow failed to light the engine, suggesting that the lightup flow can be greater than that which will accelerate the engine.

To improve lightup and starting performance the flow scheduling technique was modified to include a time ramp of fuel valve position so that lightup would occur at the optimum fuel flow for the prevailing conditions. The position of the fuel valve was dead reckoned from initialization and the fuel schedule now acts as an upper limit high enough for the maximum windmill case. A ramp start point was included to prevent wasting time in unnecessary ramping yet cater to the lowest case.

The error in the fuel valve calibration, the dead reckoning, and the uncertainty of the required lightup flow are all accommodated for within these extremes of the lightup ramp. This method automatically finds the optimum flow for lightup, eliminating temperature peaking and ensuring that the combustion system is at its most efficient at the beginning of acceleration. After lightup the engine accelerates and is controlled closed loop by the Ndot control.

Surge Protection. Some form of surge protection was needed because an Ndot-based control will push the engine further into surge if surge occurs. Usually Ndot-based systems employ a "catcher schedule" that limits the maximum fuel valve position in the event of surge. Since the fuel valve position is not measured, this method could not be easily employed. Dead reckoning of the fuel valve position in software could only be guaranteed accurate for a short time after system initialization as the stepper motor might slip. Also a power reset of the system could result in a gross absolute error in estimated position. Some consideration was given to adaptive steady-state correction of the fuel valve position model to eliminate drift errors, but was rejected as gross transient errors might still occur. Fuel flow scheduling was therefore rejected in favor of surge detection and recovery logic.

For idle to maximum power conditions, therefore, detection of surge relied upon the recognition of the divergence between demanded and achieved acceleration rate. The logic is simpler if the closed-loop response is constant under all conditions. Recovery from surge was attained by reducing fuel flow to less than that at which surge was detected and slowing down the subsequent acceleration by a factor of three until steady-state speed control was achieved. This has an advantage over the previous method as it results in a fast fuel flow reduction and not just a fuel flow limit.

This method of surge detection suffers from the drawback

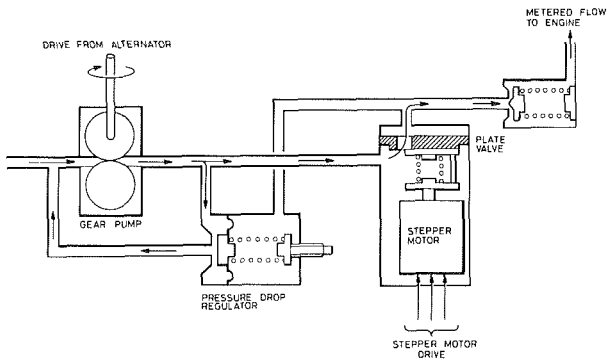

Fig. 9 FMU schematic

that it will also register a flameout, or indeed anything that prevents closed-loop control of Ndot, as a surge. The engine occasionally flames out during low Mach number high-altitude starts, but closed-loop Ndot control recovers automatically by momentarily increasing flow. The Ndot divergence method might detect the flameout as a surge which could lead to stagnation, so the benefit of Ndot control would be lost if this method of surge detection were employed.

As a result of this observation it was decided to use the "catcher schedule" approach during starts to minimize the effect of a surge but to allow the Ndot control sufficient leeway to recover from a flameout. The fuel valve position could be reliably modeled during starts by dead reckoning.

Overall Control Laws. The speed commanded by the PLA is bounded by idle and maximum speed limits. The speed governor requests an acceleration rate proportional to speed error, but this is held between acceleration and deceleration limits preventing surge and flameout. The Ndot control will attempt to open the fuel valve to achieve the requested acceleration rate. Prior to lightup the fuel valve position is limited by the time ramp; after ignition takes place the engine accelerates and the Ndot control drives the fuel valve to an intermediate setting between the fuel schedules; above 40 percent the fuel schedules and time ramp are disengaged leaving only the speed governor and acceleration control active. At 40 percent the surge detection logic is enabled. A fractional integrator is always active and provides an improvement in resolution over that provided by the stepper motor, by outputting an extra step when its input fractions accumulate to more than unity.

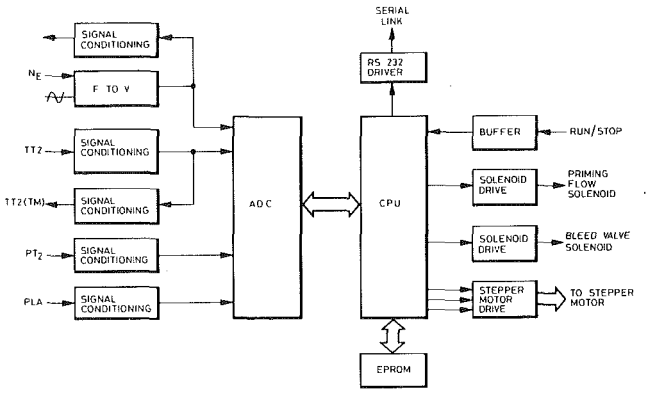

Fig. 10 DECU hardware schematic

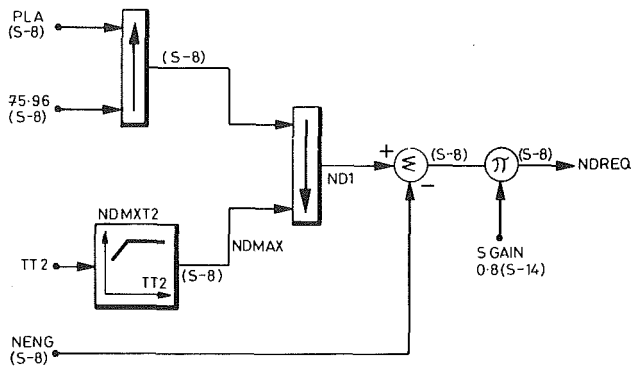

Fig. 11(*a*) Typical software module

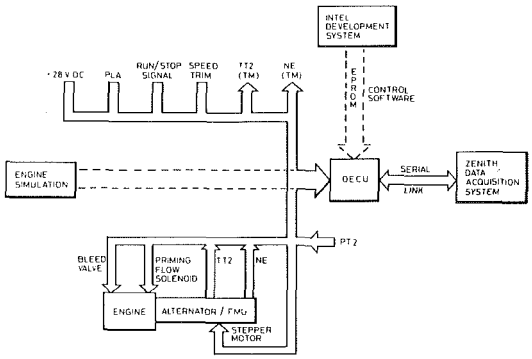

Fig. 11(*b*) Software development system schematic

FMU Design Considerations. To a great extent engine requirements dictate the component design. The HAL engine required high-pressure fuel for the burners, which led to the choice of a gear-type fuel pump to provide the necessary high-pressure fuel for engine starting. The Teledyne engine did not require high-pressure fuel for its combustion system, but high-pressure fuel from the metering system was found to be useful for bearing lubrication, and as an HP supply to the airframe for infrared generators. The metering system, a stepper motor-driven plate valve and pressure drop regulator, was chosen as it provides a unique fuel flow at a given valve position. This allowed an exponential characteristic of fuel flow versus valve position to be used that simplifies the task of the control algorithms. A constant pressure drop across the metering valve also minimizes the size of motor needed to overcome frictional forces.

A minimum pressure has to be maintained within the fuel metering unit to allow the excess fuel to be split to the pump inlet. To do this a pressurizing valve is used.

The Digital Electronic Control Unit (DECU) is an integral part of the system. The system has been designed to freeze fuel flow in the event of a DECU failure. This enables the airframe control computer to continue flight at a fixed power setting.

FMU Description. The fuel metering unit consists of an engine-driven gear pump, a stepper motor-driven plate valve, a pressure drop regulator, and a pressurizing valve.

The gear pump was designed to be capable of producing sufficient fuel flow to cater for all engine requirements, the critical condition being lightup. Due to the lightup flow requirements the pump produces a much larger flow than the engine requires at other conditions.

The pressure drop regulator is a simple diaphragm-operated device that senses the pressure either side of the plate valve. It controls the pressure drop by spilling the excess pump output back to the pump input.

The plate valve is a cam with an exponential profile and is rotated over a triangular orifice by the stepper motor. This varies the fuel flow supplied to the engine. The cam is positioned open loop by powering the stepper motor in either direction. No feedback is provided as the acceleration control does not require a knowledge of fuel flow for its operation. The increase in integrity given by fuel flow feedback is not required for unmanned aircraft applications.

To enable the pressure drop regulator to function the pump discharge pressure must be kept above a minimum value. To ensure that this occurs, the metered flow passes through a pressurizing valve before leaving the fuel control. The pressurizing valve is a spring-loaded poppet-type valve, the cracking pressure being set by the spring preload.

DECU Hardware. The DECU consists of a single Intel 8031 microcontroller containing CPU, scratchpad memory, and digital input/output. The program memory is contained in an external EPROM, which for development purposes is removable from the DECU. An 8-bit 8-channel analogue-to-digital converter that automatically scans each input channel in turn and stores the result in a buffer is used to convert the analogue inputs.

The stepper motor drive circuit is driven by three state inputs, controlled directly by the microcontroller. Since a specific phase pattern is required failures of the DECU are unlikely to result in motor movement.

The engine speed signal is derived from a winding in the alternator. The signal is first filtered to remove higher harmonics imposed on the signal when the alternator is under load. A frequency-to-voltage converter is used to produce an analogue signal that is fed into the ADC. The analogue signal is also buffered and then output to supply an engine speed telemetry signal in the airframe.

The DECU housing contains a *TT*2 probe, the output from which is conditioned before being fed into the ADC. The *TT*2 signal is also buffered and supplied to the airframe as a telemetry signal. A *PT*2 signal supplied by the airframe is conditioned before being supplied to the ADC. The engine speed demand signal can select any power setting between idle and 100 percent with a resolution of 0.1 percent. This signal is conditioned to match the ADC voltage range before being fed into the converter.

There is one state input signal supplied from the airframe. This indicates the required state of the engine, i.e., RUN/STOP. It is buffered before being fed into one of the microcontroller input ports. There are two state outputs for controlling the compressor bleed and primer flow valves. An RS232 serial link was used during control development to send control node data to an acquisition system. The DECU receives its electrical power from the aircraft 28V d-c bus.

DECU Software. The control laws were implemented us-

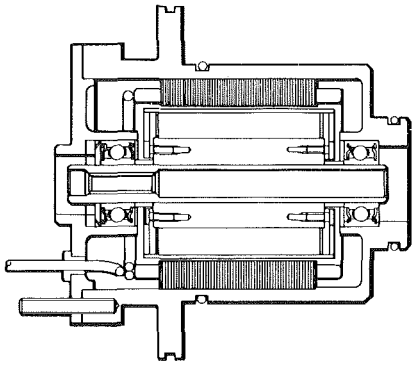

Fig. 12 Alternator section

ing macros to define a suite of primitives that would perform the basic operations necessary, i.e., protected addition, multiplication, lowest wins, lookup tables, etc. All arithmetic operations were fixed point with signed 16-bit number representation. A scaling convention was adopted so that machine integers and engineering values could be easily related.

All of the control software was written from signal flow diagrams using the above approach. This gave us a language with which to implement and modify control laws that was divorced from the specifics of the Intel macroassembler yet required consideration to be given to numerical scaling and resolution, essential for correct operation of the control.

The format of the language is shown in the following example, which is the implementation of the signal flow diagram of Fig. 11(*a*).

```
%LOADM (13107)          ; 0.8 (s-14).
%STOREM (SGAIN)         ; Speed loop gain
%GETM (TT2)             ; Total intake temperature
%LKUPM (NDMXT2)
%STOREM (NDMAX)         ; Max speed demand
%LOADM (19431)          ; 75.9 percent (s-8) = 31,500 rpm
%HWINM (PLA)
%LWINM (NDMAX)
%STOREM (ND1)           ; Limited demand
%SUBM (NENG)            ; Speed error (s-8)
%MULM (SGAIN,-2)
%STOREM (NDREQ)         ; Requested Ndot (s-8)
```

There is a high degree of correspondence between the signal flow diagram and the module listing. Each line corresponds to a single symbol on the diagram. An implied register retains intermediate results equivalent to the nodes in the diagram. The implied register can be stored under a named variable for use elsewhere or just for the sake of clarity. The left to right signal flow corresponds to the top to bottom listing. Scale factors are recorded as comments in the listing and are adjacent to the node applicable.

The close correspondence to the signal flow diagram, and the use of familiar well-tested primitives, enable control law modifications to be made with ease, and with confidence that the desired algorithm has been implemented. Moreover each function can be tested by inspecting nodes within the control program with minimal disruption of the source code.

Control Software Development System. The heart of the control software development system is the DECU. The development DECU differs from an engine-mounted unit in that the EPROM is easily accessible for software changes. Three potentiometers provide inputs to spare ADC channels so that gain changes can be easily made.

An Intel development system was used to make modificaitons to the software. A Zenith personal computer was used to collect data transmitted from the DECU along the

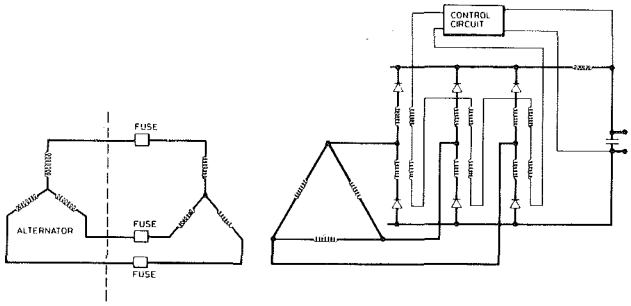

Fig. 13 Power regulation circuit

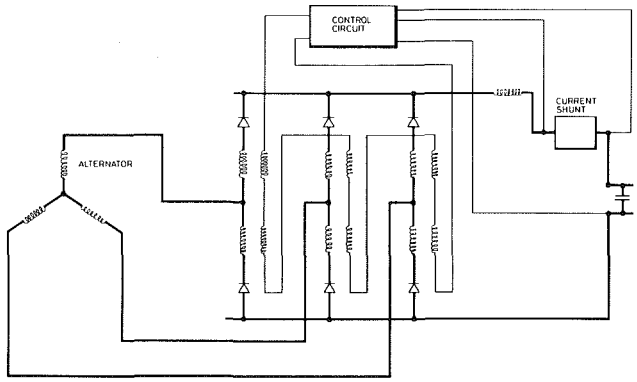

Fig. 14 Improved power circuit

serial link. In real time up to eight variables could be displayed. These were plotted in color, against time on the Zenith monitor. All data was recorded on flexible diskettes for subsequent analysis. The DECU could be connected to either the engine or to an engine simulator box.

When a change to the control laws was required the following procedure was followed. Firstly the desired modifications were made to the control software on the Intel development system. An EPROM was then programmed and installed in the DECU, which was then connected to the engine simulation. After the new control system had been exercised against the simulation, and its functioning checked, the DECU was reconnected to the engine.

Alternator Description. The aim of the alternator design was to provide an alternator with the lowest weight and size possible at the lowest cost while maintaining mechanical integrity. The alternator was designed to run at engine shaft speed thus eliminating the need for a gearbox. An extra single-phase winding on the stator provided a high-quality engine speed signal to the DECU.

The alternator comprises one three-phase power winding and one single-phase speed signal winding. A rotor turns within the stator and contains magnets to provide a rotating magnetic field. The rotor is mounted between two fixed, shielded, grease-packed bearings and is connected to the engine by a floating quill shaft.

The rotor comprises a soft iron core upon which eight trapezoidal magnets are mounted. The magnets are made from Samarium Cobalt, which has a low magnetic temperature coefficient and high maximum working temperature. The magnets are held in place by a high-tensile-strength steel sleeve, which is shrunk over the whole assembly. The rotor provides the drive for the gear pump, which also runs at engine shaft speed.

The stator consists of a number of Silicon Iron laminations electron beam welded together. Copper windings are wound around the stator teeth and held in place by nonmagnetic slot liners and wedges. The stator assembly is then vacuum im-

pregnated to ensure electrical integrity. To ensure a good thermal contact and mechanical integrity, the complete stator assembly is shrunk into the alternator housing.

Cooling is provided by mounting the alternator in a pocket in the engine compressor housing and routing the fuel supply through the pocket to the control. This reduces the surface area from that required for air cooling.

PCU Description. The alternator was first designed to match a high-voltage switched mode regulator. During development of the regulator problems were encountered that required extensive development to overcome. For expediency a simpler approach using magnetic amplifiers was chosen.

The magnetic amplifier Power Control Unit (PCU) contains a transformer in each phase that feeds a three-phase bridge rectifier. Each phase of the bridge contains a magnetic amplifier controlled by a voltage regulator circuit. The output from the three-phase bridge is filtered before being output.

The transformers are required to convert the alternator output voltage to a range that the magnetic amplifiers can control. If the alternator had been optimized for a magnetic amplifier design, the transformers would not be required.

The rectifier output is controlled by the a-c windings of the magnetic amplifiers in response to the d-c current of up to 100 mA in the amplifier control winding. The output of the rectifier and magnetic amplifier is then passed through an inductance/capacitor filter to reduce ripple voltage to comply with MIL-STD-704D.

The voltage regulator circuit consists of standard linear components. It monitors output voltage and adjusts control current to the magnetic amplifier to maintain this voltage at the specified level.

Future System Developments. The development program has shown that Ndot control is a good method of controlling a UMA engine. A small improvement to the control would be obtained by the introduction of an integrator in the forward path of the acceleration control loop. This would eliminate all the error between demanded and actual engine acceleration, and reduce variations in dynamic response. Some further tests should verify that the acceleration schedule is suitable for both air impingement and windmill starts. This would eliminate the need for a windmill/impinge state input in future systems.

The control implementation language should be updated to include some Boolean functions, for implementing surge and bleed valve operating logic.

*PT*2 signals are not always available on the airframe. To make the engine control more self-contained any future system should contain a *PT*2 probe in addition to a *TT*2 probe.

The present PCU was designed to match a high-voltage permanent magnet alternator. To reduce the size of the PCU the alternator would have to be redesigned to produce a low voltage. This would then directly feed a rectifier bridge containing magnetic amplifiers without the need for transformers. A recent material evolution is cobalt steel with a rectangular B-H loop. This material holds the promise of significantly reducing the size of the magnetic amplifiers and hence the PCU.

The only form of current limit on the existing PCU is fuses on the input from the alternator. Any future designs would have to sense current and be able to have full turndown on the magnetic amplifiers.

Since the present alternator was designed the properties of rare earth magnets have been improved and this would allow the size of the alternator to be reduced.

One of the problems with the present system is the heat generated by spilling the excess pump output flow back to the pump input. This problem could be reduced by lowering the pressure rise across the pump. This system modification would necessitate changes to the pressure drop regulator to enable it to spill the same flow with the lower pressure drop and also maintain its stability.

Recently a move has started in the UMA field for doing the engine control calculations in the Air Control Computer. If this trend becomes the universal approach then failing with a constant fuel flow does not look desirable. If the Air Control Computer fails it would be desirable for the engine to shut down. To change our design to cater for this would require a control system design review.

Conclusions

The engine running showed that the Ndot control philosophy is a valid technique for the control of gas turbines. Ndot control allows simple hydromechanics and minimizes the number of external parameters required by the control. The problem of Ndot pushing the engine further into surge, if surge occurs, has been overcome with a small amount of extra logic within the control software.

The hydromechanics have proved satisfactory for present applications, but future integration of airframe and engine control computers may necessitate a reappraisal of the hydromechanic system design.

T. Hattori

H. Ohnishi

Mechanical Engineering Research Laboratory,
Hitachi, Ltd.,
Tsuchiura, Ibaraki, Japan

M. Taneda

Production Engineering Dept.,
Hitachi, Ltd.,
Tokyo, Japan

Optimum Design Technique for Rotating Wheels

Compressor rotors and turbine rotors are subject to centrifugal and thermal loads. These loads increase proportionally with tip speed, pressure ratio, and gas temperature. On the other hand, the rotor weight must be lessened to improve rotor dynamics and restrict bearing load. Thus, an optimum design technique is required, which offers the lightest possible wheel shape under the stress limit restriction. This paper introduces an optimum design system developed for turbomachinery rotors, and discusses several application results. The sequential linear programming method is used in the optimizing process, and centrifugal and thermal stress analyses of variable thickness rotating wheels are performed using Donath's method. This system's validity is confirmed by application to uniform-strength rotating disk problems and comparison with analytical results. This optimum design program is then applied to the design of axial flow compressor wheels.

Introduction

Generally axial flow compressor rotors and turbine rotors are composed of wheels for each stage (see Fig. 1) and stacked bolts. To design these wheels, we must consider centrifugal and thermal loads. These loads have increased in proportion to recent increases in tip speed, pressure ratio, and combustion temperature. On the other hand, rotor weight must be lessened to improve rotor dynamics and restrict bearing load.

In this paper, we show the optimum wheel design system which uses the sequential linear programming method in the optimum point searching process and Donath's method [1] in the stress analysis process. Using this system, minimum-weight wheel shape can be obtained, keeping transient thermal stresses and centrifugal stresses within the allowable stress limit. Many optimum design systems have been developed and used for optimum design of disks [2, 3], dams [4], truss structures [5, 6], and so on. But these programs have restrictions, such as applicability to only one kind of load problem, neglect of stress concentration, and restriction of start design point. A flow diagram of this system is shown in Fig. 2. In this paper, we first show an outline of the sequential linear programming method and Donath's stress analysis method. The validity of this system is then confirmed by application of this program to uniform-strength rotating disk problems and comparison with analytical results. Finally, we show an application of this system to the wheels of an axial flow compressor rotor subjected to centrifugal and transient thermal loads.

Outline of Sequential Linear Programming. Generally optimum design problems are defined as follows: Obtain a set of variables which satisfies restrictive conditions g_j $(x_1, x_2, \ldots, x_n) \leq 0$ $(j=1, 2, \ldots, m)$ and makes the objective function $f(x_1, x_2 \ldots, x_m)$ minimum (or maximum), as well.

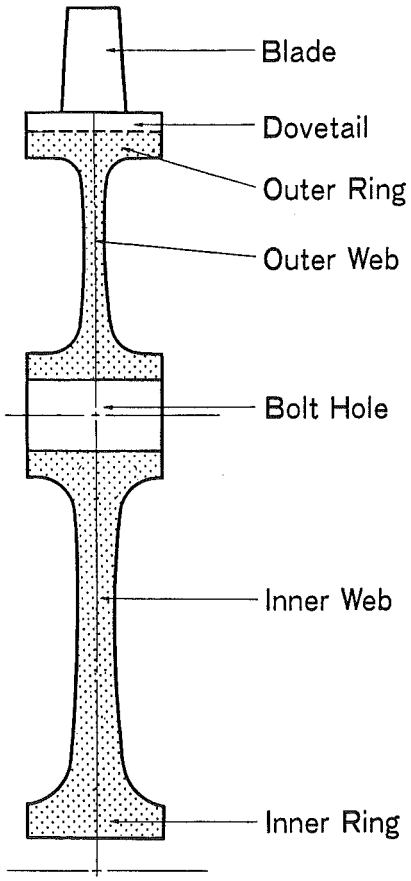

Fig. 1 General view of compressor wheel

The optimum solution can be obtained by following processes of the sequential linear programming method:

Contributed by the Gas Turbine Division of THE AMERICAN SOCIETY OF MECHANICAL ENGINEERS and presented at the 31st International Gas Turbine Conference and Exhibit, Düsseldorf, Federal Republic of Germany, June 8-12, 1986. Manuscript received at ASME Headquarters March 7, 1986. Paper No. 86-GT-255.

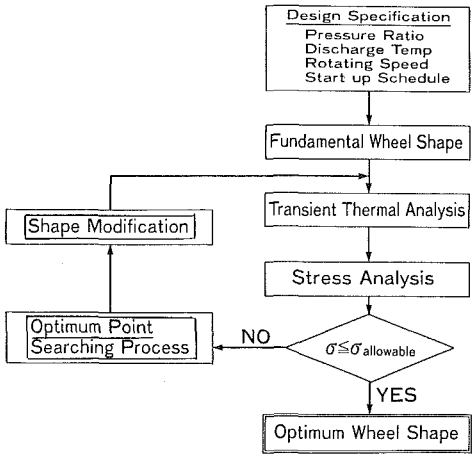

Fig. 2 Optimum wheel design system flow diagram

1 Give an initial design point

$$\mathbf{x}^{(0)} = (x_1^{(0)}, x_2^{(0)}, \ldots, x_n^{(0)}).$$

2 Linearize restrictive conditions and objective function by conducting Taylor's expansion at point $x^{(0)}$ and transform the above problem into a linear programming problem as follows:

Obtain a design point

$$\Delta\mathbf{x}^{(1)} = (\Delta x_1^{(1)}, \Delta x_2^{(1)}, \ldots, \Delta x_n^{(1)})$$

which satisfies restrictive conditions

$$\sum_{k=1}^{n} \frac{\partial g_i(\mathbf{x}^{(0)})}{\partial x_k^{(0)}} \Delta x_k^{(1)} \leq -g_j(\mathbf{x}^{(0)}) \qquad (1)$$

$$(j = 1, 2, \ldots, n)$$

and make the objective function

$$f(\mathbf{x}^{(0)}) + \sum_{k=1}^{n} \frac{\partial f(\mathbf{x}^{(0)})}{\partial x_k^{(0)}} \Delta x_k^{(1)} \qquad (2)$$

minimum (or maximum) as well.

3 Solve the above linear programming problem using the simplex method.

4 Obtain $\mathbf{x}^{(1)} = \mathbf{x}^{(0)} + \Delta\mathbf{x}^{(1)}$ as a first approximate solution, and repeat steps 1–4.

5 If the convergent condition can be satisfied, the calculation stops.

Moreover, the allowable design point search process is added in this system. By this function, we start from an arbitrary initial design point which does not satisfy certain restrictive conditions. The outline of this allowable design point searching process is as follows:

We now assume that the design point does not satisfy restrictive conditions $g_1, g_2, \ldots, g_m$ but does satisfy $g_{m+1}, g_{m+2}, \ldots, g_m$. We then introduce the new objective function $G(\mathbf{x}) = \Sigma_{j=1}^{m} g_j(\mathbf{x})$ and minimize G under restriction conditions of $g_{m+1}, g_{m+2}, \ldots, g_m$. In this process, if $g_1, g_2, \ldots, g_m$ become zero or negative, they will be removed from G and included in the restrictive conditions. If the design point, which satisfies all restrictive conditions, can be obtained, then we can turn the process into the abovementioned optimum design process. Figure 3 shows application results of the optimization system for two-dimensional problems:

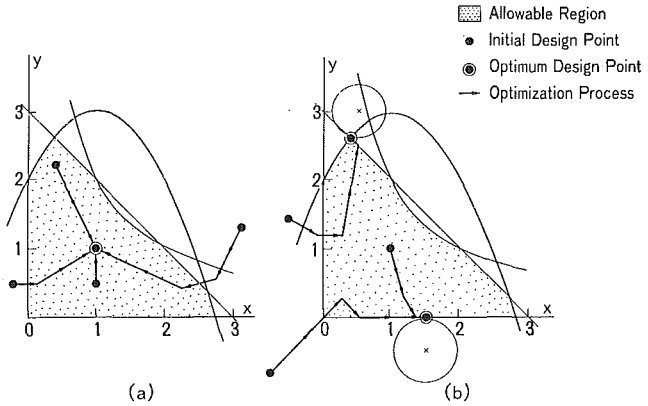

Fig. 3 Application results of optimization program for two-dimensional problems

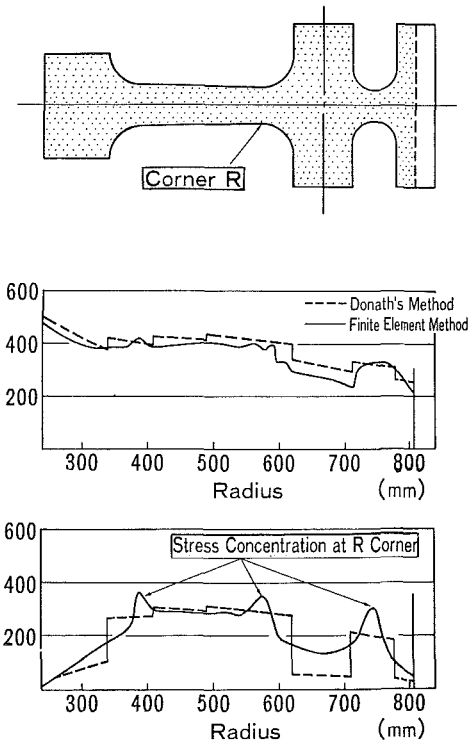

Fig. 4 Comparison of calculated stress results by Donath's method and finite element method

Objective function $f = (x-a)^2 + (y-b)^2 + 1 -$ minimize

Restrictive conditions

$$\begin{cases} g_1 = (x-1)^2 + y - 3 \leq 0 \\ g_2 = xy - 2 \leq 0 \\ g_3 = x + y - 3 \leq 0 \\ g_4 = -x \leq 0 \\ g_5 = -y \leq 0 \end{cases} \qquad (3)$$

Figure 3(a) shows the case where $a = 1$, $b = 1$. In this case, the optimum point, shown by the mark ⊙, exists inside the allowable region. Figure 3(b) shows the case where $a = 0.5$,

Nomenclature

$\mathbf{x}$ = variable
$g(\mathbf{x})$ = restrictive condition
$f(\mathbf{x})$ = objective function
h_i = thickness of each ring element (Donath's method)
r_i = radius of each node (Donath's method)
σ_r = wheel radial stress
σ_θ = wheel circumferential stress

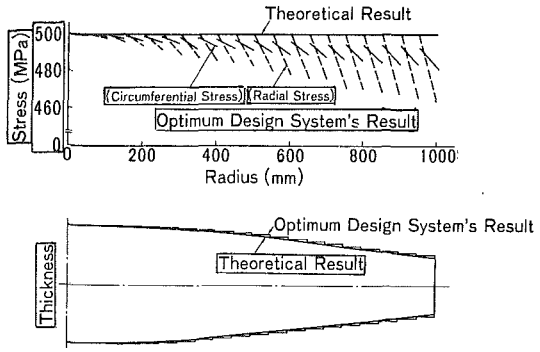

Fig. 5 Comparison of optimum design system results with theoretical results

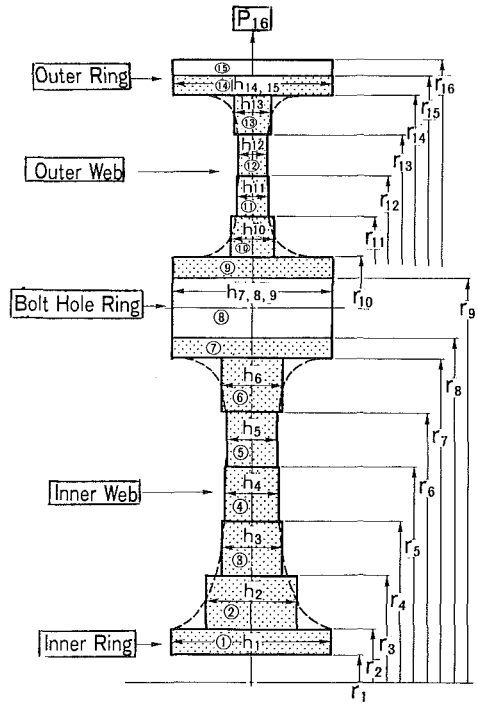

Fig. 6 Divided conditions of wheels

$b=3$, and $a=1.5$, $b=0$. In these cases, the optimum point exists just on the edge of the allowable region. From these figures, it can be confirmed that optimum design points can be obtained even if initial design points are outside the allowable region.

Centrifugal and Thermal Stress Analyses of Wheels. Centrifugal and thermal stresses of wheels are analyzed using Donath's method, popular for rough stress calculation of rotating disks. In this method, wheels are divided into many concentric rings with variable thicknesses and stress distribution can be calculated by satisfying displacement and stress conditions through whole rings. A comparison of the calculated result of the compressor wheel by Donath's method with that by the finite element method is shown in Fig. 4. Both calculated results coincide closely, except on stress concentrating portions. From this comparison, we can use 1.3 as the stress concentration factor at corner R.

Optimum Wheel Design System. The optimum wheel design system which we developed for design of turbine and compressor wheels has the following functions:

1 The lightest possible wheel shape can be obtained automatically, maintaining combined centrifugal and thermal stresses less than the allowable stress limit.

2 Allowable stress limits can be set on each ring, so that the stress concentration at corner R and strength variation in accordance with the temperature can be handled accurately.

3 Numerous pairs of load conditions and allowable stress limits can be used for optimum design of each wheel shape considering transient load conditions, can be obtained.

4 Nonchangeable dimensions such as thickness of outer ring and bolt hole ring can be fixed.

In order to confirm the validity of this optimum design system, this program is applied to the design of a uniform strength rotating disk and calculated results are compared with theoretical solutions (see Fig. 5). Although the calculated results are stepwise, because of Donath's method, the results coincide closely enough for practical usage.

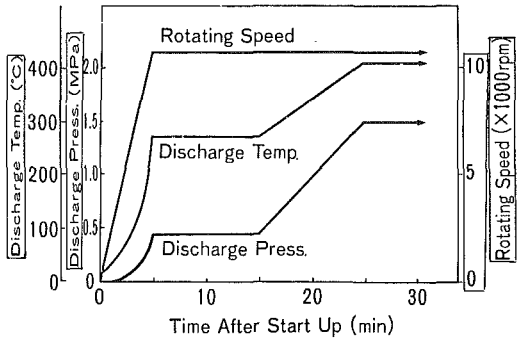

Fig. 7 Startup program used for wheel design

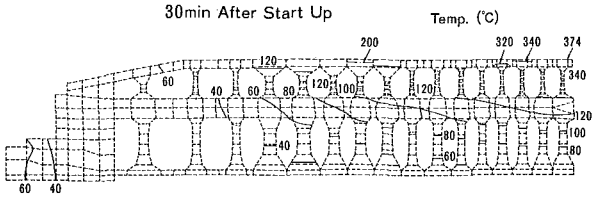

Fig. 8 Temperature distribution of compressor rotor

Application of Optimum Design System to Compressor Wheels

Calculation Conditions. The dividing condition of each wheel is shown in Fig. 6. The total number of ring elements is 15. The inner ring thickness h_1, bolt hole ring thicknesses $h_7 \sim h_9$, and outer ring thicknesses h_{14}, h_{15} are fixed according to the flow pass profile of compressor; the inner web thicknesses $h_2 \sim h_6$ and outer web thickness $h_{10} \sim h_{13}$ are taken as variables. External force P_{16} is applied as the centrifugal force of blades. The temperature distribution of each wheel each time is obtained from transient thermal analysis of the whole rotor. An example of this analytical result is shown in Fig. 7. The compressor startup program used for this thermal analysis and wheel optimization is shown in Fig. 8. The allowable stress limits are determined from the low cycle fatigue strength of materials (Ni–Cr–Mo steel) for each temperature and safety factor. The allowable radial stress limits at the ring element on the corner R ② ⑥ ⑩ ⑬ are specially divided by the stress concentration factor 1.3.

Calculated Results. The optimization of wheels is conducted by the above-described centrifugal load condition, thermal analysis, and allowable stress limits. Optimization results of the 16th stage wheel are shown in Fig. 9. In these figures, (*a*), (*b*), and (*c*) show the calculated results of temperature distribution, radial stress distribution, and circumferential stress distribution at 20 min, 30 min, and 40 min after startup, respectively. At 30 min after startup, circumferential stress at

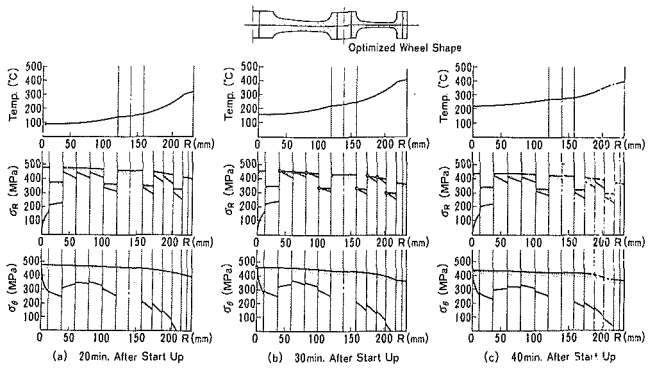

Fig. 9 Temperature and stress distributions of comrpessor wheel (16st)

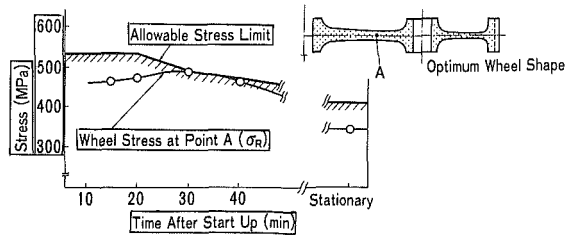

Fig. 10 Transient wheel stress and allowable stress limit (12st)

inner radius and radial stresses on inner and outer webs reach allowable stress limits. From these figures, it is shown that optimized wheel shape is determined by load conditions at this time. The optimized wheel shape is shown at the top of Fig. 9(*b*). In these cases, optimum shapes of inner and outer webs are approximated by three circular arcs, respectively. About 20 percent weight reduction compared with traditional wheels is achieved with an increase in reliabilty. Figure 10 shows the relation between radial stresses on the inner web at point *A* of the optimized wheel and allowable stresses at that point of the 12th stage wheel. From this figure, it is shown that the wheel stress becomes most severe at about 30 min after startup and maximum transient thermal stress at this point is about 150 MPa.

Conclusions

An automated-synthesis system for optimum wheel design was developed using Donath's method for centrifugal and thermal stress analyses and the sequential linear programming method for the optimization process. In this system, allowable stress limits can be set at each point, so that stress concentration at corner *R* and strength variation in accordance with the temperature at each point can be considered. Numerous pairs of load conditions and allowable stress limits, which depend on time, can be used for optimum design of each wheel, so that this system is suitable for optimum design considering transient load conditions.

This system is used in the design of axial flow compressor wheels. In this case, the optimum shape of inner and outer webs is approximated by three circular arcs. About 20 percent weight reduction, compared with traditional wheel design, is achieved with an additional increase of reliability.

References

1 Donath, M., "Die Berechnung Rotierender Sheiben und Ringe Nach Einen Neuen Verfahren," Springer, 1912.

2 de Silva, B. M. E., "The Application of Nonlinear Programming to the Automated Minimum Weight Design of Rotating Discs," in: *Optimization*, Fletcher, ed., Academic Press, 1969, pp. 115–150.

3 de Silva, B. M. E., "Minimum Weight Design of Discs Using a Frequency Constraint," ASME *J. Eng. Ind.*, Vol. 91, 1969, pp. 1091–1099.

4 Sharpe, R., "The Optimum Design of Arch Dams," *Proc. Inst. Civ. Eng.*, Paper 7200s, Suppl. vol., 1969, pp. 73–98.

5 Marcal, P. V., and Gellatly, R. A., "Application of the Created Response Surface Technique to Structural Optimization," *Proceedings of the 2nd Air Force Conference on Matrix Methods in Structural Mechanics*, Oct. 1968, AFFDL-TR-68-150.

6 Venkayya, V. B., "Design of Optimum Structures," *Computers and Structures*, Vol. 1, 1971, pp. 265–309.

On Predicting the Resonant Response of Bladed Disk Assemblies

J. H. Griffin
Department of Mechanical Engineering,
Carnegie Mellon University,
Pittsburgh, PA 15213

The vibratory responses of blades in gas turbine engines vary because of mistuning. An approach is developed for calculating the statistical distribution of peak resonant stresses in engine blading. It is used to predict the vibratory response of an unshrouded fan stage. The results of the calculation compare favorably with test data for the lower frequency modes. The procedure can be used to predict fleet durability and offers a practical engineering approach for dealing with stage mistuning.

1 Introduction

Because of the periodic nature of the bladed disk structure, small variations in the dynamic properties of the system can significantly alter the dynamic response of the blades so that their amplitudes can vary widely from blade to blade, e.g., [1-9]. Because of this "mistuning effect" it is difficult to predict fleet durability from engine test data since it is always possible that the strongly vibrating blades were not instrumented or that another engine may be assembled in such a way that some of its blades would have much higher vibratory stresses and fail from high cycle fatigue. A statistical approach for dealing with this uncertainty was presented in [1]. In that paper the statistical distribution of blade amplitudes was compiled by calculating the forced response of hundreds of randomly mistuned turbine disks. The resulting distribution of amplitudes was compared with that observed in actual engines. The predictions corresponded reasonably well with the test data after relatively large strain gage errors (which were estimated to be of the order of 50 percent) were taken into account. The turbine results were sufficiently encouraging that a follow-on study was initiated to develop a data base with smaller strain gage error, which could be utilized to assess this approach more critically. This paper reports the results of the follow-on study.

An unshrouded fan stage was selected as the focus of this work for several reasons. The first reason is that the strains could be more accurately measured on the first-stage blades. The first-stage blades are larger and, consequently, the gages can be placed more accurately on the blades. In addition, the blades are subjected to lower temperatures than in the other stages and the strain gages should be more durable and the data more accurate than if the measurements were taken on blades located farther back in the hotter sections of the engine. A second reason that a fan stage was selected is that it provides a more severe test of the flexibility of the model. The issue is: Can the same lump parameter model that was used to represent a small, high-frequency turbine stage represent a large, low-frequency fan? This assumption is questionable since the model used for the turbine stage did not include aerodynamic coupling between the blades and this effect tends to be more important as the flexibility of the blades relative to the disk increases. Lastly, this particular blade was selected because its first three modes would be excited by low engine order excitations; thus, it is possible to obtain three sets of data for comparison with the theory and to find out how well the analytical approach works for higher modes.

A model is presented for representing the bladed disk. Then the governing equations of motion for the system are formulated and the solution procedure outlined. Results from analytical simulations are then compared with engine test data. Lastly, some observations are made concerning the results.

2 Solution Technique

The problem that is described in this section and the statistical simulation techniques that are used in solving that problem are essentially the same as those used in earlier papers [1, 2]. Since the problem and the statistical approach are described in detail in [1], this aspect of the work will only be summarized here and emphasis will be placed on differences between the current and earlier models.

2.1 Problem Description. The objective of this work is to determine the resonant response of each blade in a mistuned bladed disk assembly during a slow acceleration or deceleration of the engine. The excitation of interest is that induced by the blades rotating through a circumferential variation in the flow field. Since the excitation repeats itself with each engine rotation it is periodic and can be represented by a Fourier series, which has frequencies proportional to integer multiples of the engine's rpm. As the engine changes speed, one of these frequencies may coincide with a natural frequency of the bladed disk, at which time the other terms in the Fourier series have little effect and are negligible. Thus, in considering a specific resonant response it may be assumed that each blade is exposed to a simple harmonic excitation having the same amplitude but differing in phase by an amount that is propor-

Contributed by the Gas Turbine Division of THE AMERICAN SOCIETY OF MECHANICAL ENGINEERS and presented at the 32nd International Gas Turbine Conference and Exhibit, Anaheim, California, May 31-June 4, 1987. Manuscript received at ASME Headquarters February 17, 1987. Paper No. 87-GT-158.

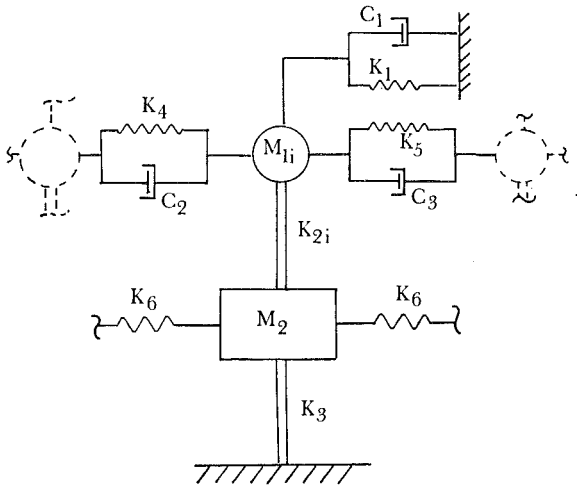

Fig. 1 Lumped parameter model

tional to the blade's circumferential position on the disk. In theory, the magnitude of the excitation could be calculated from the unsteady aerodynamic forces acting on the blades. This is quite difficult to do in practice, especially for low engine order excitations whose sources are not easily identified. Because the problem is linear, the effect of the force coefficient is to act as a scaling factor that equally affects the amplitudes of all of the blades. Consequently, for purposes of this study, it is taken as being equal to unity and the study focuses on how well the theory predicts the relative amplitudes of the blades. The phase of the excitation, on the other hand, is explicitly determined by the number of blades on the disk and the engine order of the excitation. For example, one of the cases simulated is a 2E excitation, i.e., it has a frequency of two times the engine rpm and a phase difference between adjacent blades equal to 4π divided by the number of blades, 26.

2.2 Modeling. The procedures used to establish the nominal values of the model's parameters will be discussed, then the basis for incorporating the statistical variation will be given.

2.2.1 Nominal Model. The lumped system of masses, springs, and dashpots depicted in Fig. 1 is used to represent one segment of the bladed disk. The parallel lines in Fig. 1 indicate beamlike spring elements which have zero extensional flexibility and transverse stiffnesses as noted. The "nominal" or average values of the model parameters are chosen so that the dynamic response of the nominal system corresponds as closely as possible to that predicted by finite element methods for a tuned bladed disk with nominal dimensions. The model is similar to that used in [1] with the differences that only a single mass and spring are used to represent each blade and additional elements are added to represent aerodynamic coupling between blades.

The spring and dashpot associated with the coefficients K_1 and C_1 represent the aerodynamic forces that act between the blade and the surrounding gases, whereas the springs and dashpots placed between the blades represent the in-phase and out-of-phase aerodynamic forces that act between neighboring blades. The values of the coefficients associated with each term were calculated utilizing the NASA developed aerodynamic code, RAO [10]. The approach used for calculating the aerodynamic coupling is discussed in [2]. Values of the coefficients are summarized in Table 1.

Specifying the aerodynamic terms leaves five model parameters M_{1i}, M_2, K_{2i}, K_3, and K_6 that can be used to match the structural characteristics of the bladed disk. A key feature of a system that exhibits mistuning effects is that it has system modes whose frequencies are close together, so that the

Table 1 Summary of nominal model parameters (in consistent units)

Mode	1	2	3
K_1	-7.5	-28.0	-344.0
K_{2i}	$1.09\ 10^6$	$4.85\ 10^6$	$9.90\ 10^6$
K_3	$9.26\ 10^3$	$6.48\ 10^4$	$1.91\ 10^5$
K_4	7.3	4.0	-108.0
K_5	-2.5	10.3	12.0
K_6	$1.37\ 10^6$	$8.27\ 10^5$	$1.16\ 10^6$
C_1	0.0190	0.0205	0.3548
C_2	0.0026	0.0037	0.0459
C_3	0.0024	- 0.0028	0.0763
M_{1i}	$6.05\ 10^{-4}$	$3.46\ 10^{-4}$	$4.12\ 10^{-4}$
M_2	$3.03\ 10^{-2}$	$1.75\ 10^{-2}$	$4.12\ 10^{-2}$
Excitation Order	2E	4E	6E

differences in system frequencies are comparable to variations in blade frequencies. To reflect this behavior the nominal values of the model parameters are chosen so that the lumped parameter system matches the bladed disk's response in its most important modes. If the system was tuned it would respond in only the primary mode, that having the same circumferential distribution around the disk as the excitation. To match this behavior the values of the parameters are chosen so that the mass spring system has the same system frequency and modal mass as the bladed disk in its primary mode and so that it has the same system frequency in the mode adjacent to the primary mode. For example, in the case of the 2E excitation the primary mode is the 2 nodal diameter mode of the system and the adjacent mode is the 1 nodal diameter system mode. In addition, since the mass M_{1i} and spring K_{2i} are meant to represent the blade, their nominal resonant frequency is constrained to be the same as that of the blade. One additional constraint is required to determine the system parameters fully. One condition that was tried initially was that M_{1i} should equal the modal mass of the blade. It was found in this case that the resulting spring mass system had a second radial mode in the frequency range of interest that was not present in the actual disk. By slightly relaxing the final constraint it was observed that the frequency of the spurious mode could be raised and that it would not then adversely affect the simulation. Thus, the final constraint became that the second radial mode have a sufficiently high frequency that it not affect the results. The resulting nominal values of the system parameters that meet all the above requirements are listed in Table 1.

2.2.2 Statistical Models. There are two statistical aspects that must be taken into account in computing blade amplitude scatter so that it can be compared with engine data. The first is in simulating mistuning in the analysis, the second is taking into account variations in the strain to displacement ratio that occur from blade to blade in the experimental data.

Mistuning is simulated by letting the stiffnesses associated with the blades, K_{2i}, vary from blade to blade. The stiffnesses are selected in such a way as to give rise to a random variation in blade frequencies that is consistent with that observed in bench test of the blades. The mean frequency, standard deviation, and ratio of the standard deviation to the mean fre-

Table 2 Statistical variation in blade frequencies (Hz)

Mode	1	2	3
f (mean frequency)	167	494	801
s (standard deviation)	1.1	2.8	4.3
s ÷ f	0.66%	0.57%	0.54%

quency are given in Table 2 for the first three blade modes. It is interesting to note that the ratio of the standard deviation to the mean frequency is approximately the same, 0.6 percent, for all three modes. It is assumed that this ratio is maintained under engine operating conditions. Since the blades have higher nominal frequencies under rotating conditions the frequency standard deviations used in the mistuning analyses are scaled up accordingly.

A second statistical effect that must be accounted for is that the computer algorithm calculates blade displacements, whereas the engine data are in terms of dynamic strain amplitudes. It is expected that the engine data will exhibit more scatter than that predicted by the code both because of strain gage errors and because stress ratios vary from blade to blade. This additional source of scatter was assessed by laboratory tests on a number of blades in which strains and displacements were measured for each mode of interest. The standard deviation in the ratio of the strain to the displacement varied from 8 to 13 percent for the first three modes. As planned, this error is much lower than that which was estimated for the turbine blades discussed in [1]. Consequently, because of the lower strain gage scatter, the current engine tests provide an improved assessment of the theory.

2.3 Method of Solution. The steady-state harmonic response of the mass, spring, and viscous damper system representing the bladed disk is determined in the usual fashion. The equations of motion for each of the masses in the ith blade and disk segment of the structure (Fig. 1) are written in the standard manner.

The response is assumed to be sinusoidal, i.e., the motion of each mass is represented as the sum of sin ωt and cos ωt terms with unknown coefficients where ω is the frequency of the excitation. When this representation is substituted into the equations of motion the coefficients of the linearly independent terms can be equated. This process results in four algebraic equations for each blade and disk segment. For N blades there are $4N$ simultaneous algebraic equations, which are then solved at each forcing frequency to determine the resonant response of the bladed disk.

The computer code that is used is a version of that discussed in [1], which has been modified to take into account the additional aerodynamic coupling between the blades. Consequently, details concerning the algorithm and the approach utilized in establishing the peak responses of the blades are identical to those discussed in [1]. Briefly summarized the code works as follows. A bladed disk is mathematically constructed by randomly assigning blade properties in a manner consistent with that observed in practice. Its forced response is calculated over a range of frequencies up to 20 Hz above and below the last observed blade peaks to insure that all resonances are obtained. A parabola is fitted through the points of highest response and used to calculate each blade's peak amplitude and frequency. This information is stored and the entire process repeated for a specific number of randomly assembled bladed disks.

The results from the simulation can then be analyzed in any number of ways in order to understand better the statistical aspects of mistuning. For example, one important type of postprocessing of the data involves estimating cumulative probability functions from the blade amplitude data. In this process the values of the peak amplitudes are arranged as a sequence of increasing numbers which are then assigned a probability based on their rank in the sequence [1]. Viewing the results in terms of probability is especially important in dealing with mistuning. When a bladed disk is sensitive to mistuning it is almost impossible to model in any exact manner that will accurately predict the response of each blade. This is because physical systems that are very sensitive to mistuning give rise to mathematical systems that are sensitive to model inaccuracies. (See for example the sensitivity study on the effect of aerodynamic coupling in [2].) What this means is that the more important mistuning is, the less likely that it can be modeled in a deterministic fashion on a blade-by-blade basis. However, it is the contention of this paper that simple models can be used to predict overall statistical trends adequately and that it is these trends that are really important in terms of establishing engine durability.

Results

In the previous section the procedure for establishing probability distributions is discussed. They are important because they provide a method for estimating engine durability. That is, given a group of randomly assembled bladed disks, as in the case of a fleet of engines, the worst vibratory response of any of the blades can be estimated from a cumulative probability function of the blade amplitudes. Obviously, some of the engines in the fleet will have durability problems if that stress is larger than that required to initiate high cycle fatigue.

Probability distributions may be constructed from experimental or analytical data. They are established experimentally for the fan stage by taking the strain gage data from engine tests of the bladed disk and processing them to establish peak strains for each instrumented blade in each of the three modes of interest. These data are normalized by dividing by the median value of the sample so as to provide a direct estimate of relative blade scatter. The experimental data are depicted as the open data points in Figs. 2, 3, and 4 for the three lowest frequency modes.

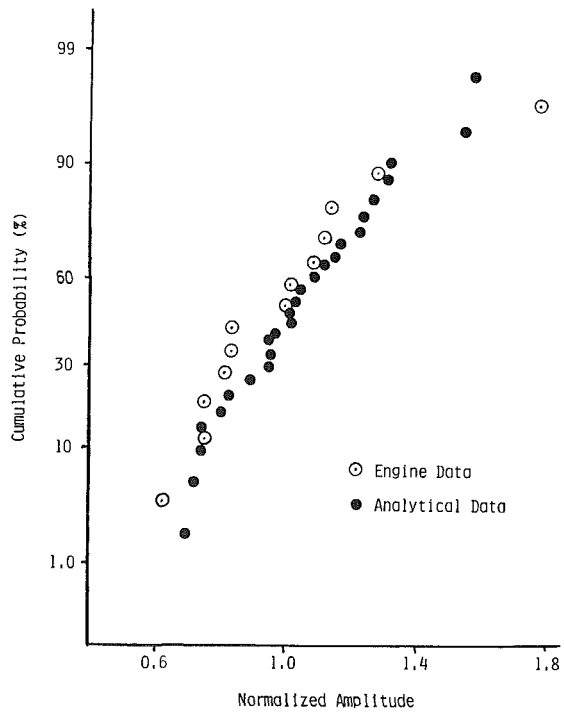

Fig. 2 Cumulative probability as a function of amplitude: first mode

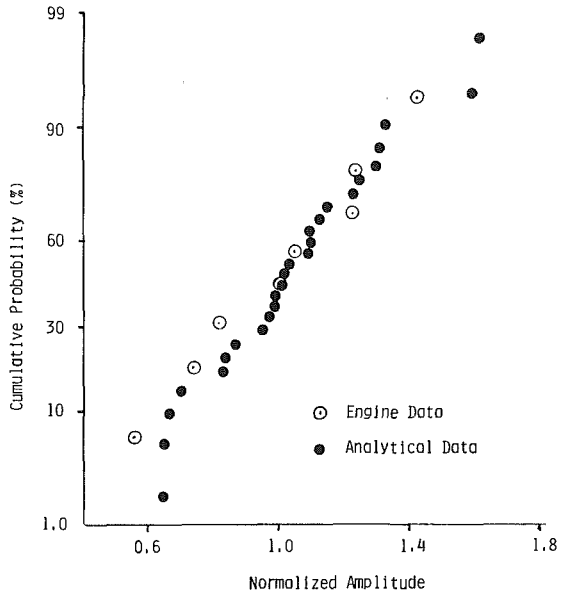

Fig. 3 Cumulative probability as a function of amplitude: second mode

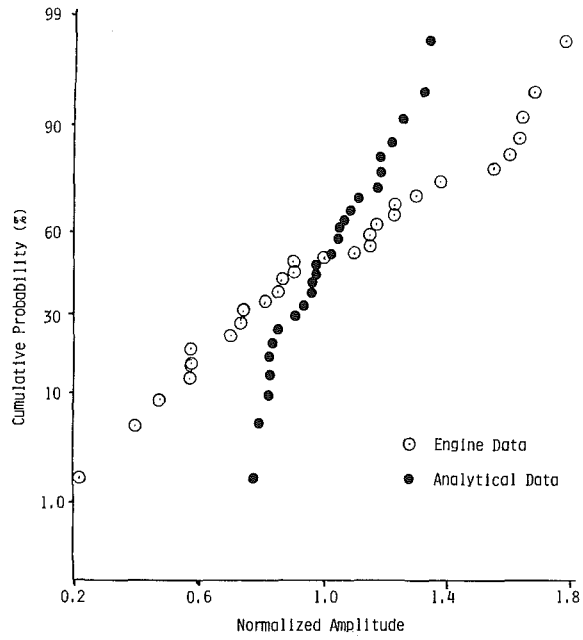

Fig. 4 Cumulative probability as a function of amplitude: third mode

The analytical method computes blade amplitudes. Consequently, before processing the data statistically it is first necessary to convert them to strains in order to have quantities that can be directly compared with the experimental data. This is done by processing the analytical amplitude data and incorporating an additional source of scatter, the variation in the strain to amplitude ratios that was observed in the laboratory tests discussed in the section on statistical models. In doing this it is assumed that the ratio is log-normally distributed (so that the measured strain amplitudes are always positive) with a standard deviation that is proportional to the value measured, i.e., approximately 10 percent of the measured value. Once the strains are calculated analytically they are then processed in the same manner as the experimental data in order to establish the probability functions. The results for the lowest three modes are depicted as the solid data points in Figs. 2, 3, and 4.

As can be seen in Figs. 2 and 3, the agreement between the experimental results and that predicted by the theory is good in the first two modes of response. The first mode corresponds to the blades vibrating in essentially a first bending mode in response to a 2E excitation. The experimental data points follow the trend predicted by the analytical model except for the point associated with the highest amplitude blade. That data point is not particularly significant since the extremes of the distribution are least reliably estimated when constructing probability distributions. The second mode corresponds to blades vibrating in predominantly a second bending mode in response to a 4E excitation. As indicated in Fig. 3, the agreement in this case is excellent.

However, from Fig. 4 it is clear that the theory does a poor job of predicting amplitude scatter in the case of the third mode. It is believed that this difficulty is in large part due to errors in calculating the aerodynamic terms in the model. The implementation of the aerodynamic code that was used allowed the blade to respond in either a bending or torsional manner but not both. In the case of the first two modes the displacements corresponded to mainly bending modes that could be represented in terms of translations of the sections; consequently, the aerodynamic terms could be calculated in a straightforward manner. It was observed that for the first two modes the values of the damping terms that were calculated were consistent with estimates of damping taken from the engine data. However, in the case of the third mode, the mode shape was more complex, exhibiting both torsion and bending components. For this case the mode shape was simplified to a simple torsional response in order to put it in a form that the aerodynamic code could accommodate. The resulting aerodynamic terms that were calculated contained damping values that were inconsistent with the experimental data (if the system were tuned they would give rise to modal damping a factor of four larger than the mean value of half-bandwidth damping observed in the engine). The calculated aerodynamic values were utilized in the mistuning code in order to establish the effect of this type of error on scatter prediction. It has been established in other studies that the scatter associated with mistuning is smaller if the damping in the system is increased [2]. The type of discrepancy exhibited in Fig. 4 is consistent with an overprediction of the aerodynamic damping terms.

In the earlier study of turbine blade mistuning [1] it was noted that the highest responding blades tended to have individual blade frequencies close to the tuned disk frequency (the frequency at which the bladed disk would respond if all the blade were tuned). Blade amplitudes are plotted as a function of their individual blade frequencies in Figs. 5 and 6 for the lowest two modes of response. The solid vertical lines correspond to the tuned system frequencies. The analytical data in these figures indicate that the fan blades exhibit the same trend as the turbine blades in that the highest responding blades tend to have frequencies near the tuned system frequency. The engine data, while exhibiting more scatter because of strain gage variations, display behavior that is consistent with this trend.

4 Closing Remarks

The work discussed in this paper is a continuation of the research reported in [1, 2]. The objective of the work was to evaluate the accuracy of the mistuning model developed in those papers. In particular it was necessary to develop a data base of blade peak amplitudes from engine tests, model the response of the stage in the modes of interest, and evaluate the results. Several observations can be made concerning these different aspects of the work.

In developing a data base from experiments it is necessary to characterize the scatter in the strain displacement ratios separately. Once the amplitude scatter from mistuning is computed then this additional source of variation is superimposed

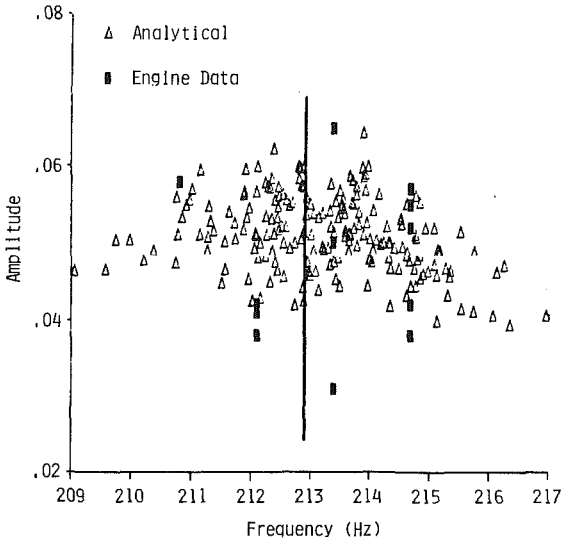

Fig. 5 Maximum amplitude versus blade frequency: first mode

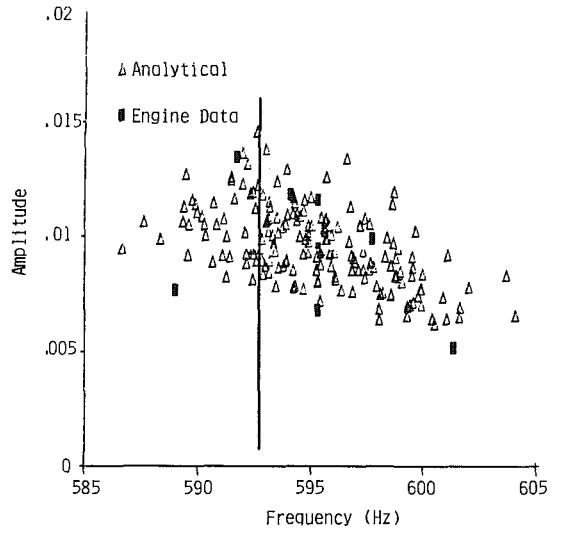

Fig. 6 Maximum amplitude versus blade frequency: second mode

in order to obtain probability distributions that can be compared with engine strain data. An underlying issue is whether the scatter in the strain displacement ratios is due to strain gage error or to variations in mode shape. If it is the first case then the true strains in the blades may be smaller than the values indicated by the engine data, i.e., the really high strain readings are due to errors in instrumentation. Consequently, they need to be "subtracted" from engine data to establish the real distribution of strains. However, if in fact the scatter in the strain displacement ratios represent true variations in the modal stresses then this is an important source of scatter that can damage blades and needs to be accounted for in any prediction of blade durability. Certainly the safest course is to assume the latter case and utilize an approach that takes this variation into account in predicting engine durability. This does mean, however, that additional work needs to be done on characterizing this type of strain variation for different classes of blades.

The approach used in modeling the turbine stage [1] had to be changed in two respects in order to model the fan stage accurately. One change was that a new strategy had to be developed in identifying the masses and springs to be used in the model since the earlier approach resulted in a spurious second radial mode at a frequency just above the blade-alone frequency. The change in procedure is discussed in the section on modeling; the point to note here is that this problem did not arise with the earlier turbine stage model and seemed to be caused by the fact that the disk of the fan stage was stiffer (relative to the blades) than in the case of the turbine stage. This problem occurred for all three modes that were modeled and may occur whenever flexible blades are mounted on a very stiff disk.[1]

A second change in the modeling process that required a different approach from that used in [1] was the method for dealing with aerodynamic damping. In the first paper the aerodynamic effects were modeled with a single viscous damper (corresponding to C_1 in this paper). Its value was assigned so as to be compatible with the experimental data in that it was chosen so as to give the same amount of system damping as was observed in tracking plots of the high response blades. This was a reasonable approach in the case of the turbine for two reasons. The experimental data were very clean and there was very little scatter in the experimentally measured values of damping. Secondly, the behavior of the resulting model was consistent with the experimental data in that the calculated behavior of the high response blades exhibited the same amount of half-bandwidth damping that was observed in the experimental data. This was not true in the case of the fan stage; the blade data exhibited multiple peaks and it was not possible to get a reliable estimate of damping. In addition, when a mean value of damping was used the model did not predict a system response that was consistent with the experimental data. For these reasons it was necessary to try an analytical approach for establishing aerodynamic effects and to modify the model to include the additional aerodynamic coupling terms.

In evaluating the results it was observed that the revised models predicted the response of the first and second modes but did not correctly predict the response of the third mode. This discrepancy was attributed to the fact that the approach used for computing the aerodynamic forces acting on the blades was not capable of simulating the more complex mode shape associated with the third mode. This result is interesting for two reasons. One is that it indicates a direction for additional work, i.e., incorporating better aerodynamic models and verifying that this is, in fact, the primary source of the discrepancy. In addition it is interesting because the approach worked well for the lower modes and could be used to compute relative blade scatter in a completely analytical fashion without recourse to engine data. This means that the method can be used before the engine is tested to decide how best to instrument the engine. For example, based on such calculations, one could establish how many blades must be instrumented on a specific stage in order to measure vibratory response within a given level of accuracy. Thus, a potential use for such codes at their present level of development is to use them to optimize the distribution of instrumentation throughout the engine.

In addition, the fact that the approach predicts the relative response of the first two modes is interesting because it indicates that with some additional work, it may be possible to achieve the ultimate goal of analytically predicting the absolute response of the stage. The current approach is quite useful in that it predicts the relative response of the blades on the stage and, by calibrating it with engine tests, it can be utilized to predict fleet durability. However, if the magnitude of the generalized force was known this approach could be used to predict the response of the stage and optimize its

[1] Sometimes the second radial system mode actually does occur in the stage at a frequency just above the blade-alone frequency. Its presence is apparent in the engine data because it causes a very distinctive double peak in the response curve. The finite element analysis of the stage and the engine data indicated that this was not the case for the fan stage under consideration and hence the model parameters were manipulated so as to eliminate its effect.

design before the engine is tested. The generalized force acting on the stage may be caused by a number of physical mechanisms, for example static structures such as struts or vanes in the flow path, mechanical imbalance, or nonuniform combustion processes. An important line of future research lies in integrating models of excitation with stage mistuning codes in order to achieve a completely predictive model of stage resonant response. Such a tool would greatly benefit the engine design process, since potential vibration problems could be detected and corrected during the initial design phase, rather than lie undetected until after the prototype hardware is built, when a major redesign would be required to correct the problem.

Acknowledgments

The author wishes to thank Mr. Thomas M. Hoosac, Mr. Carl E. Meece, Jr., and Dr. Yehia M. El-Aini of Pratt and Whitney Aircraft for their support and advice in pursuing this research. In particular this work would not have been possible without the aid of Mr. Hoosac who was the project manager for Pratt and Whitney assigned to this project. This work was supported by the Aero Propulsion Laboratory, Wright-Patterson Air Force Base, Contract No. F33615-84-C-2454, under the direction of Mr. William A. Stange.

References

1 Griffin, J. H., and Hoosac, T. M., "Model Development and Statistical Investigation of Turbine Blade Mistuning," ASME *Journal of Vibration, Acoustics, Stress, and Reliability in Design*, Vol. 106, No. 2, 1984, pp. 204–211.

2 Basu, P., and Griffin, J. H., "The Effect of Limiting Aerodynamic and Structural Coupling in Models of Mistuned Bladed Disk Vibration," ASME *Journal of Vibration, Acoustics, Stress, and Reliability in Design*, Vol. 108, 1986, pp. 132–139.

3 Kielb, R. E., and Kaza, K. R. V., "Aeroelastic Characteristic of Cascade of Mistuned Blades in Subsonic and Supersonic Flows," ASME Paper No. 81-DET-122, Sept. 1981.

4 Ewins, D. J., "The Effects of Detuning Upon the Forced Vibrations of Bladed Disks," *Journal of Sound Vibration*, Vol. 9, 1969, pp. 65–79.

5 Wagner, J. T., "Coupling of Turbomachine Blade Vibrations Through the Rotor," ASME JOURNAL OF ENGINEERING FOR POWER, Vol. 89, No. 4, 1967, pp. 502–513.

6 Armstrong, E. K., and Stevenson, R. E., "Some Practical Aspects of Compressor Blade Vibration," *Journal of the Royal Aeronautical Society*, Vol. 64, No. 591, 1960, pp. 117–130.

7 Whitehead, D. S., "Effect of Mistuning on the Vibrations of Turbomachine Blades Induced by Wakes," *Journal of Mechanical Science*, Vol. 8, No. 1, 1966, pp. 15–21.

8 Srinivasan, A. V., and Fabunmi, J. A., "Cascade Flutter Analysis of Cantilevered Blades," ASME JOURNAL OF ENGINEERING FOR POWER, Vol. 105, 1983, pp. 1–10.

9 Afolabi, D., "The Frequency Response of Mistuned Bladed Disk Assemblies," in: *Vibrations of Blades and Bladed Disk Assemblies*, R. E. Kielb and N. F. Rieger, eds., American Society of Mechanical Engineers, New York, 1985.

10 Rao, B. M., and Jones, W. P., "Unsteady Airloads for a Cascade of Staggered Blades in Subsonic Flow," 46th Propulsion Energetics Review Meeting, Monterey, CA, Sept. 1975.

Effect of Fluid Inertia on the Performance of Squeeze Film Damper Supported Rotors

L. A. San Andres
Research Associate.

J. M. Vance
Professor.

Mechanical Engineering Department,
Texas A&M University,
College Station, TX 77843

The effect of fluid inertia on the synchronous steady-state operation of a centrally preloaded single mass flexible rotor supported in squeeze film bearing dampers is examined theoretically. For a model representative of some aircraft engine applications, frequency response curves are presented exhibiting the effect of fluid inertia on rotor excursion amplitudes and imbalance transmissibilities for both pressurized and unpressurized short open-ended squeeze film damper supports. It is shown that a significant reduction in amplitude response and transmitted force is possible for dampers operating at moderately large squeeze film Reynolds numbers. Furthermore, for unpressurized dampers the possibilities of bistable operation and jump phenomena are shown to be reduced and virtually disappear at sufficiently large operating Reynolds numbers.

Introduction

Modern aircraft engines typically utilize squeeze film dampers (SFD) in conjunction with their rolling element bearings to attenuate vibration amplitudes, to reduce transmitted forces to stationary components, and in some circumstances to promote rotor stability. Satisfactory performance of SFDs is very much dependent on their design, being greatly influenced by the amount of imbalance and damping in the rotor system, the operating speed, and by the extent of pressurization of the lubricant supply. Squeeze film dampers have the potential for either significantly improving or degrading the response and stability characteristics of a rotor system.

In spite of their successful applications, conventional SFDs have characteristics that can limit their effectiveness in controlling both normal and abusive imbalance conditions. Squeeze film forces have a highly nonlinear dependence on whirl amplitude and show strong coupling to the rotordynamics of the system. The most remarkable effect, under certain operating conditions, is the existence of the so-called "jump" phenomena. This is one more example of the hysteresis effect in classical nonlinear resonant mechanical systems. For a rigid rotor on unpressurized SFD mounts, there are three equilibrium positions of the damper in certain speed ranges [1]. The lower amplitude of motion is the most desirable since the rotor mass center has effectively inverted and the transmissibility is less than one. The highest amplitude response is undesirable since it produces transmissibilities larger than one. The intermediate solution is unstable so that constant orbit radii satisfying the equilibrium do not persist and show transient excursions of the damper journal [1–4].

Contributed by the Gas Turbine Division of THE AMERICAN SOCIETY OF MECHANICAL ENGINEERS and presented at the 32nd International Gas Turbine Conference and Exhibit, Anaheim, California, May 31-June 4, 1987. Manuscript received at ASME Headquarters February 19, 1987. Paper No. 87-GT-220.

The same phenomenon has been predicted to occur for unpressurized flexible rotors and under certain conditions the high eccentricity orbit can also be unstable [5-8].

The value of the imbalance parameter U at which a jump takes place is defined as the critical imbalance U_c and indicates the upper limit of imbalance for which the SFD support is useful. Although U_c is a complicated function of the bearing parameter B and additional system parameters, it can be stated that $U_c \simeq 0.4$ for rigid rotors [1, 2], while $U_c \simeq 0.2$ for flexible rotors on unpressurized SFD mounts [5, 7]. If $U_c > 0.2$, bistable operation occurs for speeds below the first pin-pin critical speed (ω_s) and results in "lockup" of the bearing mount. For operating speeds above ω_s, bistable operation virtually disappears although when noted it extends over a narrow speed range and has no deleterious effect [5, 7, 9].

Pressurization of the SFDs (to prevent cavitation) guarantees avoidance of bistable operation and bearing lockup, although at operating speeds above the system critical speed, transmissibilities larger than those for unpressurized mounts are expected but still are well below those encountered for rigid mounts [10, 11].

In all analyses referred to above, squeeze film forces have been obtained from approximate solutions to the Reynolds equation of classical lubrication theory, which assumes the effect of fluid inertia to be negligible. Nevertheless, the drive toward higher speeds and the use of light viscosity lubricants has brought the need to include fluid inertia in the analysis and design of SFDs. The measure of fluid inertia effects on squeeze film flows is the Reynolds number defined as the product of the square of the damper radial clearance times the whirling frequency divided by the lubricant kinematic viscosity. Dampers for large propulsion turbines operate with moderately large Reynolds numbers, typically on the order of one to twenty. In terms of overall rotordynamic behavior a

virtual mass phenomenon and Bernoulli effects are to be expected [12, 13].

Under the restriction of very low Reynolds number flows, White [14], Simandiri and Hahn [15], and Rabinowitz and Hahn [16] have presented experimental measurements of the imbalance response of rotors on centralized SFD mounts that reproduced closely the response predictions obtained by assuming squeeze film forces are due solely to lubricant viscosity. These experimental investigations are most notable since they have clearly shown the benefits as well as major drawbacks of SFDs, and have addressed the importance of a careful selection of bearing parameters to obtain optimum performance.

In practice, modern aircraft engine rotors with squeeze film dampers operating at Reynolds numbers larger than one often show a very highly damped response through the first two rigid mode critical speeds with the jump phenomena rarely observed [17]. It has been thought that the rotor system presents more damping than predicted due to pressurization of the SFDs or that fluid inertia plays an important role in the rotor frequency response. The present authors [18–20] have developed experimentally verified analyses for squeeze film forces which include the effects of fluid inertia. The major effects are found to be an "added" mass (force directed radially outward from the center of the whirl orbit) and an increase in the effective damping over the predictions from the classical Reynolds solutions.

Recent trends in SFD analysis suggest that a new generation of squeeze film dampers capable of effectively controlling abnormal imbalance conditions is readily possible. These dampers would operate at squeeze film Reynolds numbers much larger than 20 due to the increased damper clearance required for imbalance control and also because film geometry discontinuities seem to amplify the beneficial effects of fluid inertia. Therefore, the role of fluid inertia in SFD forces and their effect on the response of a rotating system is a topic of major interest and current research.

It is the aim of this paper to analyze the effect of fluid inertia on the imbalance response of a simple flexible rotor on centrally preloaded squeeze film bearing dampers. The dynamics of the system without fluid inertia are well understood and the present contribution is largely based on a modification of the analysis of Rabinowitz and Hahn [5].

The results presented in this paper should not be considered of universal application but only to those rotor-damper systems in which the SFD dominates the response and in which the squeeze film Reynolds number is in the range of the reported results. The authors are aware that many SFDs in existing rotating machinery satisfy the conditions of extremely low Reynolds number flow; nevertheless, other actual applications and recent trends in the field urgently require an approximate knowledge of the rotor response for systems operating at large Reynolds numbers.

The analysis presents frequency response curves for a flexible rotor on two SFD mounts and up to a value of squeeze film Reynolds number equal to 40. The squeeze film flow is here considered to be stable and laminar. Whether the flow becomes turbulent at lower Reynolds numbers is a question that is currently being addressed by extensive experimental and analytical research at Texas A&M University.

For unpressurized SFD mounts, we assume that the π film model is valid for the range of Reynolds numbers studied. This assumption has been made partly due to limitations in the actual knowledge of the mechanics of the flow, but has been employed to produce a clear isolation of fluid inertia effects from those due solely to the viscous action of the squeeze film.

Nomenclature

a = speed parameter = ω/ω_s

B = bearing parameter = $\mu_R (L/c)^3/(M \cdot \omega_r)$

$2C$ = damping coefficient at rotor center, FT/L

c = damper radial clearance, L

CCO = circular centered orbit

$\overline{Cr}$ = $\overline{Crt} - \mathrm{Re} \cdot \overline{Drr}$ = dimensionless effective cross-coupled damping coefficient

$\overline{Ct}$ = $\overline{Ctt} - \mathrm{Re} \cdot \overline{Dtr}$ = dimensionless effective direct damping coefficient

$\overline{Crt}$ = $Crt\, c^3/\mu RL^3$ = dimensionless cross-coupled damping coefficient

$\overline{Ctt}$ = $Ctt\, c^3/\mu RL^3$ = dimensionless direct damping coefficient

$\overline{Drr}$ = $Drr\, c/\rho RL^3$ = dimensionless direct added mass coefficient

$\overline{Dtr}$ = $Dtr\, c/\rho RL^3$ = dimensionless cross-coupled added mass coefficient

D_x, D_y = coefficients defined in equations (4)

e = damper journal orbit radius

f = resonance frequency ratio = ω_r/ω_s

g = rotor excursion amplitude at midspan with respect to static deflection line

G = nondimensional rotor amplitude at midspan = g/c

K_r = retainer spring stiffness for each bearing station

$2K_s$ = rotor stiffness

L = SFD axial length

$2M$ = rotor-bearing system mass

r, t = unit vectors along and perpendicular to line of centers at bearing station

R = SFD bearing radius

Re = squeeze film Reynolds number = $\omega \cdot c^2/\nu$

Re_s = Reynolds number at pin–pin critical speed = $\omega_s \cdot c^2/\nu$

Re_r = Reynolds number at speed ω_r = $\omega_r \cdot c^2/\nu$

SFD = squeeze film bearing damper

T = transmissibility = transmitted force/$(1-\alpha)M\omega^2 u$

u = imbalance parameter = $(1-\alpha)u/c$

U = dimensionless imbalance = $(1-\alpha)u/c$

α = fraction of total mass lumped at the bearings

β = phase angle

γ = $(1-\epsilon^2)^{1/2}$

δ = retainer spring speed parameter = ω/ω_r

ϵ = dimensionless journal orbit radius = e/c

ζ = damping ratio at rotor center = $C/[2(1-\alpha)M\omega_s]$

μ = absolute viscosity of lubricant

ν = kinematic viscosity of lubricant

ρ = density of lubricant

ϕ = angular position of the bearing centerline = $\omega \cdot t$

ω = rotor speed

ω_s = first pin–pin critical speed of rotor = $\sqrt{K_s/(1-\alpha)M}$

ω_r = natural frequency of rigid rotor on retainer springs = $\sqrt{K_r/M}$

Table 1 Force coefficients for short open-end squeeze film dampers; circular centered motions (CCO)

	Full film solution (pressurized)	Cavitated solution (unpressurized)
$\overline{Ctt}$	π/γ^3	$\pi/2\gamma^3$
$\overline{Crt}$	0	$2\epsilon/\gamma^4$
$\overline{Drr}$	$\dfrac{\pi(1-\gamma)\{6/5-102(1-\gamma)/35\}}{6\epsilon^2\gamma}$	$\dfrac{\pi(1-\gamma)\{6/5-102(1-\gamma)/35\}}{12\epsilon^2\gamma}$
$\overline{Dtr}$	0	$-\dfrac{27}{70\epsilon}\left[2+\log\left(\dfrac{1-\epsilon}{1+\epsilon}\right)\right]$

Note: $\gamma=(1-\epsilon^2)^{1/2}$.

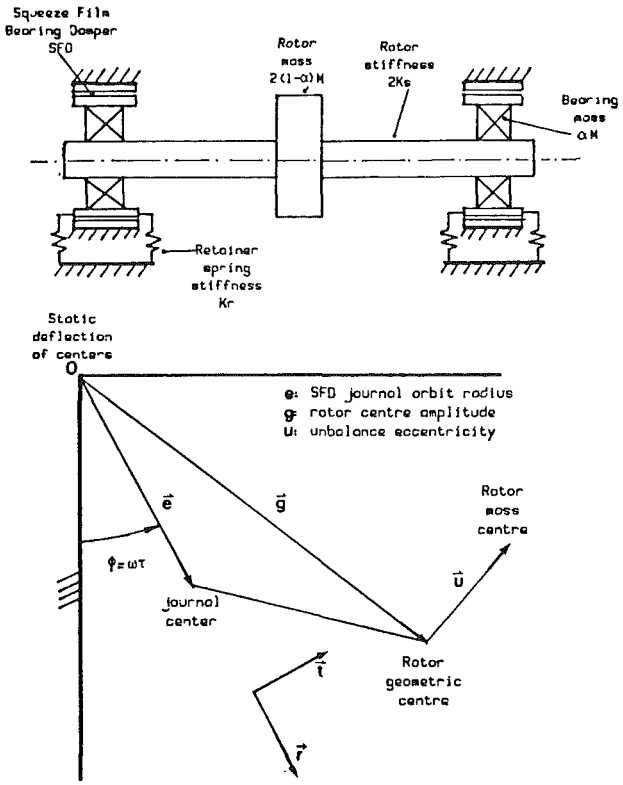

Fig. 1 Flexible rotor-bearing model with coordinates

Theoretical Analysis

Figure 1 shows schematically a flexible rotor mounted on centrally preloaded squeeze film bearing dampers. It is assumed that: (*a*) The rotor is symmetric with part of its mass lumped at the rotor center and the remainder evenly divided and lumped at the bearing stations, (*b*) the rotor speed is constant and imbalance is present only at the rotor midspan, (*c*) gyroscopic effects are negligible, and (*d*) excitation forces due to rolling element bearings are negligible.

The SFDs are assumed to have low L/D ratios (≤ 0.25) so the short open-end damper model is applicable. The flow in the damper bearing is regarded as laminar for all Reynolds numbers, and fluid inertia influences the flow within the squeeze film region but not at its axial boundaries. Thus, the pressure at the damper ends is assumed to be atmospheric or sufficiently above it to ensure full film lubrication. The assumption of laminar flow is solely based on the ground that transition to turbulence in squeeze film flows occurs at larger Reynolds numbers than for pure shear flows.

The differential equations governing the motion due to rotating imbalance are well documented [5, 9] and are not reproduced here for brevity. Under steady-state conditions, the journal and rotor centers describe circular centered orbits of amplitude e and g, respectively. In dimensionless form, the amplitudes of motion are given by [8, 9]

$$\epsilon=\frac{U\bullet a^2}{\{D_x^2+D_y^2\}^{1/2}} \tag{1}$$

$$G=\frac{U\bullet a^2\{(D_x+1-\alpha)^2+D_y^2\}^{1/2}}{(1-\alpha)\{(1-a^2)^2+(2\zeta a)^2\}^{1/2}\{D_x^2+D_y^2\}^{1/2}} \tag{2}$$

and the transmissibility T is

$$T=\frac{\epsilon}{U\bullet a^2}\{(Baf\overline{Cr}+f^2)^2+(Baf\overline{Ct})^2\}^{1/2} \tag{3}$$

where

$$D_x=f^2(1-a^2)+a^2(\alpha a^2-1)+Baf(1-a^2)\overline{Cr}-2\zeta a^2 fB\overline{Ct}$$
$$D_y=Baf(1-a^2)\overline{Ct}+2\zeta a^2 fb\overline{Cr}$$
$$+2\zeta(f^2-\alpha a^2+1-\alpha) \tag{4}$$

Refer to the Nomenclature for a definition of all parameters in these equations.

$\overline{Ct}$ and $\overline{Cr}$ denote the effective direct and cross-coupled damping coefficients, and are equal to

$$\overline{Ct}=\overline{Ctt}-\overline{Dtr}\ \mathrm{Re}_s a$$
$$\overline{Cr}=\overline{Crt}-\overline{Drr}\ \mathrm{Re}_s a \tag{6}$$

where Re_s is the squeeze film Reynolds number at the pin-pin critical speed. The dimensionless coefficients $\overline{Ctt}$, etc., are defined in the Nomenclature and the dimensional coefficients are defined by equations (7) and (8) for the tangential and radial damper forces, respectively

$$F_t=-\bar{C}t\bullet\omega e\bullet\mu RL^3/c^3 \tag{7}$$

$$F_r=-\bar{C}r\bullet\omega e\bullet\mu RL^3/c^3 \tag{8}$$

For the open-end short SFD model, the dimensionless damping ($\overline{Cij}$) and added mass ($\overline{Dij}$) force coefficients for circular centered orbits are given in Table 1. The damping coefficients are well-known expressions obtained in the limit Re $\Rightarrow$ zero. The added mass coefficients are valid for small to moderate values of the squeeze film Reynolds number [18, 19].

For the unpressurized SFD model, Figs. 2 and 3 show the effective damping coefficients for increasing orbit radii ϵ and Reynolds numbers. For a fixed orbit radius, the effective direct damping coefficient $\overline{Ct}$ increases as the Reynolds number increases and thus, more force opposed to the whirling motion of the damper journal is available than for a damper operating at Re = 0. For orbit radii $\epsilon \leq 0.8$, the effective cross coupled damping coefficient $\overline{Cr}$ decreases as Re increases and is negative for some eccentricity ranges. Without fluid inertia (Re = 0), cross-coupled damping produces a stiffening effect (radial force directed inward). The most important effect of the decrease in the cross-coupled damping $\overline{Cr}$ is that the possibilities of bistable operation are greatly reduced.

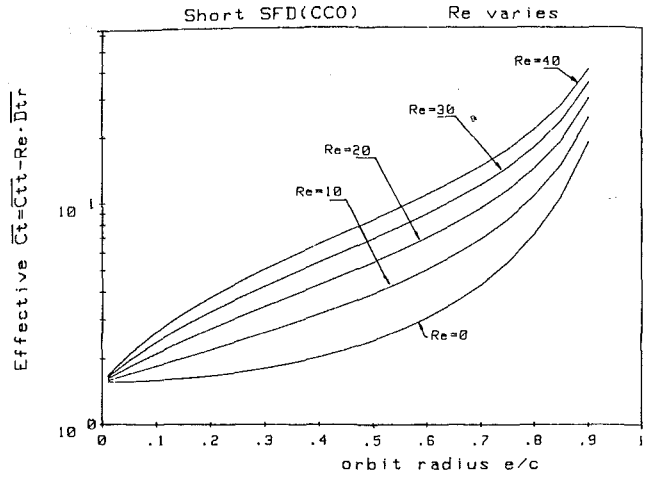

Fig. 2 Total effective damping coefficient for five values of fluid inertia, π film

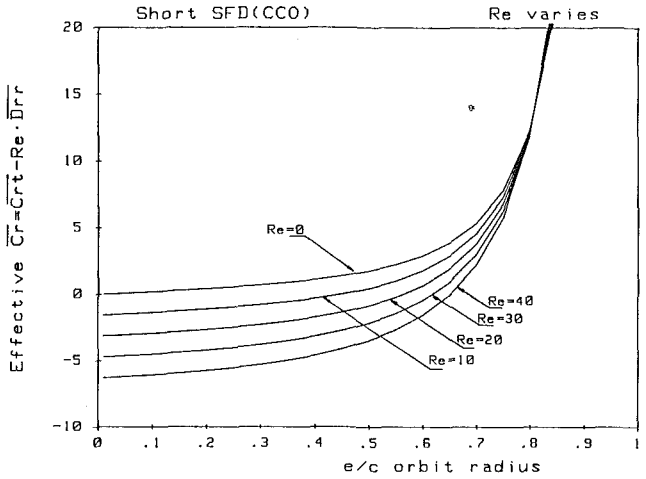

Fig. 3 Total effective cross-coupled damping coefficient for five values of fluid inertia, π fluid

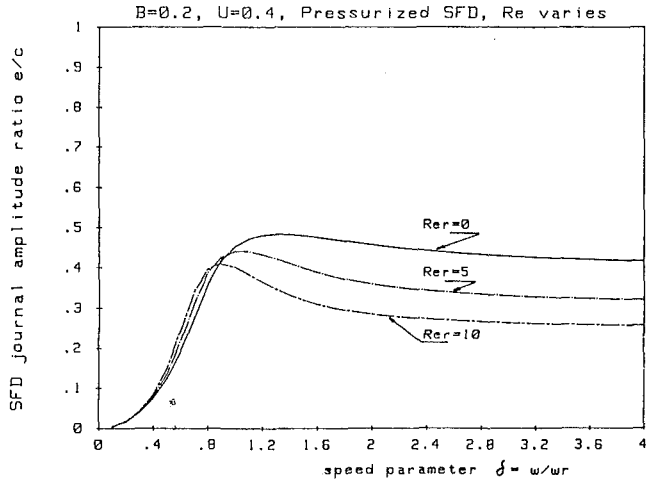

Fig. 4 Response to imbalance of a rigid rotor on SFD for three values of fluid inertia, uncavitated film

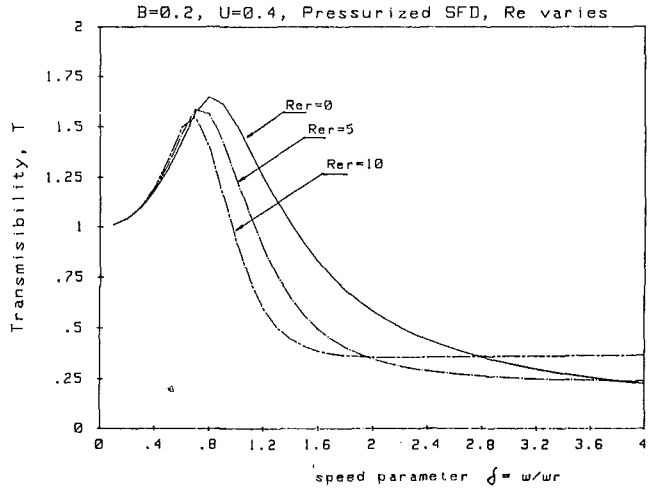

Fig. 5 Force transmissibility of a rigid rotor on SFD for three values of fluid inertia, uncavitated film

Note also that for certain Reynolds numbers, there can be an orbit radius such that the total squeeze film force is purely tangential, i.e., $\overline{Cr} = 0$, even for an unpressurized SFD.

Frequency Response for a Rigid Rotor on SFDs

The nonlinear equation (1) is solved by a modified secant algorithm as suggested in [22]. The examples presented here are representative of conditions currently found in some aircraft engines.

Figures 4 and 5 show the predicted amplitude frequency response e/c and force transmissibility T of a rigid rotor on pressurized (noncavitated) SFDs. Without film cavitation there is no damper radial stiffening effect and the jump phenomenon does not appear regardless of the amount of imbalance. For a bearing parameter $B = 0.2$, the amplitude of response to an imbalance parameter $U = 0.4$ is very well damped. As the squeeze film Reynolds number at speed ω_r increases, the orbit radius decreases and for speeds much larger than ω_r, the amplitude e/c tends to be lower than the actual imbalance eccentricity. This effect is due to fluid inertia in the squeeze film flow and increases the apparent mass of the system at large running speeds. The force transmissibility curves show approximately the same trends, although for the largest Reynolds number Re_r and due to the substantial increase in the film radial force as Re increases, T is larger than for the purely inertialess case, i.e., Re = 0.

Figures 6 and 7 show the predicted amplitude and transmissibility frequency responses for the same amount of imbalance ($U = 0.4$) when the dampers are cavitated (π film). Without the influence of fluid inertia, Re = 0, the nonlinear stiffening effect of the cross-coupled damping coefficient $\overline{Crt}$ produces a region of bistable operation above a speed parameter $\delta = 2.6$. The higher whirl amplitude produces a force transmissibility larger than the imbalance force ($T > 1$) and makes the damper ineffective in controlling such levels of imbalance. However, if the SFDs operate at Reynolds numbers $\mathrm{Re}_r = 5$ and 10, it is seen that the bistable region of operation disappears and the amplitude response e/c is very well damped. The effect of fluid inertia as Re increases is to decrease substantially the damper radial "stiffening" effect and thus, the possibilities of jump phenomena and large transmissibility regions are avoided. For the example presented here, further numerical calculations show that multiple valued response is confined to speed ranges above $\delta = 11$ for a Reynolds number $\mathrm{Re}_r = 1$, and disappears completely for Reynolds numbers Re_r larger than 2. The results of Fig. 7 show that the force transmissibility T decreases as the operating Reynolds number increases, although for large values of δ, T may increase above the value obtained for Re = 0 but is still substantially lower than the value obtained for the rotor mounted on rigid supports ($T = 1$).

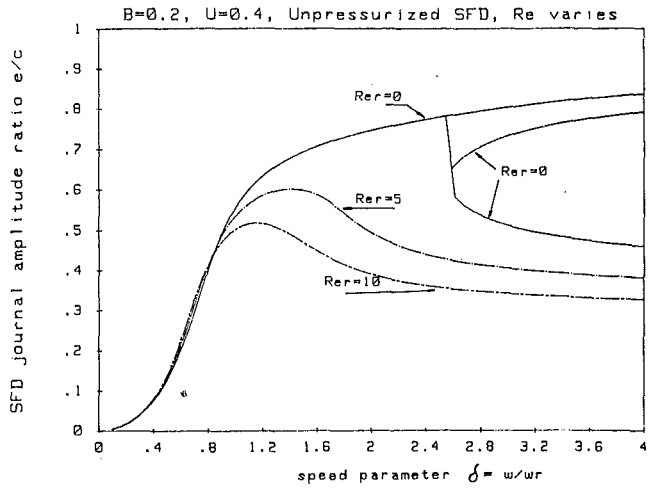

Fig. 6 Response to imbalance of a rigid rotor on SFD for three values of fluid inertia, π film

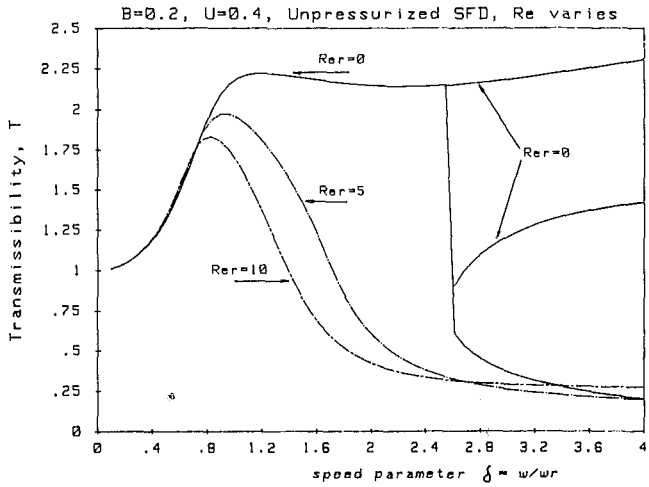

Fig. 7 Force transmissibility of a rigid rotor on SFD for three values of fluid inertia, π film

The results presented show that SFDs operating at moderate Reynolds numbers are able to control amounts of imbalance that an inertialess analysis may determine to be detrimental for rotor performance.

Frequency Response for a Flexible Rotor on SFDs

The effect of squeeze film dampers on the imbalance response of flexible rotors is complex due to the multiplicity of critical speeds. Dampers located close to a node of the whirling mode shape have a small effect on that mode due to the relatively small amplitude of journal motions. Under certain conditions nonlinear behavior and jump phenomena are also predicted for flexible rotors with dampers operating at small Reynolds numbers [5, 7, 9].

A flexible rotor with a mass ratio $\alpha = 0.20$, a resonant frequency ratio $f = 0.6$, and SFDs with a bearing parameter $B = 0.1$ approximately represent the conditions of some aircraft engines. For an imbalance parameter $U = 0.3$ and pressurized SFDs, Figs. 8 and 9 show the amplitude frequency response at the damper journal and rotor midspan, respectively, and Fig. 10 shows the force transmissibility. These figures present the rotor response for operating squeeze film Reynolds numbers Re_s equal to 0, 10, and 20. Without film cavitation there is no radial "stiffening" effect and the jump phenomenon does not appear regardless of the amount of imbalance.

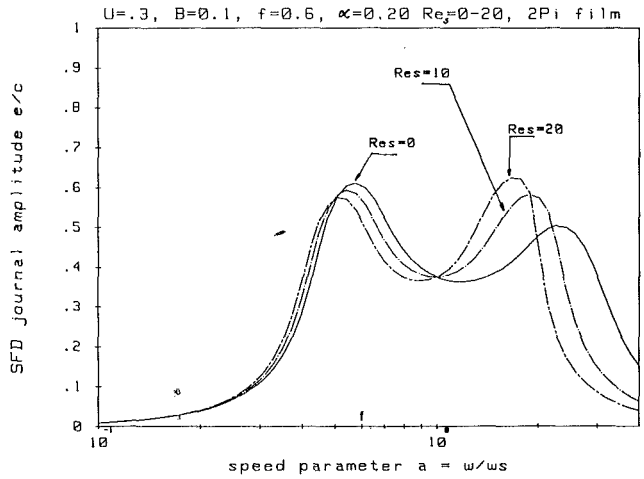

Fig. 8 Response to imbalance at the bearings of a flexible rotor on SFD for three values of fluid inertia, uncavitated film

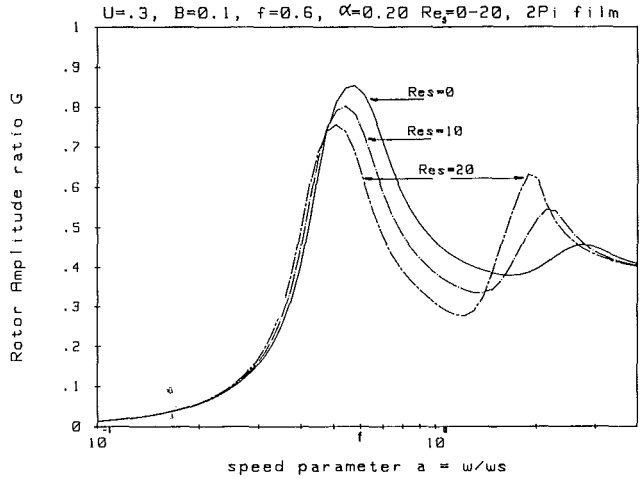

Fig. 9 Response to imbalance at midspan of a flexible rotor on SFD for three values of fluid inertia, uncavitated film

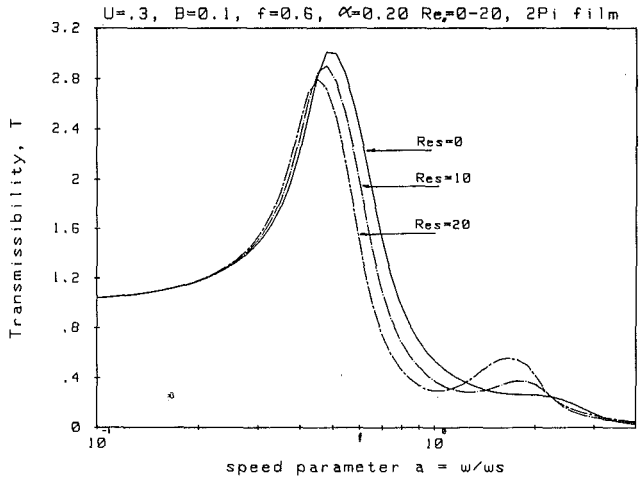

Fig. 10 Force transmissibility of a flexible rotor on SFD for three values of fluid inertia, uncavitated film

For rotor speeds less than the pin-pin critical speed ω_s, the effect of fluid inertia on the rotor response is to reduce the amplitude of motion and transmitted force to the stationary components. A slight reduction in the first critical speed is observed as the Reynolds number increases in the squeeze film flow. For operating speeds above ω_s, an important effect is the

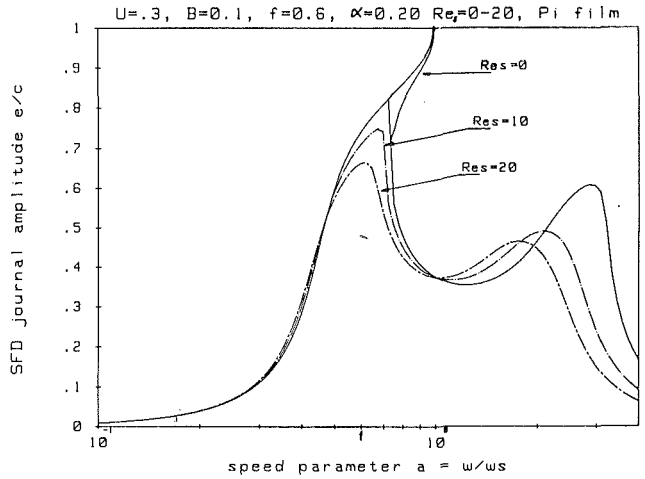

Fig. 11 Response to imbalance at the bearings of a flexible rotor on SFD for three values of fluid inertia, π film

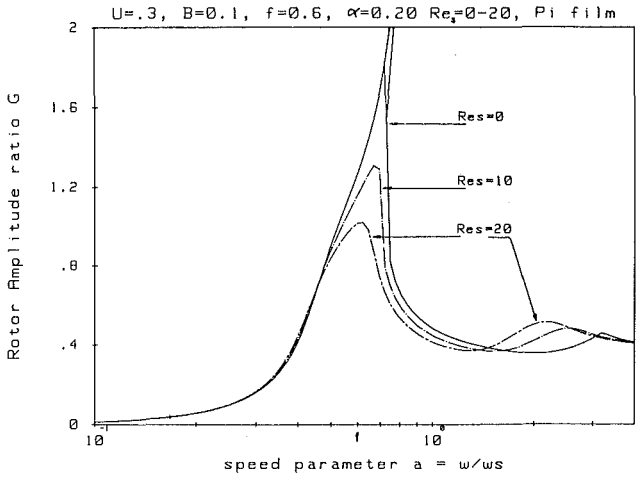

Fig. 12 Response to imbalance at midspan of a flexible rotor on SFD for three values of fluid inertia, π film

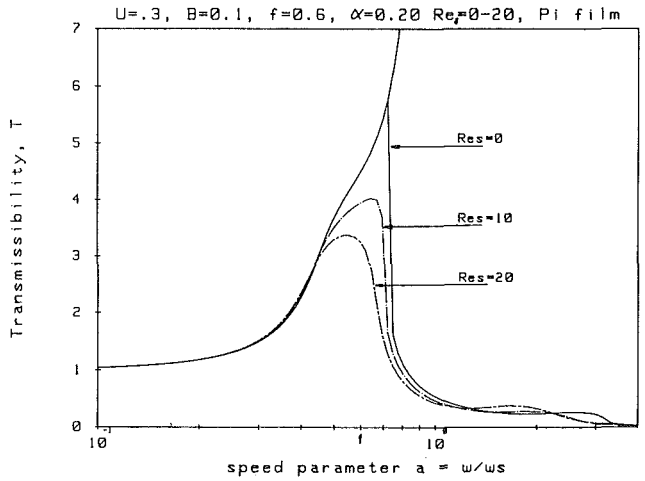

Fig. 13 Force transmissibility of a flexible rotor on SFD for three values of fluid inertia, π film

shift toward lower speeds of the second critical speed due to the substantial increase in the apparent mass of the system at the bearing location as the squeeze film Reynolds number increases. This phenomenon may not appear in rotor systems in which the SFD does not dominate the response (e.g., only one SFD on a long flexible rotor; Storace [23] reports computing contrary results for such a system). At the second critical speed, the response is less damped as the Reynolds number increases, due mainly to the invariance of the damping coefficient $\overline{Ct} = \overline{Ctt}$ as Re increases for pressurized squeeze film dampers.

For the same amount of imbalance, $U = 0.3$, and on unpressurized SFDs, Figs. 11 and 12 show the amplitude frequency response at the damper journal and rotor midspan, respectively, and Fig. 13 shows the force transmissibility T. Without fluid inertia effects on the rotor-SFD force response, a region of bistable operation exists above $a \simeq 0.7$, and the damper locks up at the pin-pin critical speed, $a = 1$, with excessive amplitude response at rotor midspan and transmitted forces to the structure.

The analysis including fluid inertia effects shows that as the operating Reynolds number (Re_s) increases, the possibilities of bistable operation and jump phenomena are reduced, and for $\mathrm{Re}_s = 10$ and 20 these undesirable conditions disappear. For operating speeds below the pin-pin critical speed ω_s, the amplitude of response at both journal and rotor center, as well as the force transmissibility, are reduced as the Reynolds number Re_s increases. As expected for operating speeds above ω_s, the location of the second critical speed is shifted to lower speeds as the Reynolds number increases; however, the amplitude response is more damped than for the pressurized case due to the substantial contribution of the cross-coupled inertia coefficient $\overline{Dtr}\cdot\mathrm{Re}$ to the effective direct damping coefficient $\overline{Ct}$.

Figure 13 shows that at the rotor natural frequency ω_r on retainer springs, $a = 0.6$, the transmissibility for a Reynolds number $\mathrm{Re}_s = 20$ is about 50 percent lower than for the inertialess case. For speeds above ω_s, there is a narrow region where T is slightly larger than the transmissibility for $\mathrm{Re}_s = 0$, although its amplitude seems not to be deleterious for rotor performance.

For the example considered and squeeze film Reynolds numbers $\mathrm{Re}_s = 10$ and 20, it is interesting to note that for operating speeds above ω_s, the rotor performance in amplitude response and transmissibility is much better for unpressurized SFDs than for pressurized ones. As before, the reason for such behavior is a substantial increase in the effective direct damping force as the Reynolds number increases for the π film SFD model.

Conclusions

The analysis presented here considers the effect of fluid inertia on the frequency response of simple rigid and flexible rotors running on squeeze film damper mounts. To the extent that the assumptions in the analysis are justified, the following conclusions are stated:

1 For pressurized SFDs, fluid inertia in the squeeze film flow gives rise to an "added" mass effect which increases the effective mass of the system. For unpressurized SFDs, fluid inertia increases substantially the effective direct damping coefficient $\overline{Ct}$ and decreases the effective cross-coupled damping coefficient $\overline{Cr}$. Thus, fluid inertia in SFDs reduces the possibilities for bistable operation and jump phenomena to occur.

2 Rotors mounted on SFDs operating at moderate values of the squeeze film Reynolds number are able to control amounts of imbalance that an inertialess analysis may determine to be deleterious for rotor performance.

3 For operating speeds below the first pin-pin critical speed, the amplitude and transmissibility frequency responses are reduced as the Reynolds number increases. Jump phenomena and bistable operation are found to be confined to

narrow high-speed ranges and disappear at sufficiently high values of the squeeze film Reynolds numbers.

4 For operating speeds above the first pin-pin critical speed ω_s, fluid inertia may lower the second critical speed of the rotor-damper system, but this appears to depend on the rotor-bearing system design. Above ω_s, the amplitude frequency response is more damped for unpressurized than for pressurized dampers.

5 The results of the analysis confirm field observations for rotor-SFD systems operating at high speeds and large Reynolds numbers where the amplitude frequency response is usually very well damped and jump phenomena are seldom observed despite predictions to the contrary using the results from classical lubrication theory, i.e., Re = 0.

The importance of fluid inertia in SFDs under certain operating conditions and bearing characteristics cannot be disregarded. Its impact on the rotor-SFD system performance appears to be significant and beneficial in most circumstances.

References

1 Mohan, S., and Hahn, E. J., "Design of Squeeze Film Damper Supports for Rigid Rotors," ASME *Journal of Engineering for Industry*, Vol. 96, 1974, pp. 976-982.

2 Gunter, E. J., Barrett, L. E., and Allaire, P. E., "Design of Nonlinear Squeeze Film Dampers for Aircraft Engines," ASME *Journal of Lubrication Technology*, Vol. 99, 1977, pp,. 57-64.

3 Taylor, D. L., and Kumar, B. R. K., "Nonlinear Response of Short Squeeze Film Dampers," ASME *Journal of Lubrication Technology*, Vol. 102, 1980, pp. 51-58.

4 Taylor, D. L., and Kumar, B. R. K., "Closed Form, Steady State Solution for the Unbalance Response of a Rigid Rotor in Squeeze Film Dampers," ASME JOURNAL OF ENGINEERING FOR POWER, Vol. 105, 1983, pp. 551-559.

5 Rabinowitz, M. D., and Hahn, E. J., "Steady State Performance of Squeeze Film Damper Supported Flexible Rotors," ASME JOURNAL OF ENGINEERING FOR POWER, Vol. 99, 1977, pp. 552-558.

6 Rabinowitz, M. D., and Hahn, E. J., "Stability of Squeeze Film Damper Supported Flexible Rotors," ASME JOURNAL OF ENGINEERING FOR POWER, Vol. 99, 1977, pp. 545-551.

7 McLean, L. J., and Hahn, E. J., "Unbalance Behavior of Squeeze Film Damped Multi-mass Flexible Rotor Bearing Systems," ASME *Journal of Lubrication Technology*, Vol. 105, 1983, pp. 22-28.

8 McLean, L. J., and Hahn, E. J., "Stability of Squeeze Film Damped Multi-mass Flexible Rotor Bearing Systems," ASME *Journal of Tribology*, Vol. 107, 1985, pp. 402-410.

9 Guang, M., and Xue, Z., "Investigation on Steady State Response and Its Nonlinear Characteristics of Flexible Rotor Squeeze Film Damper System," ASME Paper No. 85-DET-141, 1985.

10 Simandiri, S., and Hahn, E. J., "Effect of Pressurization on the Vibration Isolation Capability of Squeeze Film Bearings," ASME *Journal of Engineering for Industry*, Vol. 98, 1976, pp. 109-117.

11 Rabinowitz, M. D., and Hahn, E. J., "Optimal Design of Squeeze Film Supports for Flexible Rotors," ASME JOURNAL OF ENGINEERING FOR POWER, Vol. 105, 1983, pp. 487-494.

12 Tichy, J. A., "The Effect of Fluid Inertia in Squeeze Film Damper Bearing Analysis: a Heuristic and Physical Description," ASME Paper 83-GT-177, 1983.

13 Pan, C. H. T., "Squeeze Film Damper Technology. an Overview of Squeeze Film Damper Applications and Technological Status," *Proceedings of the Conference on the Stability and Dynamic Response of Rotors With Squeeze Film Bearings*, May 8-10, 1979, Charlottesville, VA.

14 White, D. C., "The Dynamics of a Rigid Rotor Supported on Squeeze Film Bearings," *Proceedings of the Conference on Vibrations in Rotating Systems*, London, England, Feb. 14-15, 1972; IME pp. 213-229.

15 Simandiri, S., and Hahn, E. J., "Experimental Evaluation of the Predicted Behavior of Squeeze Film Bearing Supported Rigid Rotors," *Journal of Mechanical Engineering Science*, 1979, pp. 439-451.

16 Rabinowitz, M. D. and Hahn, E. J., "Experimental Evaluation of Squeeze Film Damper Supported Flexible Rotors," ASME JOURNAL OF ENGINEERING FOR POWER, Vol. 105, 1983, pp. 495-503.

17 Storace, A., and Cline, S. J., "NASA-General Electric Energy Efficient Engine High Load Squeeze Film Damper – System Analysis and Test Results," AIAA/SAE/ASME 20th Joint Propulsion Conference, AIAA Paper No. 84-1217.

18 San Andres, L., "Effect of Fluid Inertia on Squeeze Film Damper Force Response," Ph.D. Dissertation, Texas A&M University, College Station, TX, Dec. 1985.

19 San Andres, L., and Vance, J. M., "Effects of Fluid Inertia and Turbulence on the Force Coefficients for Squeeze Film Dampers," ASME JOURNAL OF ENGINEERING FOR GAS TURBINES AND POWER, Vol. 108, 1986, pp. 332-339.

20 San Andres, L., and Vance, J. M., "Experimental Measurement of the Dynamic Pressure Distribution in a Squeeze Film Bearing Damper Executing Circular Centered Orbits," *ASLE Transactions*, Vol. 30, July 1987, pp. 383-393.

21 San Andres, L., and Vance, J. M., "Effect of Fluid Inertia on Squeeze Film Damper Forces for Small-Amplitude Circular Centered Motions," *ASLE Transactions*, Vol. 30, Jan. 1987, pp. 63-68.

22 Greenhill, L. M., and Nelson, H. D., "Iterative Determination of Squeeze Film Damper Eccentricity for Flexible Rotor Systems," ASME Paper No. 81-DET-87, 1981.

23 Storace, A. F., General Electric Aircraft Engine Business Group, Personal Communication, Jan. 20, 1987.

Flow Losses in Stirling Engine Heat Exchangers

J. D. Jones[1]
University of Reading,
Whiteknights, Reading,
United Kingdom

Closed-form expressions are sought which will allow the rapid and accurate calculation of pressure variation, flow velocities, and flow friction losses in crank-driven Stirling cycle machines. The compression and expansion spaces of the Stirling machine are assumed to be isothermal and their volumes are assumed to vary sinusoidally. It is further assumed that the cyclic pressure variation of the working fluid and the flow velocities within the passages of the machine can be represented by sinusoids. Closed-form expressions are deduced for the amplitude and phase of these variations. Using the expressions so deduced, formulae are derived for frictional losses in the three heat exchangers, taking into account the variation in mass flow rate over the cycle and the difference in amplitude of mass flow between the two ends of the regenerator. By comparing these expressions with calculations based on the assumption of an average flow rate over the cycle, it is shown that the latter method leads to flow losses being underestimated by more than 50 percent. It is recommended that the formulae deduced here be used for first-stage design work.

Introduction

Despite the widespread interest in sophisticated computer analyses of Stirling cycle machines [1–3], closed-form design formulae will continue to be required for rapid evaluation of preliminary designs. There is a particular need for a reliable method of calculating flow losses in the heat exchangers. Flow friction represents one of the major loss mechanisms in the Stirling engine [4]. The quasi-sinusoidal nature of the flow, differences in the phase and amplitude of this flow from one end of the engine to the other, and spatial and temporal variations in gas density combine to complicate its evaluation, even where the appropriate friction factor correlations for the heat exchanger geometries and operating conditions are known.

No attempt will be made in this paper to derive an improved flow correlation; such correlations may be found elsewhere [5, 6]. Rather, it is assumed that a correlation is available for the geometry and conditions under investigation. Given this correlation, a procedure will be demonstrated for calculating flow friction losses over the cycle, taking into account the complicating factors mentioned above.

Initial Assumptions

This analysis will employ the simplifying assumptions introduced by Schmidt [7]: Expansion and compression will be considered to take place isothermally, and the variations in volume of the expansion and compression spaces are considered to be sinusoidal, of known amplitude and at a known angle out of phase. Specifically, the expansion volume will be given as

$$V_e = \frac{V_E}{2} \times (1 + \sin\ \alpha)$$

where $\alpha = \omega t$ is the crank angle; ω is the angular velocity of the crank; and the compression volume is

$$V_c = \frac{V_C}{2} \times (1 + \sin\ (\alpha + \delta_v))$$

where δ_v is a phase angle. The temperatures of these two spaces remain constant at T_H and T_K, respectively.

The most drastic of these assumptions is that of isothermal expansion and compression. In most practical devices, these processes are more nearly adiabatic than isothermal. Volume variations are close to sinusoidal for many crank-driven machines; however, the important class of free-piston Stirling cycle machines ([4], Chap. 11) cannot be analyzed by the methods described here.

Heat is added to and extracted from the working gas by heat exchangers, which may reasonably be considered isothermal. Stirling cyle machines have three of these: a heater, a cooler, and a regenerator, whose properties will be distinguished by the subscripts H, K, and R, respectively.

Pressure Variations

It will be assumed that the spatial variation in gas pressure throughout the machine is small compared with the temporal variation. The mass of gas in the expansion space at any moment in time may be written as

$$m_e = \frac{pV_e}{RT_H} \tag{1}$$

and similarly for the masses in the other engine spaces. Summing these masses gives

$$M = p\left(\frac{V_H + V_e}{RT_H} + \frac{V_K + V_c}{RT_K} + \frac{V_R}{RT_R}\right) \tag{2}$$

where M, the total mass of working fluid, is constant. Hence

[1] Present address: Engine Research Department, General Motors Research Laboratories, Warren, MI 48090.

Contributed by the Advanced Energy Systems Division for publication in the JOURNAL OF ENGINEERING FOR GAS TURBINES AND POWER. Manuscript received by the Advanced Energy Systems Division March 1986.

$$p = M\left(\frac{V_H + V_e}{RT_H} + \frac{V_K + V_c}{RT_K} + \frac{V_R}{RT_R}\right)^{-1} \quad (3)$$

Given the assumptions listed above, this expression is exact. It will now be further assumed that equation (3) may be approximated by

$$p = p_m - p_a \sin(\alpha + \delta_p) \quad (4)$$

where p_m is the mean pressure, p_a the amplitude of the pressure variation, and δ_p the phase angle between the pressure variation and the variation in volume of the expansion space. Appropriate values of p_m, p_a, and δ_p may be calculated from equation (3); to locate the maximum and minimum values of pressure, we differentiate equation (2) with respect to the crank angle α and equate to zero. This yields

$$\frac{V_E}{RT_H}\cos\alpha_p + \frac{V_C}{RT_K}\cos(\alpha_p + \delta_v) = 0 \quad (5)$$

where α_p is the crank angle at which p reaches an extremum. When δ_v takes the value $\pi/2$ commonly found in Stirling machines, this takes the simple form

$$\alpha_p = \tan^{-1}\frac{T_K V_E}{T_H V_C} \quad (6)$$

By substituting the two solutions to equations (5) or (6) into equation (3), δ_p, p_a, and p_m may be immediately deduced.

For subsequent calculation, it will be found useful to rewrite equation (4) as

$$p = p_m(1 + \phi \sin(\alpha + \delta_p)) \quad (7)$$

where ϕ is the dimensionless ratio p_s/p_m.

Fluid Flow Between Engine Spaces

The fluid velocity across any cross section of the engine passages will also be assumed to vary sinusoidally, in accordance with an equation of the form

$$u = U_x \omega \sin(\alpha + \delta_u) \quad (8)$$

Methods for calculating the amplitude U_x and phasing δ_u of these variations will be derived below.

The stream velocity at any point is related to the mass flow at that point by the equation $\dot{m}_x = A_x \rho u$, where A_x is the cross-sectional area of the engine passages and ρ, the density of the working fluid, is given by

$$\rho(\alpha) = p(\alpha)/RT \quad (9)$$

Since ρ varies with time, mass flux does not necessarily attain a maximum at the same time as stream velocity. However, it is clear that both quantities must pass through zero at the same time. It is thus possible to determine the phasing of the stream velocity by establishing the point at which mass flux falls to zero.

Consider any cross section of the engine passages. The mass of working fluid contained between this cross section and the crown of the expansion-space piston can be expressed as

Nomenclature

A = coefficient in friction factor correlation for pipe flow
A_x = total cross-sectional flow area of a heat exchanger
$C_{1,2,3,4}$ = coefficients in expression for frictional work in heat exchangers
$D_{1,2}$ = coefficients in simplistic expression for frictional work in heat exchangers
D_H = hydraulic diameter of regenerator matrix
d = diameter of heat exchanger tubes
f = Fanning friction factor
L = length of a heat exchanger
M = total mass of gas in engine
M_H = mass of gas flowing through hot end of regenerator
M_K = mass of gas flowing through cold end of regenerator
M_x = mass of gas flowing through cross section of regenerator a distance x from the hot end
m = exponent in the friction factor correlation $f = A\mathrm{Re}^m$
$\dot{m}_x$ = time-varying mass flow rate at x
N_p = Poiseuille number
p_a = amplitude of pressure variation over the cycle
p_m = mean gas pressure
Δp = pressure drop across heat exchanger
R = gas constant
Re = Reynolds number
T = gas temperature
T_H = mean temperature of gas in heater and expansion space
T_K = mean temperature of gas in cooler and compression space
T_x = gas temperature a distance x from the hot end of the regenerator
t = time
U_x = amplitude of variation in flow velocity
V_C = maximum volume of compression space
V_E = maximum volume of expansion space
V_c = time-varying volume of compression space
V_e = time-varying volume of expansion space
V = volume of heat exchanger
V_R = volume of regenerator
v = dummy variable of integration
x = distance from hot end of regenerator
α = crank angle in radians, referred to variation in V_e
$\hat{\alpha}$ = crank angle in radians, referred to u
β = beta function
Γ = gamma function
δ_p = phase angle between variation in V_e and pressure variation
δ_u = phase angle between variation in V_e and in flow rate, u
$\hat{\delta}_p$ = phase angle between variation in flow rate, u and pressure variation
ζ = temporary variable used for integration
θ = dimensionless temperature = $(T_H - T)/T_H$
μ = viscosity of working fluid
ν = dimensionless mass-weighting factor
ρ = density of working fluid
ϕ = dimensionless pressure = p_a/p_m
χ = dimensionless distance along regenerator
ω = angular velocity of crank, rad/s

$$m_x = \frac{p}{R}\left(\frac{V_e}{T_H} + \Sigma\frac{V_D}{T_D}\right) \tag{10}$$

where the subscript D denotes the time-constant heat exchanger volumes and temperatures to the expansion-space side of the cross section. Substituting for p and V_e, this can be written as

$$m_x = 0.5\frac{p_m V_E}{RT_H}(1+\phi\sin(\alpha+\delta_p))(\psi+\sin\alpha) \tag{11}$$

where $\psi = (2T_H/V_E)(\Sigma V_D/T_D + 1)$. Differentiating m_x with respect to α, setting the result equal to zero, and solving for α gives the crank angles at which the mass stored to one side of the chosen cross section reaches its maximum and its minimum value. At these angles, u becomes zero; hence δ_u may be calculated. The difference between the maximum and minimum values of m_x yields the total mass of gas passing the chosen cross section over half a cycle, M_x. U_x, the amplitude of the variation in flow velocity, may then be found as follows.

To simplify notation, let $\hat{\alpha}$ denote the crank angle referred to the moment at which u passes from positive to negative, flow being positive when it is *toward* the expansion space. The phase angle of the pressure variation with respect to $\hat{\alpha}$ will be written as $\hat{\delta}_p$, and may be calculated from δ_p and δ_u, both of which are known. The expression for mass flow across the chosen cross section is then

$$\dot{m}_x = A_x\rho U_x\omega\sin\hat{\alpha} \tag{12}$$

Substituting for ρ from equation (9) and integrating over half a cycle gives

$$M_x = \frac{A_x p_m U_x}{RT_x}\int_0^{\pi}\sin\hat{\alpha}(1+\phi\sin(\hat{\alpha}+\hat{\delta}_p))d\alpha$$

$$= \frac{2A_x p_m U_x}{RT_x}\left(1+\phi\frac{\pi}{4}\cos\hat{\delta}_p\right)$$

where T_x is the mean gas temperature at the cross section being considered. Hence

$$U_x = \frac{M_x RT_x}{A_x p_m\left(1+\frac{\pi}{4}\phi\cos\hat{\delta}_p\right)} \tag{13}$$

Pressure Drop and Frictional Work

Using the expressions for flow velocity derived in the previous section, it is possible to derive closed-form expressions for the pressure drop and frictional losses in each heat exchanger. For simplicity of notation, the subscript p will henceforth be dropped from $\hat{\delta}_p$.

Cooler and Heater. For the heater and cooler, the spatial variations in u and ρ are negligible in comparison with their temporal variation. Thus a reasonable result may be obtained by taking a value of U_x calculated for the midpoint of the heat exchanger. When we come to calculate flow friction in the regenerator, it will be necessary to introduce a correction term to account for spatial variation in gas density and flow rate. At any given moment in the cycle, the pressure drop across the heater or cooler tubes is

$$\Delta p = 2\frac{fu^2\rho L}{d} \tag{14}$$

where L is the heat exchanger length, d its diameter, and f, the friction factor, is given by an equation of the form $f = A\mathrm{Re}^m$. Substituting for Re in terms of u,

$$\Delta p = 2\frac{A\rho L}{d}\left(\frac{\rho d}{\mu}\right)^m |u|^m u^2 \tag{15}$$

Now substituting the formulae derived above for u and ρ

$$\Delta p = 2A\frac{L}{d}\frac{p_m}{RT}(1+\phi\sin(\hat{\alpha}+\hat{\delta}))$$

$$\left(\frac{p_m d}{RT\mu}(1+\phi\sin(\hat{\alpha}+\hat{\delta}))\right)^m |u|^m u^2$$

$$= 2AL\left(\frac{p_m}{RT}\right)^{1+m} d^{m-1}\mu^{-m}(\omega U_x)^{2+m} \tag{16}$$

$$(1+\phi\sin(\hat{\alpha}+\hat{\delta}))^{1+m}\sin^2\hat{\alpha}|\sin\hat{\alpha}|^m$$

where T is the fluid temperature characteristic of this heat exchanger. In an interval of time dt, the work done against this pressure drop is

$$dW = A_x\Delta p|u|dt$$

$$= 2AA_xL\left(\frac{p_m}{RT}\right)^{1+m} d^{m-1}\mu^{-m}(\omega U_x)^{3+m}$$

$$(1+\phi\sin(\hat{\alpha}+\hat{\delta}))^{1+m}\sin^2\hat{\alpha}|\sin\hat{\alpha}|^{1+m}dt \tag{17}$$

The appearance of the $(3 + m)$ th power of U_x in this expression indicates that a calculation based on the cyclic mean value of gas flow rates could not be expected to give a very accurate result. In the present calculation, we integrate equation (17) over a cycle and thus obtain a formula for total work done against friction

$$W = 2AVd^{m-1}\mu^{-m}\left(\frac{p_m}{RT}\right)^{1-m} U_x^{3+m}\omega^{2+m}$$

$$\times\int_0^{2\pi}\sin^2\hat{\alpha}|\sin\hat{\alpha}|^{1+m}(1+\phi\sin(\hat{\alpha}+\hat{\delta}))^{1+m}d\hat{\alpha}$$

where V is the volume of the heat exchanger. Define the constant part of this expression as $C_1\omega^{2+m}$, where

$$C_1 = 2AVd^{m-1}\mu^{-m}\left(\frac{p_m}{RT}\right)^{1+m} U_x^{3+m} \tag{18}$$

and split the integral with respect to α into two:

$$W = C_1\omega^{2+m}\left(\int_0^{\pi}\sin^{3+m}\hat{\alpha}(1+\phi\sin(\hat{\alpha}+\hat{\delta}))^{1+m}\right.$$

$$\left.+\int_{\pi}^{2\pi}\sin^{3+m}(-\hat{\alpha})(1+\phi\sin(\hat{\alpha}+\hat{\delta}))^{1+m}\right)d\hat{\alpha}$$

We call the two integrals with respect to $\hat{\alpha}$, I_1 and I_2. For each integral, we apply the binomial theorem to the bracket $(1 + \phi\sin(\hat{\alpha}+\hat{\delta}))^{1+m}$ and expand, ignoring higher terms

$$I_1 = \int_0^{\pi}\sin^{3+m}\hat{\alpha}(1+(1+m)\phi\sin(\hat{\alpha}+\hat{\delta}))d\hat{\alpha}$$

$$= 2\int_0^{\pi/2}\sin^{3+m}\hat{\alpha}d\hat{\alpha} + 2(1+m)\phi$$

$$\left(\cos\hat{\delta}\int_0^{\pi/2}\sin^{4+m}\hat{\alpha}d\hat{\alpha} + \sin\hat{\delta}\int_0^{\pi/2}\sin^{3+m}\hat{\alpha}\cos\hat{\alpha}d\hat{\alpha}\right)$$

$$= \sqrt{\pi}\frac{\Gamma((4+m)/2)}{\Gamma((5+m)/2)} + \phi(1+m)$$

$$\left(\sqrt{\pi}\cos\hat{\delta}\frac{\Gamma((5+m)/2)}{\Gamma((6+m)/2)}\sin\hat{\delta}\beta(((6+m)/2),\ 1.5)\right) \tag{19}$$

where β is the beta function.

Similarly

$$I_2 = \sqrt{\pi}\,\frac{\Gamma((4+m)/2)}{\Gamma((5+m)/2)} + \phi(1+m)$$

$$\left(-\sqrt{\pi}\,\cos\hat{\delta}\,\frac{\Gamma((5+m)/2)}{\Gamma((6+m)/2)} + \sin\hat{\delta}\beta(((6+m)/2),\,1.5)\right)$$

Thus the total work expended in overcoming friction over a cycle is

$$\begin{aligned} W &= C_1\omega^{2+m}\left(\sqrt{\pi}\,\frac{\Gamma((4+m)/2)}{\Delta((5+m)/2)}\right. \\ &\quad \left. + 1(+m)\phi\,\sin\hat{\delta}\beta(((6+m)/2),\,1.5)\right) \\ &= 2C_1C_2\omega^{2+m} \end{aligned} \tag{20}$$

Regenerator. Evaluation of the work expended against friction in the regenerator must take into account the variation in the amplitude of gas flow with position. We therefore begin by considering the instantaneous pressure drop across a thin slice of regenerator dx

$$\Delta p = 2fu^2D_H^{-1}\rho dx \tag{22}$$

We assume that the friction factor for the regenerator material can be expressed in the form $f = A\mathrm{Re}^m$. (For most regenerator matrix geometries, the exponent m will take a different value from that for the tubular heater and cooler. In the special case of laminar flow, $m = -1$ and $A = N_p/2$, where N_p is the Poiseuille number.)

Using $\mathrm{Re} = D_H\rho|u|/\mu$, where D_H is the hydraulic diameter of the regenerator matrix, we can write

$$\begin{aligned} \Delta p &= 2Au^2\rho D_H^{-1}\left(\frac{D_H|u|\rho}{\mu}\right)^m dx \\ &= 2AD_H^{m-1}\mu^{-m}\rho^{1+m}u^2|u|^m dx \end{aligned} \tag{23}$$

Now, the work done against friction in this slice of thickness dx over an interval of time dt is

$$\begin{aligned} dW &= A_x\Delta p|u|dt \\ &= 2AA_xD_H^{m-1}\mu^{-m}u^2|u|^{m+1}\rho^{1+m}dtdx \end{aligned} \tag{24}$$

To obtain the total work done against friction, equation (24) must be integrated over the cycle and over the length of the regenerator. As before, gas density is given by equation (9), but we must now also take into account the variation in temperature along the regenerator

$$\rho(\alpha, x) = p(\alpha)/RT_x$$

and the variation in the amplitude of flow velocity, U_x. It is then possible to write

$$W = 2AV_RD_H^{m-1}\mu^{-m}\omega^{2+m}\left(\frac{p_m}{R}\right)^{1+m}\int_0^{2\pi}\sin^2\hat{\alpha}|\sin\hat{\alpha}|^{1+m}$$

$$(1+\phi\sin(\hat{\alpha}+\hat{\delta}))^{1+m}d\alpha \times \int_0^1 \frac{U_x^{3+m}}{T_x^{1+m}}\,d\chi \tag{26}$$

The integral with respect to α is recognized as C_2 from equation (20). In the appendix it is shown that the integral with respect to x, which we shall call I_3, is given by

$$I_3 = \left(\frac{RM_H}{p_mA_x\left(2+\frac{\pi}{2}\phi\,\cos\delta_p\right)}\right)^{3+m}\frac{T_H^2}{9\theta}((3+\nu)$$

$$(1-(1-\theta)^3) + 3\nu(1-\theta)^3\ln(1-\theta))$$

where M_H is the amplitude of mas flow through the hot end of the regenerator, θ is the dimensionless temperature ratio $(T_H - T_K)/T_H$, and ν is the dimensionless mass ratio $(p(\alpha_1)-p(\alpha_2))V/R\Delta TM_H$. Putting this expression into equation (26) and simplifying yields

$$W = 2A\left(\frac{RT_H}{p_m}\right)^2 V_RD_H^{m-1}\mu^{-m}$$

$$\left(\frac{M_H}{A_x\left(2+\frac{\pi}{2}\phi\,\cos\delta_p\right)}\right)^{3+m} C_2C_3\omega^{2+m} \tag{27}$$

where C_3 is given by

$$C_3 = \frac{1}{9\theta}((3+\nu)(1-(1-\theta)^3) + 3\nu(1-\theta)^3\ln(1-\theta)) \tag{28}$$

C_2 and C_3 are dimensionless. The remaining terms appearing in equation (27) may be grouped together as

$$C_4 = 2A\left(\frac{RT_H}{p_m}\right)^2 V_RD_H^{m-1}\mu^{-m}$$

$$\left(\frac{M_H}{a_x\left(2+\frac{\pi}{2}\phi\,\cos\delta_p\right)}\right)^{3+m}$$

The complete expression for work done against friction in the regenerator over a cycle is then

$$W = C_2C_3C_4\omega^{2+m} \tag{29}$$

where C_2, C_3, and C_4 are more or less constant with crank speed.

Equation (29) has a somewhat daunting appearance, but can be evaluated using a pocket calculator.

Illustrative Example. This result may be compared with that obtained by basing the calculation of flow losses on a simple mean value of flow rate. For the heater, for example, defining the mean flow rate as

$$\bar{u} = 2U_x\omega/\pi$$

and substituting $\bar{u}$ for u in equations (15) and (17) yields

$$\begin{aligned} W &= 8AV\left(\frac{2}{\pi}\right)^{2+m}d^{m-1}\mu^{-m}\left(\frac{p_m}{RT_H}\,U_x\right)^{3+m}\omega^{2+m} \\ &= D_1\omega^{2+m} \end{aligned} \tag{30}$$

for the frictional work per cycle. Comparing equations (20) and (30), it may be seen that the latter underestimates frictional work by a factor

$$\frac{2C_1C_2}{D_2} = \frac{\pi^{2+m}}{2^{3+m}}\,C_2$$

Taking $m = -0.25$, a value typical of pipe flow, this factor is found to be 1.5. Thus calculation of fluid friction on the basis of a mean flow rate underpredicts flow losses by more than 30 percent.

A smiliar comparison may be made for the regenerator. The mean mass flux through the regenerator may be approximated as

$$\bar{G}_x = \frac{M_H + M_K}{2}\,\frac{\omega}{\pi A_x}$$

Whence

$$\bar{u} = \frac{M_H + M_K}{2}\,\frac{\omega}{\bar{\rho}A_x\pi}$$

where

$$\bar{\rho} = \frac{2p_m}{R(T_H + T_K)}$$

Substituting these values into equations (22) and (26) yields

$$W = 4A\pi V\left(\frac{R(T_H+T_K)}{2p_m}\right)^2 D_H^{m-1}\mu^{-1}\left(\frac{M_H+M_K}{2\pi A_x}\right)^{3+m}\omega^{2+m}$$
$$= D_2\omega^{2+m} \tag{31}$$

Comparing equation (29) with equation (31) shows that the latter underpredicts flow friction by a factor

$$\frac{C_2C_3C_4}{D_2} = \frac{\pi^2+m}{2\left(2+\frac{\pi}{2}\phi\cos\hat{\delta}\right)}\left(\frac{2T_H}{T_H+T_K}\right)^2$$
$$\left(\frac{2M_H}{M_H+M_K}\right)^{3+m} C_3C_3$$

Evaluating this expression for a typical high-performance Stirling engine [8] gives a figure of 1.6, again indicating that analysis based on mean flow rates leads to a serious underprediction of frictional losses.

Conclusion

It is not expected that any engineer with access to a computer and a simulation program will be much inclined to spend his time evaluating formulae of the complexity of equation (29). However, it is worthwhile to derive such formulae, for several reasons. Firstly, they can provide a physical understanding of the influence of different design parameters on performance. Secondly, Stirling engines have considerable potential as a power source for developing nations [9], where computers are less readily available than in North America and Western Europe. Thirdly, a disproportionate number of contributions to Stirling cycle technology have come from hobbyists and amateur engine designers, who, lacking the computational resources available to corporate researchers, may wish to take advantage of reliable mathematical design tools. It is hoped that the formulae obtained here may prove useful in one or more of these areas.

References

1 Martini, W., "Thermodynamic Design of Stirling Engines by Computer," Martini Engineering, 1980.

2 Organ, A., "Gas Dynamics of Stirling Cycle Machines," *I. Mech. E Conference Pubications*, 1982-2.

3 Urieli, I., "A Review of Stirling Cycle Machine Analysis," *IECEC Proceedings*, 799236, 1979.

4 Walker, G., *Stirling Cycle Engines*, Oxford University, Press, 1980.

5 Nayajimo, N., Miyashita, N., and Hirate, H., "The Characteristics of Pulsating Flow Heat Transfer in Stirling Engines," *Bulletin of the MESJ*, Vol. 8, No. 3, 1980.

6 Je Chul Kim, "An Analytical and Experimental Study of Heat Transfer and Flow Friction Characteristic for Periodically Reversing Flow Through the Porous Matrix of Thermal Regenerators," Ph.D. Thesis, Purdue University, 1970.

7 Schmidt, G., "The Theory of Lehman's Heat Machine," *Journal of German Engineers' Union*, Vol. 15, No. 1, 1871.

8 Dunn, P. D., et al., "20 kW U.K. Consortium Stirling Engine—Specifications and Manufacture," *I. Mech. E Conference Publications*, 1982-2, pp. 65-76.

9 Beale, W. T., Wood, J. G., and Chagnot, B. J., "Stirling Engines for Developing Countries," *IECEC Proceedings*, 809399, 1980.

APPENDIX

In the body of this paper it has been shown that the effects on regenerator flow losses of spatial variation in gas density and flow velocity can be given by the expression

$$I_3 = \int_0^1 \frac{U_x^{3+m}}{T_x^{1+m}}\,d\chi$$

This appendix shows how the above expression may be integrated. We first substitute for U_x, using equation (13)

$$U_x = \frac{M_xRT_x}{A_xp_m\left(2+\frac{\pi}{2}\phi\cos\hat{\delta}_p\right)}$$

where T_x varies linearly with position in the regenerator according to

$$T_x = T_H - \frac{x}{L}(T_H-T_K)$$
$$= T_H(1-\chi\theta) \tag{A1}$$

where $\theta = (T_H-T_K)/T_H$. Thus I_3 may be written as

$$I_3 = \left(\frac{R}{p_mA_x\left(2+\frac{\pi}{2}\phi\cos\delta_p\right)}\right)^{3+m}\int_0^L M_x^{3+m}T_x^2\,dx \tag{A2}$$

To evaluate this, it is first necessary to write down an expression for M_x, the total mass of gas flowing past the cross section of the regenerator at x over half a cycle. The amplitude of mass flow variation through the hot end of the regenerator is defined as M_H, and the crank angles at which this mass flow passes through zero as α_1 and α_2. If we ignore the slight variation in phase of mass flow through different cross sections of the regenerator, we may express M_x in terms of M_H by

$$M_x = M_H + (p(\alpha_1)-p(\alpha_2))A_x/R\int_{v=0}^{v=x}\frac{dv}{T_x} \tag{A3}$$

where v is a dummy variable of integration. Substituting for T_x from equation (A1) and integrating, we obtain

$$M_x = M_H + (p(\alpha_1)-p(\alpha_2))\frac{V}{R\Delta T}\ln(1-\theta\chi)$$
$$= M_H(1-\nu\ln(1-\theta\chi)) \tag{A4}$$

where

$$\nu = \frac{(p(\alpha_1)-p(\alpha_2))V}{R\Delta TM_H}$$

Substituting for M_x and T_x in the integral of equation (A2), we obtain

$$\int_0^1 M_x^{3+m}T_x^2\,d\chi = T_H^2M_H^{3+m}\int_0^1(1-\nu\ln(1-\theta\chi))^{3+m}(1-\chi\theta)^2\,d\chi$$

Setting $\zeta = 1-\chi\theta$, this becomes

$$\frac{T_H^2M_H^{3+m}}{\theta}\int_{1-\theta}^1(1-\nu\ln\zeta)^{3+m}\zeta^2\,d\zeta$$

which may be evaluated to give

$$\frac{T_h^2M_H^{3+m}}{9\theta}((3+\nu)(1-(1-\theta)^3)+3\nu(1-\theta)^3\ln(1-\theta))$$

Thus I_3 is given by

$$I_3 = \left(\frac{RM_H}{p_mA_x\left(2+\frac{\pi}{2}\phi\cos\delta_p\right)}\right)^{3+m}\frac{T_h^2}{9\theta}((3+\nu)$$
$$(1-(1-\theta)^3+3\nu(1-\theta)^3\ln(1-\theta))$$

S. Wittig
Professor.
Mem. ASME

K. Jacobsen
Research Assistant.

U. Schelling
Research Assistant.

S. Kim
Section Head.

Lehrstuhl und Institut für
Thermische Strömungsmaschinen,
Universität Karlsruhe (T.H.),
7500 Karlsruhe 1,
Federal Republic of Germany

Heat Transfer in Stepped Labyrinth Seals

Leakage flow and heat transfer of scaled-up stepped labyrinth seals were investigated experimentally and numerically. The experiments were conducted in a test rig under steady conditions. For different geometries and pressure ratios a finite element program was used to determine the temperature distribution and subsequently the heat transfer coefficients. In verifying the experimental results, the flow field of the seals was calculated numerically by a finite difference program. Heat transfer coefficients were derived utilizing the well-known analogies between heat transfer and wall friction.

Introduction

In jet engines as well as in stationary turbomachinery labyrinth seals are most widely used as an important sealing element. Simplicity and compact design, reliability, and high-temperature resistance are some of their major advantages. Engine efficiency strongly depends on the leakage characteristics of the labyrinth seal. The structural analysis of engine components with high-temperature load requires additional information on the heat transfer rates within the labyrinth seal.

As indicated in an earlier discussion [1, 2], many attempts have been made in describing primarily the leakage losses through labyrinth seals. Trutnovsky [3] in his comprehensive book summarizes the early attempts by Stodola [4], Gerke [5], Egli [6], Jeri [7], Jones [8], Komotori [9], and others. However, the design of modern jet engines requires more accurate predictions, taking into account the detailed geometry of the labyrinth. Stocker [10], in his recent studies, developed advanced labyrinth seals with reduced leakage loss. The latest experimental and numerical work has been done by Wittig et al. [1] and Dörr [11], who additionally considered the problem of scaling.

In spite of the numerous investigations on labyrinth seal flow, only few papers have been published on heat transfer in labyrinth seals. The results of Sheinin [12], Shvets [13], Kapinos and Gura [14], and Kuznezov and Zuravlov [15] are not in good agreement. Moreover, only averaged heat transfer numbers for the labyrinth seals have been published. Recently, Metzger [16] investigated the local heat transfer in labyrinths, employing newly developed coating techniques. Only a small range of Reynolds numbers, however, was examined.

Up to now primary emphasis has been directed toward

Table 1 Seal dimensions: No. 1 = straight-through seal; Nos. 2, 3, 4 = stepped seal

Seal No.	n	s	t	b	h	H
1	6	o,5;1,o 1,5;2,5	12	2,5	1o,5	-
2	5	o,4;o,6 1,o;2,o	28	2	9	3,7
3	5	"	"	"	"	1,9
4 *	5	"	"	"	"	3,7

* Opposite direction of flow

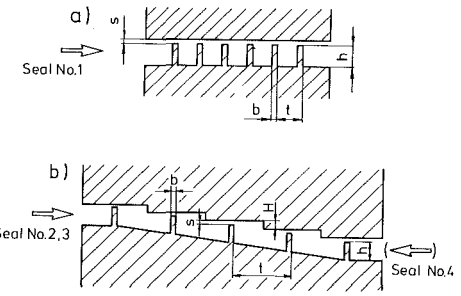

Fig. 1 Labyrinth seal geometries: (a) straight-through seal, (b) stepped seal

Contributed by the Gas Turbine Division of THE AMERICAN SOCIETY OF MECHANICAL ENGINEERS and presented at the 32nd International Gas Turbine Conference and Exhibit, Anaheim, California, May 31–June 4, 1987. Manuscript received at ASME Headquarters February 6, 1987. Paper No. 87-GT-92.

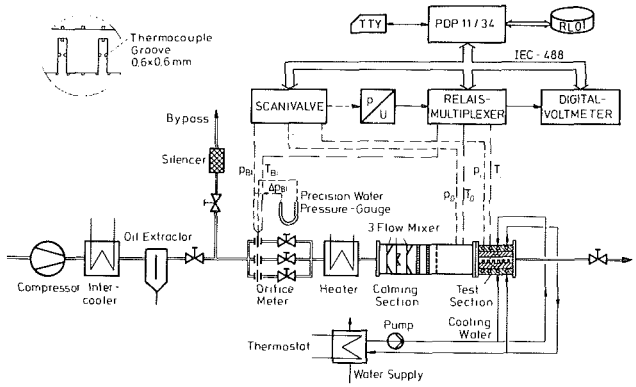

Fig. 2 Labyrinth seal test facility

straight-through labyrinth seals. Details of our own studies have been published elsewhere [17]. The present paper presents the results of experimental and numerical investigations on heat transfer in scaled-up stepped labyrinth seals (Fig. 1, Table 1), which have found increasing use in practical applications. Former data on heat transfer in straight-through labyrinth seals are included for comparison of experimental and numerical results. Rotational effects on leakage flow and heat transfer are only important for small Reynolds and high Taylor numbers, as indicated by other investigations [10, 18]. For the first phase of our work, no rotational effects have been considered. Our continuing effort, however, will include rotation with appropriate ranges of Reynolds and Taylor numbers in future work.

Experimental Approach

The experimental setup is an extension of our previously described facility [2, 17]. A schematic of the test rig is shown in Fig. 2. Air is supplied by a compressor of maximum mass flow of 0.5 kg/s and maximum pressure ratio of 4. The supply pressure is kept at constant 3.5 bar by means of a bypass. The determination of the mass flow rate, which is an extremely critical element especially for low Reynolds numbers, is accomplished by one of three parallel orifice meters, which are connected to a precision water pressure gage. The electric heater is designed for a maximum exit temperature of 400°C and can be controlled continuously from 0 to 150 kW. A mixing and settling chamber serves to obtain an even velocity and temperature profile of the flow before entering the test section. The labyrinth seal in the test section consists of an upper part with or without steps (stator) and a lower part with fins (rotor). Both parts are assembled with spacers to adjust different gap widths. The actual gap width was measured during the experiment. It was possible therefore to correct the data for temperature-dependent gap width changes. The seal is mounted directly behind the settling chamber to achieve entrance conditions for the seal comparable to those in a real engine. Due to extremely high channel width-to-labyrinth chamber depth ratio—higher than 100—side wall effects can be neglected.

For heat transfer measurements a temperature gradient normal to the axial direction can be imposed on the seal by cooling plates. Surface temperatures of the stator and rotor part were measured by NiCr-Ni (Type K) thermocouples (diameter 0.5 and 1.5 mm). Gas temperatures were recorded in the center of each chamber by thermocouple probes inserted from the side walls. The pressure distribution inside the seal was obtained from pressure taps in the stator and rotor parts. All pressure and temperature signals are recorded by a PDP 11/34 computer.

Evaluation of Measurements

Various flow parameters have been used in the literature for the analysis and description of labyrinth seal losses. The dimensionless mass flow parameter used in the present analyses is defined as

$$C_D = \frac{\dot{m}}{\dot{m}_{\text{ideal}}} \tag{1}$$

where $\dot{m}_{\text{ideal}}$ is calculated in the usual way

$$\dot{m}_{\text{ideal}} = \frac{Q_{\text{ideal}} \cdot p_0 \cdot A}{\sqrt{T_0}} \tag{2}$$

with

$$Q_{\text{ideal}} = \left(\frac{p_\infty}{p_0}\right)^{\frac{1}{\kappa}} \sqrt{\frac{2\kappa}{R(\kappa-1)}\left[1-\left(\frac{p_\infty}{p_0}\right)^{\frac{\kappa-1}{\kappa}}\right]} \tag{3}$$

for subcritical pressure ratios. For supercritical pressure ratios the value of Q_{ideal} is equal to the maximum value at

$$\left.\frac{p_\infty}{p_0}\right|_{\text{crit}} = \left(\frac{2}{\kappa+1}\right)^{\frac{\kappa}{\kappa-1}} \tag{4}$$

The local heat transfer coefficent is derived from

$$\alpha = \frac{d\dot{Q}}{dA\,(T_G - T_W)} \tag{5}$$

The gas temperature T_G as well as the wall temperature T_W are measured as described. The local heat flux $d\dot{Q}$ is determined from the two-dimensional temperature distribution in the stator and rotor part of the labyrinth seal

$$d\dot{Q} = -\lambda \cdot \nabla \cdot T|_{\text{Wall}} \tag{6}$$

A finite element program was used to calculate the

Nomenclature

A = area, m²
b = thickness of fin, m²
C = constant
C_D = discharge coefficient
c_p = constant pressure heat capacity, J/kg K
E = constant
H = step height, m
h = fin height, m
$\dot{m}$ = mass flow rate, kg/s
m = exponent
$\dot{m}_{\text{ideal}}$ = ideal mass flow rate, kg/s
n = number of fins
n = exponent
Nu = Nusselt number = $\alpha \cdot 2s/\lambda$
p_0 = settling chamber pressure, N/m²
p_∞ = pressure behind labyrinth, N/m²
Pr_l = laminar Prandtl number
Pr_t = turbulent Prandtl number
O_{ideal} = ideal flow function, s$\sqrt{\text{K}}$/m
$\dot{Q}$ = heat flux, W
$\dot{q}_W$ = wall heat flux, W/m²
Re = Reynolds number = $u \cdot 2s \cdot \rho/\mu$
S_ϕ = source term
s = gap width, m
St_W = wall Stanton number
T_0 = settling chamber temperature
T_G = gas temperature
T_W = wall temperature
t = pitch, m
u = velocity, m/s
u_W = velocity at the wall, m/s
x = coordinate, m
α = heat transfer coefficient, W/m²K
Γ_ϕ = diffusion constant
κ = specific heat ratio
λ = thermal conductivity, W/m s
ρ = specific density, kg/m²
τ_W = wall shear stress, N/m²
ϕ = general variable

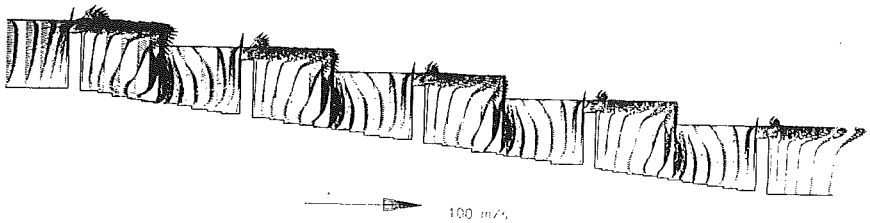

Fig. 3 Velocity field for stepped seal No. 2 (s = 2 mm, Re = 4387, $p_0/p_\infty = 1.03$)

temperature distribution from wall temperatures, which were interpolated from the measured temperatures for each boundary knot of the finite element net by rational spline functions. The gas temperatures T_G were also determined from local measurements. Finally, mean heat transfer coefficients were calculated by averaging the local values. The averaged coefficients for the stator refer to the total flow exposed surface of the stator, whereas the averaged coefficients for the rotor describe the total heat flux normalized to the rotor surface without fins. Reference gas and wall temperatures for the stator have been averaged from the local values, whereas the corresponding wall temperature for the rotor was averaged from the local values without considering the fins.

Numerical Procedure

For the calculation of the two-dimensional flow field the time-averaged Navier–Stokes equations and the energy equation have to be solved. In applying a well-established finite differencing scheme [11, 17, 19] the flow field is discretized by a Cartesian grid. Values of variables must be known at the entrance of the labyrinth and at each boundary grid point. The turbulence parameters of the flow are described by the well-known k–ϵ model [20]. The constants for this turbulence model so far have not been determined for separated regions, which are typical for labyrinth flow. However, our experience shows that with the established constants sufficient accuracy can be obtained for practical applications. Using tensor notation the momentum and energy equations as well as the two transport equations for the k–ϵ model can be written in the generalized manner

$$\frac{\partial}{\partial x_i}(\rho u_i \phi) = \frac{\partial}{\partial x_i}\left(\Gamma_\phi \cdot \frac{\partial \phi}{\partial x_i}\right) + S_\phi \tag{7}$$

The expressions for ϕ, Γ_ϕ, and S_ϕ have to be adapted to the considered equation according to [21, 22].

After the governing equations are discretized the resulting system of nonlinear algebraic equations is solved iteratively for the dependent variables by means of the SIMPLE algorithm [23]. For stability reasons all variables and the pressure-correction equation have to be intensively relaxed for the calculation of higher pressure ratios. Also a slow increase of the mass flow entering the calculation field up to the final value was necessary to avoid divergence. Relaxation factors were increased during the iteration to reduce the total CPU time. The stable upwind-differencing scheme was used for the calculation as difficulties with the convergence were experienced with the QUICK algorithm [24]. Probably this is due to high pressure gradients, which are caused by drastic changes of cross-sectional area in the labyrinth seal. For flows with low pressure gradients, as in combustion chambers, the QUICK algorithm has been used successfully [25].

For the calculation of the near-wall velocity, a logarithmic wall function was used, as an extremely dense grid would have been necessary for the complete boundary layer calculation.

For the computation of nonisothermal flows, the solution of the energy equation is necessary in addition to the equations for momentum and turbulence. The wall heat flux is

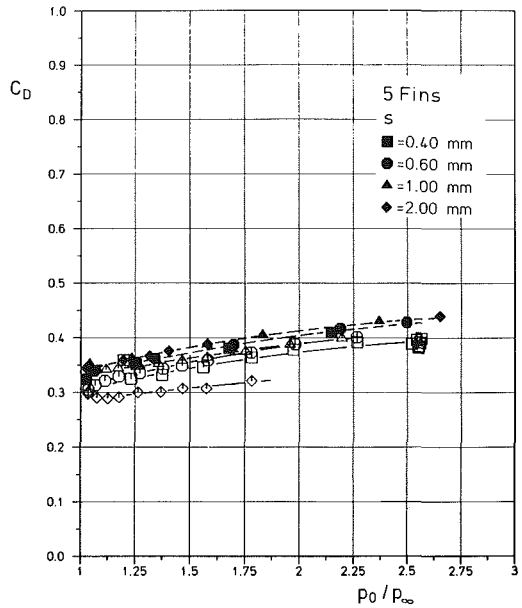

Fig. 4 Discharge coefficients for stepped seal No. 2 (• = calculations, ○ = experiment)

calculated by the analogy between momentum and heat transfer proposed by Pun and Spalding [22]

$$St_W = \frac{\frac{1}{Pr_t} \cdot \left(\frac{\tau}{\rho \cdot u^2}\right)_W}{1 + E\,\frac{Pr_l/Pr_t - 1}{\sqrt[4]{Pr_l/Pr_t}} \cdot \sqrt{\left(\frac{\tau}{\rho \cdot u^2}\right)_W}} \tag{8}$$

With the local Stanton number St_w the wall heat flux is determined as

$$\dot{q}_W = St_W \cdot \rho \cdot c_p \cdot \Delta T_W \cdot u_W \tag{9}$$

Details of the program are described in earlier reports [21, 19].

The accuracy of the discretization depends on the type of scheme as well as on the number of grid lines. Thus, the finite difference grid was adpated for each gap width. The maximum number of grid lines was 93 × 29 for straight-through labyrinths and 101 × 109 for stepped labyrinth seals.

The grid in use was sufficient for flow without heat transfer [2]. However, for flows with heat transfer a grid dependence of results was still observed. For finer grids a decrease of heat flux was observed for the rotor fins [19]. No further refinement was realized because of excessive calculation time.

Results and Discussion

Figure 3 presents the velocity distribution of the stepped labyrinth seal flow as calculated using the finite difference scheme. Two large counterrotating vortices can be seen in each labyrinth chamber. An additional small vortex is present in the

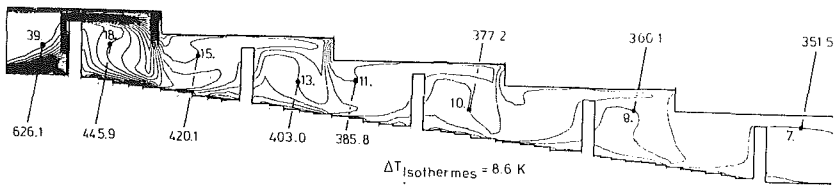

Fig. 5 Temperature field for stepped seal No. 2 ($s = 2$ mm, $Re = 4387$, $p_0/p_\infty = 1.03$)

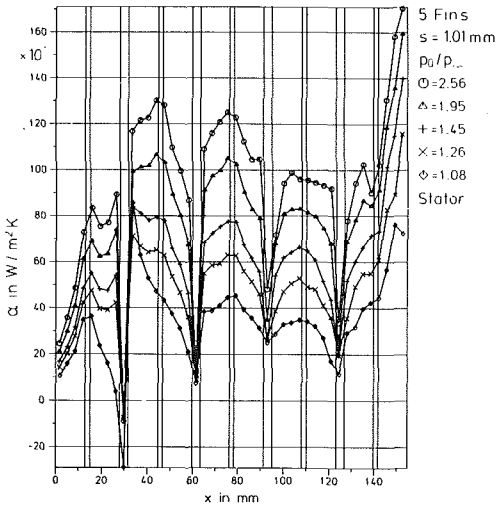

Fig. 6 Measured local heat transfer coefficients for the stator of stepped seal No. 2 (seal surface unfolded on abscissa)

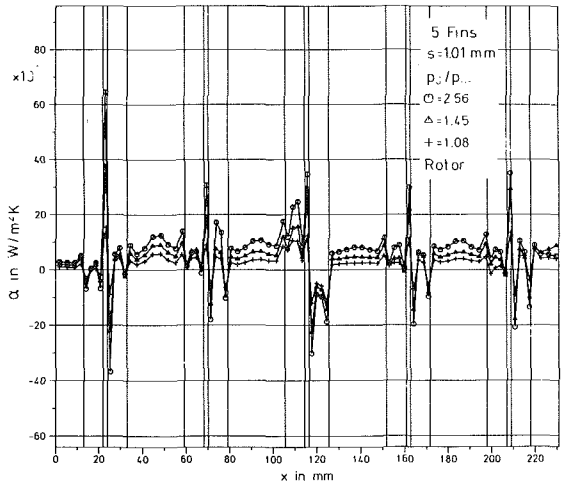

Fig. 7 Measured local heat transfer coefficients for the rotor of stepped seal No. 2 (seal surface unfolded on abscissa)

right-hand corner of each chamber. Contrary to the straight-through labyrinth seal [2] the main flow direction is diverted by the steps of the stator toward the bottom of the chambers. The numerically and experimentally derived discharge coefficents as a function of the pressure ratio and gap width are compared in Fig. 4. Considering the complex flow in the labyrinth seal, the agreement of the results is astonishingly good. Only for the large gap width, experimental results deviate from the numerical results. For smaller gap widths the dependence of the discharge coefficients on the gap width is negligible. This is in accordance with the results of Morrison and Chi [26]. The pressure distribution of straight-through and stepped labyrinth seal flow is discussed elsewhere by Wittig et al. [2].

The temperature of the hot air decreases considerably when passing the labyrinth seal. A typical temperature distribution calculated using the finite difference program is presented in Fig. 5. The highest temperature drop occurs behind the first fin. This is in general agreement with the measurements, although the finite difference program seems to overestimate the temperature drop. Specifically, a temperature deviation of approximately 20 K is observed at the labyrinth exit under identical entrance conditions.

Figures 6 and 7 show local heat transfer coefficients for stator and rotor of the stepped labyrinth seal. For the stator as well as the rotor, heat transfer coefficients increase with increasing pressure ratio. The maximum heat transfer for the stepped stator is found directly opposite the fin positions. In front of each step a distinct minimum of the heat transfer coefficient is observed. A maximum, however, could have been expected because of the impinging flow. On the other hand, a recirculating flow area in front of the steps might cause the decrease in heat transfer. Baron and Tson [27] noticed a minimum heat transfer upstream of a forward facing step and a maximum at the top of the step. A final clarification of this question from the present experiments awaits a higher resolution of the local heat transfer, i.e., a higher number of thermocouples in the step area.

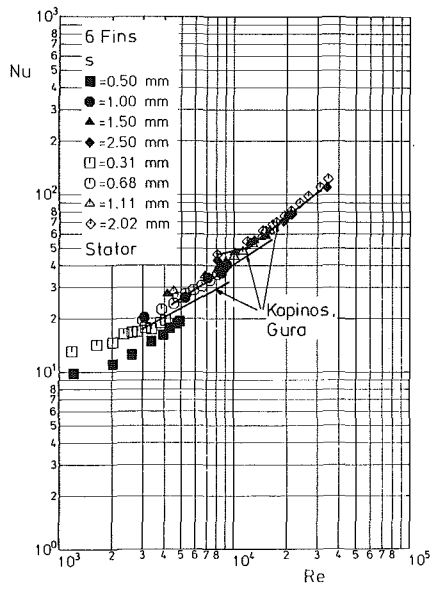

Fig. 8 Nusselt numbers for the stator of the straight-through seal (● = calculation, ○ = experiment)

Local heat transfer for the finned rotor (Fig. 7) is highest at the top of the fins. Another relative maximum heat transfer is found halfway at the bottom of each chamber, which is in agreement with the observation of impinging flow as shown in Fig. 3. The heat transfer behavior at the sides of each fin derived from the experiments utilizing the finite element analysis might be misleading because of the relatively coarse finite element net, especially for the slender fins. However, "negative" heat transfer numbers at the downstream side of the fins are not caused by numerical error but can be induced

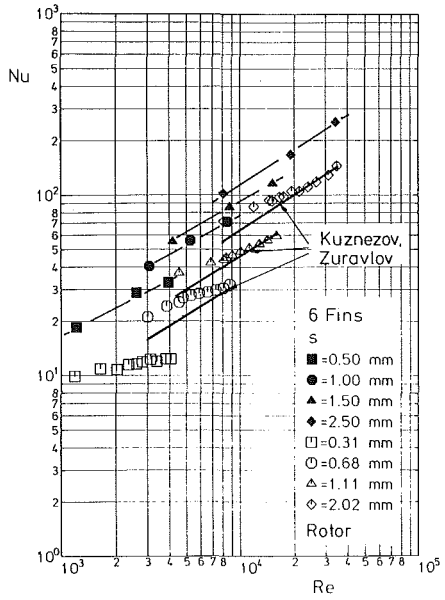

Fig. 9 Nusselt numbers for the rotor of the straight-through seal (● = calculation, ○ = experiment)

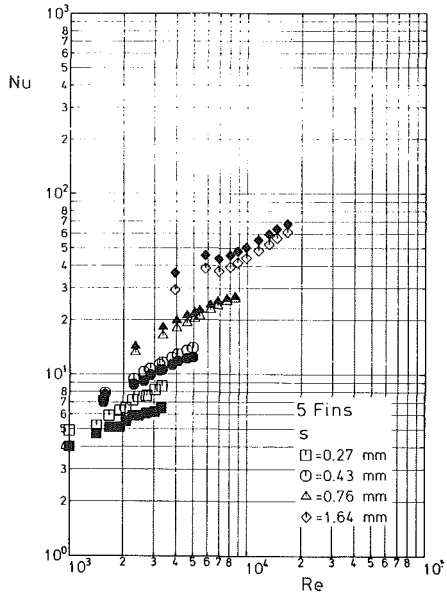

Fig. 11 Measured Nusselt numbers for the stator (○) and rotor (●) of stepped seal No. 3

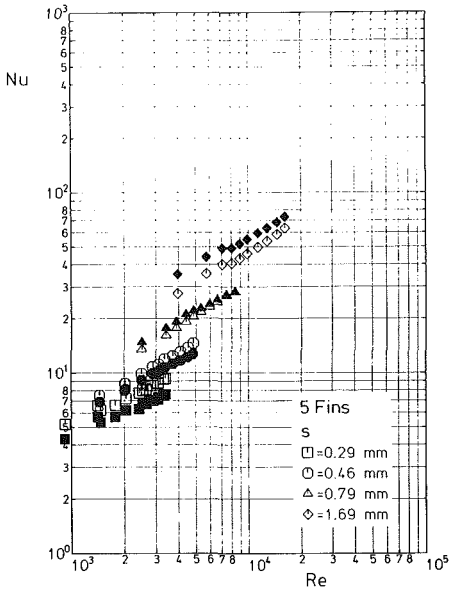

Fig. 10 Measured Nusselt numbers for the stator (○) and rotor (●) of stepped seal No. 2

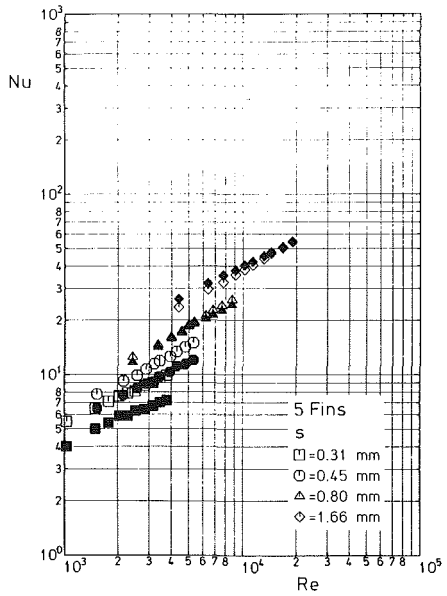

Fig. 12 Measured Nusselt numbers for the stator (○) and rotor (●) of stepped seal No. 4

by heat flux from the hot fin into the colder vortex of the next chamber.

Figures 8 and 9 present measured and calculated Nusselt numbers for the straight-through labyrinth seal. The actual gap width of the experiment was dependent on the temperature distribution of the seal; however, for practical calculations mean values are indicated. The mean gap width of the calculation and the experiment differ because the calculation did not allow for temperature-dependent gap width changes. Nusselt numbers for the stator without fins in Fig. 8 are found to be nearly independent of gap width. However, different slopes of the Nusselt versus Reynolds function seem to indicate a transition from laminar to turbulent flow at Reynolds numbers of approximately 6000. Experimental and numerical results coincide very well except for the smallest gap width. For the larger gap widths the author's results are compared with the results of Kapinos and Gura [14], which show also fairly good agreement. Figure 9 presents the Nusselt numbers for the finned rotor. The numerical results overpredict the measured data significantly. However, measured Nusselt numbers agree well with the results of Kuznezov and Zuravlov [15] for the higher Reynolds numbers of each gap width. The results of the other authors have been derived from their corresponding correlations using the dimensions of the seals discussed in this paper.

The overprediction of heat transfer rates by the finite difference program may originate from different sources:

(*i*) The analogy used in the program between wall shear stress and heat flux is invalid in the neighborhood of flow stagnation points.

(*ii*) The wall shear stress is overpredicted because of high turbulence level close to the wall as calculated by the upwind scheme or the k–ϵ model.

Table 2 Correlation coefficents

Seal No.	1			2		3		4	
	Stator		Rotor	Stator	Rotor	Stator	Rotor	Stator	Rotor
c	0,158	0,028	2,320	0,747	1,673	0,797	1,514	0,482	0,896
n	0,6	0,8	0,5	0,6	0,6	0,6	0,6	0,6	0,6
m	0	0	-0,64	-0,50	-0,71	-0,52	-0,71	-0,41	-0,62
Re	10^3-6·10^3	6·10^3-4·10^4	10^3-4·10^4	10^3 - 1,8 · 10^4		10^3 - 1,8 · 10^4		10^3 - 2 · 10^4	
$\frac{t}{s}$	5,7 - 48			15,6 - 117		16 - 122		16 - 10^4	

(*iii*) In contrast to the leakage flow calculations the grid in use is too coarse for convective heat transfer calculations.

Averaged Nusselt numbers for stepped labyrinth seals have been evaluated from the measurements for different gap widths (Figs. 10–12). The Nusselt numbers depend on the gap width for all three seals discussed above. Comparing the stator and rotor part of the seals, the Nusselt numbers reveal a characteristic behavior. At small gap width the Nusselt numbers for the stator are higher than those for the rotor, whereas at higher gap widths the Nusselt numbers for the stator are smaller than those for the rotor. This behavior can be explained by the increasing displacement of the main flow from the stator part to the rotor part. The flow displacement seems to be dependent on step height, increasing with it.

In an attempt to derive a functional dependence, which can be readily used for practical application, Nusselt numbers were correlated dependent on Reynolds number and gap width as follows:

$$\mathrm{Nu} = \mathrm{Re}^n \cdot g\left(\frac{t}{s}\right) \tag{10}$$

The exponent n can be derived from $\mathrm{Nu} = f(\mathrm{Re})$ (see Fig. 8). Values for g are calculated from

$$g\left(\frac{t}{s}\right) = \mathrm{Nu} \cdot \mathrm{Re}^{-n} \tag{11}$$

The function g was also derived graphically and was found to be

$$g = C \cdot \left(\frac{t}{s}\right)^m \tag{12}$$

Thus, the Nusselt number may be expressed as follows:

$$\mathrm{Nu} = C \cdot \mathrm{Re}^n \cdot \left(\frac{t}{s}\right)^m \tag{13}$$

The coefficients C, n, and m, as well as the lower and upper limit of Re and t/s, are listed in Table 2 for seal No. 1–4.

Summary

Leakage flow and heat transfer for straight-through and stepped labyrinth seals have been investigated experimentally and numerically. Experiments were conducted under steady, two-dimensional conditions. Discharge coefficients derived from the experiments and numerical calculations agree very well for both types of labyrinth seal. Thus, the finite difference program may be used as a valuable tool for leakage flow optimization of new seal configurations. Experimental and numerical Nusselt numbers agree very well for the plain stator part of the straight-through seal, but differ somewhat for the finned rotor part as well as for the stator and rotor of the stepped seal. However, evidence was found that further refinement of the finite difference code especially in the stagnation point flow area might lead to better agreement. Nevertheless, the present code gives valuable insight into the physics of labyrinth flow.

Experimental Nusselt numbers were found to correlate as $\mathrm{Nu} = C \cdot \mathrm{Re}^n \cdot (t/s)^m$. Thus for the first time a tool is available to calculate the heat transfer in stepped labyrinth seals. Future work is directed toward the effects of rotation on leakage flow and heat transfer of labyrinth seals.

Acknowledgments

Thanks are due to H. Zimmermann of Motoren- und Turbinen-Union, Munich, for helpful discussions. This work was supported in part by the Forschungsvereinigung Verbrennungskraftmaschinen e.V. through a grant from the AIF (Arbeitsgemeinschaft Industrieller Forschung).

References

1 Wittig, S. K. L., Dörr, L., and Kim, S., "Scaling Effects on Leakage Losses in Labyrinth Seals," ASME JOURNAL OF ENGINEERING FOR POWER, Vol. 105, 1983, pp. 305–309.

2 Wittig, S. K. L., Schelling, U., Kim, S., and Jacobsen, K., "Numerical Prediction and Measurement of Discharge Coefficients in Labyrinth Seals," ASME Paper No. 87-GT-188.

3 Trutnovsky, K., and Komotori, K., *Berührungsfreie Dichtungen*, Vol. 4, VDI-Verlag, Düsseldorf, 1981.

4 Stodola. A., *Dampf- und Gasturbinen*, Vol. 5, Springer-Verlag, Berlin, 1922.

5 Gerke, M. J., "Berechnung der Ausflussmengen von Labyrinthdichtungen," *Wärme*, Vol. 57, 1934, pp. 513–517.

6 Egli, A., "The Leakage of Steam Through Labyrinth Seals," *Trans. ASME*, Vol. 57, 1935, pp. 115–122.

7 Jerie, J., "Flow Through Straight-Through Labyrinth Seals," *Proc. Seventh International Congress of Applied Mechanics*, Vol. 2, Part F, 1948, pp. 70–82.

8 Jones, J. S., "Communication to Kearton, W. J., and T. H. Keh, 'Leakage of Air Through Labyrinth Glands of Staggered Type', " *Proc. Inst. Mech. Engrs.*, Vol. 166, 1952, p. 189.

9 Komotori, K., "Probleme bei Labyrinth-Stopfbüchsen," *Proc. of the Fujihara Memorial Faculty of Engineering*, Keio University, Vol. 14, 1961, pp. 1–48.

10 Stocker, H. L., "Determining and Improving Labyrinth Seal Performance in Current and Advanced High Performance Gas Turbines," AGARD-CP-237, Conference Proceedings, 1978, pp. 13/1–13/22.

11 Dörr, L. "Modellmessungen und Berechnungen zum Durchflussverhalten von Durchblicklabyrinthen unter Berücksichtigung der Übertragbarkeit," Dissertation, Universität Karlsruhe, 1985.

12 Sheinin, E. I., "Experimentelle Untersuchungen des Wärmeübergangs in der Zone der Endabdichtungen von Gasturbinen" [in Russian], *Energomashinostroenie*, Vol. 7, 1961, pp. 25–27.

13 Shvets, I. T., and Dyban, E. P., "Heat Exchange in Labyrinth Seals of Turbine Rotors" [in Russian], *Energomashinostroenie*, Vol. 12, 1963, pp. 8–11.

14 Kapinos, V. M., and Gura, L. A., "Investigation of Heat Transfer in Labyrinth Glands on Static Models," *Thermal Engineering*, Vol. 17, 1970, pp. 53–56.

15 Kuznezov, A. L., and Zuravlov, O. A., "Wärmeübergang in den Labyrinthdichtungen von Gasturbinen" [in Russian], *Energomashinostroenie*, No. 5, 1972, pp. 10–12.

16 Metzger, D. E., and Bunker, R. S., "Heat Transfer for Flow Through Simulated Labyrinth Seals," Symposium on Transport Phenomena in Rotating Machinery, Honolulu, HI, April 2–May 3, 1985.

17 Wittig, S. K. L., Jacobsen, K., Schelling, U., and Kim, S., "Wärmeübergangszahlen in Labyrinthdichtungen," VDI-Berichte 572.1, 1985, pp. 337–356.

18 Kapinos, V. M., and Gura, L. A., "Heat Transfer in a Stepped Labyrinth Seal" [in Russian], *Teploenergetika*, Vol. 20, 1973, pp. 22–25.

19 Wittig, S. L. K., Kim, S., Jacobsen, K., and Schelling, U., "Experimentelle und theoretische Untersuchungen zum Durchflussverhalten und

Wärmeübergang in Labyrinthdichtungen," Abschlussbericht, Forschungsgemeinschaft Verbrennungskraftmaschinen e.V., 1986.

20 Rodi, W., *Turbulence Models and Their Application in Hydraulics*, IAHR, Delft, The Netherlands, 1980.

21 Elbahar, O. M. F., "Zum Einfluss von Kühlluftstrahlen und Mischzonengeometrie auf die Temperaturprofilentwicklung in Gasturbinen-Brennkammern," Dissertation, Universität Kurlsruhe, 1982.

22 Pun, W. M., and Spalding, D. B., "A General Computer Program for Two-Dimensional Elliptic Flows," Imperial College, London, report No. HTS/76/2, 1976.

23 Patankar, S. V., *Numerical Heat Transfer and Fluid Flow*, Hemisphere, Washington, DC, 1980.

24 Leonard, B. P., "The QUICK Algorithm, a Uniformly Third-Order Finite Difference Method for Highly Convective Flows," in: K. Morgan and C. Taylor, *Computer Methods in Fluids*, 1981, pp. 159–195.

25 Wittig, S. L. K., Elbahar, O. M. F., and Noll, B. E., "Temperature Profile Development in Turbulent Mixing of Coolant Jets With a Confined Hot Crossflow," ASME JOURNAL OF ENGINEERING FOR GAS TURBINES AND POWER, Vol. 106, 1984, pp. 193–197.

26 Morrison, G. L., and Chi, D., "Incompressible Flow in Stepped Labyrinth Seals," ASME Paper No. 85-FE-4.

27 Baron, A., and Tson, F.-K., "Flow Field and Heat Transfer Associated With Laminar Flow Over a Forward-Facing Step," *Proc. of the 8th Int. Heat Transfer Conf.*, San Francisco, CA, 1986.

The Effect of Disk Geometry on Heat Transfer in a Rotating Cavity With a Radial Outflow of Fluid

P. R. Farthing

J. M. Owen

Thermo-Fluid Mechanics Research Centre,
School of Engineering and
Applied Sciences,
University of Sussex,
Brighton, Sussex, United Kingdom

Flow visualization and heat transfer measurements have been made in a cavity comprising two nonplane disks of 762 mm diameter and a peripheral shroud, all of which could be rotated up to 2000 rpm. "Cobs," made from a lightweight foam material and shaped to model the geometry of turbine disks, were attached to the center of each disk. Cooling air at flow rates up to 0.1 kg/s entered the cavity through the center of the "upstream" disk and left via holes in the shroud. The flow structure was found to be similar to that observed in earlier tests for the plane-disk case: a source region, Ekman layers, sink layer, and interior core were observed by flow visualization. Providing the source region did not fill the entire cavity, solutions of the turbulent integral boundary-layer equations provided a reasonable approximation to the Nusselt numbers measured on the heated "downstream" disk.

Introduction

In advanced gas turbines, the turbine disks are cooled by the radial flow of air over their surfaces. The disk geometry is often complex: There is usually a hub or "cob" at the disk center, and the addition of a flange and bolts near the outer radius is not uncommon. Most of the understanding about rotating disk systems has been obtained by using a plane disk, which either rotates close to a plane stator (the so-called rotor–stator system) or is one of a pair of corotating disks (the rotating cavity). A review of flow and heat transfer in plane rotating-disk systems is given in [1].

It is the rotating cavity with nonplane disks that is the subject of the present paper. Flow and heat transfer in cavities with plane disks have been studied by a number of research workers (see [2–16]), and the basic flow structure for the case of a rotating cavity with an isothermal radial outflow of fluid is shown in Fig. 1. For the radial-inlet case illustrated in Fig. 1(*a*), the source region distributes the incoming flow equally into each of the Ekman layers (an Ekman layer being a boundary layer in which the nonlinear inertial forces are much smaller than the Coriolis forces), and the sink layer distributes the flow from the Ekman layers into the holes in the peripheral shroud. In the interior core between the Ekman layers, viscous forces are negligible, the radial and axial components of velocity are zero, and the fluid rotates relative to the disks. For the axial-inlet case shown in Fig. 1(*b*), the incoming flow impinges on the downstream disk and flows outward in the source region as a radial wall-jet. Although the flow structure in the source region is different for the radial- and axial-inlet cases, in all other regions it is unaltered.

Transition from laminar to turbulent flow occurs in the Ekman layers when $Re_r \simeq 180$ (where Re_r and other symbols are defined in the Nomenclature), and the overall flow structure for turbulent flow is qualitatively similar to that for laminar flow. However, if one disk is heated, buoyancy effects can result in the axial transfer of fluid from one Ekman layer to the other. At sufficiently high rotational speeds, the buoyancy forces can reverse the direction of flow in the Ekman layer on the heated disk (that is, flow near the disk periphery can move radially inward rather than outward). This can create flow instability and ultimately leads to transition from forced to free convection.

In [15], the effect of inlet conditions on the flow and heat transfer in a rotating cavity with plane disks was discussed. Air was admitted either axially at a radius ratio of $a/b = 0.1$ or radially at $a/b = 0.5$. In this paper, air is admitted axially at $a/b = 0.1$ but "cobs" are attached to the disks to simulate more closely the geometry of actual gas turbine disks. Section 2 outlines the apparatus and data analysis, and Sections 3 and

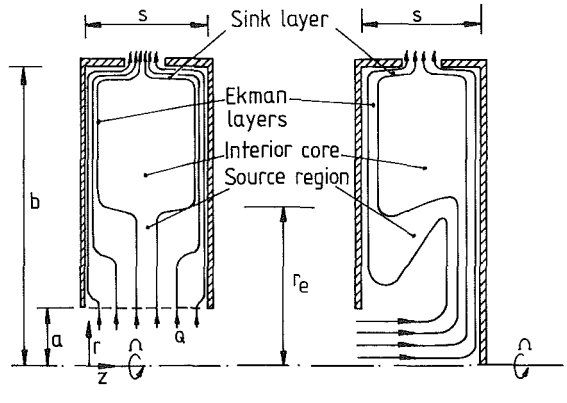

Fig. 1 Schematic diagram of the flow structure inside a rotating cavity with a radial outflow of fluid

Contributed by the Gas Turbine Division of THE AMERICAN SOCIETY OF MECHANICAL ENGINEERS and presented at the 32nd International Gas Turbine Conference and Exhibit, Anaheim, California, May 31–June 4, 1987. Manuscript received at ASME Headquarters February 17, 1987. Paper No. 87-GT-163.

4 discuss the results obtained from flow visualization and heat transfer measurements, respectively.

2 Experimental Apparatus and Data Analysis

The rig and data analysis were similar to those outlined in [15] so only the salient features are presented here.

2.1 Experimental Apparatus. A simplified section through the rotating cavity is shown in Fig. 2. The cavity was formed from two steel disks, 762 mm in diameter, 13 mm thick and spaced 102 mm apart, together with a peripheral shroud 1.5 mm thick. For the heat transfer tests, the shroud was made from paxolin (a fiber-reinforced plastic) and contained 30 equispaced holes of 28.6 mm diameter; for the flow visualization, it was made from polycarbonate and the 30 holes were of 6.8 mm diameter. The two disks were connected by a central drive shaft 25 mm in diameter, and cooling air was fed into the cavity via the annular space between the disk shaft and inlet tube, which had an internal diameter of 76 mm, and left through the holes in the shroud.

The cobs, attached to the center of each disk, were made from Rohacell, a lightweight high-strength foam material that was easy to machine and could be readily bonded to the steel disks. The shape of the cobs was chosen to be representative of that used in gas turbine design. The minimum axial spacing between the cobs was 33 mm, and the parallel section, which extended to a radius of 107 mm, was blended into the steel disks at a radius of 168 mm. As Rohacell is an excellent thermal insulator ($k \simeq 0.03$ W/mK), the disks were effectively adiabatic for $r \leq 168$ mm, which meant that heat transfer measurements could only be made at larger radii on the steel disk.

The cooling air was supplied at flow rates up to approximately 0.1 kg/s by a centrifugal blower and was cooled to approximately 20°C at inlet to the rig. The disks were rotated up to 2000 rpm by a variable-speed electric motor and a toothed-belt drive, and the "downstream disk" was heated to a maximum temperature of approximately 100°C by an equispaced array of thirty 750 W radiant "firebar" elements. Each element was positioned about 30 mm from the "back face" of the disk on a radial line extending from $r = 230$ mm to $r = 380$ mm. The radial profile of the disk temperature could not be controlled, but the temperature level could be varied by altering the power supplied to the heaters.

Twelve thermocouples were embedded on either face of the downstream disk at radially weighted intervals, but two of the innermost thermocouples on the front face were covered by the cob. The thermocouple signals were brought out through silver slip rings, and the temperatures of the disk surface and of the cooling air were measured, with a resolution better than

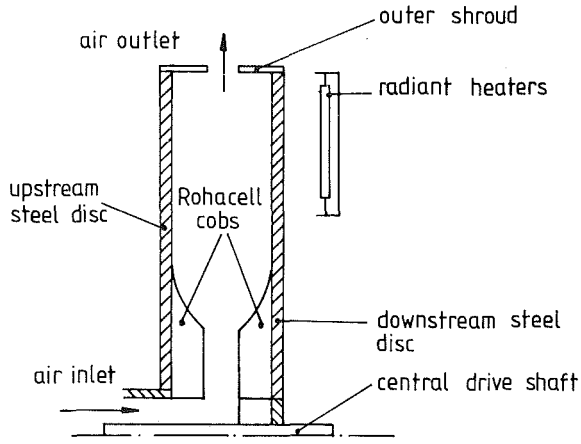

Fig. 2 Simplified diagram of the rotating-cavity rig

0.1°C, by means of a Solartron IMS 3510 data-logger, which could scan at a rate of 33 channels/s and was controlled by a PDP 11/44 minicomputer.

For the flow-visualization studies, a 4 W argon-ion laser and cylindrical lens were used to produce a flat sheet of light. This was passed through the transparent polycarbonate shroud to illuminate the r–z plane of the cavity (that is, the plane corresponding to that shown in Fig. 2). A smoke-generator produced clouds of micron-sized oil particles, which were injected into the inlet of the blower supplying the cooling air, and video recordings and photographs were used to study the flow structure in the cavity. It should be pointed out that the holes in the polycarbonate shroud had a 6.8 mm diameter compared with 28.6 mm diameter for the paxolin shroud used in the heat transfer tests. The large-hole shroud tended to create instabilities at the lower flow rates, whereas the small-hole shroud made the flow visualization easier to interpret.

2.2 Data Analysis. The Nusselt numbers on the front face of the downstream disk were determined from the numerical solution of Fourier's transient conduction equation, as described in [9]. The rotating disk was heated until the maximum temperature was approximately 100°C and the heaters were then turned off. As the disk cooled down, the temperatures were measured, recorded and, after smoothing both in time and in the radial direction, used as boundary conditions for the solution of the Fourier equation. For the region on the front face that was covered by the cob, the disk surface was assumed to be adiabatic. The initial temperature distribution inside the disk was obtained using linear interpolation

Nomenclature

A, B = constants in equations (3.1) and (3.2)
a, b = inner and outer radii of disks
C_w = $Q/\nu b$ = dimensionless flow rate
G = s/b = gap ratio
k = thermal conductivity
N = number of finite-difference time steps
Nu = $q_s r/k(T_s - T_I)$ = local Nusselt number
$\langle \mathrm{Nu} \rangle$ = ensemble-averaged Nusselt number
q_s = heat flux from disk to cooling air
Q = volumetric flow rate
r = radial coordinate
R_k = ratio of effective thermal conductivity of disk to thermocouple
Re_r = $Q/2\pi\nu r$ = radial Reynolds number
Re_ϕ = $\Omega b^2/\nu$ = rotational Reynolds number
s = axial spacing between disks
t = time
T = temperature
x = r/b = dimensionless radial coordinate
Δt = finite-difference time step
θ = $(T_s - T_I)/(T_{ss} - T_I)$ = dimensionless disk temperature
ν = kinematic viscosity
Ω = angular speed of cavity

Subscripts

b = back (heated) face of disk
e = edge of source region
f = front (cavity-side)face of disk
I = inlet to cavity
s = surface of heated disk
ss = steady-state value

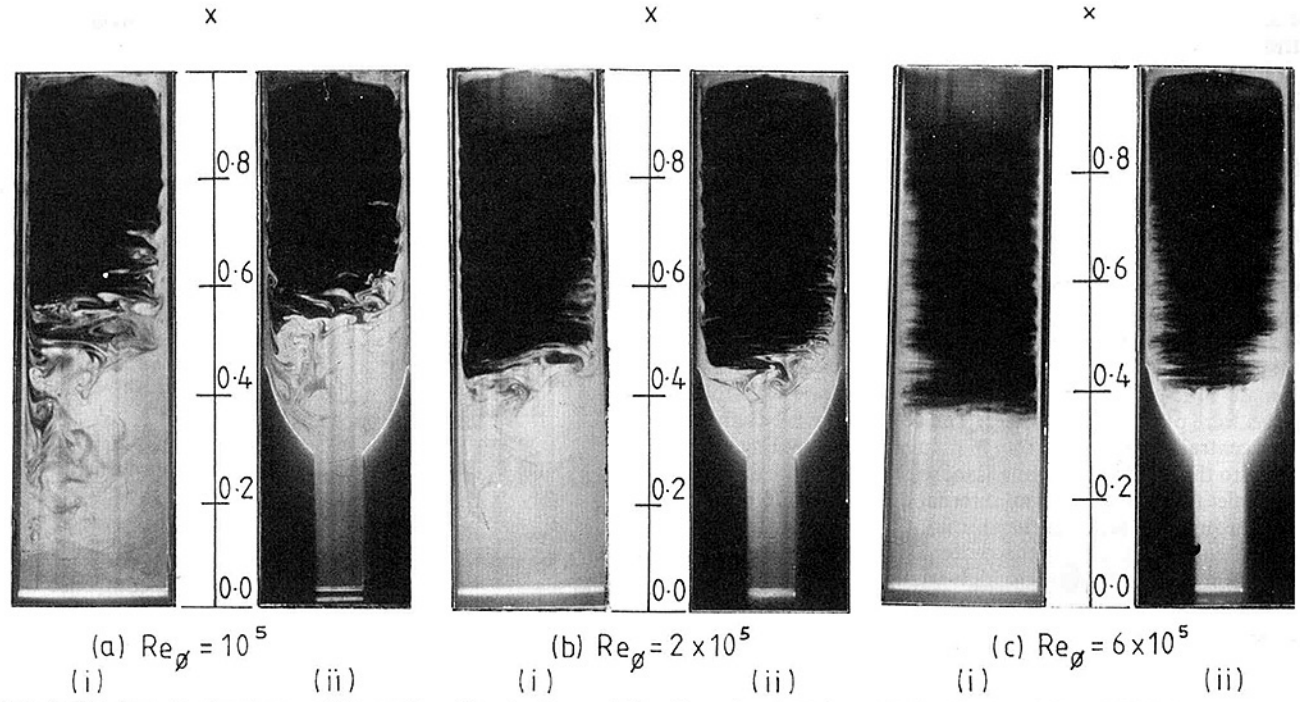

Fig. 3 The flow structure in a rotating cavity with a laminar radial outflow of coolant, C_w = 440, for (*i*) plane disks and (*ii*) disks with cobs

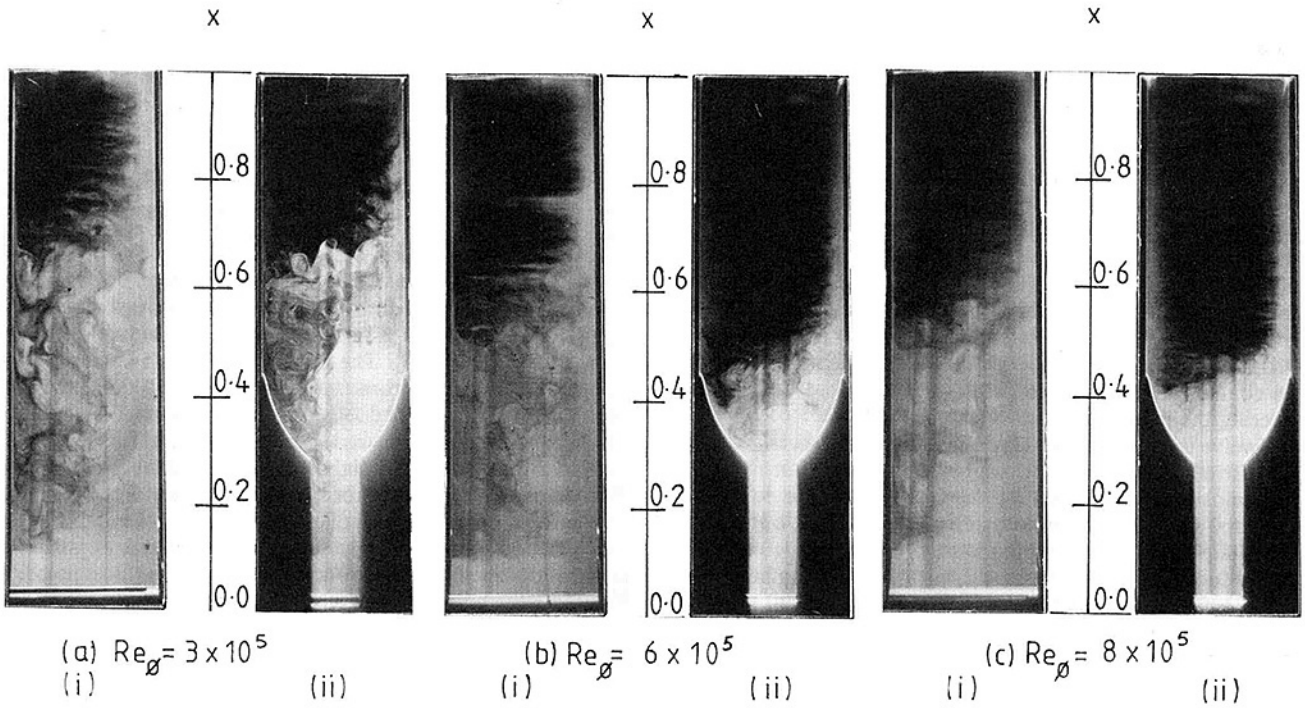

Fig. 4 The flow structure in a rotating cavity with a turbulent radial outflow of coolant, C_w = 1760, for (*i*) plane disks and (*ii*) disks with cobs

between the measured values on the surfaces. While not correct, particularly in the region covered by the cob, any errors in the assumed initial condition decay with time and are usually negligible after the tenth time step.

A finite-difference grid with 21 radial and 7 axial nodes and 100 time steps was used. At each time step, the local heat fluxes were computed using second-order differences, and the convective flux q_s was calculated by subtracting the estimated radiant flux from the computed flux. Further details of the technique and a discussion of its accuracy are given in [9, 17, 18].

3 Flow Visualization

3.1 The Flow Structure. Figures 3 and 4 show photographs, for laminar and turbulent flow, respectively, that were taken using the flow-visualization apparatus referred to in Section 2, and interpretation of the flow structure is aided by reference to Fig. 1. The bottom of each photograph corresponds to the centerline of the cavity, and the top to the shroud. The left-hand side corresponds to the upstream disk, through which flow can be seen to enter the cavity at the bottom left-hand corner of each photograph. The left-hand

photograph in each pair were obtained from [9] for the plane-disk case; the cobs appear as black regions at the bottom of the right-hand photographs.

In Fig. 3, for $C_w = 440$, the white smoke-filled source region, Ekman layers and sink layer stand out in contrast to the black interior core. For this flow rate, the flow in the Ekman layers is expected to be laminar (that is, $Re_r < 180$) for $x > 0.39$. For the plane-disk case, the flow tends to impinge on the downstream (right-hand) disk and then moves outward as a radial wall-jet in the source region. This effect is more pronounced at $Re_\phi = 10^5$ than at the higher values of Re_ϕ. The cobs tend to reduce the "wall-jet effect," and the flow enters the cavity in a manner that is closer to the radial-inlet than to the axial-inlet case shown in Fig. 1. It can be seen that the size of the source region, which decreases with increasing Re_ϕ, is not significantly affected by the presence of the cobs. The flow structure outside the source region also appears to be similar for both cases.

Figure 4 shows the flow structure for $C_w = 1760$ where the flow in the Ekman layers is expected to be turbulent over the whole disk surface. Referring to Fig. 4(*a*) for $Re_\phi = 3 \times 10^5$, there is evidence of jet impingement on the downstream disk for both the plane disk and the disk with the cob, and the size of the source region is similar for both cases. At the higher rotational speeds, the "wall-jet effect" is attenuated, particularly for the cavity with the cobs, and in Fig. 4(*c*) the "radial-inlet effect" of the cobs causes a reduction in the size of the source region. As for the laminar case, the size of the source region decreases with increasing Re_ϕ.

3.2 Size of the Source Region. In [12], the size of the source region was calculated by assuming that the entrainment into the boundary layers on the disks was the same as that for a disk rotating in a quiescent environment, the so-called free disk. The outer edge of the source region was assumed to correspond to the radius r_e at which all the available fluid had been entrained; at larger radii, the mass flow rate in the Ekman layers is constant. From this assumption it follows that

$$x_e = AC_w^{1/2}Re_\phi^{-1/4} \tag{3.1}$$

for laminar flow, and

$$x_e = BC_w^{5/13}Re_\phi^{-4/13} \tag{3.2}$$

for turbulent flow. For the radial-inlet case, $A = 0.424$ and $B = 1.37$. For the axial-inlet case, these values of A and B are still appropriate if the flow is distributed equally between the disks (for example, at the lower flow rates and higher rotational speeds). However, if the incoming flow impinges on the downstream disk, forming a wall jet, then the appropriate values are $A = 0.599$ and $B = 1.79$.

A series of tests was conducted for $440 \le C_w \le 1760$ and $0.16 \le Re_\phi/10^6 \le 1$, and the size of the source region was measured, to an estimated accuracy of ± 10 mm, from video recordings of the flow structure. The results for laminar and turbulent flow are shown in Figs. 5 and 6, respectively. For the plane disk case (without the cobs) the results were taken from [9].

Referring to Fig. 5, the experimental results for the smaller values of $C_w^{1/2}Re_\phi^{-1/4}$ are scattered about the radial-inlet curve (equation (3.1) with $A = 0.424$). At the higher values of $C_w^{1/2}Re_\phi^{-1/4}$, where the wall-jet effect becomes more significant, the radial-inlet curve underestimates the size of the source region. Given the amount of scatter in the data, the cobs do not appear to have a significant effect on the size of the source region for laminar flow.

The data shown in Fig. 6 for turbulent flow are reasonably close to the axial-inlet curve (equation (3.2) with $B = 1.79$). At the lower values of $C_w^{5/13}Re_\phi^{-4/13}$, the cobs appear to cause a slight reduction in the size of the source region; at higher values, the differences appear to be insignificant.

For the range of C_w and Re_ϕ tested, it would appear from flow visualization that the cobs have only a relatively small effect on the size of the source region and on the flow structure outside this region.

4 Heat Transfer Results

4.1 The Measured Nusselt Numbers. Figure 7 shows typical variations of temperature and Nusselt number, for the front face of the downstream disk, for $C_w = 3500$ and $Re_\phi = 0.25 \times 10^6$. The dimensionless temperature θ is defined as

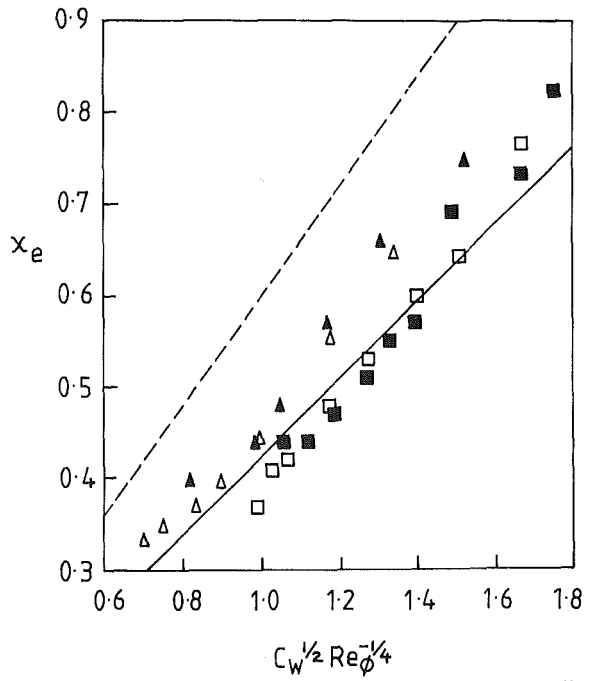

Fig. 5 Size of the source region for laminar flow; —— equation (3.1), $A = 0.424$; --- equation (3.1), $A = 0.599$; ▲ $C_w = 440$, experimental data for cavity with cobs; ■ $C_w = 880$ (open symbols refer to cavity with plane disks)

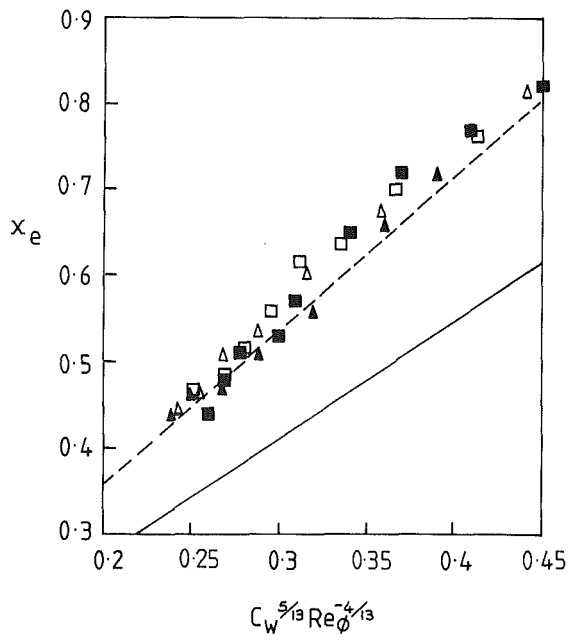

Fig. 6 Size of the source region for turbulent flow; —— equation (3.2), $B = 1.37$; --- equation (3.2), $B = 1.79$; ▲ $C_w = 1200$, experimental data for cavity with cobs; ■ $C_w = 1760$ (open symbols refer to cavity with plane disks)

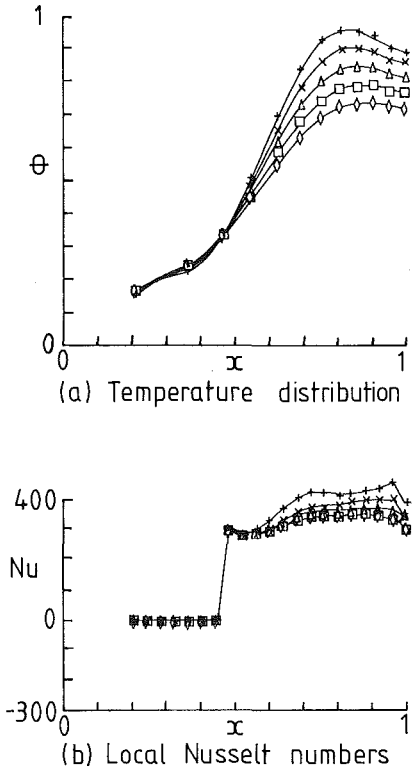

Fig. 7 Heat transfer measurements for the disk with the cob for C_w = 3500, Re_ϕ = 0.25 × 10^6, Δt = 3.7 s

Symbol	+	×	△	□	◇
N (equation (4.3))	10	30	50	70	90
Smoothing curves					

$$\theta = (T_s - T_I)/(T_{ss} - T_I) \tag{4.1}$$

where T_s is the local surface temperature, T_{ss} the maximum steady-state temperature (immediately before the heaters were turned off), and T_I the temperature of the cooling air at inlet to the cavity. The local Nusselt number Nu is defined as

$$\mathrm{Nu} = q_s r/k(T_s - T_I) \tag{4.2}$$

where q_s is the convective heat flux from the disk to the cooling air. The numerical results were obtained for 100 time steps, and the time t can be calculated from

$$t = N\Delta t \tag{4.3}$$

where N is the number of the time step and Δt is the step length, which for this case was 3.7 s.

Figure 7(*a*) shows how the measured surface temperature varied with time from N = 10 to 90 (a period of 296 s), and Fig. 7(*b*) shows the Nusselt numbers computed from the Fourier equation as outlined in Section 2. It should be noted that, as there was not a finite-difference node at x = 0.44 (the edge of the cob), the discontinuity in the computed Nusselt number occurs between the nodes at x = 0.43 and 0.45; for x < 0.43, the disk surface is taken to be adiabatic (Nu = 0). The variation of Nu with time is attributed to inaccuracies in the temperature measurements, or in the numerical solutions, rather than to physical reasons. Buoyancy effects can cause the Nusselt number to decrease with decreasing temperature difference, but these effects are expected to be small for the values of C_w and Re_ϕ used for this test.

As the values of the computed Nusselt numbers changed from one time step to the next, ensemble averages ⟨Nu⟩ and 95 percent confidence intervals were determined. These were based on the computed values between N = 10 and 90, and the confidence interval provides an estimate of the "scatter" of the experimental data; it should not be interpreted as an indication of the accuracy of the measured Nusselt numbers. A brief description of the method used to correct the Nusselt numbers for thermocouple bias (caused by thermocouple embedding errors) is given in the Appendix.

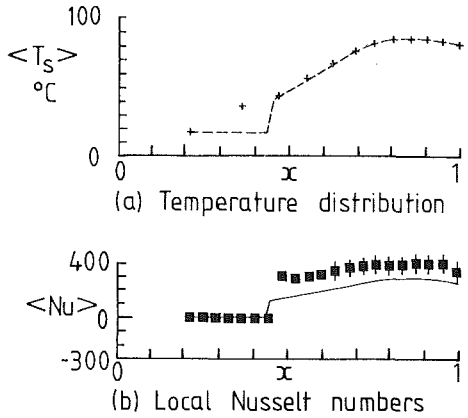

Fig. 8 Heat transfer for the disk with the cob for C_w = 3500, Re_ϕ = 0.25 × 10^6: comparison between theory and experiment; + average of measured surface temperatures; ■ average of measured Nusselt numbers (and confidence interval); --- fitted temperature used as boundary condition; —— theoretical Nusselt numbers

4.2 Comparisons Between Theory and Experiment. As well as the experimental results, theoretical values of Nu were calculated using a computer program based on the method given in [19]. This involved solution of the momentum- and energy-integral equations for turbulent flow using measured surface temperatures as boundary conditions. An ensemble average of each surface temperature was taken and the average values were then smoothed in the radial direction. For x > 0.44, these smoothed values were used to provide the boundary condition T_s for the energy equation; for $x \le 0.44$, it was assumed that the surface temperature of the cob was equal to that of the fluid entering the cavity (that is, $T_s = T_I$).

For C_w = 3500 and Re_ϕ = 0.25 × 10^6, which are the conditions used in Fig. 7, Fig. 8 shows the radial variation of T_s used for the energy equation and the Nusselt numbers computed from this equation. Other techniques of providing the thermal boundary condition for the energy equation were tried, but the discontinuity in temperature gradient at x = 0.44 tended to create "overshoots" or "undershoots" of Nu in this region. It should also be pointed out that the integral equations were solved without taking account of the cob geometry: Any differences between solutions of the integral equations for the plane disk and for the disk with the cob are caused solely by differences between the thermal boundary conditions.

Figures 9–11 show the radial variation of ⟨Nu⟩ for C_w = 3500, 7000, and 14,000, respectively, with $Re_\phi/10^6$ = 0.25, 0.6, 1.2, and 2.0. The experimental data for the plane disk and for the disk with the cob are shown together with the theoretical curves obtained from solutions of the integral equations. Also shown, where appropriate, is the radial extent of the source region according to equation (3.2) with B = 1.79 (the axial-inlet case).

Referring to Fig. 9 for C_w = 3500, it can be seen that for x > 0.44 (that is, for radii larger than the cob radius), the differences between the Nusselt numbers for the disks with and without the cobs increase with increasing Re_ϕ. The bias, discussed in the Appendix, is small for the measured Nusselt numbers for the disk with the cobs shown in Figs. 9(*i*) and (*ii*) but it is large in Figs. 9(*iii*) and (*iv*). This is caused by the fact that the ratio of Nusselt numbers on the front and back faces

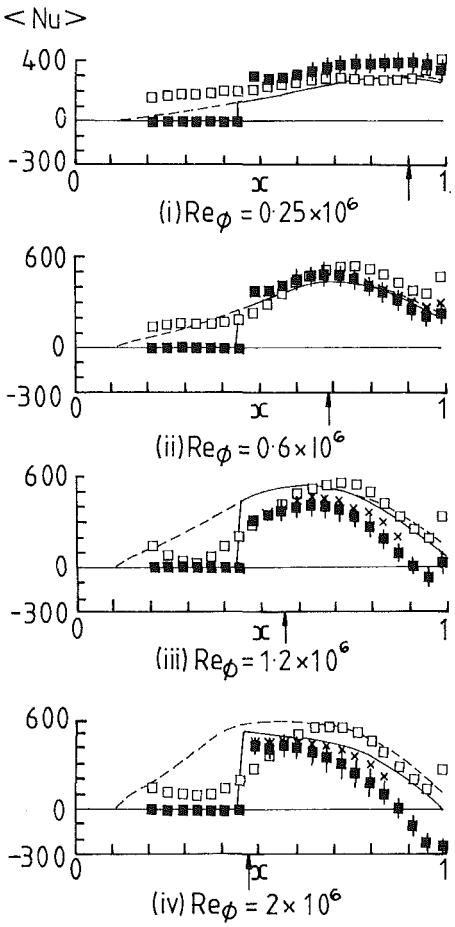

Fig. 9 Comparison between theoretical and experimental Nusselt numbers for C_w = 3500; experimental measurements: ■ disk with cob (× corrected values); □ plane disk; theoretical curves: —— disk with cob; --- plane disk; edge of source region: ↑; equation (4.4): —·—

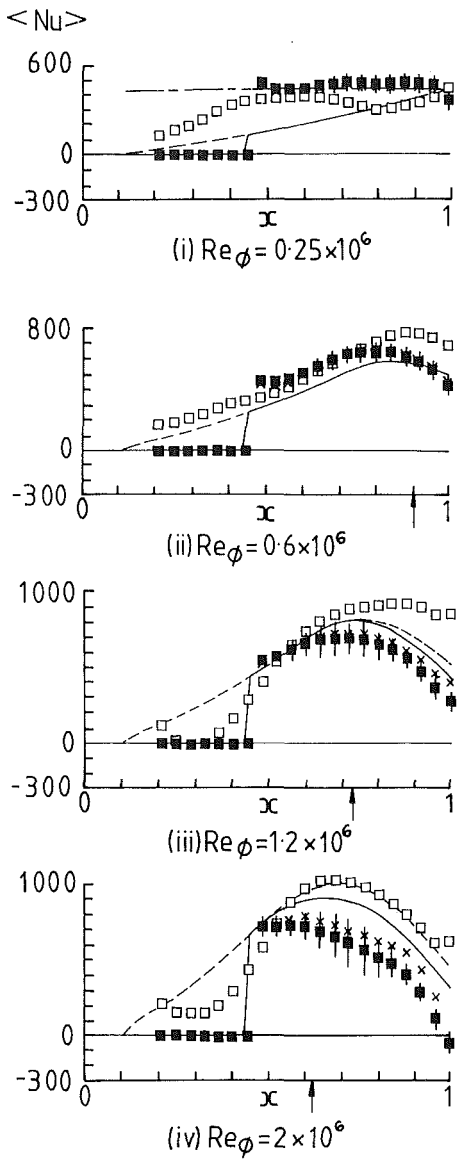

Fig. 10 Comparison between theoretical and experimental Nusselt numbers for C_w = 7000; see Fig. 9 for legend

of the disk decreases with increasing rotational Reynolds numbers. At the outer radii, where the measured Nusselt numbers are small, the ratio could be less than 0.1. Under these conditions, corrections were not possible.

It can be seen in Fig. 9 that the corrected Nusselt numbers are much closer to the theoretical curves than are the uncorrected values. It can also be seen that the maximum values of ⟨Nu⟩ occur, approximately, at the edge of the source region. For larger radii, where nonentraining Ekman layers are formed, the local fluid temperature approaches that of the disk and ⟨Nu⟩ is reduced; under some conditions, ⟨Nu⟩ can become negative.

Figure 10 shows the radial distribution of the Nusselt number for C_w = 7000. For this flow rate, the source region is, according to equation (3.2) with B = 1.79, expected to extend throughout the cavity for $Re_\phi < 0.4\times 10^6$. Under these conditions, Ekman-layer flow cannot occur and the wall-jet correlation [9] is more appropriate, such that

$$Nu = 1.46 C_w^{2/3} G^{1/6} \tag{4.4}$$

and, for C_w = 7000 and G = 0.267, Nu = 428. It can be seen in Fig. 10(*i*) for $Re_\phi = 0.25\times10^6$ that the experimental data are fitted better by equation (4.4) than by the integral theory. For $Re_\phi \geq 0.6\times10^6$, where Ekman layer flow occurs over part of the disk surface, the theoretical curves provide a reasonable approximation to the corrected data.

In Fig. 11, the variation of the local Nusselt numbers are shown for C_w = 14,000. For this flow rate, the source region is expected to extend throughout the cavity for $Re_\phi < 10^6$, and equation (4.4) is included in Figs. 11(*i*) and (*ii*) for $Re_\phi/10^6$ = 0.25 and 0.6. At the higher values of Re_ϕ in Figs. 11(*iii*) and (*iv*), Ekman-layer flow occurs over part of the disk surface. In Fig. 11(*iii*), the theoretical curves for the disk with the cob is in reasonable agreement with the corrected values of ⟨Nu⟩. However, in Fig. 11(*iv*), the differences between some of the corrected Nusselt numbers and the theoretical curves lie outside the 95 percent confidence interval.

It should be borne in mind that the corrections made to the experimentally measured Nusselt numbers for the disk with the cob were approximations based on a number of assumptions. It should also be remembered that the integral solutions took no account of the cob geometry. Although the agreement between the theory and experiments presented above was not good under all conditions, it is believed to be sufficiently close to justify the use of the integral equations for design purposes. Support for this assertion is provided in [11] where it was shown that comparatively crude approximations of the Nusselt numbers on an air-cooled rotating disk could, when used as boundary conditions for Fourier's equation, produce reasonable estimates of the disk temperature. Additional support will come from results, to be submitted for publication in the near future, that show good agreement between Nusselt numbers predicted from the integral equations and those

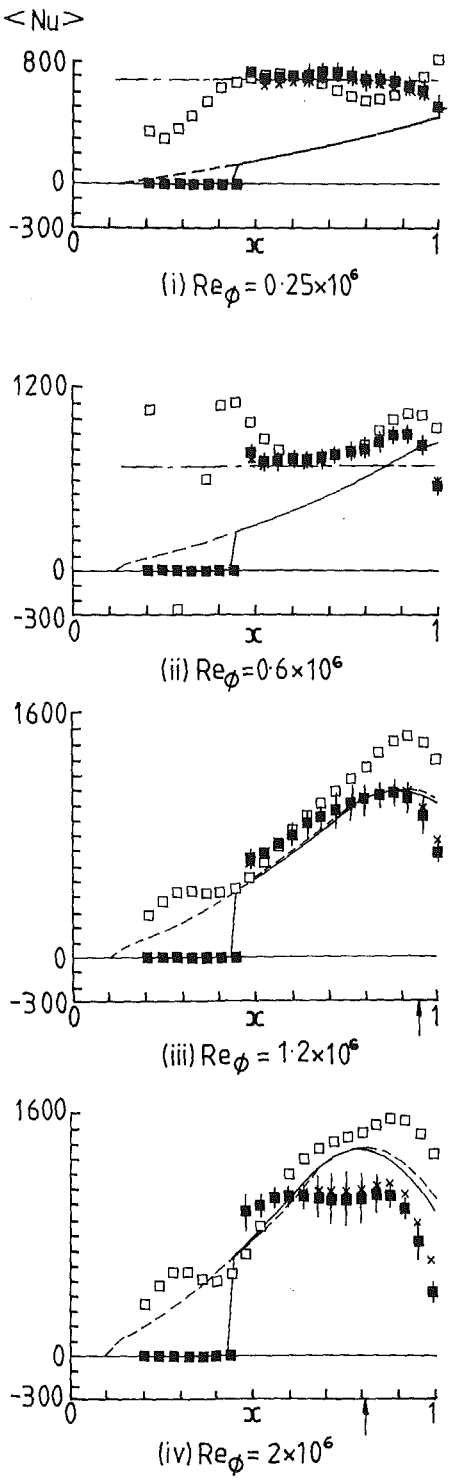

Fig. 11 Comparison between theoretical and experimental Nusselt numbers for C_w = 14,000; see Fig. 9 for legend

determined experimentally both from the conduction solution and from fluxmeters attached to the internally heated disks in a rotating cavity.

5 Conclusions

Flow visualization conducted for $440 \leq C_w \leq 1760$ and $0.16 \leq Re_\phi/10^6 \leq 1$ has shown that cobs have very little effect on the isothermal flow structure inside a rotating cavity with a radial outflow of air. As was previously observed for a cavity with plane disks, the flow structure comprises a source region, Ekman layers, sink layer, and an interior core. While the cobs appear to attenuate the wall-jet effect (where flow entering the cavity axially, through the upstream disk, impinges on the downstream disk forming a radial wallet), the size of the source region and the flow structure outside this region do not appear to be affected significantly by the cobs.

The Nusselt numbers measured on the heated downstream disk of the cavity, for $3500 \leq C_w \leq 14{,}000$ and $0.25 \leq Re_\phi/10^6 \leq 2$, have been compared with theoretical curves obtained from solutions of the turbulent integral boundary-layer equations. Providing the source region does not fill the entire cavity, the theoretical curves can provide a reasonable approximation to the measured Nusselt numbers. If the source region fills the cavity, an existing wall-jet correlation provides a reasonable fit to the measured values.

Acknowledgments

The authors are indebted to SERC, Rolls Royce plc, and GEC-Ruston Gas Turbines plc for funding the research described in this paper. We also wish to thank Dr. C. A. Long, Dr. J. R. Pincombe, and Dr. R. H. Rogers, together with the technicians who contributed to the project, for their invaluable assistance. In addition, we are grateful to the referee who pointed out the need for an error analysis!

References

1 Owen, J. M., "Fluid Flow and Heat Transfer in Rotating Disc Systems," in: *Heat and Mass Transfer in Rotating Machinery*, D. E. Metzger and N. H. Afgan, eds., Hemisphere, Washington, 1984, p. 81.

2 Hide, R., "On Source-Sink Flows in a Rotating Fluid," *J. Fluid Mech.*, Vol. 32, 1968, p. 737.

3 Bennetts, D. A., and Hocking, L. M., "On Nonlinear Ekman and Stewartson Layers in a Rotating Fluid," *Proceedings of the Royal Society of London*, Vol. A333, 1973, p. 469.

4 Bennetts, D. A., and Jackson, W. D. N., "Source-Sink Flow in a Rotating Annulus: A Combined Laboratory and Numerical Study," *J. Fluid Mech.*, Vol. 66, 1974, p. 689.

5 Owen, J. M., and Bilimoria, E. D., "Heat Transfer in Rotating Cylindrical Cavities," *J. Mech. Engng. Sci.*, Vol. 19, 1977, p. 175.

6 Owen, J. M., and Pincombe, J. R., "Velocity Measurements Inside a Rotating Cylindrical Cavity With a Radial Outflow of Fluid," *J. Fluid Mech.*, Vol. 99, 1980, p. 111.

7 Owen, J. M., and Onur, H. S., "Convective Heat Transfer in a Rotating Cylindrical Cavity," ASME JOURNAL OF ENGINEERING FOR POWER, Vol. 105, 1983, p. 265.

8 Chew, J. W., Owen, J. M. and Pincombe, J. R., "Numerical Predictions for Laminar Source-Sink Flow in a Rotating Cylindrical Cavity," *J. Fluid Mech.*, Vol. 143, 1984, p. 451.

9 Long, C. A., "Transient Heat Transfer in a Rotating Cylindrical Cavity," D. Phil. Thesis, University of Sussex, United Kingdom, 1984.

10 Chew, J. W., "Computation of a Convective Laminar Flow in Rotating Cavities," *J. Fluid Mech.*, Vol. 158, 1985, p. 339.

11 Long, C. A., and Owen, J. M., "Prediction of Transient Temperature for an Air-Cooled Rotating Disc," *AGARD CP390*, 1985, p. 21-1.

12 Owen, J. M., Pincombe, J. R., and Rogers, R. H., "Source-Sink Flow Inside a Rotating Cylindrical Cavity," *J. Fluid Mech.*, Vol. 155, 1985, p. 233.

13 Firouzian, M., Owen, J. M., Pincombe, J. R., and Rogers, R. H., "Fluid Dynamics and Heat Transfer in a Rotating Cylindrical Cavity With a Radial Inflow of Fluid. Part 1: The Flow Structure," *International Journal of Heat and Fluid Flow*, Vol. 6, 1985, p. 228.

14 Firouzian, M., Owen, J. M., Pincombe, J. R., and Rogers, R. H., "Fluid Dynamics and Heat Transfer in a Rotating Cylindrical Cavity With a Radial Inflow of Fluid. Part 2: Velocity, Pressure and Heat Transfer Measurements," *International Journal of Heat and Fluid Flow*, Vol. 7, 1986, p. 21.

15 Long, C. A., and Owen, J. M., "The Effect of Inlet Conditions on Heat Transfer in a Rotating Cavity With a Radial Outflow of Fluid," ASME *Journal of Turbomachinery*, Vol. 108, 1986, p. 145.

16 Long, C. A., and Owen, J. M., "Transient Analysis of Heat Transfer in a Rotating Cavity With a Radial Outflow of Fluid," *8th International Heat Transfer Conference*, San Francisco, CA, 1986, Paper No. JW-18.

17 Owen, J. M., "On the Computation of Heat Transfer Coefficients From Imperfect Temperature Measurements," *J. Mech. Eng. Sci.*, Vol. 21, 1979, p. 323.

18 Long, C. A., "The Effect of Thermocouple Disturbance Errors on the Measurement of Local Heat Transfer Coefficients," *Test and Transducer Conference*, Wembley, London, Vol. 3, 1985, p. 73.

19 Rogers, R. H., "Computation of Heat Transfer in a Rotating Cavity With a Radial Outflow of Fluid," Report No. 85/TFMRC/71, Thermo-Fluid Mechanics Research Centre, University of Sussex, England, 1985.

APPENDIX

Corrected Nusselt Numbers

As noted by Owen [17] and Long [18], solution of Fourier's conduction equation, using measured surface temperatures as boundary conditions, can give rise to significant errors in the subsequent computation of the Nusselt numbers. One particularly serious error is that caused by thermocouple bias: A thermocouple embedded in a slot in a metal surface can create a distortion of the local temperature distribution. In the present experiments, the thermocouples were cemented into slots in the steel disk and the ratio R_k of the effective thermal conductivity of the disk to that of the thermocouple and adhesive was estimated to be 33.

In [8] it is shown that the resulting error in the computed Nusselt numbers depends on R_k and on the ratio of the Biot numbers on the two faces of the disk (that is, on the ratio of the Nusselt numbers on the front and back faces). For example, for cooling tests conducted with $R_k = 33$ and $\mathrm{Nu}_f/\mathrm{Nu}_b = 0.1$, $\epsilon_h \doteq -0.65$ where

$$\epsilon_h = (\mathrm{Nu}_{f,e} - \mathrm{Nu}_f)/\mathrm{Nu}_f \tag{A1}$$

Nu_b and Nu_f are the true back-face and front-face Nusselt numbers, respectively, and $\mathrm{Nu}_{f,e}$ is the experimentally determined front-face value (obtained from the "conduction solution"). Thus, in this example, the "experimental value" significantly underestimates the true Nusselt number. For $\mathrm{Nu}_f/\mathrm{Nu}_b = 10$, $\epsilon_h \doteq 0.1$, and for $\mathrm{Nu}_f/\mathrm{Nu}_b = 1$, $\epsilon_h = 0$.

Using the results given for ϵ_h in [18], for $0.1 < \mathrm{Nu}_f/\mathrm{Nu}_b < 10$, approximate corrections were made to the Nusselt numbers presented in Section 4.2. The free disk value was assumed for Nu_b, and iteration was necessary to determine Nu_f; the iteration was started using the known ratio $\mathrm{Nu}_{f,e}/\mathrm{Nu}_b$. In Section 4.2, Nu is taken to refer to Nu_f.

F. Haaser

J. Jack

W. McGreehan

GE Aircraft Engines,
Cincinnati, OH 45215

Windage Rise and Flowpath Gas Ingestion in Turbine Rim Cavities

Typically cooling air must be metered into cavities bordering turbine disks to offset cavity air temperature rise due to windage generated by air drag from rotating and stationary surfaces and the ingestion of hot mainstream gas. Being able to estimate the minimum amount of cooling air required to purge turbine rim cavities accurately is important toward providing optimum turbine cycle performance and hardware durability. Presented is an overview of a method used to model windage rise and ingestion on a macroscopic scale. Comparisons of model results to engine test data are included.

Introduction

Modern aircraft jet engines may typically operate with mainstream gas temperatures exceeding 2500°F (1357°C) downstream of the combustor. Although turbine blades and vanes are designed to withstand these temperatures, current material rotor disks, blade retainers, and internal stationary support hardware cannot. Therefore, it is necessary at the interface of rotating-to-stationary turbine parts to provide sealing designs to restrict the ingestion of hot mainstream gas. Cooling air is usually injected into the cavities between the rotor and stator and cool the cavity positively, to reduce windage, and to lower or prevent hot mainstream ingestion (Fig. 1).

Benefits of Accurate Predictions

Being able to predict rim cavity temperatures accurately using analytical methods offers the cooling flow designer important benefits. The designer knows that too little flow results in hotter cavity temperatures and reduced parts life. Too much flow results in reduced engine performance. A balance can be achieved between engine performance and parts life by running an analytical model with varying amounts of cooling flow rates and estimating cavity temperatures. Full-scale engine test costs can be prohibitive. Predicting accurate rim temperatures can reduce the number of design iterations and subsequent tests required to achieve an optimum design.

A constant goal of new engine design is to lower fuel consumption. One manner by which to lower fuel consumption is to reduce the amount of cooling air required to cool turbine parts. Up to 20 percent or more of mainstream flow may be extracted and used for cooling in today's large aircraft turbofan engines. By modeling improved mainstream sealing configurations and reducing surface drag, the cooling flow designer can estimate how much less cooling flow is required. A reduction in rim cooling flow rates of 1 percent mainstream flow or more over previous generation designs may be possible.

A well-correlated model provides the designer with a tool to estimate the impact of safety and failure hazards. The impact of a cracked cooling supply pipe, worn seals, missing inspection plugs, loss of seal overlap, etc., can be estimated without requiring engine tests.

Lastly, being able accurately to predict the pressure distribution acting on the face of the rotating disk gives improved estimates of the axial thrust load acting on ball bearings.

Background

A significant body of literature exists on the study of flow due to a rotating surface. For the purposes of this paper, only a few landmark papers are referenced.

The study of viscous fluid flow due to rotating disks began historically with simple geometries, with subsequent studies adding the more complex effects related to turbine design. Initial studies of the steady-state motion of an incompressible viscous fluid on an infinite rotating plane in an infinite medium were reported by Von Karman [1]. For turbulent flow he obtained a solution using the momentum integral equations of the boundary layer.

Completely Enclosed Disk. Schultz-Grunow [2] added the effect of completely enclosing a right cylindrical disk in a housing (also termed casing or shroud). Schultz-Grunow assumed: All radial flow occurs within the boundary layer, with flow moving radially outward on the disk, away from the disk at the rim toward the wall, and radially inward on the stationary wall; fluid outside the boundary layer rotates as a solid body (core flow); and the torque acting on the disk is equal and opposite to the torque acting on the stationary wall. Major drawbacks to this solution are that it does not account for throughflow rate and the axial spacing between the disk and wall (endwall effects).

Wall Spacing, Flow Regimes. A major advance in wheel space flow theory was reported by Daily and Nece [3] who

Contributed by the Gas Turbine Division of THE AMERICAN SOCIETY OF MECHANICAL ENGINEERS and presented at the 32nd International Gas Turbine Conference and Exhibit, Anaheim, California, May 31–June 4, 1987. Manuscript received at ASME Headquarters February 17, 1987. Paper No. 87-GT-164.

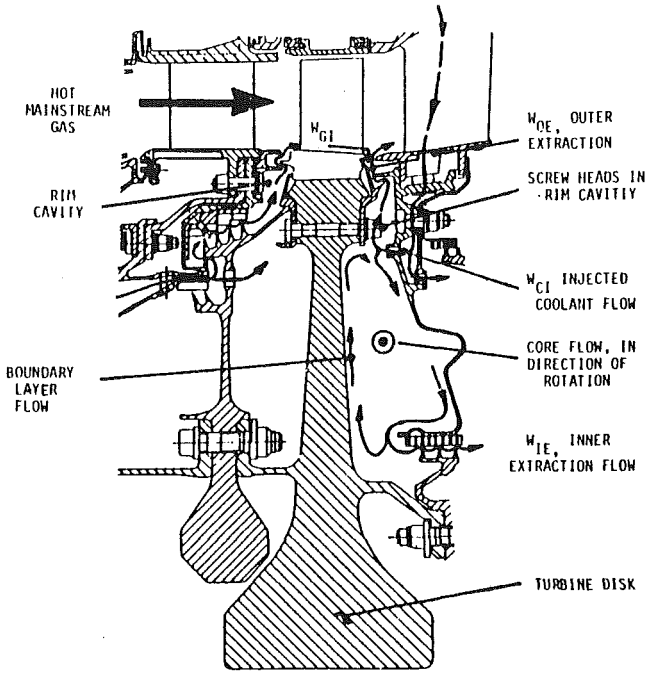

Fig. 1 Turbine wheel space cooling and cavity terminology (bolted retainer design)

studied the effect of wall spacing on disk torque. Axial wall spacing to disk radius ratios, s/a, from 0.0127 to 0.217 were studied for a full range of Reynolds number (10^3 to 10^7). Experimental disk friction data were taken and successfully compared to analytical theory. Daily and Nece proposed, for the first time, the existence of four possible wheel space flow regimes, namely:

(I) Laminar flow, rotor and casing boundary layers merged.
(II) Laminar flow, rotor and casing boundary layers separate.
(III) Turbulent flow, rotor and casing boundary layers merged.
(IV) Turbulent flow, rotor and casing boundary layers separate.

Regime (IV) is of interest to gas turbine cooling flow designers since it is the regime most often encountered in modern turbine engines.

Rim Inflow/Outflow. Maroti et al. [4] experimentally demonstrated that time-variant, periodic pie-shaped sectors of inflow and outflow can occur at the rim whenever the casing radius was greater than the disk radius. They were able to show: The inflow/outflow sectors rotate at a slower speed than the disk, the number of sectors increases with speed, number of sectors decreases with axial spacing, and flow reversals could be eliminated with sufficient radial throughflow. (Authors' note: For most turbine rim cavities, however, the casing radius is less than or equal to the disk radius. The observation of sectors of inflow/outflow into a wheelspace in this case may be due to dynamic pressure gradients at the rim due to main flowstream pressure wakes from blades and vanes, and due to nonconcentric rotor and casing radii resulting in a repeating sinusoidal rim seal clearance.)

Throughflow. In 1966 a detailed literature survey was conducted by corporate research summarizing wheel space literature with the purpose of finding out which factors would allow a reduction in wheel space coolant flow. It was concluded that the Schultz-Grunow method is valid for calculating disk torque, but is not valid for radial flow rate calculations, since an order-of-magnitude discrepancy in predicting radial inflow results. From the literature it was concluded that the boundary layers on the disk and casing are extensively affected by throughflow. For increasing radially outward throughflow, the following trends were noted:

1 Angular velocity of the core flow decreases (reduced vortex strength).
2 Thickness of boundary layers on the disk increases with radius.
3 Tangential boundary layer thickness on the stator is almost constant with radius, and insensitive to changes in throughflow rate.
4 Disk torque transmitted to the casing decreases while the angular momentum transmitted to the core fluid increases.

Axial Mainstream Flow. A series of corporate experiments was conducted wherein axial flow at the rim's periphery was included to simulate mainstream flow. A condensation nuclei counter was used to "sniff" wheel space air samples near the rim to detect the inflow of particle contamination from the mainstream. A sudden rise in particle count within the wheel space, as throughflow was reduced, indicated mainstream ingestion. The throughflow rate just prior to particle count increase is the critical flow rate. It was found that external axial flow over the rim resulted in a substantial increase in required critical flow. Reducing the rim's radial seal clearance reduced the critical flow, as expected; however the percent of critical flow reduction was less than the percent reduction in clearance. Multiple seals provided only a small reduction in ingestion over a single seal. Lastly, having the rotating member of the overlapping seal at a greater radius than the stationary

Nomenclature

a = disk radius, at outer seal
C_{FR} = rotor friction coefficient
C_{FS} = stator friction coefficient
C_{FL} = throughflow number, defined by $W_{CI}/a\mu$
C_p = specific heat of fluid
K = ratio of core to disk angular velocities
Re = rotational Reynolds number, defined by $\rho\omega a^2/\mu$
r = radius
s = rotor-to-stator axial distance
t = minimum rotor-stator gap at rim
M_R = torque acting on one side of rotor
M_{RB} = torque acting on rotor bolts
M_S = torque acting on stator and endwall
M_{SB} = torque acting on stator bolts
M_{IE} = torque lost to inner radius flow extraction
M_{OE} = torque lost to outer radius flow extraction
T_B = bulk coolant and ingestion core gas temperature
T_C = average core gas temperature
T_{CI} = injected coolant gas temperature
T_{GI} = gas ingestion gas temperature
T_W = core windage temperature rise
W_{CI} = injected coolant flow rate
W_{GI} = gas ingestion flow rate
W_{IE} = inner radius extraction flow rate
W_{OE} = outer radius extraction flow rate
β = core air angular velocitiy
μ = fluid viscosity
ρ = density of fluid (at radius a)
ω = disk angular velocity

member resulted in only a small improvement in sealing effectiveness.

Inward and Outward Throughflow With Swirl. The strong impact of throughflow on critical flow is corroborated by Dibelius et al. [5] who experimentally investigated the effects of: axial clearance, imposed air flow with and without swirl in both the centripetal (inward) and centrifugal (outward) directions, and screw heads mounted on the disk. Mainstream flow was not simulated. The impacts of these effects on velocity field, pressure distribution, axial thrust, and frictional torque were recorded and plotted.

Radially inward throughflow changed the core rotation from radially constant K to increasing K. Decreases in pressure accompanied the increasing K at smaller radius due to the acceleration (free vortexing) of the flow (Figs. 6, 8, and 9 [5]). For constant $\mathrm{Re} = 4.2 \times 10^6$, increasing amounts of inward flow with 12 deg swirl preserved and then reduced disk frictional torque. Increasing amounts of outward flow with 12 deg swirl initially preserved and then increased frictional torque (Figs. 14 and 15 [5]).

Effect of Screw Heads. Dibelius et al. [5] studied the effect of adding eight 0.78 in. (0.3 mm) high screwheads at a radius of 11.8 in. (20 mm) on a 15.7 in. radius disk. For $\mathrm{Re} = 4.2 \times 10^6$ the increase in friction drag increased by 40 percent for no throughflow and approximately 100 percent for large throughflow numbers.

Nonaxial Mainstream Flow. Elaborate rig testing to evaluate the impact of throughflow and various mainstream sealing designs has been reported by Abe et al. [6]. Right cylindrical disks and casings as well as disk and casing shapes with profiles more typical of turbine hardware were tested. The rig included the capability to simulate mainstream flow and used 27 nozzle vanes to turn the air 50 deg off axis centerline. Radially outward throughflow could be modulated from 0.5 to 3 percent of the mainstream flow rate and disk rotation could be varied from 0 to 6500 rpm. For a mainstream gas flow angle of 50 deg versus pure axial flow, the amount of mainstream ingestion was roughly doubled (Fig. 12 [6]). The explanation given for this increase was that the axial gap width relative to the mainstream flow is increased by the inverse of the cosine of the gas flow angle. Another possible explanation is that the presence of a mainstream tangential velocity component reduces the turning pressure loss required for mainstream air to pass through the wheel space seal (due to momentum carryover).

Measuring Ingestion by Trace Gas Dilution. Abe et al. [6] also evaluated how effective different rim sealing designs are in preventing mainstream ingestion. They introduced throughflow air with a known concentration of propane at the inner radius of a wheel space. Wheel space gas samples were drawn at various radii and axial penetrations into the core flow and analyzed by gas chromatography. The amount of propane dilution corresponded to the amount and penetration of mainstream ingestion into the wheel space. Test results demonstrated that the ingestion remained constant as long as the ratio of throughflow to mainstream flow remained constant.

Abe et al. found that even some overlap of rim seals provided resistance to ingestion; however, dramatic increases in ingestion were observed for no seal overlap. In all cases the ingestion was more heavily concentrated along the casing than along the disk confirming inflow along the stator and outflow along the disk. In general, seal fins were found to be more effective on the rotor than on the stator, which appeared to be a result of induced secondary flows underneath the rotor fin inhibiting inflow.

Modeling Wheel Space Cavities

A proprietary Fortran time-share program for modeling wheel space cavities was written in order to predict cavity windage temperature rise and amount, if any, of mainstream gas ingestion. Four cases of its satisfactory use by the authors are described below. The program performs a cavity angular momentum balance accounting for many of the factors that affect the net steady-state angular momentum. Balanced are those effects that increase angular momentum and hence core flow rotation, and those effects that decrease angular momentum thereby inhibiting core air rotation. For a steady-state solution to satisfy continuity:

$$\text{Angular momenta added} = \text{angular momenta subtracted} \quad (1)$$

where time-variant phenomena such as inflow/outflow at the rim are accounted for via mixing and extraction losses.

Sources of angular momentum addition include injected cooling air and ingestion flows where tangential velocities are coincident with the direction of wheel speed. Pumping by rotor surface drag, rotor bolt drag, and by other rotor surface imperfections, such as instrumentation wires, also increase angular momentum. Angular momentum subtraction is caused by loss of flow extracted at the cavity's inner and outer radii through seals or leakages, by stator surface and stator bolt drag, and by other stator surface imperfections.

Based on user-provided initial estimates of K and ingestion flow rate, the program calculates the angular momentum for each of the above factors. If continuity as shown in equation (1) is not satisfied, an iteration on K is conducted until the added and subtracted angular mementa are equal. Generalized expressions used within the program for the momentum factors and coefficients of friction for rotor and stator surfaces are shown in the appendix.

Rim and Gas Ingestion Flow Rates. The program solves for the outer extraction flow rate (W_{OE}) by treating the rim seal gap as an orifice. Since the flow mechanism through a rim seal is in reality extremely complex, a simplified approach was required that would respond reasonably well to changes in gap area and disk pumping rate. To determine W_{OE} a dummy or pseudopressure is calculated below the rim seal. This fictitious pressure, being greater than flowpath pressure, gives rise to flow through the rim seal in proportion to an effective area (AC_d) for the seal using the physical gap area (A) times a discharge factor (C_d). Typical values for C_d have been determined empirically by test and model correlation experience. Enhancements to model rim seal flow accurately using boundary layer theory are desirable; however, the results obtained to date have shown the simplified approach to be acceptable.

By mass flow continuity (terminology on Fig. 1)

$$W_{GI} + W_{CI} = W_{OE} + W_{IE} \quad (2)$$

where the injected coolant flow W_{CI}, and the inner extraction flow loss to seals W_{IE}, are input by the user as predetermined knowns. Once W_{OE} is calculated using the pseudopressure procedure described above, the only unknown in equation (2) is the ingestion flow rate W_{GI}, which can then be determined.

Windage Temperature Rise. The bulk temperature of the wheel space core flow is a flow-weighted mixing of injected coolant flow and mainstream ingestion flow

$$T_B = \frac{(T_{CI})(W_{CI}) + (T_{GI})(W_{GI})}{(W_{CI} + W_{GI})} \quad (3)$$

Once the rotor drag and rotor bolt drag is known by the resolution of K (Appendix I), the cavity temperature rise due to windage can be calculated

$$T_W = \frac{(M_R + M_{RB})}{(778)(C_p)(W_{GI} + W_{CI})} \quad (4)$$

The net wheel space core temperature is the sum of the bulk gas temperature of equation (3) and the windage rise from equation (4)

$$T_C = T_B + T_W \tag{5}$$

Heat Transfer. If the amount of heat transfer into or out of the wheel space cavity is large in comparison to the windage enthalpy increase, then this heat energy increment or decrement can be combined with equation (4). Typically in turbine rim cavities the disk rims are thick enough to prevent significant heat transfer in comparison to windage and gas ingestion heat addition. In disk web cavities, however, heat transfer gain or loss may be large enough to give errors in calculated core fluid temperature if ignored.

Model Results

Examples of measured results compared to model predictions are presented below for four different cases illustrating different aspects of modeling turbine rim cavities.

Case 1: Prediction of Critical Flow. A turbine aerospace performance rig test was run using the turbine configuration as shown in Fig. 2. In the interest of determining the critical throughflow rate for the rim cavity (as indicated on Fig. 2), the injected cooling flow was modulated from 0 to 2 percent of mainstream flow rate using slave test facility air. The temperature in the rim cavity was measured as a function of the amount of throughflow. Wheel space related parameters for the test were:

$t/a = 0.007$ (smaller of double overlap, est.)
$s/a = 0.029$
$\mathrm{Re} = 8.0 \times 10^6$
$0 < C_{FL} < 3.7 \times 10^4$

Based on cavity geometry and sealing clearances, it was predicted prior to testing that a critical flow of 0.8 percent of mainstream gas flow was required to prevent ingestion. Figure 3 shows measured temperature data as a function of the throughflow rate. As can be seen, the measured critical flow rate appeared near 0.85 percent of mainstream, as evidenced by the increase in temperature slope for flows less than 0.85 percent.

Case 2: Boltless Blade Retainer Design. Two different designs for high pressure turbine blade retainers are shown in Figs. 1 and 4. Current generation blade retainers (Fig. 1) use bolts to hold the retainer in place. One of the goals for a new generation turbine engine was to reduce the amount of cooling air required on the aft face of the disk in the region of the retainer. A boltless retainer (Fig. 4) was proposed as a means to reduce wheel space windage. In addition, the rim seal design was improved from a single overlap to a double overlap (as opposed to two single overlap seals). This reduced the effective area for ingestion thereby reducing the amount of air required to satisfy the critical flow rate. A test was run with parameters:

$t/a = 0.002$ (smaller of double overlap, est.)
$s/a = 0.041$
$\mathrm{Re} = 1.05 \times 10^7$
$C_{FL} = 4.7 \times 10^4$

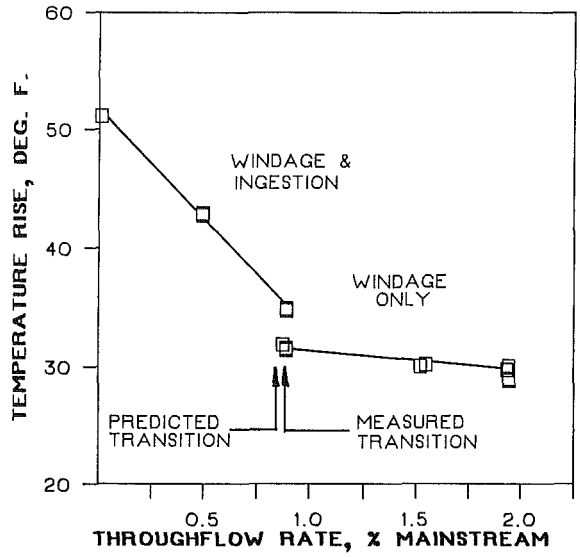

Fig. 3 Results of modulated rim cavity flow on turbine rig test (configuration as in Fig. 2)

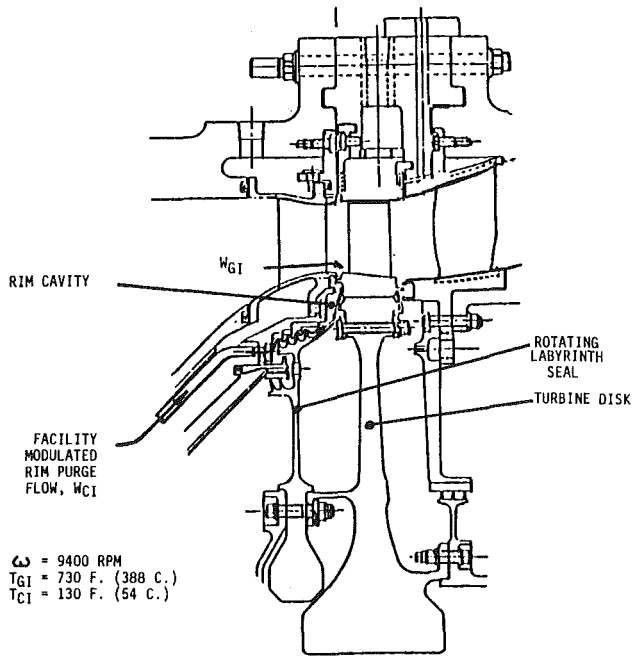

Fig. 2 Modulated rim cavity purge rate turbine rig test configuration

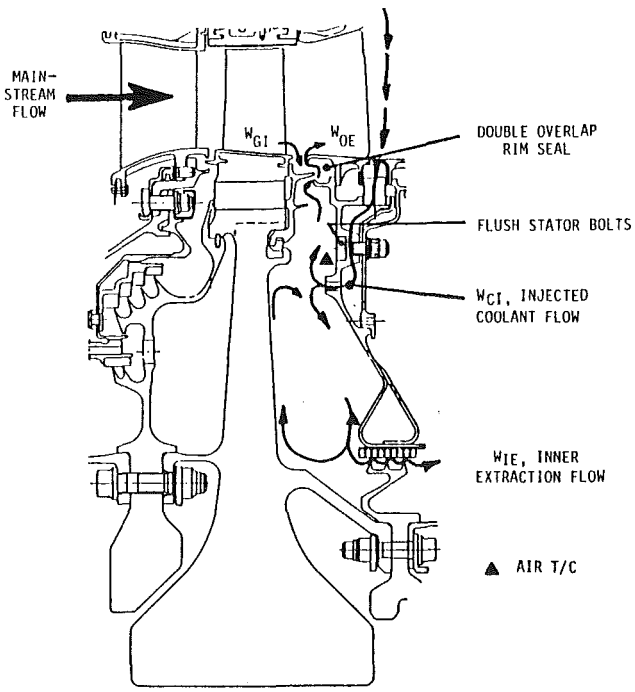

Fig. 4 Boltless blade retainer design

The coolant flow for this wheel space is injected 15 deg off the tangential axis into the cavity to provide a significant amount of angular momentum to reduce windage drag. Based on cavity geometry and a targeted rim flow of 0.7 percent of mainstream flow rate, it was predicted that a significant reduction in windage rise would occur.

Measured full-scale engine test results for the bolted and boltless designs are compared in Fig. 5 for varying disk speed. T_{CI} for this test was about 950°F (510°C) at high speed. The boltless retainer design measured a cavity windage rise 95°F (53°C) cooler than the bolted design. It is now possible, based on the encouraging results shown in Fig. 5, to use the rim model to analyze further reductions in the coolant flow for increased engine cycle performance.

Case 3: Impact of Instrumentation Wire. A high-pressure turbine (HPT) configuration, as shown in Fig. 4, was assembled into a rig to measure turbine temperatures and efficiency. A large amount of thermocouple leadout wire was attached to the face of the disk within the wheel space. Of concern was the amount of increased windage drag that would occur due to the presence of these wires. The wire tangential spacing (pitch) was large enough to expect that tangential drag would act on each wire without shielding by upstream wires.

A rim and web cavity model was generated to estimate the amount of expected windage rise. The wire drag area was integrated and treated as a rotor bolt using an average radius as the moment arm. An equivalent "bolt" drag area of 17 in.^{2} (110 cm^2) was input into the model for the instrumentation drag area, compared to a typical rim bolt area input of 4.3 in.^{2} (28 cm^2).

The rim to inner seal model predicted a +256°F (142°C) windage rise at 14,573 rpm. Actual measurements at 14,516 rpm indicated a windage rise of +226°F (126°C) in the rim area, but only +97°F (54°C) near the inner seal. For case 3, the authors recognize that the modeling technique was being used to generate a rough estimate of windage. The test data clearly indicates that a modeling technique that predicts only one gross temperature rise cannot match two different measured temperature values. An alternate solution would be to model two cavities with a common set of bordering boundary conditions.

Case 4: Modulated Throughflow Test. HPT blade retainer distress on one engine model resulted in a full-scale engine test to modulate the throughflow in the retainer cavity. Figure 6 shows how flow modulation was accomplished. Turbine cooling air normally directed to the wheel space was bled overboard through a pipe threaded into a borescope port (ports that allow fiber optic viewing of the turbine without engine teardown). It was possible to reduce the amount of air injected into the rim cavity by varying the amount of cooling air bled overboard. The reduction in system coolant flow dropped the pressure source of the injection holes thereby reducing both the flow rate and injection velocity. Wheel space related parameters for the test were:

$t/a = 0.006$–0.011 (est.)
$s/a = 0.048$
$\mathrm{Re} = 6.3 \times 10^6$
$3.1 \times 10^4 < C_{FL} < 4.1 \times 10^4$

Rim cavity temperature rise data from the modulation test (engine A data) as well as data from subsequent higher flow

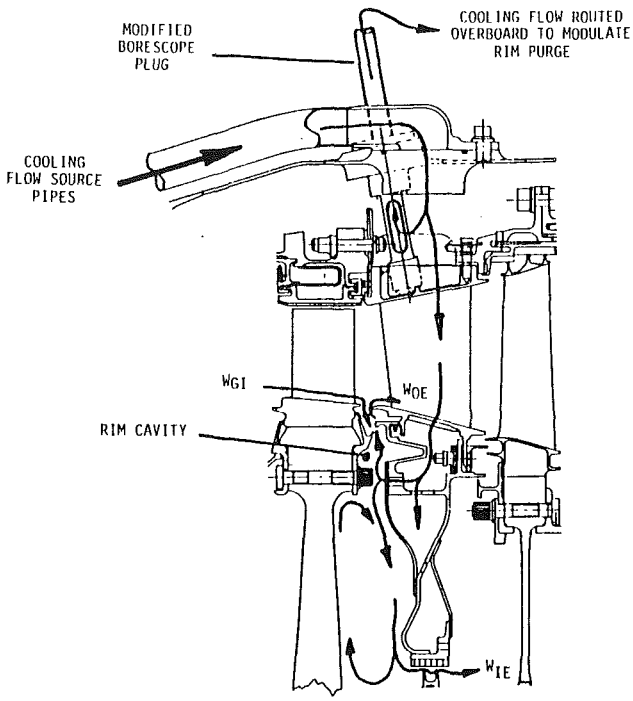

Fig. 6 Modulated rim purge rate flow test to study rim cavity temperatures as a function of throughflow rate

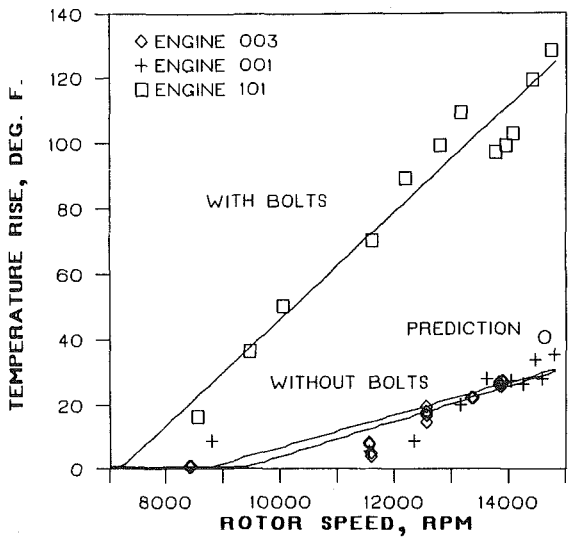

Fig. 5 Comparison of rim cavity temperature rise from coolant temperature for bolted and boltless designs

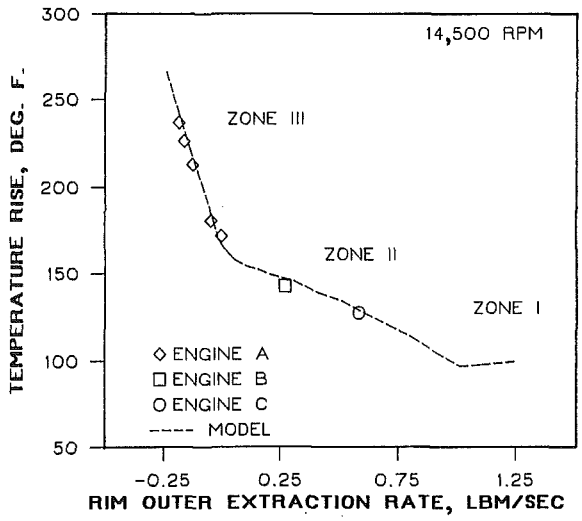

Fig. 7 Results of modulated rim purge flow test to study effect of rim purge variation on retainer cavity temperature

engines are shown on Fig. 7. A wheel space model of the rim cavity was correlated to test data after considerable effort.

When the model is run for a wide range of throughflow, it becomes clear that three zones of temperature rise may occur. The wheel space temperature rise for throughflows exceeding the critical flow rate is found to be due to windage only (Zone I). For throughflows lower than the critical flow rate, ingestion begins and the temperature rise is found to be the addition of windage rise and mainstream ingestion (Zone II). Note that for Zone II the rim cavity still experiences a net outflow. When the coolant flow injected into the wheel space cavity is insufficient to supply inner seal extractions, then a net rim inflow occurs resulting in much sharper temperature rise due to the much hotter mainstream temperature (Zone III). It is obvious that wheel space temperatures for cavities operating within Zone III are much more sensitive to injection flow rate variation.

Parametric Studies

The effect of a boltless retainer on rim cavity temperature rise was discussed in case 2. Since the rim modeling program gave excellent agreement to test data and since the model is felt to model rim cavity phenomena adequately, the authors thought it would be of interest to vary some of the key parameters in the model to illustrate their impact on ingestion rate and/or windage rise. For the case 2 baseline configuration model, the following four parameters were varied:

	Shown on
Rotor bolt area added and varied	Fig. 8
Injected coolant velocity varied	Fig. 9
Cavity inner flow extraction varied	Fig. 10
Injected coolant flow rate varied for constant inner extraction flow rate	Fig. 11

Figure 8 shows that a significant increase in windage rise occurs when rotor bolts are added. As the drag area increases the K factor also increases, however, at a decreasing rate. It is interesting to note that for a bolt drag area of 4.3 in.^{2} (28 cm^2) that the "boltless" retainer design approaches the same rim temperature rise as noted for the bolted design (Fig. 5).

Figure 9 shows, for constant injection flow rate, that bolt windage can be partially counteracted by increasing the tangential injection velocity. Figure 9 also shows that adding a typical ring of stator bolts (assuming 1/3 drag area of rotor bolts) has only a small windage impact. The same stator bolts in conjunction with the rotor bolts, however, cause a significant increase in windage rise illustrating the interaction be-

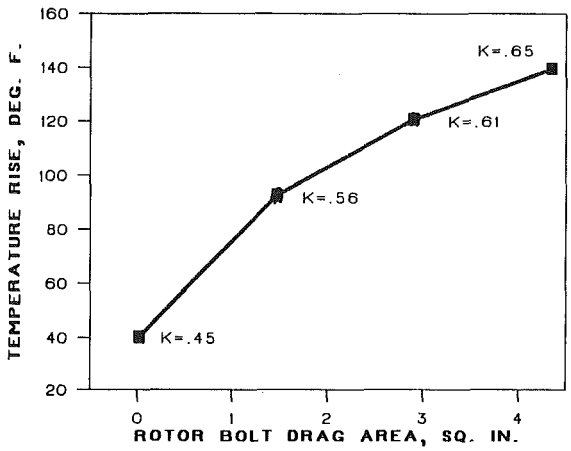

Fig. 8 Parametric effect on varying rotor bolt area on rim cavity temperature (configuration as shown on Fig. 4)

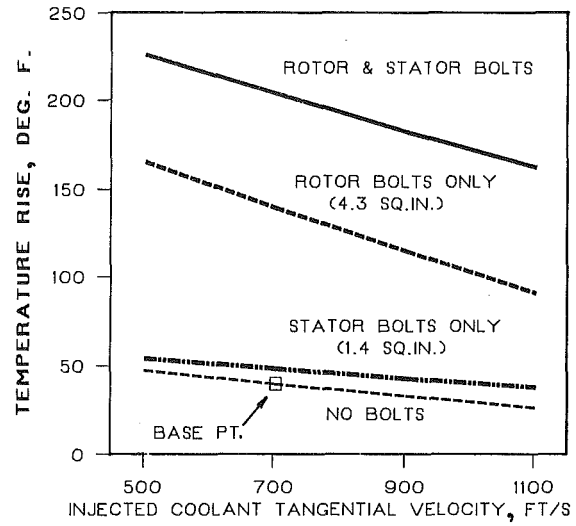

Fig. 9 Parametric effects on varying coolant injection tangential velocity and rotor/stator bolts on rim temperature (configuration as shown on Fig. 4)

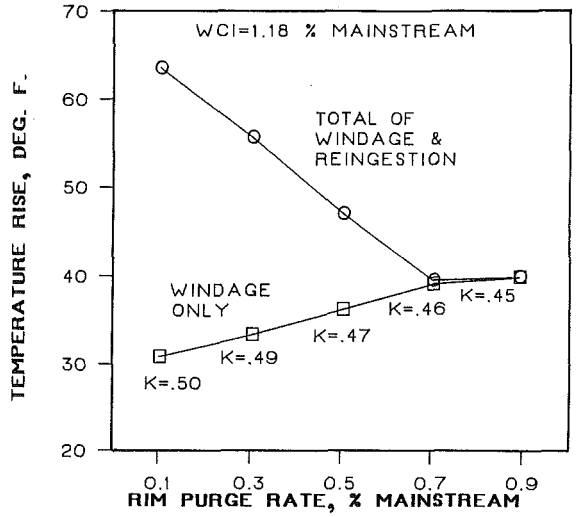

Fig. 10 Parametric effect of varying rim cavity inner flow extraction on rim cavity temperature (configuration as shown on Fig. 4)

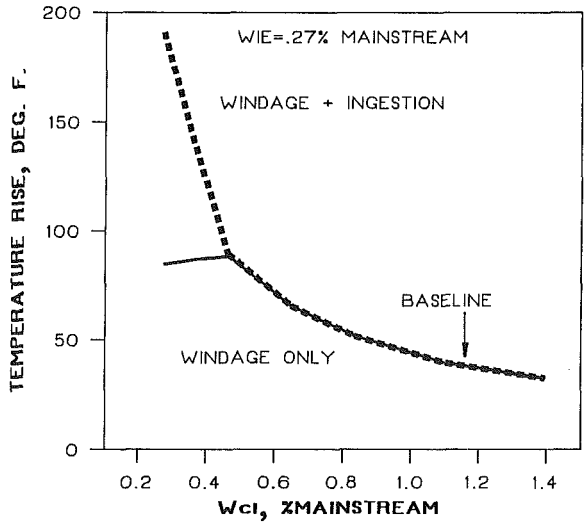

Fig. 11 Parametric effect of varying injection flow rate at constant velocity and constant inner extraction flow rate (configuration as shown on Fig. 4)

tween the two sets of bolts. That is, the windage caused by the stator bolts is compounded by the rotor bolts.

Figure 10 shows a parametric study for a constant 1.18 percent mainstream coolant injection with the inner extraction flow (W_{IE}) varied. Since the injected cooling flow is constant, increases in W_{IE} result in decreases in the rim's outer extraction flow (W_{OE}). Only windage occurs in the rim cavity as long as W_{IE} does not reduce W_{OE} below the critical flow rate (about 0.7 percent mainstream). When W_{OE} is less than 0.7 percent mainstream, ingestion occurs resulting in a sharp increase in rim cavity temperature.

A similar parametric study is shown in Fig. 11. In this case the inner extraction flow W_{IE} was kept constant at 0.27 percent mainstream while the injection flow rate was varied from about 0.2 to 1.4 percent of mainstream flow rate. The injection velocity was maintained constant. For this case the critical throughflow rate drops from 0.7 percent to only 0.45 percent of mainstream. The reduction in throughflow rate results in a higher value of K.

Summary and Conclusions

Although it is currently not possible to model turbulent flow within a wheel space cavity on a microscopic scale accurately, the authors have been able to model wheel space cavities on a macroscopic basis successfully using conservation of angular momenta. In order to generate accurate models, the effects of inner and outer flow extraction, rotor and stator drag, rotor and stator bolt drag, leakages, and injection momentum must all be accounted for in a wheel space model. The s/a relationship researched by Daily and Nece [3] has been accounted for in the current modeling technique by adding endwall drag as part of the stator wall drag and by accounting for ingestion mixing losses.

The initiation of hot mainstream ingestion has been experimentally measured on full-scale engine and rig tests. Cavity temperature measurements showing a marked increase in wheel space temperature for small reductions in throughflow have demonstrated the critical throughflow rate. The effect of rotor bolts has been experimentally shown to be one of the strongest causes of windage rise, in agreement with Dibelius et al. [5]. The importance of wheel space rim sealing is paramount to reducing mainstream ingestion with minimum throughflows, in agreement with the experiments of Abe et al. [6]. For new turbine designs the authors recommend double overlap seal designs (Fig. 4) as opposed to single overlap designs (Fig. 1) or twin single overlap seals.

An end goal for cooling flow designers is to be able more accurately to predict required rim cavity temperatures and flow rates in order to optimize engine performance. Full-scale engine as well as rig test data have been correlated by the authors in reasonably good agreement with model predictions. The correlated models have allowed the authors to recommend hardware and cooling changes to optimize wheel space cavities.

The authors recognize a need for improved modeling techniques for understanding flows and momenta balance within rim cavities. Ongoing use of the current method should help refine the macroscopic approach; however, it is expected that the next advancement will be development of a true three dimensional code requiring solution on a supercomputer. The authors are not currently involved in developing such a code.

Acknowledgments

The work reported in this paper has been funded by GE Aircraft Engines, Cincinnati, OH where the three authors are currently employed in the analysis of secondary air (cooling) systems for turbofan engines in the 20,000 to 30,000 lbf (8.9×10^4 to 13.3×10^4 N) thrust class range. The authors would like to extend credit to H. P. Rieck and R. W. Brown, also of GE, for their derivation of the wheel space modeling computer program, without which the results reported in this paper could not have been correlated.

References

1 Von Karman, T. H., "Uber laminare und turbulente Reibung (On Laminar and Turbulent Friction)," *Zeitschrift für Angewandte Mathematik*, Vol. 1, 1921 (as NACA TM 1092, Sept. 1946), p. 233.

2 Schultz-Grunow, F., "Der Reibungswiderstand rotierender Scheiben in Gehausen," *Zeitschrift für Angewandte Mathematik und Mechanik*, Vol. 15, 1935, pp. 191–204.

3 Daily, J. W., and Nece, R. E., "Chamber Dimension Effects on Induced Flow and Frictional Resistance of Enclosed Rotating Disks," ASME *J. of Basic Eng.*, Vol. 82, 1960, pp. 217–232.

4 Maroti, L. A., Deak, G., and Kreith, F., "Flow Phenomena of Partially Enclosed Rotating Disks," ASME *J. of Basic Eng.*, Vol. 82, 1960, pp. 539–552.

5 Dibelius, G., Radke, F., and Ziemann, M., "Experiments on Friction, Velocity and Pressure Distribution of Rotating Discs," *Heat and Mass Transfer in Rotating Machinery*, XIV International Centre for Heat and Mass Transfer Symposium, Aug. 30–Sept. 3, 1982.

6 Abe, T., Kikuchi, J., and Takeuchi, H., "An Investigation and Observation of Hot Gas Flow into a Wheel Space)," 13th International Congress on Combustion Engines, May 10, 1979.

7 Hoerner, S. F., "Fluid-Dynamic Drag, Theoretical, Experimental and Statistical Information," 1965, book available through author.

APPENDIX

Wheel Space Modeling Equations

The Fortran time-share program performs a cavity angular momentum balance taking into account those effects that increase or decrease angular momentum.

Effects Increasing Angular Momentum and K

- Rotor surface drag (disk pumping)
- Rotor screw head drag
- Coolant injected with tangential velocity same direction as rotor spin
- Ingestion flow with tangential velocity same direction as rotor spin
- Drag due to rotor surface imperfections such as instrumentation wires

Effects Decreasing Angular Momentum and K

- Coolant injected axially or in tangential direction opposite to rotor spin
- Inner radius flow extraction
- Stator surface drag
- Stator screw head drag
- Outer radius flow extraction and miscellaneous leakages
- Drag due to stator surface imperfections such as instrumentation wires

Rotor Surface Drag. For disk surface drag Daily and Nece [3] derived

$$M_R = (C_M)(0.5\rho\omega^2 a^5) \tag{6}$$

where C_M is the moment coefficient and equation (6) is for both faces of the disk. Equation (6) was converted to the more generalized form

$$M_R = (C_{FR}/g)\left(0.5\rho\omega^2 a^2 \int rds\right) \tag{7}$$

where C_{FR} is the rotor surface friction coefficient, and the integral is the sum of moment-weighted rotor surface drag areas for only the side of the disk of interest. Through test experience, and the experimental data of Daily and Nece [3], C_{FR} is taken as

$$C_{FR} = 0.042(1-K)^{1.35}/\mathrm{Re}^{0.2} \tag{8}$$

with the Reynolds number modified as

$$\mathrm{Re} = \rho\omega a(a - R_I)/\mu \tag{9}$$

where a and R_I are the cavity's outer and inner radius, respectively.

Rotor Bolt Drag. The pumping action due to rotor screw heads follows from classic theory using a velocity-squared relationship

$$M_{RB} = (A_{RB})(R_{RB})^3(\rho\omega^2/2g)(1-K)^2 \tag{10}$$

where A_{RB} is the effective screw head projected area and R_{RB} the screw radius. Screw head pitch, that is spacing compared to head diameter, determines whether or not core air trips over each screw head or whether the preceeding head shields the next head. For estimates of drag coefficient and impact of pitch see Hoerner [7]. Instrumentation wire attached to the side of a disk can be treated as an equivalent screw head.

Coolant Injection Flow. The angular momentum addition or subtraction caused by throughflow injection is taken as fluid mass times its tangential velocity, V_{CI}, times moment arm, R_{CI}

$$M_{CI} = (W_{CI})(V_{CI})(R_{CI})/g \tag{11}$$

where a positive injection velocity is one in the direction of rotor spin.

Ingestion Flow. The amount of mainstream ingestion flow into a wheel space depends on the disk pumping flow requirement and effectiveness of rim sealing. As long as the injected coolant flow rate exceeds the critical throughflow rate, no ingestion occurs. The angular momentum change is taken as positive if ingestion flows enter with a tangential velocity component V_{GI} in the direction of rotor spin

$$M_{GI} = (W_{GI})(V_{GI})(R_{GI})/g \tag{12}$$

where R_{GI} is the ingestion radius.

Inner Extraction Flow. The loss of angular momentum to inner extraction flow is the flow rate times its velocity (assumed at core rotation) times inner extraction radius R_{IE}

$$M_{IE} = (W_{IE})(K\omega R_{IE})(R_{IE})/g \tag{13}$$

Outer Extraction Flow. Similarly, for outer extraction angular momentum loss at R_{OE}

$$M_{OE} = (W_{OE})(K\omega R_{OE})(R_{OE})/g \tag{14}$$

Stator Surface Drag. For loss of angular momentum due to stator surface drag, Rieck uses the generalized form

$$M_S = (C_{FS}/g)\left(0.5\rho\omega^2 a^2 \int rds\right) \tag{15}$$

where through the experimental data of Daily and Nece [3] and test experience the stator coefficient of friction is taken as

$$C_{FS} = 0.063(K)^{1.87}/\mathrm{Re}^{0.2} \tag{16}$$

with Reynolds number as in equation (9). The integral in equation (15) includes the endwall static surface area thereby accounting for (s/a) drag as discussed by Daily and Nece.

Stator Screw Head Drag. Similar as for rotor screw heads, but at velocity proportional to K

$$M_{SB} = (A_{SB})(R_{SB})^3(\rho\omega^2/2g)K^2 \tag{17}$$

where A_{SB} and R_{SB} are stator bolt area and radius, respectively. Stator surface instrumentation can be treated as an equivalent screw head.

Solution for Core Rotation, K. By continuity of angular momentum (equation (1)), there is one value of K such that the sum of added angular momentum is equivalent to the sum of subtracted angular momentum. Simplifying the eight angular momentum equations above reveals:

$$\begin{aligned}
M_R &= \text{const} \times (1-K)^{1.35} \\
M_{RB} &= \text{const} \times (1-K)^2 \\
M_{CI} &= \text{const} \\
M_{GI} &= \text{const} \\
M_{IE} &= \text{const} \times (K) \\
M_{OE} &= \text{const} \times (K) \\
M_S &= \text{const} \times (K)^{1.87} \\
M_{SB} &= \text{const} \times (K)^2
\end{aligned}$$

By simple process of iteration on K, the solution for angular momentum balance is achieved. Accordingly, resolution of K also solves the "steady-state" values for each of the six angular momentum equations.

Experiments on Spray Interactions in the Wake of a Bluff Body

R. C. Rudoff

M. J. Houser

W. D. Bachalo

Aerometrics, Inc.
Mountain View, CA 94042

The dynamics of spray drop interaction within the turbulent wake of a bluff body were investigated using the Aerometrics Phase Doppler Particle Analyzer, which determines both drop size and velocity. Detailed measurements obtained included spray drop size, axial and radial velocity, angle of trajectory, and size-velocity correlations. The gas-phase flow field was also ascertained via the behavior of the smallest drops. Results showed dramatic differences in drop behavior when interacting with turbulence for the various size classes. Small drops were recirculated in a pair of toroidal vortices located behind the bluff body, whereas the larger drops followed the general direction of the spray cone angle. This was documented via backlit photography. Local changes in number density were produced as a result of lateral convection and streamwise accelerations and decelerations of various drop size classes. The spray field interaction illustrated by these data effectively reveals the complexity associated with the development of the spray and casts some doubts toward attempting to describe sprays via simple integral quantities such as the Sauter mean diameter.

Introduction

Practical gas turbine combustion may be characterized as a complex two-phase flow in which atomized fuel interacts with a turbulent, recirculating airflow field. Detailed experimental measurements of spray interactions with turbulent flows and combustion are necessary to assist the development and understanding of these complicated flow fields. In particular, the advent of analytical models has created a need for an accurate data base of experimental measurements of turbulent two-phase flow interactions. The data necessary to guide and validate the computational models must include spatially resolved simultaneous measurements of droplet size and velocity. Data are especially required at points close to the injector and within the spray sheet where high drop number densities create additional demands on the measuring instrument.

To date, spray measurements have been performed largely in quiescent environments. Even in this case, and even with simple pressure atomizers, it is well documented that spray formation and interaction are strongly complicated by the entrainment and inflow of surrounding air, relaxation behavior of various size classes, drop–drop interaction, and coalescence (Bachalo and Houser, 1985; Solomon et al., 1984; Chin et al., 1986; Rizk and Lefebvre, 1985). When the complexity of continuous phase turbulence and recirculation are added, the flow behavior becomes even more involved and difficult to elucidate.

The instrumentation used in most earlier studies has hampered the measurements made in two-phase flows. Size and velocity data have been determined by the tedious means of double pulse imaging (Tishkoff, 1982) or by means of hybrid light scatter and laser-Doppler velocimetry instruments (LDV) (Yule et al., 1977). The double pulse technique also suffers from errors introduced by the difficulty in correcting for depth of field biasing. LDV measurements of gas phase velocity do not allow size discrimination and hence, suffer from contamination of the gas-phase velocities by droplets. In addition, previous light scatter detection techniques have not proven to be suitable in the very dense sprays that often occur in practical environments.

The phase Doppler method based upon light scattering interferometry provides a means for obtaining these difficult measurements (Bachalo, 1980; Bachalo and Houser, 1984). The method has been compared to other methods (Jackson and Samuelsen, 1985) and has proven reliable. It has been applied to both cold and burning environments. For cold sprays in a quiescent environment, Bachalo and Houser (1986) showed that the phase-Doppler measured mass flux was in good agreement with physically measured mass flux. Recent work has included the determination of drop size, axial and radial velocity along with size-velocity correlations and angles of trajectory for individual size classes. Testing has been performed on sprays in both quiescent (Bachalo et al., 1986) and flow fields (Bachalo and Rudoff, 1986) with coflowing boundary conditions.

In this study, the interaction of a spray produced by a pressure atomizer with the turbulent wake flow field of a bluff body were considered. The parameters obtained included drop size and axial and radial velocity, as well as size-velocity correlations and angles of trajectory by size class throughout the wake flow. The gas-phase parameters were considered to be determined by the behavior of the smallest drops. These data will serve to: (1) enhance the understanding of the complex behavior of spray interactions with turbulence, and (2) provide a valuable data base to further the development and validation of computational codes.

Contributed by the Gas Turbine Division of THE AMERICAN SOCIETY OF MECHANICAL ENGINEERS and presented at the 32nd International Gas Turbine Conference and Exhibit, Anaheim, California, May 31–June 4, 1987. Manuscript received at ASME Headquarters February 4, 1987. Paper No. 87-GT-48.

Experimental Approach

Two-Phase Flow Tunnel. The two-phase flow tunnel (2-PFT) (Fig. 1) was designed to allow testing of a wide variety of sprays in a well-defined, turbulent environment. The 2-PFT is capable of air flow speeds up to 40 m/s. The design of the tunnel was based upon references such as Mehta (1977) and Bradshaw and Pankhurst (1964). Further details of the 2-PFT and its various elements may be found in Bachalo and Rudoff (1986).

The test section consists of a 38 cm × 38 cm square cross section that is 1.82 m in length. Clear acrylic walls allow optical access for instrumentation and visualization. Laser velocimetry measurements of the test section indicated that the effect of the settling chamber's honeycomb and screens yielded excellent flow uniformity and a free-stream turbulence of approximately 2 percent.

The support for the bluff body is shown in Fig. 2(*a*), with a detail of the bluff body depicted in Fig. 2(*b*). The bluff body created the complex large-scale eddies whose interaction with the spray was the focus of the study. The bluff body was 15 cm long and 5 cm in diameter. The downstream face was flat and the nozzle orifice protruded 0.5 cm. Note that the support and the upstream end of the bluff body were designed to create minimal disturbances to the free-stream flow field.

The tested nozzle was a Hago 3.00 45 deg H swirl chamber pressure atomizer. For this series of tests, the atomizer was operated at 415 kPa with a corresponding flow rate of 0.19 ml/min and a nominal spray angle of 45 deg. Water was supplied to the atomizer at 21 deg C and the fluid pressure at the atomizer was monitored continuously. All data were collected with a free-stream air velocity of 20.9 m/s.

The Phase Doppler Particle Analyzer (PDPA), described in the following section, was utilized to measure drop size and both axial and radial velocity. The PDPA was mounted on a three-dimensional orthogonal traverse system that allowed positioning the probe volume to within 0.05 cm anywhere within the spray field. Measurements were performed for a matrix consisting of axial locations (x) 1, 2, 3, 4, 5, 7.5, and 10 cm downstream of the nozzle orifice. The radial points in the measurement matrix (r) were from centerline to the outermost extent of the spray at 0.5 cm intervals.

Phase Doppler Particle Analyzer. The Phase Doppler Particle Analyzer (PDPA) produced by Aerometrics, Inc., was used in these experiments (Bachalo, 1980; Bachalo and Houser, 1984). This instrument is similar to a conventional LDV except that three detectors are used in the receiver. Since all of the detectors are located behind a common aperture, the system operation remains the same as for an LDV (Fig. 3).

As with the LDV, when a particle or drop passes through the intersection of two laser beams, the scattered light forms an interference fringe pattern that appears to move at the Doppler difference frequency. This temporal frequency is a function of the beam intersection angle, light wavelength, and the velocity of the particle. The spatial frequency of the scattered interference fringe pattern is dependent upon the angle of observation, particle index of refraction, beam intersection angle, laser wavelength, and particle diameter. The spatial frequency of the scattered fringe pattern is measured using three detectors. Each detector produces a similar Doppler burst signal but with a phase shift between them. The phase shift is proportional to the detector spacing and drop size. Three detectors are required to ensure that measurement ambiguity does not occur. They also serve to cover a drop size range over a factor of 100 at a single optical setting.

Although a size range of 100:1 is possible, the actual dynamic range is limited by the signal amplitude range. Particles larger than 5 μm scatter light in proportion to their diameter squared. Thus, a size range of 35:1 requires an amplitude range of approximately 1000:1. This was considered a practical limit on the signal-to-noise for most applications.

With simple changes to the optics, the overall size range of the method is 0.5 to 3000 or greater provided that the drops remain spherical. Extensive testing of the method has been carried out. These tests included the measurement of monodisperse drop streams and the comparison of spray measurements to results obtained by other methods. With the use of highly focused beams and off-axis scatter detection, these measurements have been made with high spatial resolution and in high particle number density environments.

Since both the drop size and velocity are measured simultaneously, the method provides a complete description of the spray drop size distribution including both the spatial

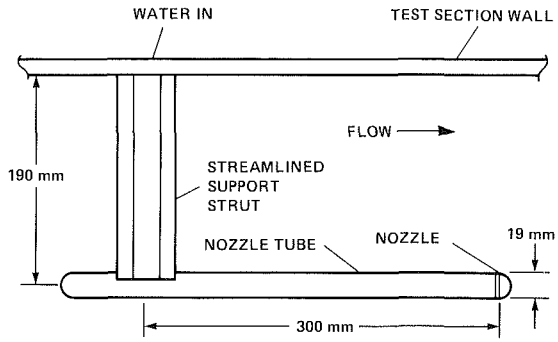

Fig. 2(*a*) Nozzle support

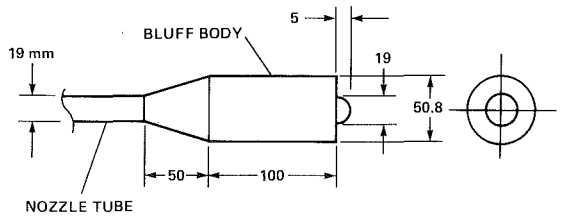

Fig. 2(*b*) Bluff body detail

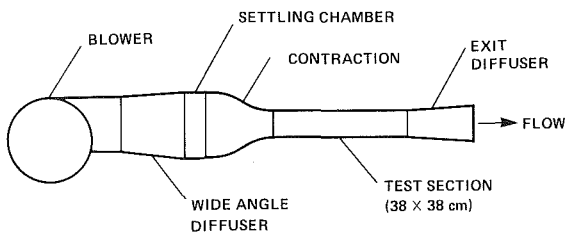

Fig. 1 Schematic of two-phase flow tunnel

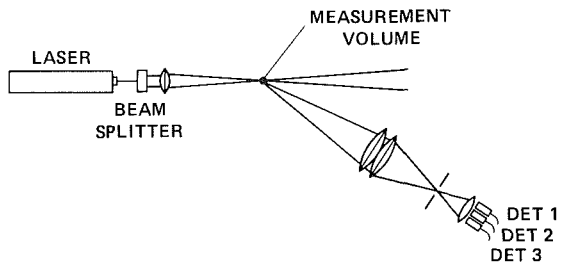

Fig. 3 Optical schematic for the Phase Doppler Particle Analyzer

and temporal distributions. Unlike the scattering intensity measurement techniques, the results are unaffected by beam attenuations or slight misalignment due to beam deflections.

The instrument was interfaced to an IBM PC/AT computer. Data acquisition and transfer to computer memory requires 20 μs per particle. Several tests were performed on each set of signals before they were accepted as a valid measurement. Histograms of the drop size and velocity distributions were displayed on the video monitor while data was acquired. The data were normalized to account for the change in sample volume with drop size before computing the mean values. The size, velocity, and time-of-arrival of each drop were stored for later statistical analyses.

In order to handle a wide velocity range, negative velocities, and to measure two orthogonal velocity components, frequency shifting was used. Because the beam spacing must be selectable and remain independent of the shift frequency, a rotating diffraction grating was used. The grating had three tracks, which allowed three beam spacings. A motor and a tachometer were interfaced to the data management computer to allow keyboard control of the shift frequency, grating track, and continuous control of the speed. A frequency shift from 0 to 8 MHz was possible.

Several tests were conducted to ensure that the computer control of the motor was accurate and that the rotational speed remained constant. A monodisperse velocity distribution was measured without shifting and then with several shift frequencies. The system was stable to ± 1 percent on the velocities measured. Polydispersed sprays were similarly measured and proved that the frequency shift improved the signal processing and reported the same size and velocity distributions.

The data were normalized using direct measurements of the sampling cross section for each size class which was accomplished automatically by the Phase Doppler Particle Analyzer. A representative normalization curve showing the sample volume diameter t versus drop size is shown in Fig. 4. Also shown for comparison is the theoretically predicted curve for the experimental conditions.

Results

Figure 5 shows a backlit flash photo of the bluff body with an operating spray. The exposure was fairly long and hence the drops appear as streaks. In particular, the spray sheet is clearly seen, with long streaks indicating a high velocity. Drops are seen to exit out of the spray and return to the recirculation zone situated in front of the bluff body face. The shorter, more randomly oriented streaks show that the region has slower velocities and greater turbulence. The droplets on the face of the bluff body are indicative of impaction of recirculated drops.

A conceptual sketch of the spray and flow field is provided in Fig. 6 to aid the reader in following the description and interpretation of the results. This figure should be regarded as

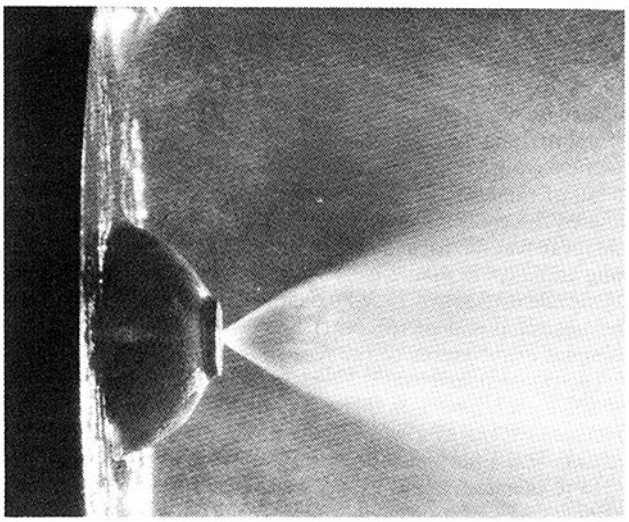

Fig. 5 Bluff body in operation, HAGO 3.00 GPH 45 deg H, $\bar{U} = 20.9$ m/s

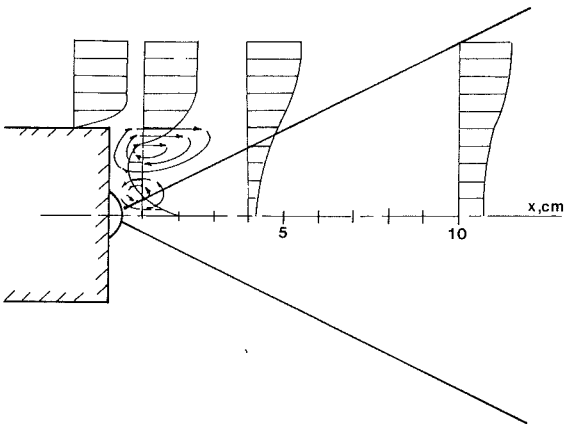

Fig. 6 Conceptual sketch of bluff body flow field

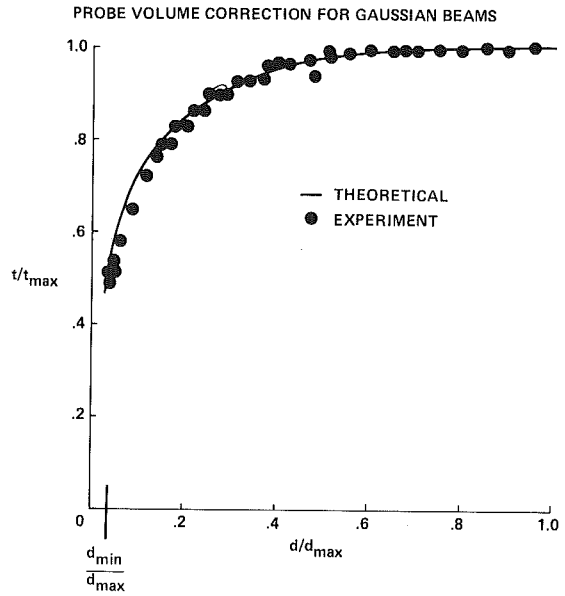

Fig. 4 Sample volume normalization for Gaussian beams

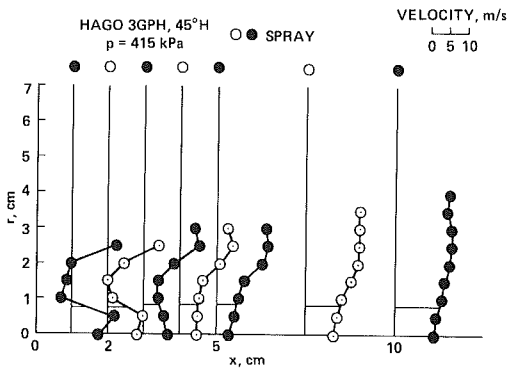

Fig. 7 Bluff body mean axial spray velocities, $\bar{U} = 20.9$ m/s

showing only the general features of the flow field since various drop size classes behave quite differently. Note that two main counterrotating toroidal vortices were formed; one next to the spray exit was produced by the entrainment of the high momentum spray sheet and the other at the outer edge of the bluff body was produced by the air flow shear layer. These toroidal vortices may not have been stationary. Smaller, secondary vortices were undoubtedly present, but more detailed measurements are required to identify these features.

Figure 7 shows the mean axial velocities of the spray drops, averaged over all drop size classes. The velocity profile at $x=1$ cm downstream of the nozzle orifice showed the exit velocity of the spray near centerline, a reversed flow region between $r=1$ and $r=2$ cm, and followed by a rapid increase in velocity due to interaction with the air flow. The shear layer leaving the forebody provided a strong flow entrainment which drove the spray drops downstream. At the $x=2$ cm station, the spray velocity on the axis began a continuous decrease with downstream distance to the $x=5$ cm station. This deceleration was due to the air flow recirculation and wake produced by the bluff body. The minimum mean velocity was approximately zero at $r=1.5$ cm for this station ($x = 2$ cm). However, it will be seen later that the smaller drops in the size distribution still had a negative velocity at this station. Spray drops in the outer part of the spray ($r=1$–2.5 cm) continued to increase in velocity with downstream distance in response to the shear flow. At $x=7.5$ cm, the spray drop velocity profile developed a wakelike character and the centerline velocity began to increase from $x=5$ cm onward.

The corresponding mean radial velocity profiles are shown in Fig. 8. On the axis of the spray, the radial velocities were approximately zero for all streamwise stations. A peak in the radial velocity at the $x=1$ cm and $r=0.5$ cm station corresponded to the outer part of the spray cone. The radial velocity was approximately zero when the axial velocities were negative. Positive radial velocities at the $x=2$, 3, and 4 cm stations reflected the radial development of the main spray sheet. In the shear layer, the entrainment and acceleration of the spray by the outer flow produced a net radial outflow of drops.

Figure 9 shows the radial distributions of SMD at downstream stations. Drops in the recirculation region outside of the main spray cone had an SMD of approximately 20 μm. It is also interesting to note that the largest values of SMD occurred beyond the radius of the bluff body. The positive mean radial velocities presumably served to propel the larger drops outward from the spray sheet. Another interesting observation was that the spray evolved with characteristics of a solid cone spray with a nearly uniform radial distribution of SMD beyond the $x=5$ cm station.

Size-velocity correlation plots are shown in Figs. 10(*a*, *b*, *c*, *d*, *e*, *f*), for axial stations of $x=1$, 2, 3, 4, 5, and 10 cm downstream of the nozzle orifice, respectively. At $x=1$ cm, the axial size-velocity correlation at the centerline showed a relatively high velocity for all drop sizes and a significant velocity difference between the small and large drops, which is characteristic of a pressure atomizer. Just outside of the spray cone, the small drops were moving in a negative direction as a result of the recirculation in the toroidal vortex behind the bluff body formed by the spray jet. Larger drops coming from the edge of the spray had sufficient momentum to pass through the reversed air flow. Near the outer edge of the bluff body, the small drops were stopped in the air stagnation region below the shear layer, whereas the larger drops caught in the recirculating flow continued to move in the reverse direction. Axial size-velocity correlations on the axis at the $x=2$ cm station (Fig. 10*b*) were similar to the previous station but had some larger drops moving at higher speeds. This was also true at the $r=1.0$ cm location. For the $r=2.0$ cm station, the drops in the size range of 2.5 to 40 μm in diameter showed a similar negative correlation to the $x=1$ cm axial station, but with larger velocity. The larger drops that were present at the $x=2$ cm station increased in velocity with size. Apparently, the smaller drops were driven by the toroidal vortex produced by the air shear layer, whereas the larger drops were moving with higher speed based on the spray injection velocity.

Measurements at the $x=3$ cm station (Fig. 10*c*) showed a significant decrease in the axial velocity of the small drops to approximately 1 m/s. Larger drops reached velocities similar to the previous case. It is important to recognize that these relative accelerations and decelerations of the different size classes produce corresponding changes in the number densities of the various drop sizes. This, in turn, will affect local evaporation rates and hence, fuel vapor concentration. The smallest drops at the 1 cm radial station were still moving in a reverse direction, while the larger drops had a velocity similar to the previous axial location; but the largest drops had a slightly greater velocity. This characteristic development continued with downstream distance. Small drops, just beyond the wake of the bluff body, had reached the approximate air flow velocity. On the axis, the smallest drops reached a minimum velocity at approximately 4 cm (Fig. 10*d*) and then began to accelerate to the 5 cm axial station (Fig. 10*e*). Once again, the drops were following the acceleration of the air flow in the wake.

At $x=10$ cm downstream (Fig. 10*f*), the size-velocity correlations showed a minimum at the midsize of the range. Recognizing that the smaller drops were responding to the air flow, whereas the largest drops were continuing at their injection velocity, this result should be expected.

Figure 11 is the centerline size-velocity correlations for the axial stations measured. Looking at the velocities of the small drops, their velocity was approximately 6 m/s, decreased to 1 m/s at $r=3$ cm and then increased to 12 m/s at $x=10$ cm.

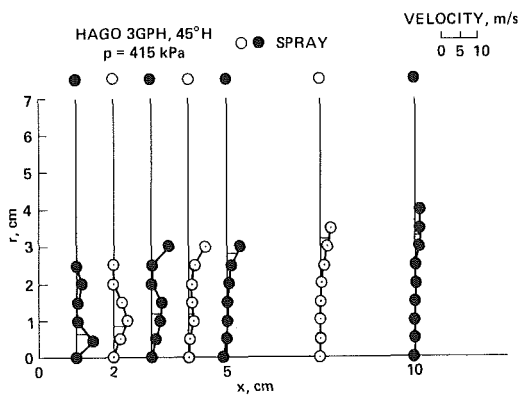

Fig. 8 Bluff body mean radial spray velocities, $\bar{U}=20.9$ m/s

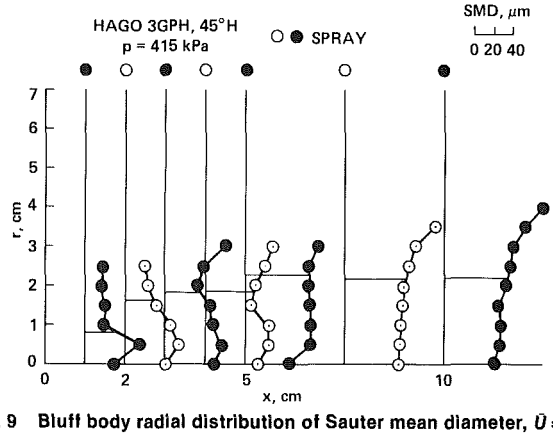

Fig. 9 Bluff body radial distribution of Sauter mean diameter, $\bar{U}=20.9$ m/s

These small drops (~ 2.5 μm) can be assumed approximately to follow the gas phase velocity. Thus, the axial velocity response corresponded to the air flow behavior behind the bluff body plus the induced flow produced by the spray. The largest drops started out at a higher velocity and decreased gradually toward the local velocity in the wake.

To illustrate this behavior further, Fig. 12 shows the axial velocity response of four drop size classes: 10, 30, 50, and 70 μm. The smallest drops showed a deceleration to the $x = 3$ cm axial station followed by a continuous acceleration. As stressed previously, the decrease in velocity of the small drops resulted in a corresponding increase in the number density

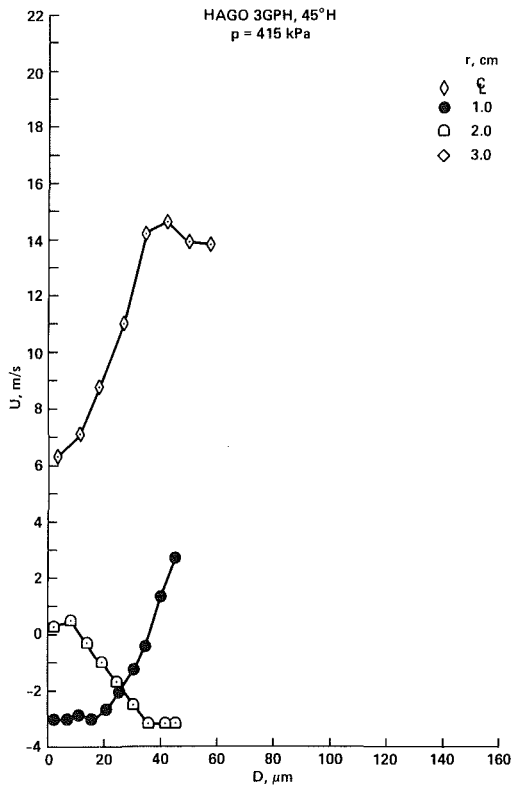

Fig. 10(*a*) $X = 1$ cm

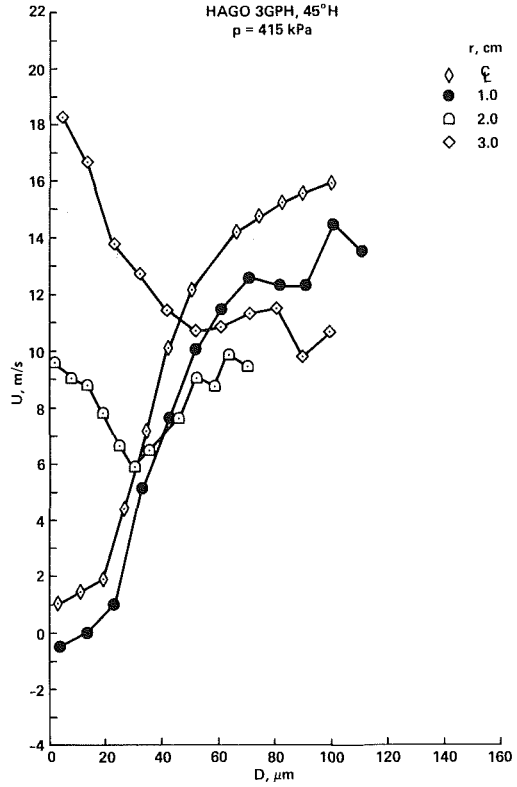

Fig. 10(*c*) $X = 3$ cm

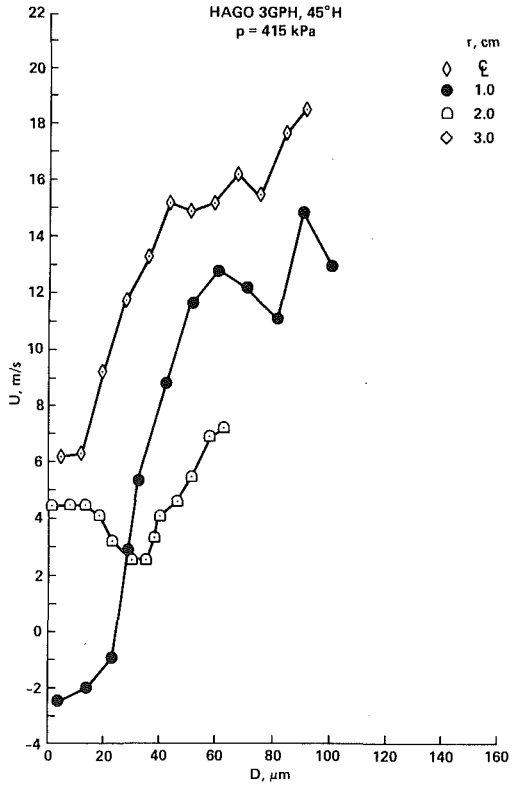

Fig. 10(*b*) $X = 2$ cm

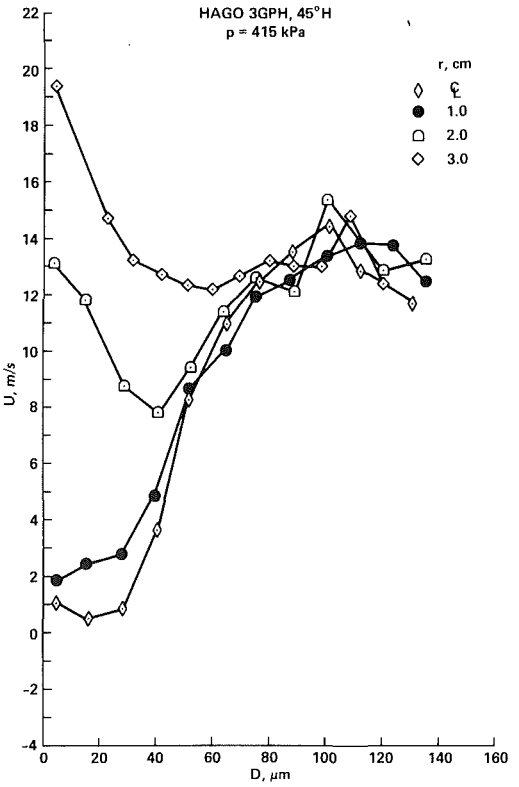

Fig. 10(*d*) $X = 4$ cm

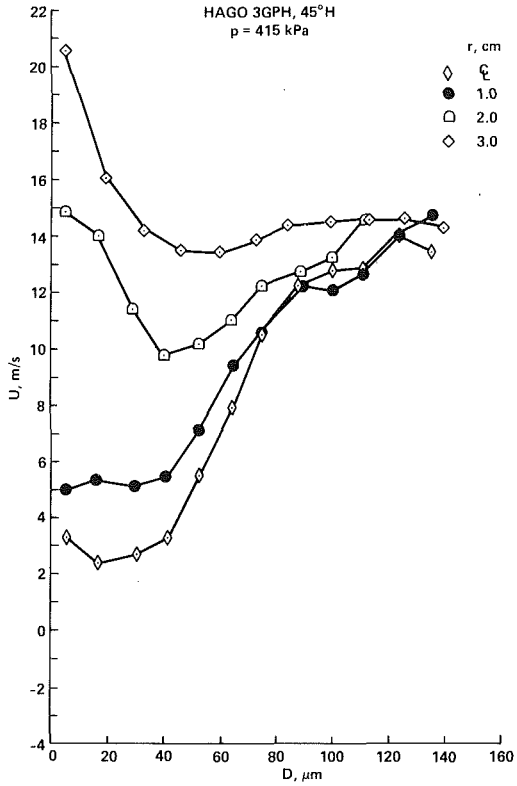

Fig. 10(e) $X = 5$ cm

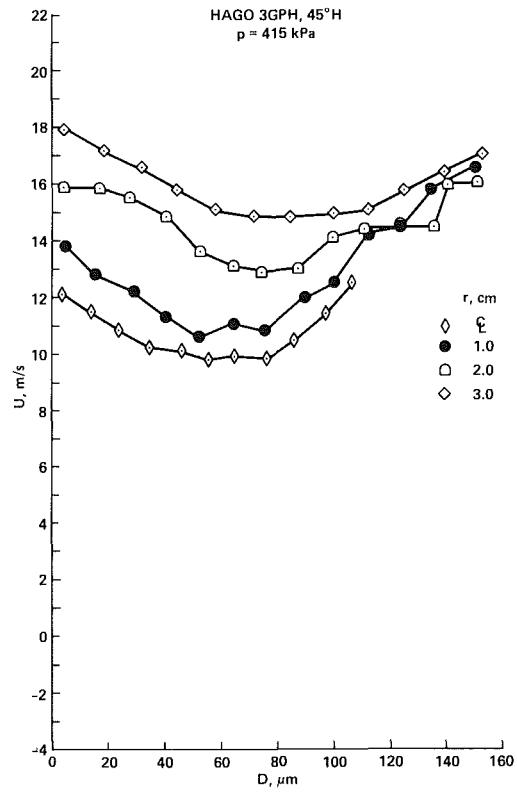

Fig. 10(f) $X = 10$ cm

Fig. 10 Bluff body radial development of size-velocity correlation, $\bar{U} = 20.9$ m/s

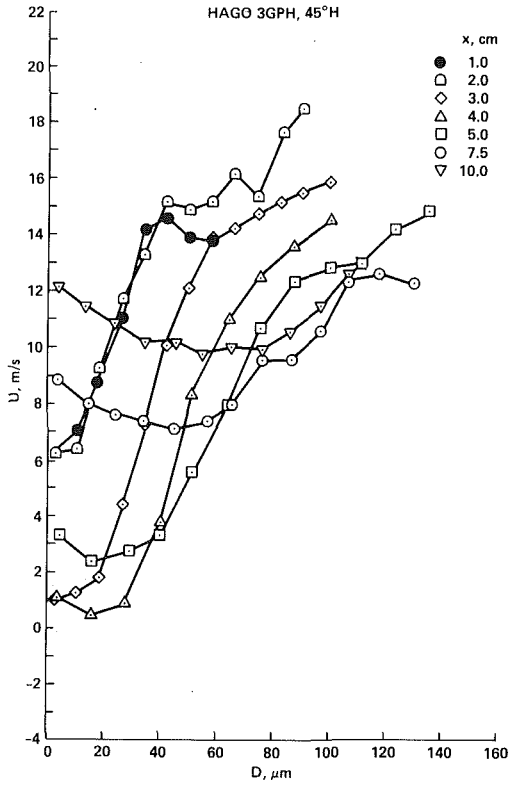

Fig. 11 Bluff body axial development of size-velocity correlation, $r = 0$ cm, $U = 20.9$ m/s

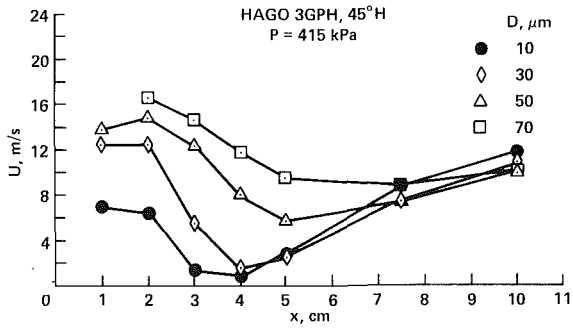

Fig. 12 Bluff body axial development of velocity for varying size classes, $\bar{U} = 20.9$ m/s

which should result in a maximum near the $x = 3$ cm station, followed by a progressive decrease. Velocities of all drop size classes converged to a similar velocity well downstream.

Number density distributions, shown in Fig. 13, reflected the anticipated behavior. On the axis, the number density started out high, further increased to the $x = 2$ cm station and then decreased. In the recirculation region, radii of $r = 0.5$ and $r = 1.5$ cm at the $x = 1$ cm axial station, the number density was still relatively high (1200/cc). Downstream, the overall number density decreased with the increase in flow velocity and spreading of the spray.

Further information on the spray behavior may be obtained from the drop angle of trajectory, measured for each size class (Figs. 14*a*, *b*, *c*, *d*). The largest range of angles of trajectory occurred at the 1 cm axial station (Fig. 14*a*). On the centerline, the angles were essentially zero. At a radius of 1 cm, all drop sizes had uniform drop angles of trajectory corresponding to the spray angle. The smallest drops showed a larger angle of deflection as they began to be entrained out of the spray. At

$r = 1$ cm, the small drops had a reversed flow direction (180 deg), followed by a steep decrease in angle with increasing drop size. Further outward, the angles of trajectory of the small drops decreased, turning outward, and at the outer edge of the bluff body, turned downstream with the air flow. The large drops maintained their reversed flow direction. Many of these large drops apparently impacted the bluff body contributing to the buildup of water on the face. At the outer edge of the bluff body, all drop sizes had a zero angle of trajectory.

A similar behavior occurred at $x = 2$ cm (Fig. 14*b*). Figure 14(*c*), which shows the angle of trajectory at $x = 3$ cm, revealed an interesting result. Since the nominal spray half angle was 22.5 deg, the spray sheet was at $r = 1.25$ cm. Nonetheless, the small drops at $r = 0.5$ cm were moving at 90 deg which was a large angle relative to the main spray direction. Clearly, the small drops were propelled out of the spray cone because of the mass injection and air recirculation. At $r = 1.0$ cm, the angle was even larger indicating that the small drops were moving upward with a small reverse flow component even though this station was within the spray sheet.

Outside of the spray cone, at $r = 2$ cm, the small drops have acquired a small positive angle, whereas drops 20 μm diameter had a small negative angle of trajectory. These drops seemed to be following the downward deflection of the upper vortex. The larger drops followed the nominal spray cone half-angle of 22.5 deg. Similar behavior was evident at $x = 5$ cm (Fig. 14*d*). The negative angles of trajectory occurred for larger drops and affected the drops at the inner radii, including the centerline. It is not clear why drops on the centerline would have a negative deflection angle. One might expect the momentum of the drops being propelled inward to cause them to overshoot. However, these are average angles of trajectory for each size class and thus, such an asymmetry would not be expected. Since the result is consistent for several radial locations, it may be due to an asymmetry in the spray formation.

Summary and Conclusions

These preliminary results provide reinforcement to our previous statements that there is no such thing as a simple spray. As shown here, the various drop size classes respond very differently to the prevailing flow conditions. The drop dynamics significantly change the spray drop size and number density distributions. This also casts further doubt on the value of describing sprays by a simple integral quantity such as the SMD and especially, line-of-sight measurement of SMD. Further work is clearly needed in mapping the air flow in this and similar spray flow fields in detail. Also, the mapping of the velocities and angles of trajectory for each size class clearly provides good insight into the development of the spray.

These data will provide valuable information to the modellers. The rather simplistic boundary and initial condi-

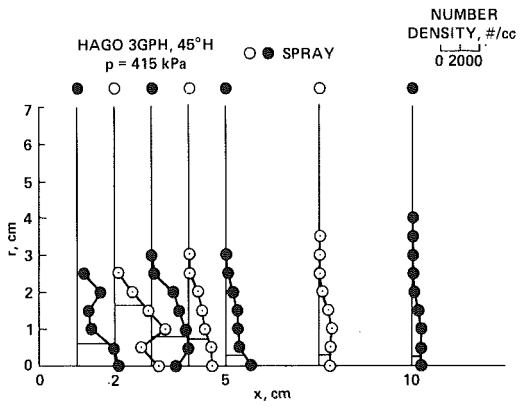

Fig. 13 Bluff body number density, $U = 20.9$ m/s

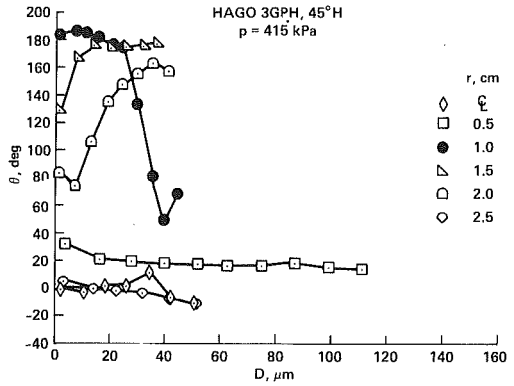

Fig. 14(*a*) $X = 1$ cm

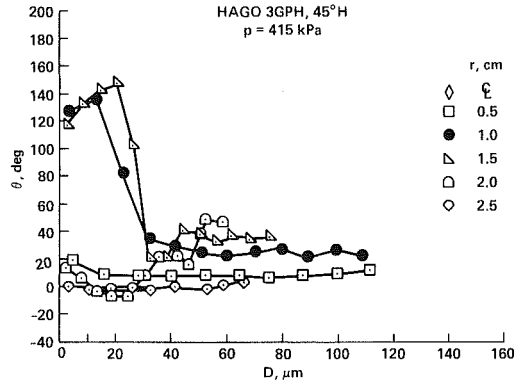

Fig. 14(*b*) $X = 2$ cm

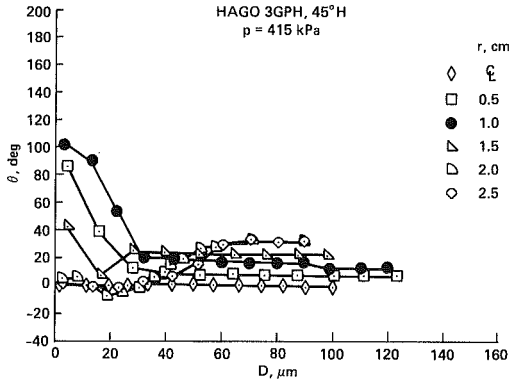

Fig. 14(*c*) $X = 3$ cm

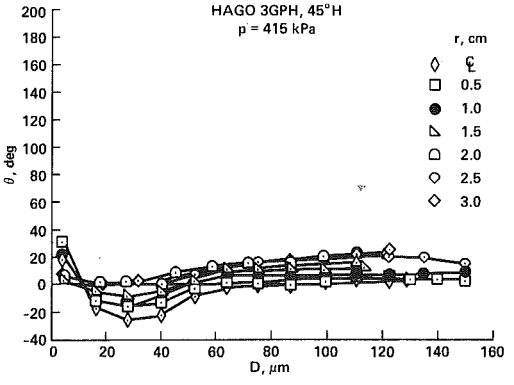

Fig. 14(*d*) $X = 5$ cm

Fig. 14 Bluff body angle of trajectory versus size, $U = 20.9$ m/s

tions currently used are less than representative of those existing in combustor flow fields. Further research will serve to greatly extend the data base required to better define the initial conditions and assess the performance of the codes. Among geometries studied will be bluff bodies generating higher degrees of turbulence and/or incorporating swirl.

Acknowledgments

The guidance of Drs. R. Mehta and R. V. Westphal of NASA Ames in the design stages of the 2-PFT is gratefully acknowledged. This research was supported by NASA Lewis Research Center, Contract No. NAS3-24844, Ms. Valerie Lyons, Contract Monitor.

References

Bachalo, W. D., 1980, "Methods for Measuring the Size and Velocity of Spheres by Dual-Beam Light-Scatter Interferometry," *Applied Optics*, Vol. 19, No. 3.

Bachalo, W. D., and Houser, M. J., 1984, "Phase/Doppler Spray Analyzer for Simultaneous Measurements of Drop Size and Velocity Distributions," *Optical Engineering*, Vol. 23, No. 5.

Bachalo, W. D., and Houser, M. J., 1985, "Spray Drop Size and Velocity Measurements Using the Phase/Doppler Particle Analyzer," presented at the International Conference on Liquid Atomization and Spray Systems, Imperial College, London.

Bachalo, W. D., and Houser, M. J., 1986, "Measurements of Drop Dynamics and Mass Flux in Sprays," presented at the Spring Central States Meeting of the Combustion Institute, Cleveland, OH.

Bachalo, W. D., Houser, M. J., and Smith, J. N., 1986, "Evolutionary Behavior of Sprays Produced by Pressure Atomizers," AIAA 24th Aerospace Sciences Meeting, Reno, NV, Paper No. 86-0296.

Bachalo, W. D., and Rudoff, R. C., 1986, "Fuel Atomization and Air–Fuel Interactions in a Turbulent Environment," NASA SBIR Phase I Final Report.

Bradshaw, D., and Pankhurst, R. C., 1964, "The Design of Low Speed Wind Tunnels," *Prog. in Aeronautic Science*, Pergamon, NY, Vol. 5, pp. 1–66.

Chin, J. S., Nicolaus, D., and Lefebvre, A. N., 1986, "Influence of Downstream Distance on the Spray Characteristics of Pressure-Swirl Atomizers," ASME JOURNAL OF ENGINEERING FOR GAS TURBINES AND POWER, Vol. 108, pp. 219–224.

Jackson, T. A., and Samuelson, G. S., 1985, "Performance Comparison of Two Interferometric Droplet Sizing Techniques," presented at SPIE 19th Annual International Technical Symposium on Optical Electro-Optical Engineering, San Diego, CA.

Mehta, R. D., 1977, "The Aerodynamic Design of Wind Tunnels With Wide Angle Diffusers," *Prog. Aerospace Sci.*, Vol. 18, No. 1, pp. 59–120.

Rizk, N. K., and Lefebvre, H., 1985, "Drop-Size Distribution Characteristics of Spill-Return Atomizers," *AIAA Journal of Propulsion and Power*, Vol. 1, No. 1, pp. 16–22.

Solomon, A. S. P., Shuen, J.-S., Zhang, Q-F., and Faeth, G. M., 1984, "A Theoretical and Experimental Study of Turbulent Evaporating Sprays," NASA Lewis Contractor Report 174760.

Tishkoff, J. M., 1982, "Measurements of Particle Size and Velocity in a Fuel Spray," *Proceedings of the 2nd International Conference on Liquid Atomization and Spray Systems*, pp. 245–252.

Yule, A. J., Chigier, N. A., Atakan, S., and Ungut, A., 1977, "Particle Size and Velocity Measurements by Laser Anemometry," AIAA 15th Aerospace Sciences Meeting, Los Angeles, CA, Paper No. 77-214.

Combustion Gas Properties: Part III—Prediction of the Thermodynamic Properties of Combustion Gases of Aviation and Diesel Fuels

Ömer L. Gülder
National Research Council of Canada,
Division of Mechanical Engineering,
Ottawa, Ontario, K1A OR6, Canada

Empirical formulae are presented by means of which the specific heat, mean molecular weight, density, and specific heat ratio of aviation fuel–air and diesel fuel–air systems can be calculated as functions of pressure, temperature, equivalence ratio, and hydrogen-to-carbon atomic ratio of the fuel. The formulae have been developed by fitting the data from a detailed chemical equilibrium code to a functional expression. Comparisons of the results from the proposed formulae with the results obtained from a chemical equilibrium code have shown that the mean absolute error in predicted specific heat is 0.8 percent, and that for molecular weight is 0.25 percent. These formulae provide a very fast and easy means of predicting the thermodynamic properties of combustion gases as compared to detailed equilibrium calculations, and they are also valid for a wide range of complex hydrocarbon mixtures and pure hydrocarbons as well as aviation and diesel fuels.

Introduction

Most of the energy conversion devices for propulsion and power generation fueled with complex hydrocarbon mixtures involve complex chemical gas systems resulting from combustion at high temperatures and pressures. Thus, ideal combustion and simple ideal gas models fail to predict thermodynamic properties with required accuracy. In gas turbine and reciprocating internal combustion engine calculations related to design, performance, and emissions, an accurate knowledge of the thermodynamic properties of the combustion products is of prime importance.

Thermodynamic properties of the combustion gases such as enthalpy, specific heat and mean molecular weight (= relative molecular mass) are dependent on the fuel type (characterized by H/C ratio ψ), fuel–air equivalence ratio ϕ, composition of the gas mixture, temperature, and pressure. For lean and stoichiometric mixtures, i.e., $0 \leq \phi \leq 1.0$, these properties can be calculated accurately by assuming chemical equilibrium of the species. Then for a given fuel, temperature, and pressure, the mass action equations can be solved directly for species concentrations, from which other thermodynamic properties can be derived. Although this is a fairly straightforward calculation procedure, for multiple calculations such as those in simulation models, it may result in time-consuming and expensive computer runs.

Contributed by the Gas Turbine Division of THE AMERICAN SOCIETY OF MECHANICAL ENGINEERS and presented at the 32nd International Gas Turbine Conference and Exhibit, Anaheim, California, May 31–June 4, 1987. Manuscript received at ASME Headquarters February 4, 1987. Paper No. 87-GT-49.

Available thermodynamic tables of combustion gases are usually limited to specific fuels (limited to certain H/C ratios) and pressures, and are not suitable for computer calculations. Approximate but much simpler methods of estimating the thermodynamic properties of combustion gases of complex hydrocarbon mixture–air systems can provide appreciable advantages in routine calculations and simulation studies of gas turbines and reciprocating internal combustion engines.

In this paper, simple formulae which predict the specific heat at constant pressure, and mean molecular weight of the combustion gases as functions of atomic hydrogen-to-carbon ratio of the fuel, equivalence ratio, gas temperature, and pressure, will be presented and their accuracies will be evaluated. The equations have been developed by curve fitting of data obtained from a detailed chemical equilibrium code (Gülder, 1982). The proposed equations have been obtained from the data of the following ranges: $0 \leq \phi \leq 1.0$, 0.1 MPa $\leq P \leq$ 7.5 MPa, 300 K $\leq T \leq$ 2500 K, and $0.8 \leq$ H/C $\leq$ 2.5. These ranges cover the conditions of interest in gas turbines and diesel engines, and the properties of conventional and future liquid hydrocarbon aviation and diesel fuels. This work constitutes the third part of the previously reported approximate expressions developed to predict adiabatic flame temperature (Gülder, 1986a) and partial pressures of CO_2 and H_2O in combustion gases of aviation and diesel fuels (Gülder, 1986b).

Background

Specific heat at constant pressure of a reacting gas mixture

can be calculated from the enthalpy of the system as follows: The total enthalpy of the system, assuming an ideal gas mixture, is

$$H = \sum_{i=1}^{\nu} \xi_i H_i \tag{1}$$

where H_i is the enthalpy of the ith species with mole fraction of ξ_i, and ν is the total number of species in the mixture. From the definition of specific heat at constant pressure, assuming chemical equilibrium of the species, one can write the specific heat as

$$C_{pm} = \frac{\partial}{\partial T} \sum_{i=1}^{\nu} \xi_i H_i \tag{2}$$

or

$$C_{pm} = \sum_{i=1}^{\nu} \xi_i C_{pi} + \sum_{i=1}^{\nu} H_i \left[\frac{\partial \xi_i}{\partial T} \right]_p \tag{3}$$

in which the specific heat of the gas mixture at equilibrium has been separated into frozen and reacting components, first and second terms on the right-hand side, respectively.

C_{pi} is the value of the ideal gas specific heat of a nonreacting species and can be found in tabular (Stull and Prophet, 1971) or in functional form (Prothero, 1969). ξ_i must be computed from full chemical equilibrium calculations. The term $(\partial \xi_i / \partial T)$ can be computed by the technique described by Svehla and Brokaw (1966). An alternate way is to use the following approximation:

$$\frac{\Delta \xi_i}{\Delta T} \simeq \left[\frac{\partial \xi_i}{\partial T} \right]_p \tag{4}$$

For lean and stoichiometric mixtures a ΔT value around 5–10 gives accurate results.

Molecular weight (= relative molecular mass) of the gas system is

$$MW = \sum_{i=1}^{\nu} \xi_i MW_i \tag{5}$$

assuming an ideal gas mixture. MW_i is the molecular weight of the ith species. Then, the density of the gas mixture is

$$\rho_g = \frac{MW \cdot P}{R^0 T} \tag{6}$$

where R^0 is the universal gas constant, P is pressure, and T is temperature.

In this work, C_p is reported as kJ/kg K; the ratio of specific heats γ is

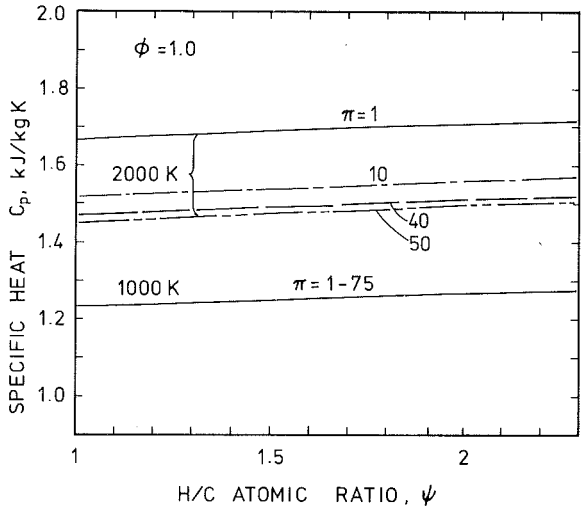

Fig. 1 Variation of the specific heat at constant pressure of the combustion gases with H/C atomic ratio

$$\gamma = C_p / [C_p - R] \tag{7}$$

where R is the specific gas constant of the mixture, R^0/MW.

Effect of Different Parameters on C_p and MW

In this section, dependence of the specific heat and molecular weight on fuel type, equivalence ratio, pressure, and temperature will be presented.

Equilibrium specific heat of the combustion products varies rather slowly with the hydrogen-to-carbon ratio ψ of the fuel (Fig. 1). Variation is even slower for leaner mixtures.

Variation of specific heat with temperature is shown in Figs. 2, 3, and 4 at π = 1, 10, and 50, respectively, for different equivalence ratios. π is the dimensionless pressure P/P_0, and P = 101.3 kPa. A close inspection of Figs. 2–4 shows that pressure does not affect the specific heat for $T < 1400$ K; however above 1500 K, effect of pressure is quite significant. Note that $\phi = 0$ corresponds to pure air.

Below 1500 K, the effect of temperature on specific heat is small as compared to its effect for temperatures above 1500 K. Due to increasing extent of dissociation, and in turn chemical activity, specific heat increases drastically with temperature above 1500 K (Figs. 2–4). Similar trends have been observed at different H/C ratios.

The effect of fuel–air equivalence ratio on the specific heat of combustion products for the range $0 \le \phi \le 1.0$ is shown in Fig. 5 at 10 atm pressure for a fuel with a hydrogen-to-carbon

Nomenclature

A = constant, equation (8)
a_j = constants, equations (12)–(14) and (18)–(20)
b_j = constants, equations (12)–(14) and (18)–(20)
C_p = specific heat at constant pressure, kJ/kg K
C_{pm} = specific heat at constant pressure, kJ/kmol K
c_j = constants, equations (12)–(14) and (18)–(20)
H = total enthalpy of gases, kJ/kmol K
H_i = enthalpy of the ith species, kJ/kmol K
MW = mean molecular weight (=relative molecular mass)
P = pressure, kPa
P_0 = reference pressure = 101.3 kPa (=1 atm)
R = specific gas constant = R^0/MW
R^0 = universal gas constant = 8.3143 kJ/kmol K
S = t or σ
T = temperature, K
t = $T/1000$
x = pressure exponent, equations (12) and (18)
y = temperature exponent, equations (13) and (19)
z = exponent for ψ, equations (14) and (20)
α = constant, equation (8)
β = constant, equation (8)
γ = ratio of specific heats
θ = equations (11) and (21)
λ = constant, equation (8)
ν = number of gases in the products
ξ_i = mole fraction of the ith species
π = dimensionless pressure = P/P_0
ϕ = fuel–air equivalence ratio
ψ = H/C atomic ratio

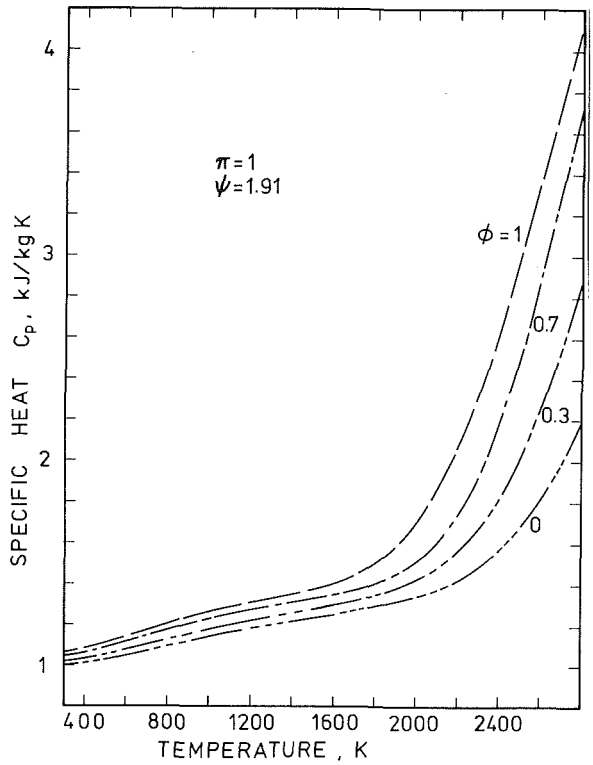

Fig. 2 Variation of the specific heat with gas temperature at 1 atm pressure for various equivalence ratios

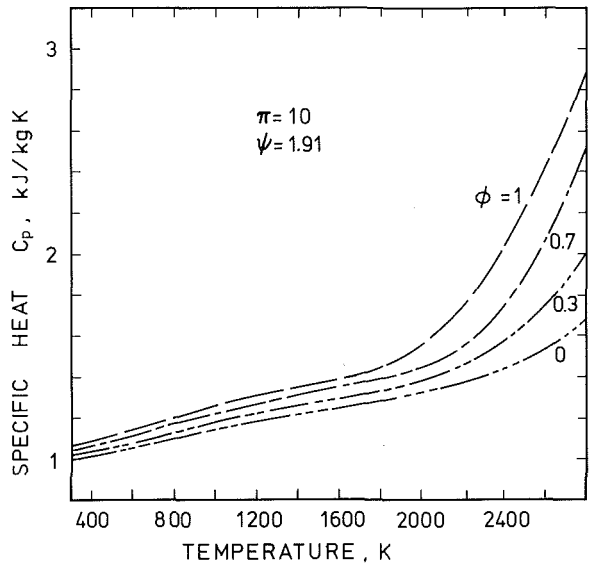

Fig. 3 Variation of the specific heat with gas temperature at 10 atm pressure for various equivalence ratios

ratio of 1.906. Increasing temperature increases the effect of equivalence ratio on specific heat. At temperatures lower than 1500 K, the relationship between C_p and ϕ seem to be almost linear.

The variation of the mean molecular weight of the combustion gases with hydrogen-to-carbon ratio of the fuel at different temperatures, pressures, and equivalence ratios is shown in Fig. 6. MW increases with decreasing ψ, π, and ϕ. Dependence of MW on temperature is complicated; however, at a given pressure and H/C ratio, increasing gas temperature decreases the MW for $T > 1500$ K (Figs. 7 and 8). Lower MW at high temperatures is due to the increased extent of dissociation of triatomic and diatomic species into diatomic and monatomic ones.

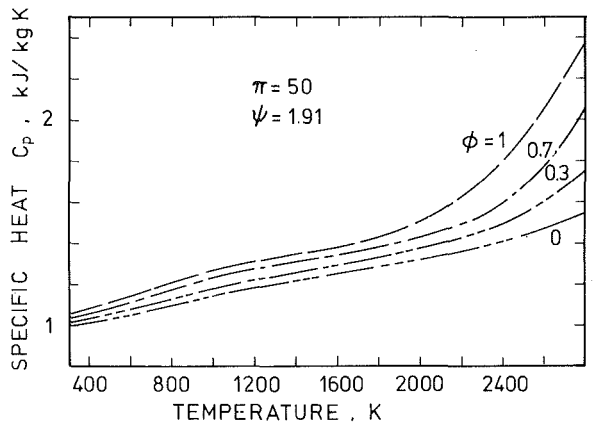

Fig. 4 Variation of the specific heat with gas temperature at 50 atm pressure for various equivalence ratios

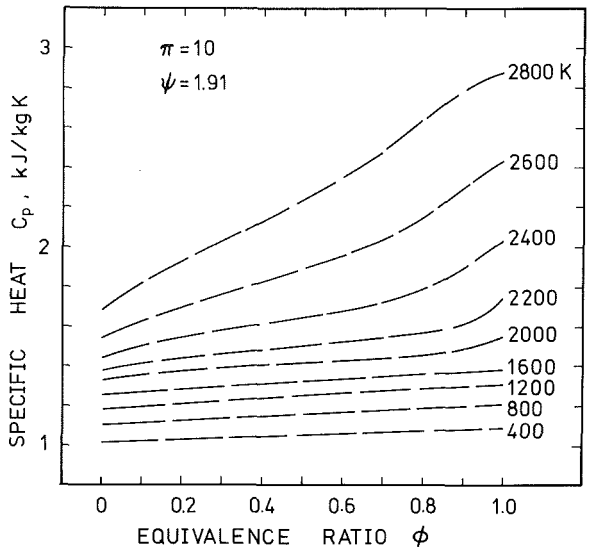

Fig. 5 Dependence of specific heat on the equivalence ratio

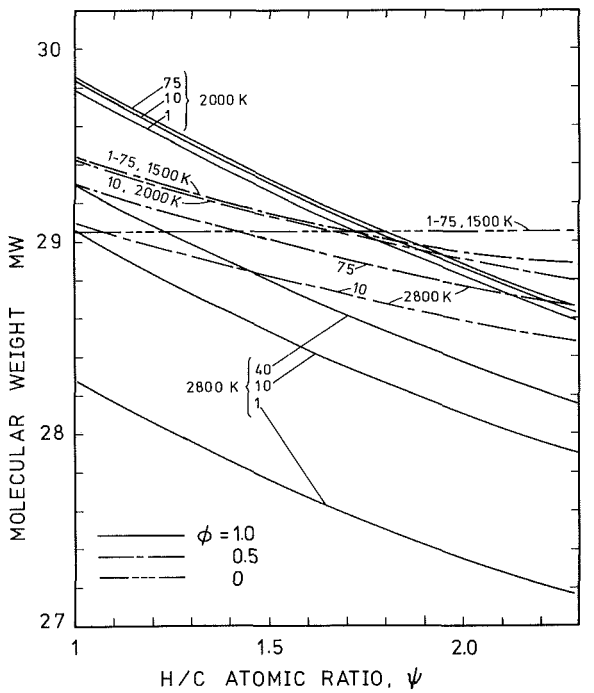

Fig. 6 Variation of the molecular weight with the H/C atomic ratio of the fuel

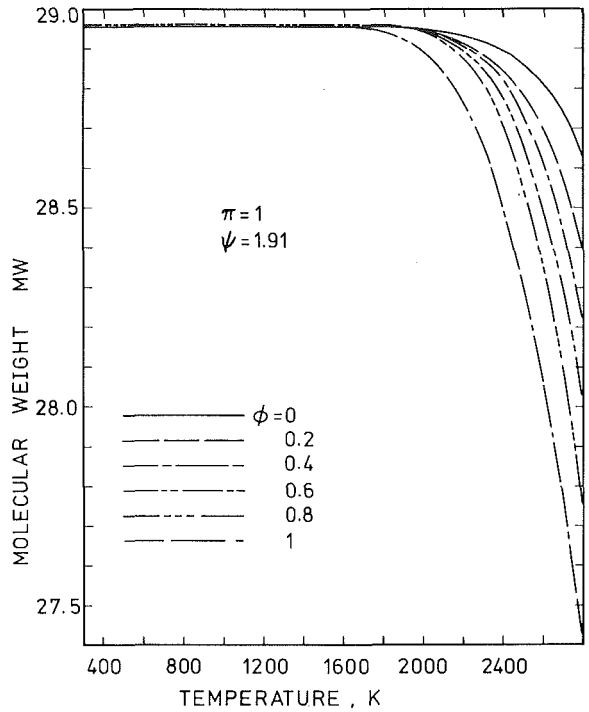

Fig. 7 Dependence of molecular weight on the gas temperature at 1 atm

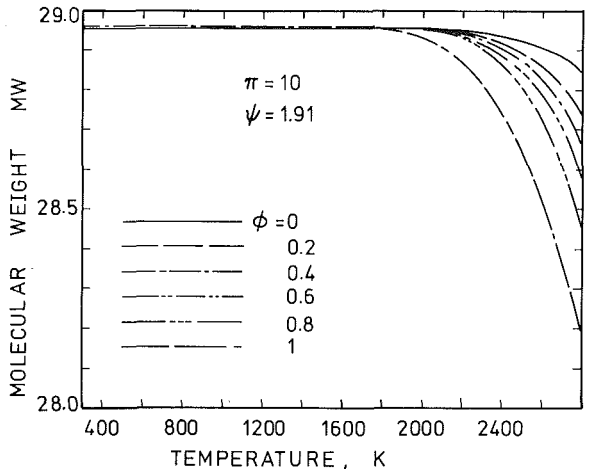

Fig. 8 Dependence of molecular weight on the gas temperature at 10 atm

The results presented in Figs. 1–8 are for model fuels consisting of different proportions of pure hydrocarbons. The specific heats and molecular weights were computed by using a chemical equilibrium code which considers 14 species in the products, namely H_2, H, O_2, N_2, N, OH, H_2O, O, NO, NO_2, N_2O, CO, CO_2, and Ar. Thermochemical data were taken from standard tables (Stull and Prophet, 1971; Reid et al., 1977). The solution procedure of the code is similar to that described by Benson et al. (1975). The accuracy of the equilibrium code (Gülder, 1982) was checked against a NASA-Lewis program (Gordon and McBride, 1971) and published tables (Jones et al., 1984), and good agreement has been obtained.

Empirical Formulae

A functional expression of the following form has been adapted to predict the specific heat and the molecular weight of the combustion gases of complex hydrocarbon mixture–air systems as functions of equivalence ratio, pressure, temperature, and hydrogen-to-carbon ratio of the fuel

$$\Omega_k = AS^{\alpha} \exp[\beta(\sigma+\lambda)^2]\ \pi^x \theta^y \psi^z \tag{8}$$

For the temperature range $1500 < T \leq 2500$ K

$$\Omega_1 = C_p \tag{9}$$

$$S = t = T/1000 \tag{10}$$

$$\theta = 1.2358 + 1.03316t - 2.63325t^2 + 3.77256t^3 - 1.07368t^4 \tag{11}$$

$$x = a_1 + b_1 t + c_1 t^2 \tag{12}$$

$$y = a_2 + b_2 t + c_2 t^2 \tag{13}$$

$$z = a_3 + b_3 \sigma + c_3 \sigma t \tag{14}$$

where

$$\sigma = \phi - 0.45 \tag{15}$$

ψ is the H/C atomic ratio of the fuel, and T is the absolute temperature in K.

For the temperature range $400 \leq T \leq 1500$ K

$$\Omega_2 = C_p^{0.5} \tag{16}$$

$$S = \sigma = (\phi + 0.5)^2 \tag{17}$$

$$x = a_1 + b_1 \sigma + c_1 \sigma^2 \tag{18}$$

$$y = a_2 + b_2 \sigma + c_2 \sigma^2 \tag{19}$$

$$z = a_3 + b_3 \sigma + c_3 \sigma^2 \tag{20}$$

and θ is the dimensionless temperature, i.e.,

$$\theta = T/300 \tag{21}$$

For the temperature range $300 \leq T \leq 1500$ K

$$\Omega_3 = MW \tag{22}$$

$$\sigma = S = (\phi + 1)^2 \tag{23}$$

x, y, z, and θ are the same as those given by equations (18)–(21).

For the temperature range $1500 \leq T \leq 2500$ K

$$\Omega_4 = MW \tag{24}$$

$$\sigma = S = (\phi + 1)^2 \tag{25}$$

x, y, z and θ are the same as those given by equations (18)–(21).

A, α, β, λ, a_j, b_j, and c_j are constants, and their values are tabulated in Table 1 for the two temperature ranges for both C_p and MW. It should be noted that equation (8) has the same functional form as the prediction equations for combustion gas properties reported previously (Gülder, 1986a, 1986b). The H/C ratio of the aviation and diesel fuels can be determined experimentally or by the predictive equation given by Gülder (1986b).

Table 1 Constants of equation (8)

	Specific Heat, C_p		Molecular Weight, MW	
Const.	$400 \leq T \leq 1500$	$1500 < T \leq 2500$	$300 \leq T \leq 1500$	$1500 < T \leq 2800$
A	0.99318	0.91153	30.0346	0.20501
α	0.006	1.	0.00266	-0.01537
β	0.00098	0.02103	-0.00121	0.000091
λ	-0.96083	1.8395	-6.48722	232.731
a_1	0.	-0.33224	0.	0.000013
b_1	0.	0.3948	0.	0.00112
c_1	0.	-0.11764	0.	-0.000029
a_2	0.06712	0.27269	0.	-0.00435
b_2	0.01452	-0.57967	0.	-0.00643
c_2	-0.00282	0.15654	0.	-0.00176
a_3	-0.00405	0.02401	0.02478	0.02502
b_3	0.01853	-0.53774	-0.02762	-0.02809
c_3	-0.00246	0.323	0.00219	0.00232

Accuracy of Approximate Formulae

To evaluate the accuracy of the empirical formulae for

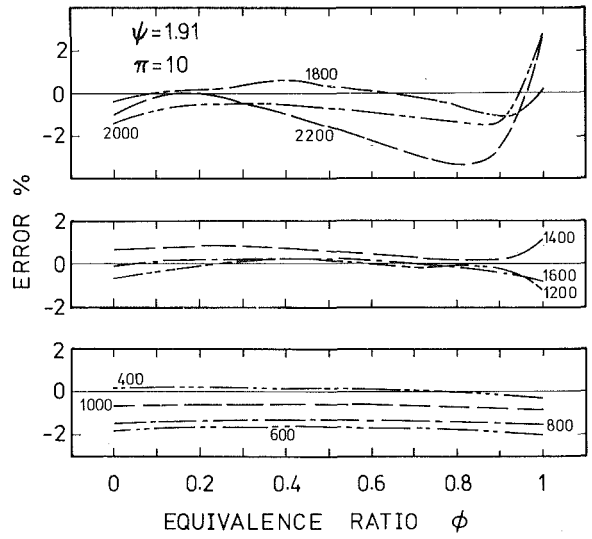

Fig. 9 Error in the predicted specific heat versus equivalence ratio for various temperatures at $\pi = 10$

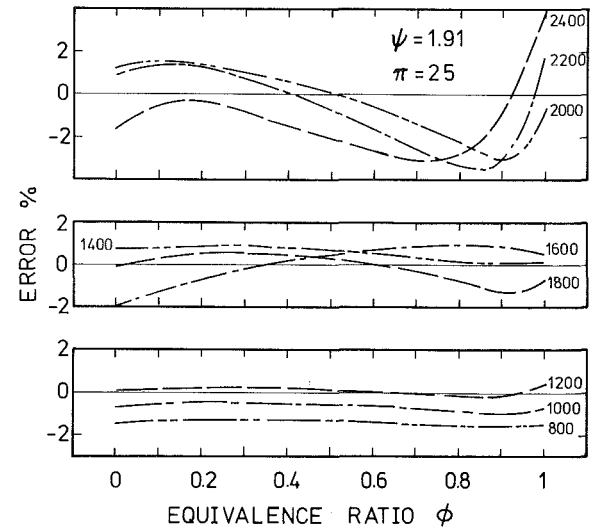

Fig. 10 Error in the predicted specific heat versus equivalence ratio for various temperatures at $\pi = 25$

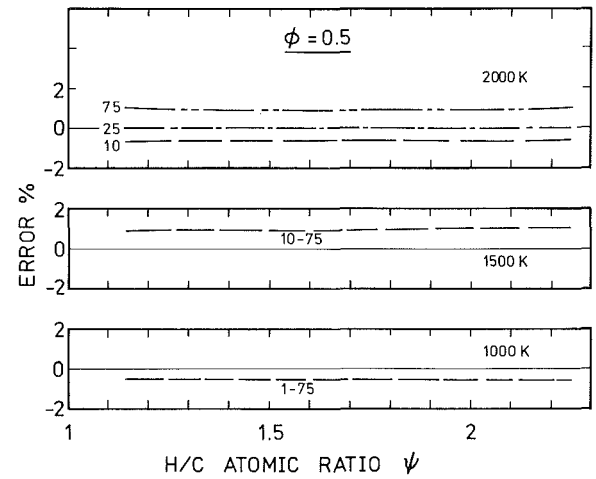

Fig. 11 Error in the predicted specific heat versus H/C atomic ratio for various pressures and temperatures, at $\phi = 0.5$

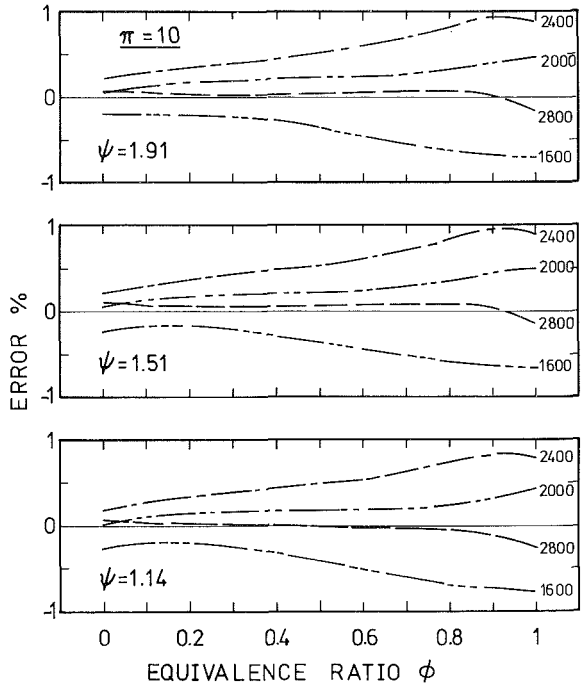

Fig. 12 Error in the predicted molecular weight versus equivalence ratio at $\pi = 10$

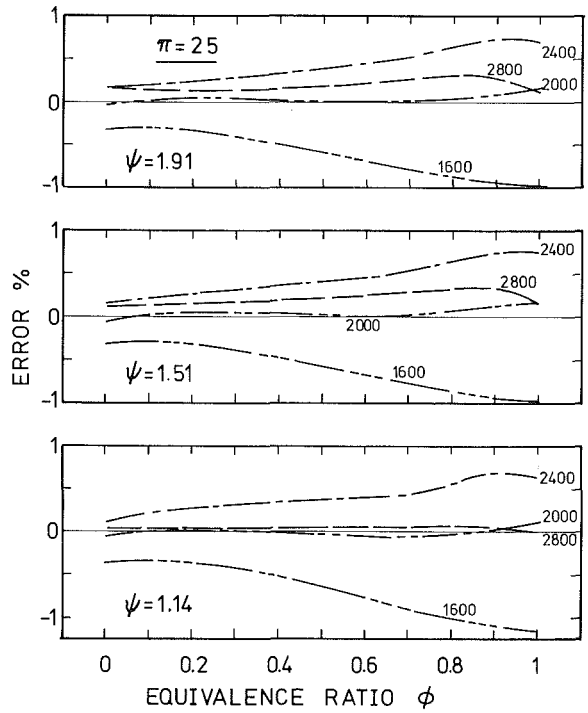

Fig. 13 Error in the predicted molecular weight versus equivalence ratio at $\pi = 25$

specific heat and molecular weight, a set of comparisons of results obtained from equation (8) and those obtained from a detailed chemical equilibrium code, which is briefly described in the Background section, has been made. Results are compared for all possible combinations of the following values of H/C atomic ratio, pressure, temperature, and equivalence ratio:

$\psi = 2.25, 1.906, 1.725, 1.508, 1.316, 1.143$
$\pi = 1, 10, 25, 50, 75$
$T = 300$ K to 2500 K with 100 K increments
$\phi = 0$ to 1.0 with 0.1 increments

Comparisons made at $\pi = 10$ and $\pi = 25$ for specific heat are shown in Figs. 9 and 10, respectively, for a fuel with $\psi = 1.906$. Percentage error is defined as $(C_p - C_p')/C_p$, where C_p' is the predicted specific heat. Percentage errors similar to those of Figs. 9 and 10 have been observed at other conditions considered (Fig. 11). For the whole range considered, the mean absolute error is 0.85 percent.

Comparisons made at $\pi = 10$ and $\pi = 25$ for molecular weight are shown in Figs. 12 and 13, respectively. For the whole range considered, the mean absolute error is 0.25 percent.

The proposed formulae predict the specific heat and molecular weight of the combustion products with reasonable accuracy within the following ranges:

$0 \leq \phi \leq 1.0$
$400 \leq T \leq 2400$ ($300 \leq T \leq 2500$ for MW)
$1.0 \leq \pi \leq 75$ for $T \leq 1500$ K
$10.0 \leq \pi \leq 75$ for $T > 1500$ K
$0.8 \leq \psi \leq 2.5$

The temperature range can be extended to 2500 K for specific heat, and to 2800 K for molecular weight with a slight increase in mean absolute error. The formulae are valid for pure hydrocarbons as well as complex hydrocarbon mixtures, within specified limits.

Concluding Remarks

Functional expressions are presented by means of which the specific heat, molecular weight, gas density, and ratio of specific heats of combustion gases of complex hydrocarbon mixture–air systems can be calculated as functions of pressure, temperature, equivalence ratio, and H/C atomic ratio of the fuel. These equations provide a very fast and easy means of predicting thermodynamic properties as compared to chemical equilibrium calculations. Results of the predictions using the proposed equations are compared with the results obtained from a detailed chemical equilibrium code incorporating 14 species in the combustion products, and it is shown that the accuracy of the approximate equations is very good over the conditions of interest for a very wide range of fuel characteristics.

The developed formulae are expected to reduce the computation time in gas turbine and other internal combustion engine calculations. Especially for the development of simulation models the proposed formulae, with the previously reported ones for temperature (Gülder, 1986a) and partial pressures of CO_2 and H_2O (Gülder, 1986b), provide distinct advantages over the chemical equilibrium codes.

References

Benson, R. S., Annand, W. J. D., and Baruah, P. C., 1975, "A Simulation Model Including Intake and Exhaust Systems for a Single Cylinder Four-Stroke Cycle Spark Ignition Engine," *International Journal of Mechanical Engineering Science*, Vol. 17, pp. 97–124.

Gordon, S., and McBride, B. J., 1971, "Complex Chemical Equilibrium Calculation," NASA SP-273, Lewis Research Center, Cleveland, OH.

Gülder, Ö. L., 1982, "A Computer Program for Calculating Thermodynamic Properties of Equilibrium Combustion Products of Multiple Fuel Mixtures," unpublished work, Fuels and Lubricants Lab., Division of Mechanical Engineering, NRC, Ottawa, Canada.

Gülder, Ö. L., 1986a, "Flame Temperature Estimation of Conventional and Future Jet Fuels," ASME JOURNAL OF ENGINEERING FOR GAS TURBINES AND POWER, Vol. 108, pp. 376–380.

Gülder, Ö. L., 1986b, "Combustion Gas Properties: Part II – Prediction of Partial Pressures of CO_2 and H_2O in Combustion Gases of Aviation and Diesel Fuels," ASME JOURNAL OF ENGINEERING FOR GAS TURBINES AND POWER, Vol. 108, pp. 455–459.

Jones, R. E., Trout, A. M., Wear, J. D., and McBride, B. J., 1984, "Combustion Gas Properties I-ASTM Jet A Fuel and Dry Air," NASA TN-2359, Lewis Research Center, Cleveland, OH.

Prothero, A., 1969, "Computing With Thermochemical Data," *Combustion and Flame*, Vol. 13, pp. 399–408.

Reid, R. C., Prausnitz, J. M., and Sherwood, T. K., 1977, *The Properties of Gases and Liquids*, 3rd ed., McGraw-Hill, New York.

Stull, D. R., and Prophet, H., eds., 1971, *JANAF Thermochemical Tables*, U.S. National Bureau of Standards Publication, NSRDS-NBS 37 and supplement.

Svehla, R. A., and Brokaw, R. S., 1966, "Heat Capacity and the Lewis Number of a Reacting Gas," *AIAA Journal*, Vol. 4, pp. 182–184.

D. M. Carrier

R. J. Wetton

Shell Research Limited,
Thornton Research Centre,
Chester, CH1 3SH, United Kingdom

Prediction of Combustion Performance of Aviation Kerosines Using a Novel Premixed Flame Technique

A novel method for predicting aviation fuel combustion performance has been developed in which the sooting point of a premixed flame is detected automatically. Comparisons with full-scale combustor data confirm that the technique is a more realistic index of combustion quality than Smoke Point or hydrogen content.

Introduction

At present the combustion performance of an aviation gas turbine fuel is controlled by specifying limits for its Smoke Point and compositional parameters—traditionally aromatics content and naphthalenes content; the possibility of using hydrogen content has also been proposed in recent years (Blazowski, 1979; Bowden and Pearson, 1983, 1984; Bowden et al., 1984; Moses and Naegeli, 1979; Naegeli and Moses, 1980; Naegeli et al., 1981). However, there is evidence that these parameters do not adequately predict the combustion performance of certain present-day fuels and candidate future fuels (Gleason and Bahr, 1979a, 1979b; Moses, 1983). This has been supported by recent studies at Thornton, which compared the above four properties with combustion data obtained from a realistic, high-pressure combustion rig (Bowden and Pearson, 1985). In particular, the poorest predictions were obtained for fuels derived from less conventional sources such as shale oils, tar sands, and upgraded petroleum residues. Overall, of these parameters, naphthalenes and aromatics content are the least effective predictors of combustion performance; hydrogen content is appreciably better and Smoke Point is the most effective.

Unfortunately, the Smoke Point test has several important limitations. In addition to failing to predict the performance of some possible future fuels, there are serious inherent limitations in the test method itself. A study of the intrinsic errors involved in the Smoke Point determination shows that, although the test procedure itself is satisfactory, operator error could have a significant effect on the accuracy of the observed Smoke Point. It may thus be concluded that some degree of instrumentation, and ultimately automation, would be advantageous in this respect. Various such modifications have been attempted. For example, the Luminometer, as detailed in ASTM D1740-75, is essentially a standard Smoke Point lamp that employs instrumentation to determine a "smoke point." However, the operating principles of the Smoke Point lamp impose a significantly more fundamental, and intractable, limitation upon its application to gas turbine fuels. The combustion from such lamps takes place in a wick-fed laminar diffusion flame and hence the flame size and shape will depend, inter alia, upon the viscosity and density of the fuel. Furthermore, the performance of such a flame can never successfully simulate the more complex process of combustion in a gas turbine engine, where the flame may be considered as most realistically characterized by a turbulent diffusion flame.

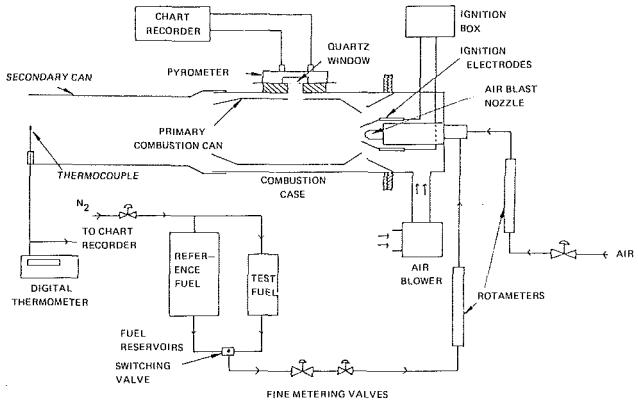

Fig. 1 Schematic of Miniburner system

Clearly, in seeking an improved fuel combustion quality test, it would be desirable to use a technique more closely resembling combustion within a gas turbine engine. This paper describes the development and evaluation of a procedure capable of unequivocally predicting the combustion performance of all aviation kerosines—the Shell Premixed Burner.

Experimental

Two techniques for evaluating fuel combustion quality were studied initially. One employs an atomized fuel spray and thereby simulates a turbulent diffusion flame, whereas the other is based on a premixed flame.

Diffusion Flame Apparatus—the Shell Miniburner. This apparatus (Fig. 1) consists of an airblast-type atomizer located

Contributed by the Gas Turbine Division of THE AMERICAN SOCIETY OF MECHANICAL ENGINEERS and presented at the 32nd International Gas Turbine Conference and Exhibit, Anaheim, California, May 31–June 4, 1987. Manuscript received at ASME Headquarters February 10, 1987. Paper No. 87-GT-125.

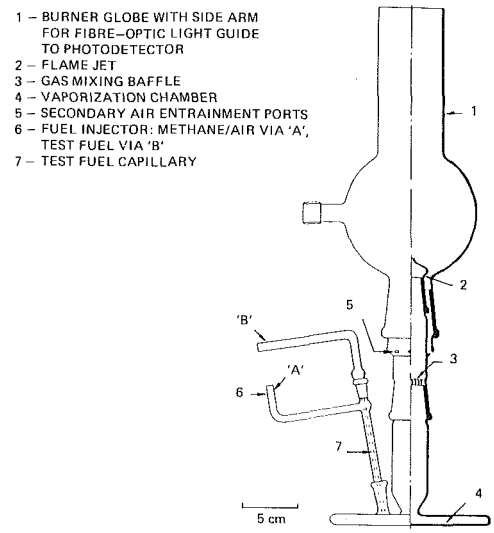

Fig. 2

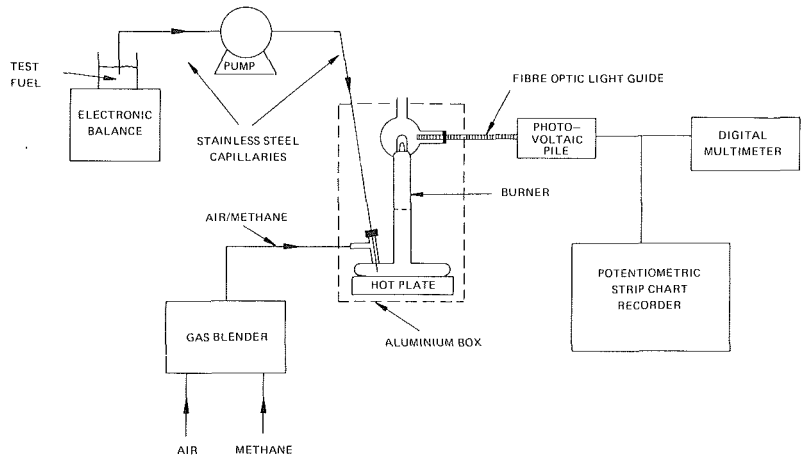

Fig. 3

Fig. 2 The premixed burner assembly (test fuel capillary not to scale)

Fig. 3 Schematic of premixed burner and ancillary equipment

in a suitable primary combustion can and outer casing. The primary can has a diameter of 7 cm and the overall length of the combustor (primary and secondary cans) is 45 cm. Combustion air is supplied by an electric blower, which also provides cooling air. Fuels are delivered from pressurized reservoirs via a series of precision needle valves and a rotameter. The fuel flow is adjusted so that the gas temperature, measured by a thermocouple situated at the end of the outer casing, is constant during the test. The flame radiation is monitored through an observation port in the primary can by a Moll-type pyrometer. Both thermocouple and pyrometer outputs are monitored and recorded continuously.

To reduce errors, each test fuel is evaluated between two reference fuels, one a highly paraffinic solvent to represent a clean burning fuel, the other a highly aromatic solvent representing a very poor fuel. Fuel combustion quality is determined from the observed flame radiation levels via the following expression, which states the performance of the test fuel in terms of a dimensionless number, the Miniburner Test Number (cf. Luminometer Number):

$$\text{Miniburner Test Number} = \frac{(RT - RP) \times 100}{(RA - RP)} \qquad (1)$$

where RT = flame radiation of test fuel at constant exhaust temperature
RP = flame radiation of paraffinic reference fuel
RA = flame radiation of aromatic reference fuel

In practice it was found that the Miniburner was difficult to set up and maintain at a stable condition; the fuel burned with a violent and unpredictable flame some 60 cm long. For these reasons, which militate against automation and ease of operation, and in light of the somewhat disappointing ability of the device to predict combustion performance, it was concluded that this approach lacked promise as a candidate routine test method. Accordingly work was terminated after an initial series of experiments and effort concentrated on the premixed flame alternative.

Premixed Flame Device—the Shell Premixed Burner. The basic methodology of the premixed flame technique, the Shell Premixed Burner, may be summarized as follows. A small quantity of vaporized test fuel is added at a controlled flow rate to a premixed methane/air supply, which is burning as a stable Bunsen-type flame, thereby reducing its air/fuel ratio. As the rate of test fuel addition is increased, the onset of carbon formation in the resulting richer flame is indicated by a yellow coloration, the so-called "sooting point." The corresponding rate of liquid test fuel supply at this sooting point is then a measure of the intrinsic propensity of the fuel to form soot.

The Premixed Burner in its original configuration employed a complex copper mixing chamber and burner arrangement that was inherently difficult, and therefore expensive, to manufacture and was prone to large thermally induced dimensional changes. Furthermore, the detection of the sooting point relied upon visual observation by the operator. The equipment and technique outlined in this paper are therefore the culmination of a development program seeking to evolve a simple, cheap, and durable apparatus, from which the human element in the sooting point detection process is removed.

The core of the Premixed Burner (Fig. 2) is a borosilicate glass assembly consisting of a shallow cylindrical vaporization chamber, a riser comprising a mixing column and burner jet, and a protective glass chimney. The overall height of the device is approximately 50 cm. Substitution of low thermal expansion glass for copper answered many of the immediate problems encountered with the initial version of the burner. Glass construction conferred the additional advantage of permitting direct observation of events occurring within the burner; in particular, the accumulation of any fuel residues in the vaporization chamber would be immediately apparent. Although the form of the assembly remains somewhat complex, the process of manufacture is fairly routine and employs many elements of standard laboratory glassware.

The vaporization chamber is heated by placing the assembly on a suitable hotplate. Liquid test fuel in a glass capillary and the methane/air mixture are fed co-annularly through a common injection port into the heated chamber. The jet of liquid fuel emerging from the capillary, which terminates at an optimum distance above the chamber base, flash vaporizes instantaneously and is carried away by the surrounding methane/air stream. This co-annular arrangement both permits the methane/air flow to cool the test fuel in the capillary, so reducing the possibility of premature vaporization and vapour locking, and provides a degree of airblast-type atomization at the capillary orifice. The resulting mixture travels through the riser, whose length and the presence of an intermediate baffle ensure fully intimate mixing, and burns at a "fishtail" jet. The whole assembly is contained in an aluminum box which ensures that a uniform temperature and

a draft-free environment are maintained in the vicinity of the burner.

The associated equipment supplying and metering liquid and gaseous fuels and the sooting point detection system outlined below have been selected as a matter of policy from commonly available proprietary units. The general layout is illustrated in Fig. 3.

The test fuel is contained in a suitable vessel located on an electronic top-pan balance. It is supplied to the burner via a stainless steel capillary using a precision pump that is capable of delivering extremely small volumes of liquid. During development work, a pump from a high-pressure liquid chromatograph has been used.

Premixed methane/air is supplied to the burner at a flowrate of 3.2 liter min^{-1} and with a molar air/fuel ratio (MAFR) of 5.9:1 (14.4 percent vol methane), which is considerably richer than stoichiometric. Combustion thus takes place in two distinct zones. At the core of the flame there is a region of premixed combustion; this is surrounded by a mantle of laminar diffusion combustion, the secondary air for which is entrained via ports at the base of the upper burner assembly such that the overall MAFR is close to stoichiometric. The selection of a rich premixed gas mixture accordingly provides a stable, quiescent flame that requires only a small quantity of additional fuel to initiate soot formation; hence the title "Premixed Burner." Both factors are essential to the successful application of instrumented detection insofar as they ensure that the flame shape and spatial location remain virtually constant, irrespective of test fuel, at the sooting point.

Initially, the sooting point of the flame was determined by eye. This approach required a skilled operator and introduced a high degree of inherent subjectivity (cf. Smoke Point determination). To remove this operator dependency and to make the technique more amenable to eventual routine quality control application, an instrumented sooting point detection method has been developed. Of the various possible techniques for flame soot detection only optical methods were seen as appropriate to this application. Accordingly several optical approaches were considered and of these four were selected for appraisal, namely:

(*a*) laser light scattering and absorption employing a He–Ne laser source;

(*b*) low-level visible light detection by a photomultiplier tube at various selected wavelengths;

(*c*) infrared emission measurements using a Golay-type detector;

(*d*) visible light detection using a solid-state photovoltaic pile.

The method finally chosen, on grounds of simplicity, safety and effectiveness, was the fourth. The particular component used in these studies has an operating range of 500–900 nm. A fiber-optic light guide, positioned in the side arm of the chimney to view the appropriate portion of the flame, carries the light directly to the window of the device. In the present system the output is fed both to a potentiometric strip chart recorder and a microprocessor-controlled digital voltmeter (DVM). The DVM that has been used offers several inbuilt signal filtering and averaging programs, which are particularly beneficial for reducing the instrument noise associated with such a system.

Premixed Burner Number, PMBN. The index of fuel combustion quality determined by this device, the Premixed Burner Number, PMBN, has been defined as follows:

PMBN = time, in seconds, for 0.5 g of test fuel to flow when the flame is at the predefined "sooting point" (2)

During these development studies, a proprietary paraffinic solvent, Shellshol T, has been used to define the sooting point, which corresponds to an unambiguous level of DC output from the photodetector when viewing a flame in which visible luminous characteristics have become established. The PMBN so defined is clearly a function of the reference fuel and the discrimination of the ancillary equipment; however, any future standardized premixed flame combustion quality specification would address this with the appropriate calibrations.

Table 1 Combustion-related inspection properties of test fuels

Fuel	Hydrogen content, %w	Smoke point, mm	Aromatics content, %v
Reference Jet A1	13.81	24	19.0
Shellsol T	15.16	45	1.6
Mexican MGO	13.23	17	25.1
Monogas	13.34	19	20.4
ERBS 1	13.22	16	28.6
Mexican kerosine	13.96	27	18.7
Jet A1	13.81	23	21.2
Jet A1	14.19	26	9.8
BS2	14.17	25	11.2
BS3	13.06	17	23.0
BS4	14.03	24	15.5
BS6	13.75	23	6.7
BS10 (tar sands)	13.15	18	23.2
BS13 (tar sands)	12.68	14	37.6
Jet A1	13.66	22	24.7
JP 5 (oil shale)	13.76	25	20.1
High naphthalene kerosine	13.70	20	19.1

Notes: (a) BS = kerosine blending stream
(b) Monogas and MGO are similar to No. 2 fuel oils (ASTM D396)

Evaluations of the Premixed Burner Number of Selected Fuels and Correlations With Full-Scale Combustion Performance. The Premixed Burner Numbers of a set of 17 fuels have been determined. The fuels were selected to embrace a wide variation in hydrogen content, aromatic content, and Smoke Point. Fuel sources included, in addition to traditional petroleum-derived materials, oil shale and tar sand-derived products and covered several processing routes (straight run, hydrocracked, sweetened, hydrotreated). The combustion-related properties of the test fuels are presented in Table 1.

To enable a realistic assessment of the validity of the Premixed Burner approach to be made, the above fuels were assessed in the Thornton high-pressure aviation combustion facility. For this purpose a single Rolls-Royce Tyne combustor was used; both the combustor and the experimental facility have been described in full elsewhere (Bowden and Pearson, 1984, 1985; Bowden et al., 1984). The combustion conditions chosen were: pressure 1.0 MPa, air/fuel ratio 60/1, air inlet temperature 330°C, and air mass flow rate 1.5 kg s^{-1}, which corresponds to 83 percent of the full power conditions for the Tyne.

The combustion parameters that have been used for this assessment are primary zone flame radiation and exhaust soot concentration. Flame radiation is measured using a wide-angle Moll-type pyrometer; the soot concentration is an average measurement over the combustor exhaust plane. In order to compensate for run-to-run variation, each test fuel evaluation was bracketed by runs with a Jet A1 reference fuel, permitting the results to be nondimensionalized as follows:

$$\text{Normalized Flame Radiation, NFR} = \frac{R_t}{R_r} \quad (3)$$

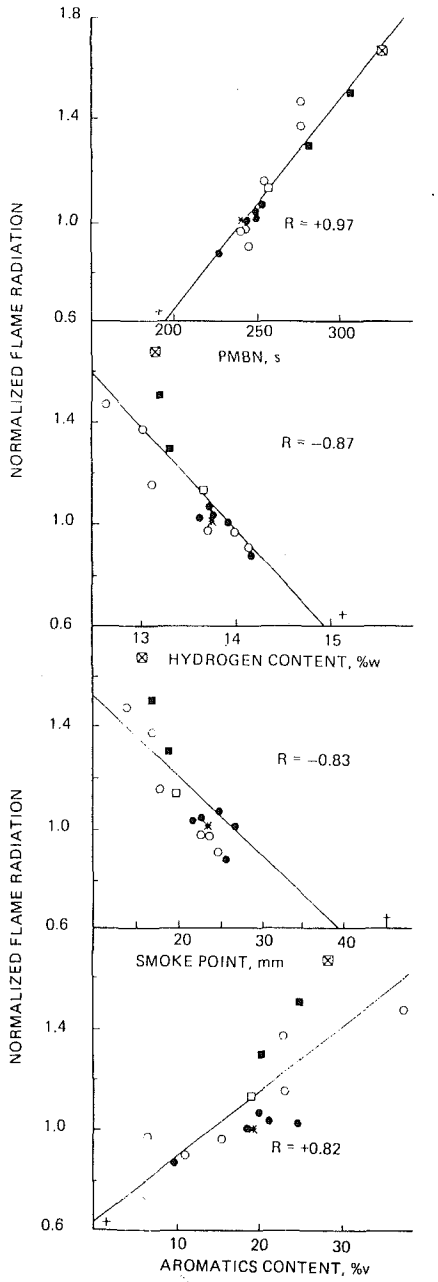

Fig. 4 Normalized flame radiation results for Tyne combustion tests versus Premixed Burner Number, hydrogen content, Smoke Point, aromatics content; R = Pearson correlation coefficient; key for Figs. 4 and 5:

- * REFERENCE JET AI
- \+ SHELLSOL T
- ● JET A1 TYPE FUELS
- ○ BLENDING STREAMS
- ⊠ ERBS FUEL
- ■ GAS OILS
- □ HIGH NAPHTHALENE FUEL

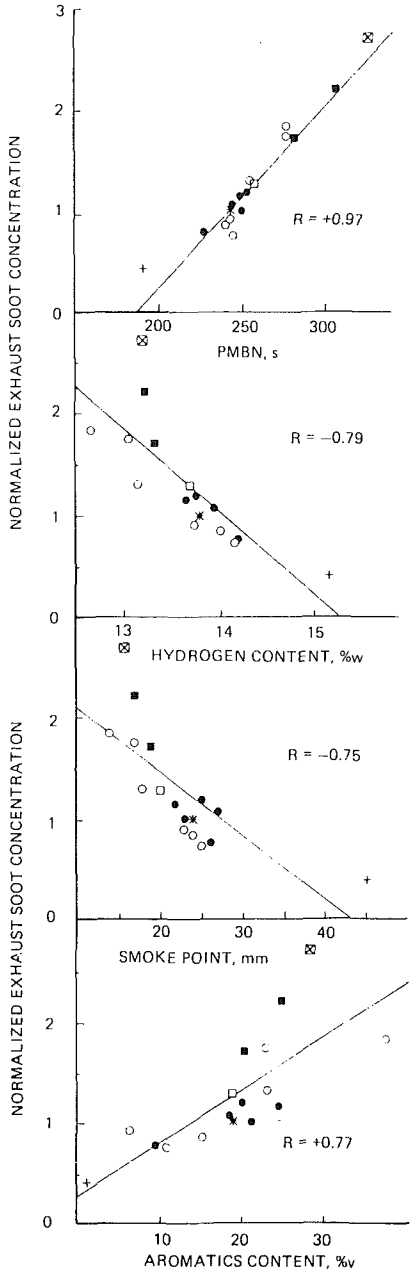

Fig. 5 Normalized exhaust soot results for Tyne combustion tests versus Premixed Burner Number, hydrogen content, Smoke Point, and aromatics content; R = Pearson correlation coefficient

where R_t = radiation from test fuel
R_r = radiation from reference fuel

$$\text{Normalized Exhaust Soot Concentration, NES} = \frac{ES_t}{ES_r} \quad (4)$$

where ES_t = exhaust soot from test fuel
ES_r = exhaust soot from reference fuel

Results and Discussion

The results of the combustion tests and the corresponding Premixed Burner Number for each fuel are presented in Table 2. Exhaust soot concentration and flame radiation are shown plotted against aromatics content, hydrogen content, Smoke Point and PMBN in Figs. 4 and 5, respectively.

On each graph, the best-fit straight line obtained by linear regression has been shown and the Pearson correlation coefficients, which indicate the quality of the linear fit, are quoted. It will be seen that the PMBN is a significantly better predictor of combustion performance than either of the two existing international combustion quality parameters, aromatics content and Smoke Point. It is also a much better predictor than hydrogen content, which has been proposed as a supplement

Table 2 Test fuel Premixed Burner Numbers and results of combustion tests with Tyne combustor: pressure = 1.0 MPa; inlet air temperature = 330°C; AFR = 60/1

Fuel	Premixed Burner Number, s	Tyne combustor results*	
		Normalized flame radiation	Normalized exhaust soot concentration
Reference Jet A1	244	1.00	1.00
Shellsol T	191	0.64	0.40
Mexican MGO	308	1.50	2.20
Monogas	283	1.29	1.70
ERBS 1	327	1.67	2.70
Mexican kerosine	245	1.00	1.07
Jet A1	250	1.03	1.00
Jet A1	228	0.87	0.76
BS2	246	0.90	0.74
BS3	278	1.37	1.73
BS4	242	0.96	0.85
BS6	243	0.97	0.91
BS10 (tar sands)	255	1.15	1.30
BS13 (tar sands)	278	1.47	1.83
Jet A1	250	1.02	1.15
JP 5 (oil shale)	254	1.06	1.19
High naphthalene kerosine	257	1.13	1.28

* Results normalized with respect to the Reference Jet A1

to the present combustion quality descriptors in the ASTM D1655 specification.

The Premixed Burner thus appears to be a comprehensive predictor of aviation fuel quality embracing not only current Jet A1 kerosines but also nonstandard aviation fuels (gas oils, ERBS fuels) and fuels derived from unconventional sources. Furthermore, preliminary analysis indicates that the precision of the technique is significantly better than that of the Smoke Point test: For a fuel of nominal 20 mm Smoke Point, the PMBN repeatability of ±2 percent compares favorably with the Smoke Point figure of ±10 percent.

The Premixed Burner hardware and technique are now undergoing further refinement. To assist with this, a group of prototype units has been manufactured and distributed to interested authorities in the UK and USA. This stage is a prelude to a possible ASTM candidate test method submission.

Conclusions

1 An instrumented device for determining aviation fuel combustion quality, based on a premixed methane/air Bunsen-type flame and referred to as the Premixed Burner, has been developed.

2 The index of fuel combustion quality derived from the Premixed Burner, the Premixed Burner Number (PMBN), exhibits a markedly better correlation with observed full-scale combustion performance than aromatics content, hydrogen content, or Smoke Point.

3 The PMBN appears to be capable of predicting the aviation combustion performance of a very wide range of traditional and unconventional fuels.

4 The Premixed Burner has a higher precision than the Smoke Point test.

Acknowledgments

The authors wish to thank the management of Shell Research for permission to publish this paper and the British Ministry of Defence for their support in this work. Acknowledgments are also due to Mr. J. Milner and Mr. A. T. Pritchard for fabrication of the prototype Premixed Burner and its forerunners and for their valued comments and suggestions.

References

Blazowski, W. S., 1979, "Dependence of Soot Production on Fuel Blend Characteristics and Combustion Conditions," ASME Paper No. 79-GT-155.

Bowden, T. T., and Pearson, J. H., 1983, "The Influence of Fuel Composition Upon Soot Emissions and Flame Radiation in a Model Gas-Turbine Combustor," *International Conference on Combustion in Engineering*, Paper C70/83, Vol. 2, I. Mech. E. Conference Publication 1983-3.

Bowden, T. T., and Pearson, J. H., 1984, "The Effect of Hydrocarbon Structure Upon Fuel Sooting Tendency in a Turbulent Spray Diffusion Flame," ASME JOURNAL OF ENGINEERING FOR GAS TURBINES AND POWER, Vol. 106, pp. 109-114.

Bowden, T. T., Pearson, J. H., and Wetton, R. J., 1984, "The Influence of Fuel Hydrogen Content Upon Soot Formation in a Model Gas Turbine Combustor," ASME JOURNAL OF ENGINEERING FOR GAS TURBINES AND POWER, Vol. 106, pp. 789-794.

Bowden, T. T., and Pearson, J. H., 1985, "The Effect of Fuel Composition Upon Combustion Performance in a Rolls Royce Tyne Combustor," ASME Paper No. 85-GT-39.

Gleason, C. C., and Bahr, D. W., 1979a, "Evaluation of Fuel Character Effects on the J79 Engine Combustion System," AFAPL-TR-79-2015.

Gleason, C. C., and Bahr, D. W., 1979b, "Evaluation of Fuel Character Effects on the F101 Engine Combustion System," AFAPL-TR-79-2018.

Moses, C. A., 1983, "Fuel Effects on Engine and Combustion Performance and Durability," presented at the CRC Symposium on Combustion Characteristics of Aviation Turbine Fuels, Dayton, OH, May 13, 1983.

Moses, C. A., and Naegeli, D. W., 1979, "Fuel Property Effects on Combustor Performance," ASME Paper No. 79-GT-178.

Naegeli, D. W., and Moses, C. A., 1980, "Effect of Fuel Molecular Structure on Soot Formation in Gas-Turbine Engines," ASME Paper No. 80-GT-62.

Naegeli, D. W., Dodge, L. G., and Moses, C. A., 1981, AFLRL-158.

Swirl and Counterswirl Effects in Prefilming Airblast Atomizers

M. Aigner[1]

S. Wittig
Mem. ASME

Lehrstuhl und Institut für Thermische Strömungsmaschinen, Universität Karlsruhe, Karlsruhe, Federal Republic of Germany

The performance characteristics of prefilming airblast atomizers depend largely on the shear stresses in each of the two air supply channels. As an extension of previously reported results, experiments were conducted using an atomizer model with separately controlled air ducts and typical prototype nozzles. It was shown that the quality of atomization can be limited due to internal droplet formation. However, the velocity profiles of the atomization air and the properties of the liquid are the dominant parameters that determine the drop-size distribution generated at the atomization edge. The shear flow at the nozzle exit and the recirculation zone depend largely on the swirl or counterswirl of the exiting air. Correlations have been obtained between the spray characteristics and the relevant parameters.

Introduction

Increasing use is being made of airblast atomizers in stationary combustion processes and for fuel preparation, particularly in gas turbine combustion chambers. An almost ideal combination results in cases where the atomization performance can be matched to the required operating parameters. These are mainly the mass flow provided for the combustion at a given load point and the pressure loss in the primary air needed to stabilize the flame. For this, it is advantageous to swirl the primary air used for flame stabilization before atomization of the fuel.

Unlike pressurized atomizers that are also used quite extensively, airblast nozzles feature a significant control range as a result of the decoupling of atomization quality and the fuel mass flow. In addition, it is easier to control the spatial distribution of droplets. The advantages and problems associated with these nozzles have already been discussed in detail [1–7].

The principle of the "prefilmer," as shown in Fig. 1, has become of particular importance in recent years. Here, an air stream drives the fuel to the atomization edge in the form of a thin, wavy film. A second air stream is used to prevent the fuel from accumulating at the edge, and atomization occurs in the shear zone between the two air streams.

Several authors have studied this and similar atomization principles. Extensive bibliographies have been presented by several authors, especially by Lefebvre [3]. Generally, though, only global empirical dependencies of an average droplet diameter on the entry parameters are reported. Processes within the nozzle, such as the reciprocal effects between the liquid film and the air stream, have generally been neglected, although, as Wittig and Sattelmayer [4, 5] have shown, they can be of significant importance. Nor was there consideration given to the fact that the atomization air at the atomization edge possesses a flow profile which, under the influence of the gap height or the pressure gradients in the air channels, can greatly affect the breakup of the liquid [6, 7]. For these reasons, the effects that the suggested swirling of the atomization air will have on the flow within the nozzle, and thus on droplet formation, must be carefully analyzed. The swirl naturally has a considerable effect on the flow field and the droplet path downstream from the nozzle. Details of these phenomena are reported elsewhere [6] and will be discussed in the near future.

Test Procedure

Within the scope of an extensive test program to study the various parameters of influence, several airblast atomizers were built. Most of the measurements discussed here were taken on a model atomizer of axial symmetry (Fig. 2). The scaling and applicability of the data were rechecked on nozzles similar to those used in practical applications. A typical example is illustrated in Fig. 1.

All nozzles were modular in design, which made it possible to vary the channel heights, pressure gradients, and swirl components. Untwisted and unbent axial guide vane cascades were used to generate the swirl. Detailed flow measurements and photographs of flow rivulets (Fig. 3) confirmed that the desired swirl angles of $\alpha = 0$, 15, 30, 45, 60, and 70 deg were maintained across the entire height of the channel within tolerances of less than 5 deg. In the model nozzle, unlike those similar to actual practice, the inner and outer air channel each had its own supply line and each could thus be controlled independently of the other.

The surface tension, viscosity, and density of the liquid were varied within the following ranges:

$$\sigma : 23 \text{ to } 73 \text{ dyn/cm}$$
$$\mu_L : 0.8 \text{ to } 33 \text{ cP}$$
$$\rho_L : 850 \text{ to } 1050 \text{ kg/m}^3$$

by using various mixtures of water, glycerine, and ethanol. In

[1] Current address: BBC Brown, Boveri & Cie. AG, Baden, Switzerland.

Contributed by the Gas Turbine Division of The American Society of Mechanical Engineers and presented at the 32nd International Gas Turbine Conference and Exhibit, Anaheim, California, May 31–June 4, 1987. Manuscript received at ASME Headquarters February 19, 1987. Paper No. 87-GT-204.

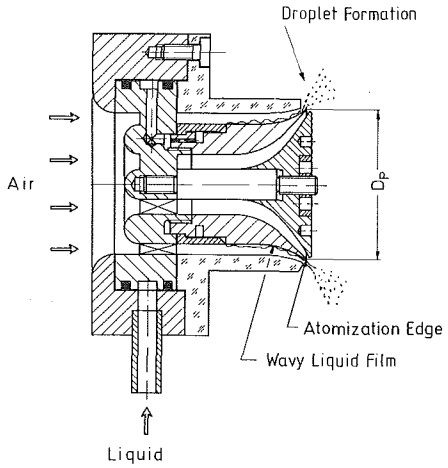

Fig. 1(*a*) Airblast atomizer

Fig. 1(*b*) Photograph of a working airblast atomizer

studying the swirl, however, only water was used. Series of holes made it possible to apply the film of liquid in the inner channel, the outer channel, or in both channels simultaneously. Because the outermost channel wall was made of plexiglass, the film could be observed quite clearly when it was admitted to the outer channel (Fig. 3).

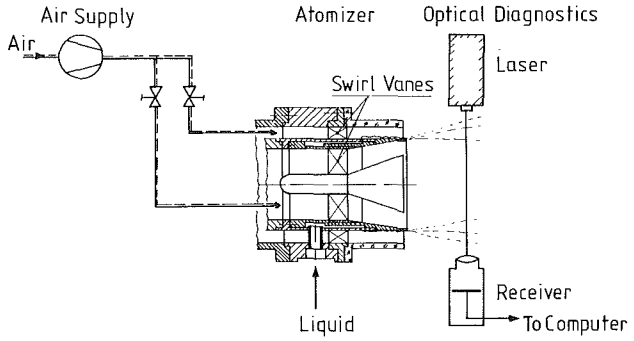

Fig. 2 Model atomizer

Measuring Equipment

The instrumentation and the principles of measurement employed and the initial testing of the equipment have been discussed earlier by us in detail [6–8] and will therefore merely be mentioned briefly here. Calibrated rotameters and standard orifices were used to determine the mass flows. Static and total pressure measurements were used in the deriving of the velocity and, following the Preston method, the wall shear stress.

The atomization of the liquid and the droplet paths were observed using, among other equipment, a high-speed spark camera (illumination time 10^{-7} s). The droplet size distribution and concentration were measured using a Malvern Particle-Sizer, Type ST 2200. Calibration tests, using glass balls and Hirleman's [9] glass reticles, confirmed the accuracy of the data. The diode measurements were corrected using the method suggested by Dodge [10]. As demonstrated by Aigner and Wittig [7, 8], a necessary requirement for accurate data interpretation is knowledge of the velocity of each droplet class. The simplest case, though, is found when all droplets have the same velocity. Otherwise misinterpretations of up to 50 percent in concentration and size not only are possible, but have actually been made, in evaluating atomization nozzles.

As the local concentration distribution is important for fuel nozzles, however, the evaluation was supported by a tomographic procedure. The attempt to describe the technique would lead too far in the context of this paper. Details have been reported by Aigner [6] and will be discussed in an upcoming paper [16].

Results

As has been reported on several occasions [2, 4–8], the volumetric flow of the liquid, i.e., the thickness of the film, is not a parameter that directly influences the breakup at the atomization edge. This must be attributed to the fact that the liquid is stored in the wake of the edge in the form of a bulge. This bulge increases in thickness until the aerodynamic forces

Nomenclature

$b = \pi \cdot D_p$ = circumference of the atomization edge, m
D_p = diameter of the atomization edge, m
$D_{V,0.5}$ = volumetrically averaged mean diameter, μm
$D_{V,0.16}$ = mean diameter; 16 percent by volume of the drops are smaller than $D_{V,0.16}$, μm
$D_{V,0.84}$ = mean diameter; 84 percent by volume of the drops are smaller than $D_{V,0.84}$, μm
Δp = pressure loss, N/m^2
u = velocity, m/s
$\bar{u}$ = volumetrically averaged velocity
$\dot{V}$ = volume flow rate, L/h
$\dot{V}_L/b$ = relative flow volume rate, cm^3/(s cm) = (10^{-4} m^2/s)
α = swirl angle, deg
μ = viscosity, cP
ρ = density, kg/m^3
σ = surface tension, dyn/cm = 10^{-3} N/m
τ = friction, N/m^2

Subscripts

A = air
ax = axial
i = inner
L = liquid
max = maximum
o = outer
Pr = Preston
W = water

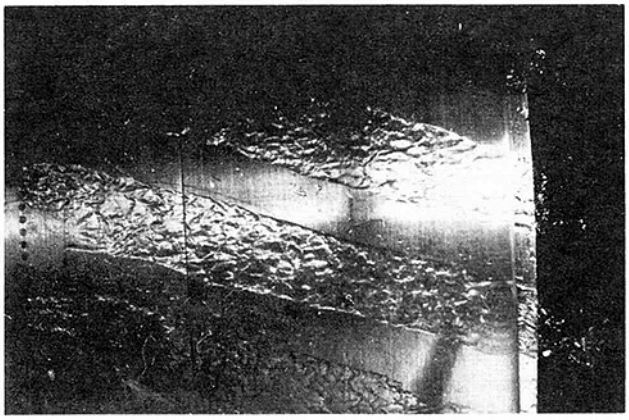

$\alpha = 15°$

$\alpha = 45°$

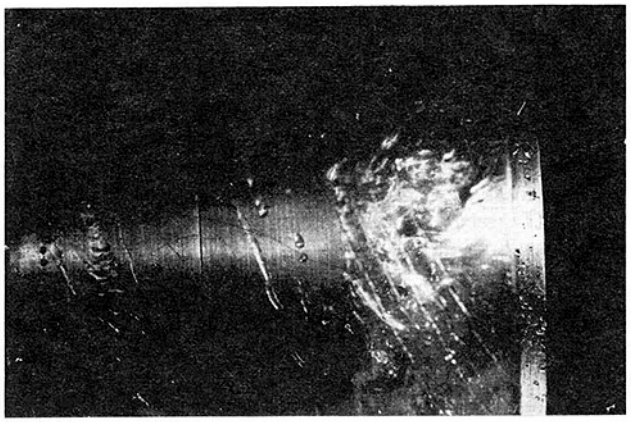

$\alpha = 70°$

Fig. 3 Photograph of film rivulets

exceed the surface forces (Fig. 4). During acceleration to the air speed, the drawn-out rivulets in the liquid disintegrate into droplets directly behind the acceleration edge. This leads to the conclusion that whenever the air velocity in both channels is identical and constant, no effect on the size of the droplets is observed (Fig. 5 for $u_{\max,o} = u_{\max,i} = \text{const}$).

Of course, in nozzles with narrow air channels and an increasing volumetric flow of liquid, the air velocity in the channel carrying the film drops considerably due to the effects of displacement and roughness of the liquid film. For the nozzle

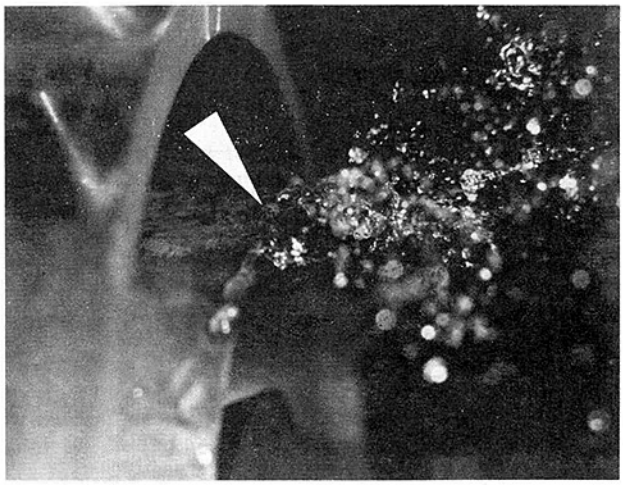

Fig. 4 Liquid atomization ($u_a = 30$ m/s, $\dot{V}_w/b = 0.61 \times 10^{-4}$ m^2/s)

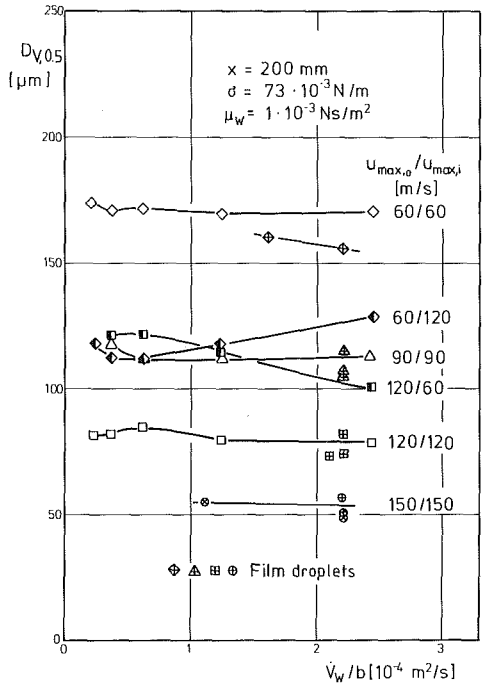

Fig. 5 Influence of the liquid flow on the drop size, with balanced and unbalanced air velocities

shown in Fig. 1, the flow rate was measured at constant supply pressure of the atomization air, which generally is the controlling parameter. A reduction in the mass flow up to 70 percent in the outer channel was observed. With decreasing air flow and other conditions unchanged, the droplets become larger.

As indicated, the two air channels in airblast atomizers commonly used are both supplied from a single pressure reservoir. This leads to an additional effect produced within the nozzle itself. Because of the reaction of the liquid film, there is always an imbalance between the air velocities in the two channels. Regardless of the channel geometry and the parameters of the liquid, the air velocities can easily differ by a factor of more than two. If, at the same time, the volumetric flow of liquid exceeds a "critical" point, the wave structure of the film changes and droplets are pulled out of the film before it reaches the atomization edge (e.g., [11, 5]). The critical liquid volumetric flow, normalized to the wetted perimeter, is found to be between 0.6 and 0.8 cm^2/s and in actual practice will frequently exceed these values by a factor of five. The drops thus

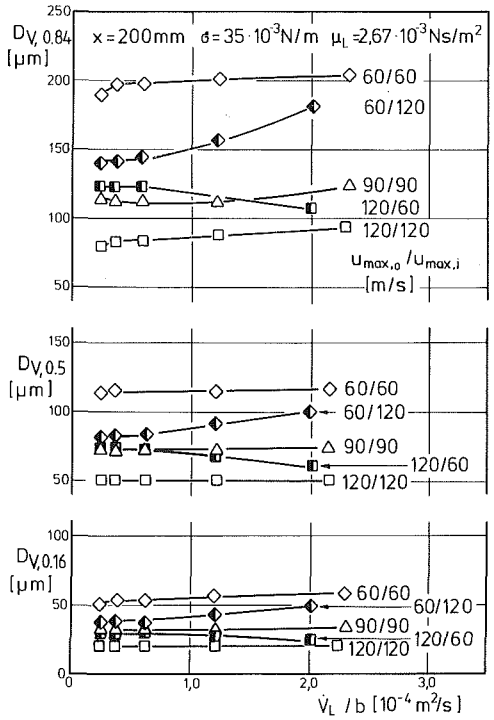

Fig. 6 Influence of the film droplets at low surface tension

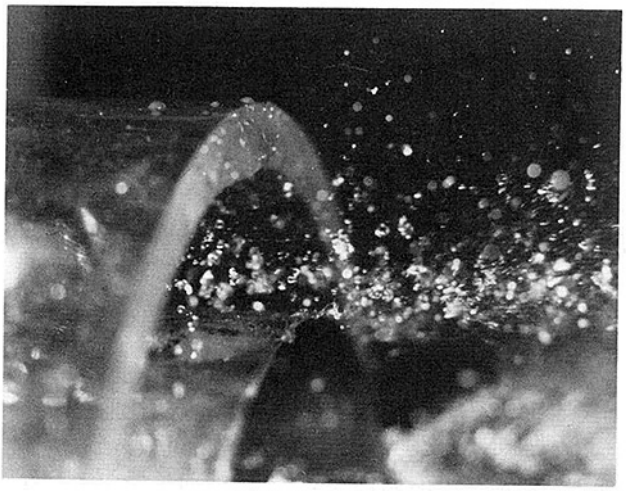

Fig. 7 Internal atomization of the liquid film ($u_A = 30$ m/s, $\dot{V}_W/b = 1.21 \times 10^{-4}$ m²/s)

formed, referred to as "film droplets," have been measured and surprisingly agree quite well in size with the droplets formed on the atomization edge at the same air velocities (Fig. 5). For this reason, when the air velocities in the outer and the inner channels are the same, no effect can be observed unless the opposite wall of the channel also becomes wetted. When the air velocities differ, however, an increasing volumetric flow of the liquid and, with that, an increasing proportion of film droplets cause the drop spectrum to shift more and more to the drop sizes that are typical for the air velocity in the channel carrying the liquid (Fig. 5). This effect becomes more evident when surface tension is low (Fig. 6) as, under these conditions, the portion of film droplets increases drastically [12]. On the other hand, a rise in the viscosity of the liquid does not show any effect on drop size despite an increasing film thickness.

In comparing Figs. 4 and 7, it should be noted that, with an excessive film thickness, proper functioning of the nozzle is not assured.

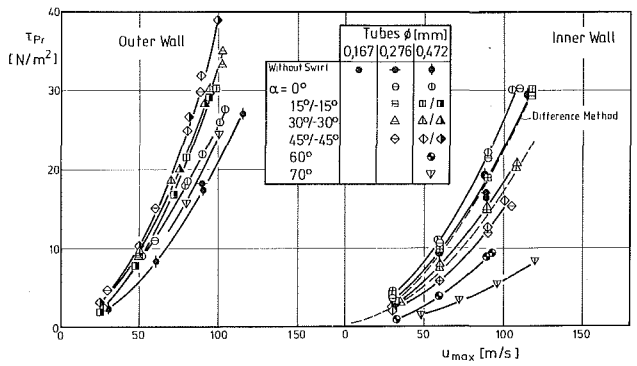

Fig. 8 Frictions determined by the Preston method for different swirls

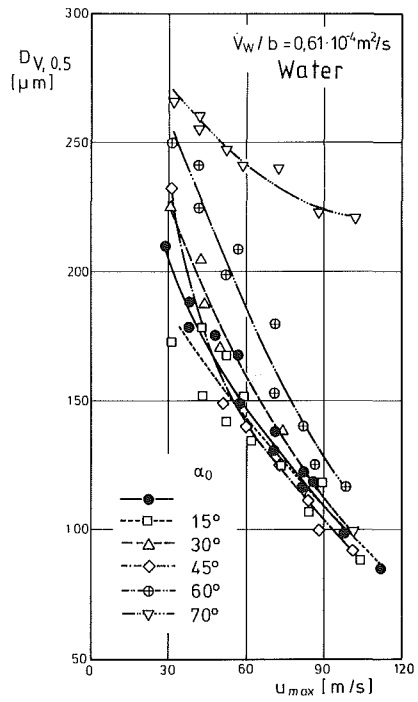

Fig. 9 Single-sided swirling of the outer channel

Effect of the Swirl

As explained above, the sizes of the droplets produced are not only inversely proportional to the air velocity, as, for example, shown in Figs. 5 and 6, but the breakdown is also strongly affected by the flow profile of the atomization air at the atomization edge [6]. In an attempt to determine the changes of the flow profile with a swirl, the wall shear stresses are compared. Figure 8 shows the values obtained applying the Preston method. As the reliability of this procedure is not assured in swirling flows, additional measurements were taken with other tube diameters for comparison, as suggested by Rechenberg [13] and Patel [14]. The check showed that up to a swirl angle of 45 deg, there is close agreement. On the other hand, the Preston stresses τ_{Pr} for larger swirl angles can only be considered as rough approximations for the wall shear stress. There was actually a stall found in the air flow on the inner wall with a swirl angle exceeding 60 deg. Accordingly, the wall shear stress should approach zero for $\alpha = 70$ deg.

For the swirl-free air flow, a numerical finite difference code originally developed for blade heat transfer problems [15] was used to calculate the boundary layer parameters. The results differ only insignificantly from the measurements.

It is interesting to note that the wall shear stresses will in-

crease by approximately 20 percent along both channel walls if a 0 deg vane cascade is installed. If there is an additional swirl imposed, the wall shear stress decreases steadily on the inner wall with increasing swirl angle and increases, as expected, on the outer wall. The air flow in the inner channel exerts a shear stress on its outer wall, while the air flow in the outer channel exerts a shear stress on its inner wall. Both these stresses are effective at the atomization edge. Consequently, to interpret the droplet sizes that result, a superposition of these two stresses should be used. A series of tests, with additional correlations of measured droplet sizes, shows that the mean stress

$$\bar{\tau} = \sqrt{\tau_{\mathrm{Pr},o} \cdot \tau_{\mathrm{Pr},i}} \tag{1}$$

will lead to an optimal correlation.

Compared to the flow with no interference, the 0 deg swirl generator causes an improvement of 10 μm of the volumetric mean droplet size $D_{V,0.5}$. This should probably be attributed to the higher wall shear stress and turbulence level. A single-sided swirling of the outer channel by up to 45 deg likewise has only a slight effect. On the other hand, for swirl angles exceeding 60 deg, the quality of the atomization increasingly deteriorates (Fig. 9) because of the detached flow at the atomization edge. With a single-sided swirling of the inner channel, the wall shear stress at its outer wall increases. That produces a slight improvement in the droplet spectrum up to 10 percent whenever the inner film applicator is in use.

When cocurrent swirl is applied in both channels, the small droplets remain unchanged. Initially, the medium-sized droplets $D_{V,0.84}$ and $D_{V,0.5}$ decrease in size as the swirl angle increases up to 30 deg, but thereafter will increase again (Fig. 10). An explanation can be found in the superposition of the wall shear stresses from the two channels, which, as confirmed by the Preston method (Fig. 8), follows the inverse trend. On the other hand, atomization is significantly finer with counterswirl, which should be attributed to the high additional turbulence intensity generated in the shear zone downstream of the atomization edge. Here it is mainly the average diameter of the large droplets $D_{V,0.84}$ where a clear reduction occurs: The small droplets are scarcely affected.

Figure 11 indicates one of the major advantages of swirling air flows from the viewpoint of the designer. While the effective atomization forces are determined by the air velocity in the direction of flow ($u_{\max}$), the mass flow through the nozzle is proportional to the axial velocity (u_{ax}). An increase in the swirl velocity produces a clear reduction in axial velocity. At the same time, the pressure loss in the air increases. The design of the swirl vanes used for the present study, though, has not been optimized. With an identical pressure loss, however, a finer atomization would have been attainable only by utilizing counterswirl.

This is consistent with the information obtained from the attempts in reducing the air channel heights [6, 7]. It was found that a proper geometric arrangement can indeed greatly reduce the air consumption of an atomizer. However, an appropriate pressure difference across the nozzle is always required in order to produce a given fineness of the droplet size. The correlation

$$D = C\sqrt{\frac{\sigma}{\Delta p}} \quad \text{using} \quad c_{v,0.5} \approx 0.0026 \tag{2}$$

describes quite well the droplet sizes measured. This may be attributed to the fact that the pressure loss as well as the forces acting on the fluid element show analog characteristics over wide ranges.

Conclusions

In analyzing the performance characteristics of airblast atomizers, internal processes such as the interaction of the liquid film with the driving air flow and the developing boundary layers have to be considered. The following major aspects should be recognized:

- The volumetric flow and the viscosity of the liquid do not show a direct effect on the droplet size produced at the atomization edge. However, the air velocity in the channel carrying the film will be reduced with increasing liquid flow. This is due to the apparent roughness effects. In practical application the droplet size will therefore increase.
- In addition, once the volumetric flow exceeds a certain critical point, droplets are drawn from the film before it reaches the atomization edge. If the surface tension is low, the portion of these droplets can be significant. The drop-size spectrum produced will be negatively affected.
- Swirling the atomization air in order to stabilize the flame can be achieved without reducing the atomization efficiency. Flow stall at the atomization edge should be avoided if the swirl is strong ($\alpha > 60$ deg).
- With a proper selection of swirl elements, and particularly with counterswirl, the shear stresses effective on the atomization edge can increase, resulting in a finer atomization. Particularly the size of the largest droplet classes is reduced.
- In all cases, the amount of air required by the atomizer to

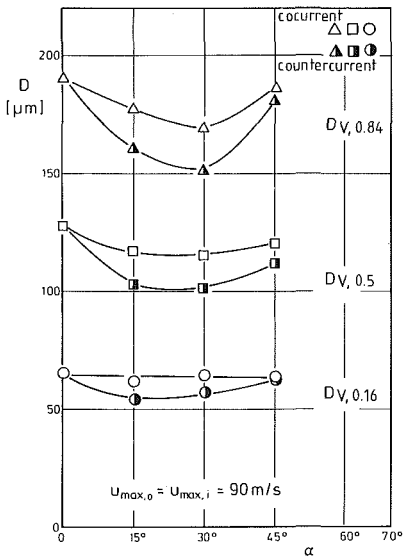

Fig. 10 The influence of swirl on the droplet spectrum

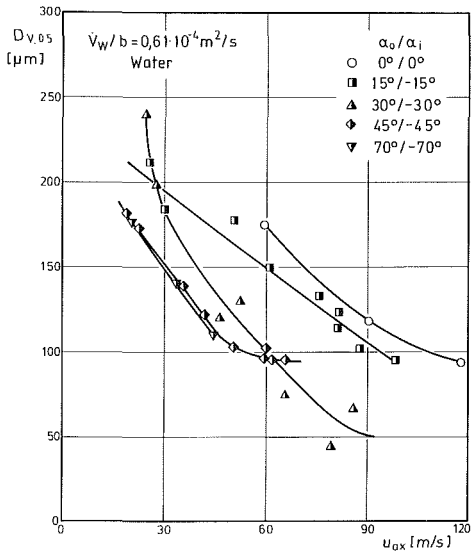

Fig. 11 The influence of swirl on the air consumption of an atomizer

produce a constant quality of atomization is significantly reduced by employing swirl.

- The droplet size attainable can be estimated from the pressure loss available in the atomization air by using a simple correlating equation.
- These results can be extended to other atomizer designs if the flow conditions, and especially the wall shear stress at the atomization edge, can be determined. It is possible to do this in several ways: for larger nozzles, by means of measurement, or, more generally, by using empirical correlations or difference methods as shown in Fig. 8 to calculate the channel flow [4, 5].

It should be emphasized that swirl can also be employed to influence the spatial distribution of droplet sizes and the uniformity of local rivulets (see [6]).

Acknowledgments

Thanks are due to the Forschungsvereinigung Verbrennungskraftmaschinen, e.V. for initiating this research program on atomizers and to the Deutsche Forschungsgemeinschaft (German National Science Foundation) for their support in various aspects of the study within the larger context. of the "Sonderforschungsbereich SFB 167, 'High Intensity Combustors'."

References

1 Wittig, S., Sattelmayer, Th., Aigner, M., and Sakbani, K., "Untersuchung der Strömung und Tropfenbildungsmechanismen in luftgestützen Zerstäubungsdüsen," *Brennstoff-Wärme-Kraft*, Vol. 37, No. 10, 1985, pp. 380–387.

2 Wittig, S., Leuckel, W., Sakbani, K., Aigner, M., Horvay, M., and Sattelmayer, Th., "Experimentelle und theoretische Untersuchung der Strömung und Tropfenbildungsmechanismen in Zerstäubungsdüsen für Gasturbinenbrennkammern," Forschungsvereinigung Verbrennungskraftmaschinen, Abschlussbericht. No. 347, 1984.

3 Lefebvre, A. H., "Airblast Atomization," *Prog. Energy Combust. Sc.*, Vol. 6, 1980, pp. 233–261.

4 Sattelmayer, Th., "Zum Einfluss der ausgebildeten, turbulenten Luft-Flüssigkeitsfilm-Strömung auf den Filmzerfall und die Tropfenbildung am Austritt von Spalten geringer Höhe," Dissertation, University of Karlsruhe, 1985.

5 Sattelmayer, Th., and Wittig, S., "Internal Flow Effects in Prefilming Airblast Atomizers: Mechanisms of Atomization and Droplet Spectra," ASME JOURNAL OF ENGINEERING FOR GAS TURBINES AND POWER, Vol. 108, 1986, pp. 465–472.

6 Aigner, M., "Charakterisierung der bestimmenden Einflussgrössen bei der luftgestützen Zerstäubung: Physikalische Grundlagen und messtechnische Erfassung," Dissertation, University of Karlsruhe, 1986.

7 Aigner, M., and Wittig, S., "Performance and Optimization of an Airblast Nozzle: Drop Size Distribution and Volumetric Air Flow," *Proceedings of the International Conference on Liquid Atomization and Spray Systems*, London, 1985, Vol. IIC/3, pp. 1–8.

8 Wittig, S., Aigner, M., Sakbani, K., and Sattelmayer, Th., "Optical Measurement of Droplet Size Distribution. Special Considerations in the Parameter Definition of Fuel Atomizers," AGARD, 62nd PEP-Symposium on Combustion Problems in Turbine Engines, Turkey, Conference Proceedings No. 353, 1983.

9 Hirleman, E. D., "On-Line Calibration for Laser Diffraction Droplet Sizing Instruments," ASME Paper No. 83-GT-232, 1983.

10 Dodge, L. G., "Calibration of the Malvern Particle Sizer," *Applied Optics*, Vol. 23, No. 14, 1984.

11 Wurz, D., "Experimentelle Untersuchung des Stömungsverhaltens dünner Wasserfilme und deren Rückwirkung auf einen gleichgerichteten Luftstrom mässiger bis hoher Unterschallgeschwindigkeit," Dissertation, University of Karlsruhe, 1971.

12 Gater, R. A., "A Fundamental Investigation of the Phenomena that Characterize Liquid-Film Cooling," Purdue Univ., Rep. No. TM-69-1 and NASA CR-105904, 1969.

13 Rechenberg, I., "Messung der turbulenten Wandschubspannung," *Zeitschrift für Flugwissenschaft*, Vol. 11, No. 11, 1963, pp. 429–438.

14 Patel, V. C., "Calibration of the Preston Tube and Limitations on Its Use in Pressure Gradients," *J. Fluid Mech.*, Vol. 23, Part 1, 1965, pp. 185–208.

15 Scheuerer, G., "Entwicklung eines Verfahrens zur Berechnung zweidimensionaler Grenzschichten an Gasturbinenschaufeln," Dissertation, University of Karlsruhe, 1983.

16 Aigner, M., and Wittig, S., "Entwicklung, Einsatz und Vergleich von Tropfenmessverfahren," in preparation.

R. J. Martin[1]

J. T. Kelly[2]

S. Ohmine[3]

E. K. Chu

Acurex Corporation,
Mountain View, CA 94039

Pilot-Scale Characterization of Dry Sorbent Injection for SO_2 Control in a Low-NO_x Tangential System

A 380-kW (1.3 million Btu/hr) two-burner level, tangentially fired, pilot-scale facility was used to characterize a dry-calcium-based sorbent SO_2 capture technique combined with an offset auxiliary air low-NO_x burner. Baseline tests showed that the facility properly simulates full-scale temperatures and emission levels. Dry sorbent SO_2 test results suggest that for enhanced sorbent SO_2 capture, injection should take place away from the burner zone where temperatures are lower, and that the time sorbent particles spend in the optimal temperature range should be extended as much as possible through sorbent injection methods and temperature profile modification.

Introduction

The significant contribution of coal-fired tangential boilers to national NO_x and SO_x emissions (Lim et al., 1980), and the expected future increase in the number of these boilers, make them candidates for emission control development. Demonstration of cost-effective NO_x and SO_x reduction technology for these boilers will provide regulatory agencies with additional emission control options, which could be exercised by coal users in the future to prevent environmental degradation.

A low-NO_x, tangential burner, which incorporates auxiliary air jets offset toward the wall relative to the primary fuel jets, has been tested in pilot scale, and has been shown to have the potential for achieving NO_x emissions in the range of 90 to 120 ng NO_2 per J (0.2 to 0.3 lb NO_2 per million Btu) (Kelly et al., 1981). Given the desirability of combined NO_x and SO_2 control, low-NO_x burner dry sorbent injection experiments were performed to determine the feasibility of achieving good SO_2 sorption in a low-NO_x system, and the influence of combustor design and injection system variables on SO_2 capture.

Facility

The experimental combustor used for this program is an approximate 1 to 14 geometric scaling of an existing, modern-design, tangentially fired boiler. The overall external height of the furnace is 3.7 m (12 ft), and the firebox interior cross section is 0.9 m by 1.1 m (3.0 ft by 3.5 ft). Combustion products travel upward from the firebox section into a smaller (0.6 m by 0.6 m [25 in. by 25 in.]) convective section and finally to an external baghouse and exhaust. Low-conductivity refractory linings are permanently cast into the radiant and convective sections to maintain gas temperatures at full-scale levels.

Burner geometry and combustor cross section are shown in Figs. 1(*a*) and 1(*b*), respectively. Each burner set includes two levels of primary and fuel (or annular) air ports. Above, below, and between these ports are auxiliary air ports. Overfire air (OFA) ports are also installed 0.4 m (15 in.) above the burner centerline, at each corner.

The primary and fuel air jets have a small degree of yaw angle[4] variability: up to 8 deg from the firebox diagonal. The auxiliary and OFA jets can be aligned at yaw angles of 6, 21, or 37 deg. In the 37-deg position, two of the auxiliary air jets are aligned parallel to the furnace wall. This low-NO_x configuration is denoted offset auxiliary air (OAA).

Air is supplied from a 23 Nm^3/min (800 scfm) centrifugal blower (Spencer 8050) and can be preheated up to 588 K (600°F) by a 100 kW electric resistance heater (Chromalox TDH-60WXX). Air flow rates are measured by sharp-edged orifice plate sets (Vickery-Sims Mark 52) with flange taps connected to differential pressure manometers (Dwyer 1235-16-D).

Pre-pulverized coals are transported pneumatically to the furnace along eight feed lines. Four independently controlled auger feeders (Acrison 105Z-C) are used to meter the coal feed rate. Natural gas firing is used during warmup and cooldown of the facility.

Heat removal in the convective section is accomplished by a closed-loop, Dowtherm-G heat exchange system. Tube surface temperatures were maintained at 395 to 478 K (250 to 400°F) during operation.

Furnace operating temperatures are monitored continuously by unshielded, type J, K, and R thermocouples (Omega), which are connected through an analog-to-digital converter (Tecmar DT-701-T) to a microcomputer (Apple Two Plus, 48K RAM) for processing, display, and storage. Continuous

[1] Currently on educational leave to the Department of Mechanical Engineering, University of California, Berkeley, CA.

[2] Currently with Altex Technologies Corporation, San Jose, CA.

[3] Currently with Gemini Research, Inc., Fremont, CA.

Contributed by the Power Division for publication in the JOURNAL OF ENGINEERING FOR GAS TURBINES AND POWER. Manuscript received at ASME Headquarters July 1, 1987.

[4] Yaw angle is defined as the angle the burner port centerline makes with respect to the firebox diagonal.

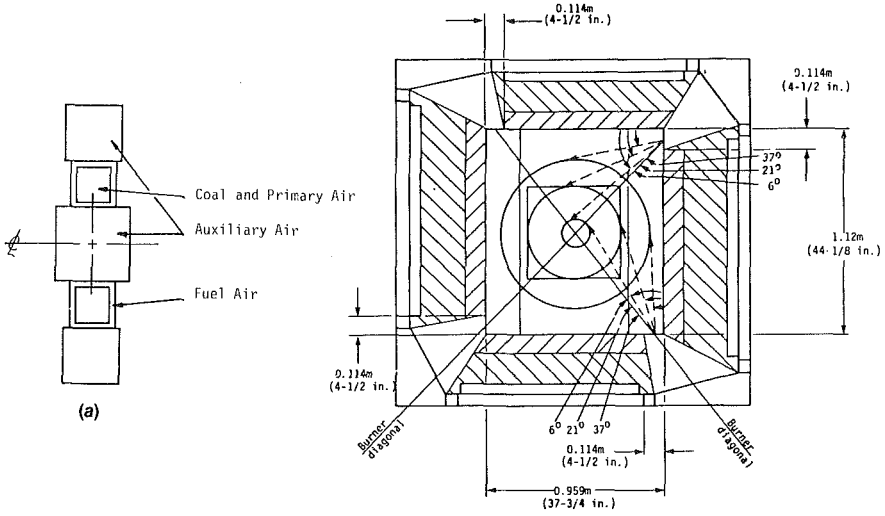

Fig. 1(a) Front view of pilot-scale burner configuration; (b) top view of cross section of tangentially fired pilot-scale furnace

gas analyzers for O_2 (Teledyne 326-A), CO_2 (Anarad AR-600R), CO (Anarad 500-R), hydrocarbons (Beckman 400), NO_x (Thermo-Electron 10), and SO_2 (Teledyne 600) are used to identify major and minor combustion species at a wide range of concentrations. Moisture is removed prior to sample analysis by a pair of customized refrigeration dryers.

Pulverized sorbents, or other solid additives, are injected into the combustor from an auger-feed/pneumatic-transport system (Acrison 105Z-D) that is similar to the coal feeding unit. Sorbent injection is performed through either the existing combustion air ports or through an injector inserted into one of several wall ports along the furnace length. The injector consists of a water-cooled, stainless-steel tube equipped with a right angle, non-diverging, 2.0 cm (0.8 in.) diameter nozzle. Gases are sampled from the downstream end of the convective section where temperatures are approximately 533 K (500°F).

A flue gas recirculation (FGR) system (with blower, Spencer G1503-MOD) is incorporated to allow re-introduction of as much as 40 percent of the filtered exhaust gases into the furnace at the nominal firing rate. This alters the gas temperature history for NO_x or SO_x control purposes.

Verification tests with this facility (Ohmine et al., 1983) have shown that radiant and convective section gas temperatures are in good agreement with full-scale practice (Hazard, 1980; Abele et al., 1982), NO_x emissions for conventional and OFA operating conditions agree in both level and trend with full-scale data (Kokkinos et al., 1983; Habelt, 1977), and reasonable agreement was obtained between pilot- and full-scale limestone/SO_2 capture results for conditions where sorbents were injected through the OFA ports (TVA, 1973; Kellog Co., 1972; Murthi et al., 1981; Ishihara et al., 1975). Based on these comparisons, it was concluded that the pilot-scale facility could be used to evaluate the effectiveness of dry sorbent injection in conventional and low-NO_x tangentially fired systems.

Experimental Results

The goal of the pilot-scale experiments was to characterize the effect of design and operating conditions on dry sorbent injection SO_2 reduction in the tangentially fired system. Emphasis was placed on testing under the low-NO_x firing condition (OAA) to investigate the effectiveness of simultaneous NO_x/SO_x control.

The major parameters studied in these tests included firing rate, excess air, flue gas recirculation (FGR), convective heat exchanger tube arrangement, and sorbent injection method and location. Sorbent particle temperature history was varied implicitly by the variation of these system parameters. During the tests described, the sorbent transport air flow was fixed at 22.7 kg/hr (50 lb/hr). All Ca/S ratios reported do not include the inherent calcium present in the coal.

Illinois number 6 bituminous coal was the fuel used during these experiments. Table 1 gives its properties, as well as those of the limestone sorbent.

All tests were conducted using the following distribution of combustion air: primary air, 12.5 percent; fuel air, 8.5 percent; offset auxiliary air, 79 percent; overfire air, 0 percent. The baseline configuration for the convective tube bank was

Nomenclature

A = calcine area, m^2 (CaO)•(kg(CaO))$^{-1}$
A' = Arrhenius pre-exponential, kg (CaO)•(m^2(CaO) s)$^{-1}$
B = $A' \cdot Z_0 \cdot \exp(-E/R_0 \cdot T_{sorb})$, K•$s^{-1}$
E = Arrhenius activation energy, kJ•kg^{-1}
R_0 = ideal gas constant, kJ•(kg•K)$^{-1}$
R = actual fraction of SO_2 reduction = $(SO_{2_i} - SO_{2_f})/(SO_{2_i})$
S_{max} = asymptotic sorption limit = $(SO_{2_i} - SO_{2_\infty})/(SO_{2_i})$
t = time, s
T = temperature, K
Z_0 = proportionality constant, m^2(CaO)•K•(kg(CaO))$^{-1}$
α = degree of advancement = $(SO_2(t) - SO_{2_i} \cdot (1 - S_{max}))/(SO_{2_i} \cdot S_{max})$

Subscripts

f = final
i = initial
inj = at the point where sorbent is injected
sorb = at the condition chosen to represent rapid sorption
∞ = asymptotic limit

Table 1 Fuel and sorbent properties

Illinois No. 6 Bituminous (percent by weight)						
C	H	O	N	S	H_2O	ash
62.0	4.5	7.6	1.0	3.7	9.6	11.5

El Dorado Coarse Grain Limestone

$CaCO_3$: 98.0 percent $MgCO_3$: 0.9 percent Ground to: 98.0 percent below 44 μm

8-0-8, which signifies the number of 16 mm (0.63 in.) diameter U-tubes extended across the flow channel at the first three heat exchanger locations.

Thermal Conditions. While space does not permit a detailed description of the thermal environment for each test condition, a summary of the impacts of variations in load, convective section tube arrangement, and flue gas recirculation (FGR) on gas temperature history is presented.

Figure 2 plots measured gas temperature versus bulk gas residence time for four different firing conditions with Illinois coal. Residence time is estimated using a variable-density, plug-flow model. It can be seen from the figure that reducing load from nominal decreases temperature at each of the fixed measurement positions, and also increases bulk residence time. Removal of the first two convective tube bundles, as indicated by the line denoted "convective," increases the upper-radiant and convective section temperatures with little alteration in residence time. The use of FGR at the burner level reduced both gas residence time and temperature (by dilution).

Gas temperature affects sorbent SO_2 capture performance through the kinetic processes of calcination, deactivation, and sulfation. For optimal calcination, particle heatup must be rapid and peak temperatures controlled to below 1573 K (2372°F) to avoid deactivation (Coutant et al., 1970). Sulfation should immediately follow calcination, when active surface area is likely to peak, and should take place within a temperature band of 1255 to 1505 K (1800 to 2250°F). Higher temperatures are thermodynamically unfavorable due to $CaSO_4$ dissociation, and at lower temperatures the kinetics are too slow for significant sulfation within the available residence time.

The influence on sorption of changes in the thermal environment will now be discussed.

Firing Rate. Firing rate variations produce the most dramatic effect on the temperature–time profiles of the combustion gases. Figure 3 shows the difference in sulfur capture for nominal and low-load conditions. In these tests, sorbent was injected upward in the center of the furnace through a single 20 mm (0.8 in.) diameter nozzle, 0.3 m (12 in.) above the burner centerline. For reduced load, the combined effects of lower peak temperatures and longer residence times (as illustrated in Fig. 2) at optimum sulfation temperatures serve to increase SO_2 reduction at Ca/S = 2.0 from 22 to 42 percent.

Flue Gas Recirculation. The effect of FGR on SO_2 reduction was determined by recirculating filtered flue gas out of the baghouse (at approximately 450 K [350°F]) and back into the furnace through the overfire air ports. Despite some scatter in the data, the test results in Fig. 4 show that the addition of FGR improves SO_2 reduction from 22 to 33 percent at Ca/S = 2.0. This trend was expected because FGR acted to cool the combustion products in the lower furnace, thereby creating a more favorable temperature profile, as illustrated in Fig. 2, for avoiding deactivation. Apparently, the more favorable temperature conditions overcame any negative impact on SO_2 capture caused by the reduction in residence time.

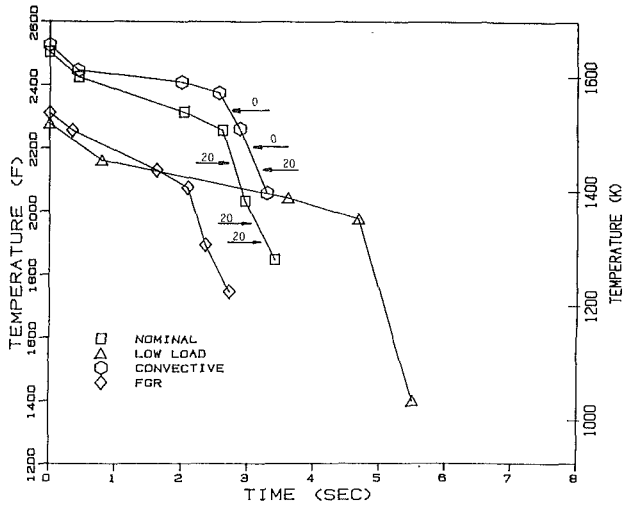

Fig. 2 Example of pilot-scale furnace temperature profiles (nominal is 380 kW, 20 percent excess air, no FGR, 20-20-20 convective arrangement; low load is 300 kW; convective is 0-0-20 convective arrangement; FGR is with 24 percent FGR)

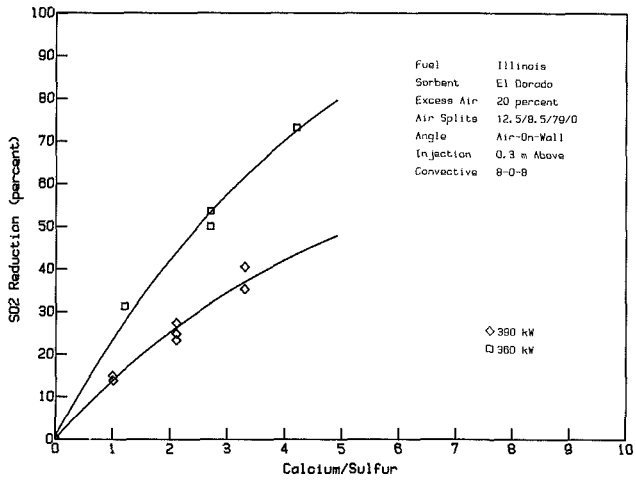

Fig. 3 Effect of firing rate on SO_2 reduction

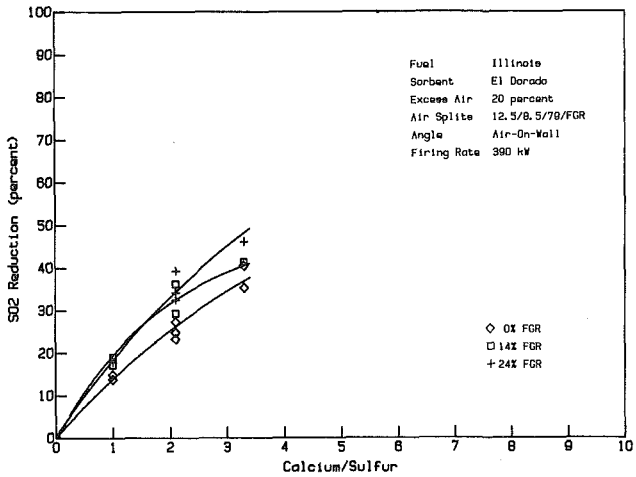

Fig. 4 Effect of flue gas recirculation on SO_2 reduction

Convective Tube Bank Configuration. By changing load or recirculating flue gas, mixing and heat release conditions are altered in addition to temperature history. To alter the temperature profile without disturbing the mixing and heat release patterns in the lower furnace, the convective heat transfer tubes at the entry region of the convective section were rearranged. The location of the three heat exchangers subject to rearrangement is shown relative to the fixed thermocouple locations in Fig. 2.

Results for probe injection of sorbent in the center of the furnace with three heat transfer tube configurations are presented in Fig. 5. The 0-0-20 arrangement was roughly 130 K (235°F) hotter in the convective section than the 20-20-20 arrangement. Although not plotted, the measured temperatures for the 8-0-8 configuration were nearly the same as the 20-20-20 configuration throughout the radiant section, and less than 50 K (90°F) higher in the convective section. As Fig. 5 indicates, the small temperature differences between the 8-0-8 and 20-20-20 configurations apparently did little to affect sorption. However, the 0-0-20 configuration temperature history produced a significant reduction in overall SO_2 capture from 22 to 14 percent. This effect could be due to the sorbent particles experiencing partial deactivation at the higher peak temperatures and/or to less residence time being available at the optimum sulfation temperatures.

Sorbent Injection Location. The objective of this test sequence was to determine the effect of sorbent injection method and location on SO_2 reduction. Changing the sorbent injection method causes variations in sorbent particle mixing and temperature histories. Figure 6 shows the effect on sulfur capture of injecting sorbent in the overfire, lower auxiliary, and primary air ports. In these tests, the sorbent was thoroughly mixed with the tangentially directed combustion air flows prior to injection. The SO_2 reduction results show that lower auxiliary air sorbent injection produced capture similar to, but slightly worse than, OFA sorbent injection. A separate test, where OFA injector yaw angles were varied, showed no difference in SO_2 capture. Primary air injection of sorbent consistently gave the lowest SO_2 reduction levels, only 11 percent at Ca/S = 2.0. With primary air injection, sorbent particles are expected to be in immediate contact with devolatilizing and burning fuel and therefore may deactivate due to high peak temperatures and interfering species which evolve from the coal.

SO_2 reduction results for probe sorbent injection 0.3 m (12 in.) above and 0.2 m (8 in.) below the burner zone were also obtained. These results are given in Fig. 7. The sorbent was injected upward into the center of the furnace through a 20 mm (0.8 in) diameter nozzle. SO_2 reduction levels for the two probe injection locations were found to be similar to the OFA and lower-auxiliary port data.

Figure 8 illustrates that injecting sorbent into the convective section from the radiant section or into the convective section, counter to the gas flow, gave results similar to all injection locations, except the primary air and the ceiling-down injection locations. The reason ceiling-down injection of sorbent produced low SO_2 reduction levels is not understood. It could be speculated that ceiling-down injection directs some of the

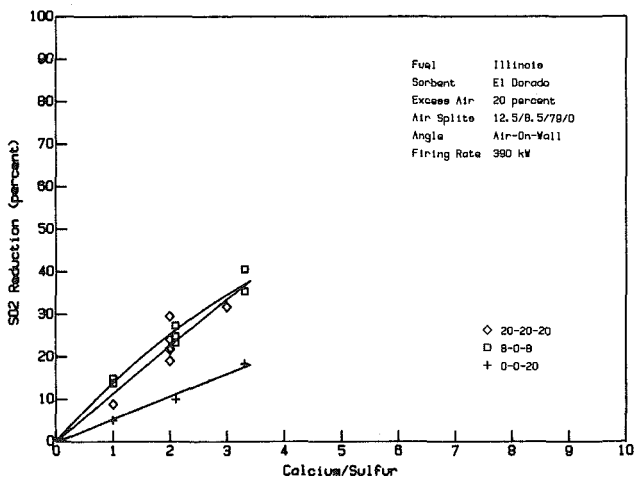

Fig. 5 Effect of convective tube bank arrangement with probe injection above burner on SO_2 reduction

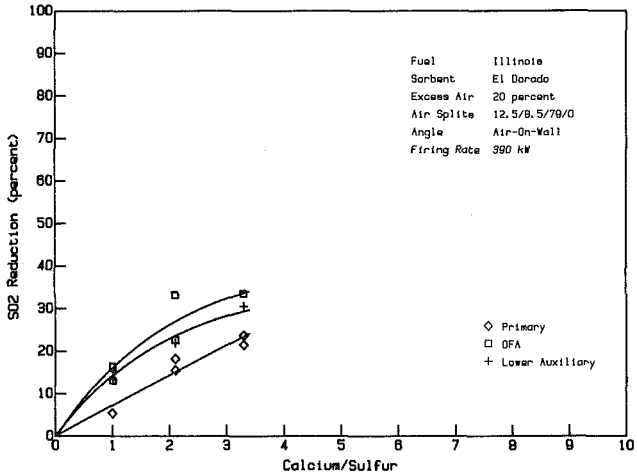

Fig. 6 Effect of sorbent injection location on SO_2 reduction

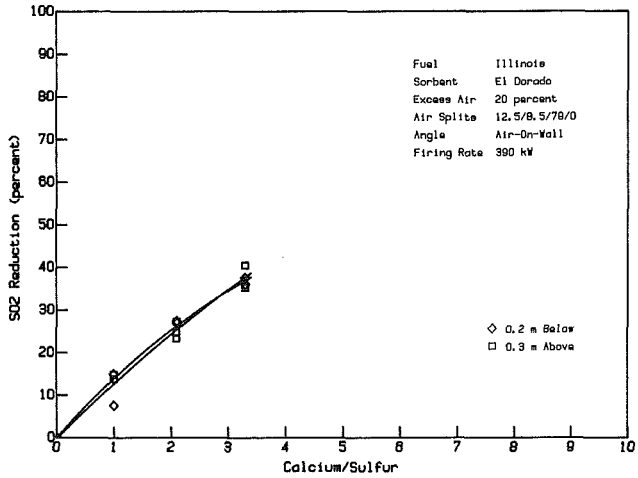

Fig. 7 Effect of sorbent injection location on SO_2 reduction

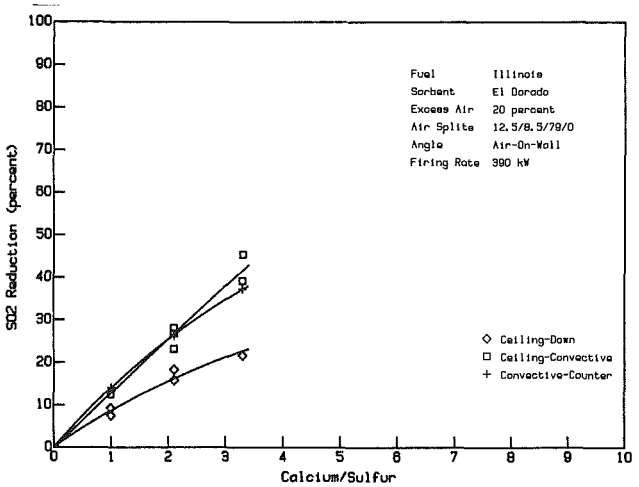

Fig. 8 Effect of sorbent injection location on SO_2 reduction

sorbent into flame zones, where deactivation of the sorbent (similar to primary injection) occurs. No data are available to support this conjecture, however.

The similarity of most of these results, for different injection locations, implies that stable SO_2 capture is taking place in the convective section where temperatures are below 1533 K (2300°F) and that there is no net capture occurring in the radiant section.

Thermal Condition SO_2 Capture Correlation. These results suggest that there are two main constraints limiting SO_2 capture performance in this system. One constraint is sorbent injection temperature, or proximity to burning coal particles, and the second constraint is the time spent by the sorbent particle in the optimal sulfation temperature zone. Assuming these to be the primary constraints, a simple, physically based model was developed to correlate a selected amount of data.

Sorption rate is expected to be proportional to SO_2 concentration and "available" calcine surface area. Surface areas for calcined limestones and dolomites have been shown to vary inversely with exposure temperature (Borgwardt et al., 1971, 1984; Kellog Co., 1972; Coutant et al., 1970), and there is evidence that sulfation may ultimately be limited by the porosity of the stone (Garman et al., 1984). Finally, the overall rate coefficient of reaction (1) is temperature dependent for a given calcine, and the fastest net sulfation is known to occur at temperatures between 1255 and 1505 K (1800 and 2250°F) (Borgwardt et al., 1971, 1984; Kellog Co., 1972; Coutant et al., 1970)

$$CaO\ (s) + SO_2 + 0.5\ O_2 \rightarrow CaSO_4\ (s) \qquad (1)$$

For this analysis, calcine surface area was assumed to be dependent on α, the degree of advancement of reaction (1), and on two parameters: T_{inj} (peak sorbent exposure temperature) and S_{max} (an asymptotic limit which may depend on Ca/S, particle size, porosity, or other physical parameters). Equation (2) expresses the relation for surface area as a function of these variables

$$A = (Z_0 \cdot \alpha) \cdot (T_{inj})^{-1} \qquad (2)$$

In equation (2), α varies from 1 to 0, according to the relationship given in the nomenclature.

Assuming fixed oxygen concentration, and solving the resulting first-order rate equation for R (SO_2 reduction), the following result is obtained:

$$(1 - R/S_{max}) \cdot (1 - R)^{-1} = \exp[B \cdot t \cdot (1 - S_{max}) \cdot (T_{inj} \cdot S_{max})^{-1}] \qquad (3)$$

For purposes of correlation, T_{sorb} (included in the parameter B) is assumed constant, and time (t) is estimated as the period in which the reactant temperature is between 1255 and 1505 K (1800 and 2250°F).

Figure 9 shows a plot of ln $[(1 - R/S_{max}) \cdot (1 - R)^{-1}]$ versus $t \cdot (1 - S_{max}) \cdot (T_{inj} \cdot S_{max})^{-1}$ for the experiments previously described. All data correspond to a molar Ca/S ratio of 2.1, and S_{max} was chosen as 50 percent. At the nominal Ca/S ratio, this would yield an overall calcium utilization of 24 percent. The range of injection temperatures for these data was from 1470 to 1690 K (2190 to 2585°F) and the range of sulfation times was from 0.3 to 4.1 s. Extrapolation beyond these limits is not advisable, especially for T_{inj} below 1200 K (1700°F), where the slower rate of calcination will provide less than 100 percent conversion of $CaCO_3$ to CaO.

On the logarithmic axes of Fig. 9, the plot is linear with moderate scatter; however, the trend toward greater SO_2 reduction (more negative ordinate) with higher values of the time-temperature quotient is evident. Variation of the parameter S_{max} does not affect the logarithmic nature of this correlation.

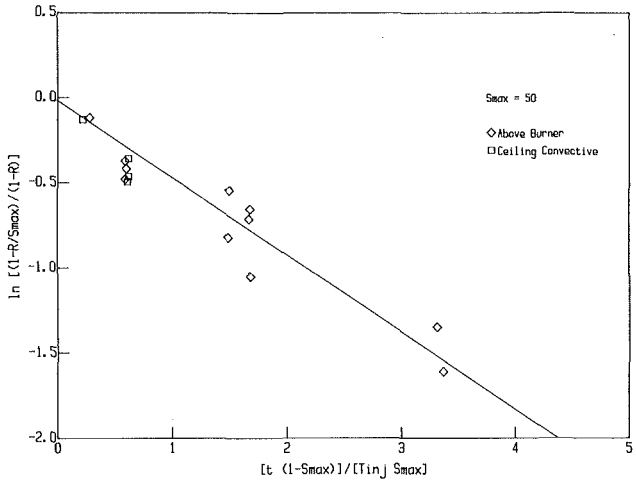

Fig. 9 Effect of time-temperature parameter $[t(1 - S_{max})/(T_{inj}\ S_{max})]$ on SO_2 reduction parameter $\ln[(1 - R/S_{max})/(1 - R)]$

Although calcium utilization remained fairly low (21 percent maximum), the fact that the plot is exponential indicates that the reaction is indeed first order in CaO, and that some asymptotic limit to CaO availability may in fact exist. The results are also seen to collapse for the two injection locations shown.

Conclusions

Tangentially fired low-NO_x pilot-scale test results have shown the importance of temperature history on sorbent particle SO_2 capture performance. A simple correlation that incorporates the effects of sorbent injection temperature and residence time in the optimal sulfation temperature range has successfully correlated data for a range of injection temperatures, residence times, and injection locations. These results show that better SO_2 capture is achieved for lower injection temperatures and longer residence times in the optimum sulfation regime.

All of these results suggest that, for optimal sorbent SO_2 capture, injection should take place away from the burner zone where temperatures are lower, and that the time in the optimal sulfation temperature range should be extended as much as possible, through sorbent injection techniques and temperature profile modification.

Acknowledgments

The authors wish to acknowledge John Boney, William Miller, and Sheldon Cooper (late) for their innovative and tireless assistance during the execution of this program. Thanks are also due to Eric Swenson for the facility construction effort, and to Dr. Howard Mason and Dr. Dennis Drehmel for their helpful comments on this document. Support for this work was provided by the U.S. Environmental Protection Agency under contract No. 68-02-3684, project officer Dr. Dennis C. Drehmel.

References

Abele, A. R., Rees, D. P., and Zallen, D. M., 1982, "A Laboratory Method to Simulate Utility Boiler Flyash," EPRI Interim Report Project 629-4.

Borgwardt, R. H., Drehmel, D. C., Kittleman, T. A., Mayfield, D. R., and Bowen, J. S., 1971, "Alkaline Additives for Sulfur Dioxide Control," EPA/DCS/RLB-71-1.

Borgwardt, R. H., Bruce, K. R., and Blake, J., 1984, "EPA Experimental Studies of the Mechanisms of Sulfur Capture by Limestone," presented at the First Joint Symposium on Dry SO_2 and Simultaneous SO_2/NO_x Control Technologies, EPRI/EPA.

Coutant, R. W., Simon, R., Campbell, B., and Barrett, R. E., 1970, "Summary Report on Investigation of the Reactivity of Limestone and Dolomite for Capturing SO_2 From Flue Gas," NTIS PB-196-749, Battelle Rept. APTD-0802.

Garman, A. R., Simons, G. A., and Boni, A. A., 1984, "Surrogate Fuels Exploratory Tests: Vol. II, High-Temperature, Pressurized Sulfur Capture by Calcium-Based Sorbents," U.S. Dept. of Energy, DE/MC/20486-1711.

Habelt, W. W., 1977, "The Influence of the Coal Oxygen to Coal Nitrogen Ratio on NO_x Formation," presented at the 70th Annual AIChE meeting.

Hazard, H. R., 1980, "Influence of Coal Mineral Matter on Slagging of Utility Boiler Flyash," EPRI Interim Report CS-1418.

Ishihara, Y., Fukuzawa, H., and Asakawa, C., 1975, "Studies on Sulfur Dioxides Removal from Flue Gas by Dry Limestone Injection Process (V)," *J. Fuel Soc. Japan*, Vol. 54, pp. 973-982.

M. W. Kellog Co., 1972, "Review of the Dry Limestone Injection Process," EPA/APTD-1136 (NTIS PB 211431).

Kelly, J. T., Brown, R. A., Chu, E. K., Wightman, J. B., Pam, R. L., Swenson, E. L., Merrick, E. B., and Busch, C. F., 1981, "Pilot-Scale Development of a Low-NO_x, Coal Fired Tangential System," Acurex Final Report No. 68-02-3684.

Kokkinos, A., Lewis, R. D., Rorio, D. C., McCartney, M. S., Ferraro, J. M., and Keele, K. E., 1983, "Low-NO_x Firing System for Tangentially Coal-Fired Utility Boilers—Preliminary Testing," *Proceedings of the 1982 Joint Symposium on Stationary Combustion NO_x Control*, Vol. 1, EPRI CS-3182.

Lim, K. J., Waterland, L. R., Castaldini, C., Chiba, Z., and Higginbotham, E. B., 1980, "Environmental Assessment of Utility Boiler Combustion Modification NO_x Control," EPA-600/7-80-075a.

Murthi, K. S., Harrison, D., and Chan, R. K., 1981, "Reaction of Sulfur Dioxide With Calcined Limestones and Dolomites," *Env. Sci. Tech.*, Vol. 5, pp. 776-781.

Ohmine, S., Martin, R. J., Kelly, J. T., and Chu, E. K., 1983, "Low-NO_x Tangential System SO_x Control Through Sorbent Injection," *Proceedings of the 1982 Joint Symposium on Stationary Combustion NO_x Control*, Vol. 1, EPRI-CS-3182.

Tennessee Valley Authority, 1973, "Full-Scale Desulfurization of Stack Gas by Dry Limestone Injection," Vol. 1, EPA-650/2-73-019c.

Numerical Model for Predicting Performance of Three-Dimensional Pulverized-Fuel Fired Furnaces

W. A. Fiveland

R. A. Wessel

The Babcock & Wilcox Company,
Research and Development Division,
Alliance Research Center,
Alliance, OH 44601

A numerical furnace model (FURMO) was developed to model steady-state, three-dimensional pulverized-fuel combustion in practical furnace geometries. This model is based on a fundamental description of various interacting processes which occur during combustion: turbulent flow, heterogeneous and homogeneous chemical reaction, and heat transfer. The detailed analysis achieved by the method is useful for evaluating furnace performance and in the interpretation of laboratory, intermediate, and utility test data. In this paper, three-dimensional pulverized coal combustion is investigated for a 560 MW utility boiler. Numerical results for flow, heat transfer, and chemistry are presented. Contour maps are exhibited to describe these complex three-dimensional interactions. Model sensitivity is evaluated for changes in slag layer thickness, particle size distribution, and devolatilization and char oxidation rates.

Introduction

Pulverized coal (PC) is used extensively in utility and industrial boilers. The need to design more efficient combustion devices is quite clear with rising costs and increasing demand for energy. The existing technology base for designing utility and industrial boilers is primarily empirical and cannot be logically extended to study various effects (e.g., fuels, burner position and orientation, and boiler geometry) on system performance. Therefore, the technology base for PC combustion must be expanded if we are to understand the complex combustion processes better. One way to understand these fundamental aspects of furnace performance is through the application of computational methods.

Computational methods in fluid flow and heat transfer have been advanced to the point that such methods are being applied to the simulation of complex, yet practical combustion systems. The simulation of a pulverized-fuel combustion system involves modeling a number of complex, simultaneous, interdependent processes. The model must account for fluid flow, turbulence, particle transport, combustion, and radiation heat transfer. Gas-fired processes have been modeled with reasonable success by a number of investigators (Gosman et al., 1969; Abou Ellail et al., 1978; Mitchell et al., 1980). However pulverized-coal combustion has received less attention, partly because of the significant increase in complexity required to model the coal particles and their effect on the gas phase. The first such computational method for pulverized coal (PC) was from Gibson and Morgan (1970). Recent studies by Richter and Fleischhans (1976), Lockwood et al. (1980), Smith and Smoot (1982), and Fiveland et al. (1984) have employed more sophisticated techniques and demonstrated promise in predicting PC combustor performance.

In this paper a three-dimensional furnace model (FURMO) is presented to assess pulverized-coal combustion and heat transfer in practical furnace geometries. Results are presented for a utility size furnace and show promise of assisting engineers and designers in the optimization and design of combustion equipment.

Governing Equation for Gas Particle Mixture: General Transport Equation

In the method described in this paper, all transport processes are represented by a general convective transport equation which can be written for a Cartesian geometry as

$$\frac{\partial}{\partial x_j}(\bar{\rho}\tilde{u}_j\phi) - \frac{\partial}{\partial x_j}\Gamma_\phi\frac{\partial\phi}{\partial x_j} = S_\phi \tag{1}$$

where ϕ is the dependent variable, Γ_ϕ is the effective diffusion coefficient, and S_ϕ is the source of ϕ per unit volume. The index j in equation (1) denotes summation over the three coordinate directions. Conservation equations similar to equation (1) can be written (mass, three components of momentum, energy, and others) and are mathematically elliptic. Boundary conditions are prescribed around the computational domain, and consist of prescribed values of ϕ or its derivative. Source terms S_ϕ can arise as volumetric sources from redistribution of mass (particle-to-gas phase), gain of energy by radiation, etc.

Gosman et al. (1969) have discussed the solutions for these equations based on a macrocontrol volume formulation. The geometry is subdivided into control volumes as shown in Fig. 1. In the flow model, equations for mass, momentum, and turbulence are solved using the fine grid to provide the required detail in the complex flow patterns: flow redistribution

Contributed by the Fuels and Combustion Technology Division and presented at the Joint AIAA/ASME Thermophysics and Heat Transfer Conference, Boston, Massachusetts, June 2-4, 1986. Manuscript received at ASME Headquarters March 27, 1987. Paper No. 86-HT-35.

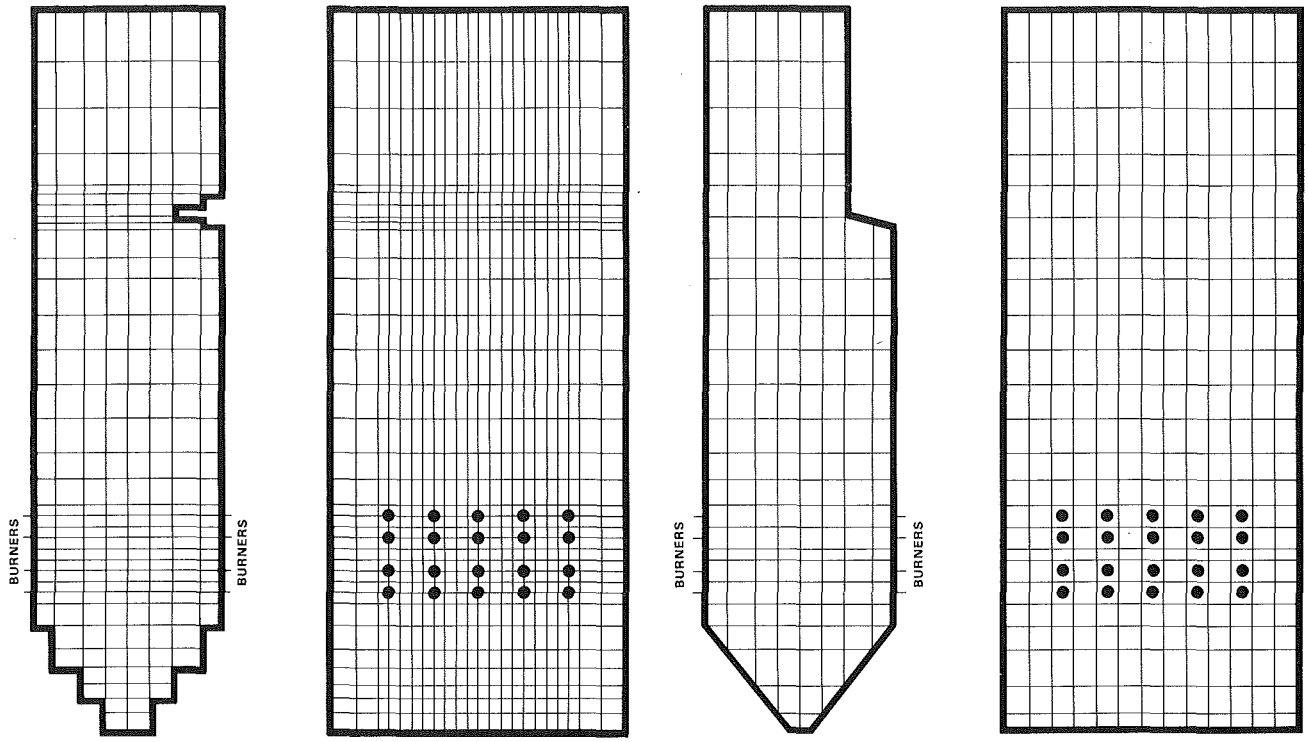

Fig. 1 Control volume layout for flow and combustion models

and recirculation. In the combustion model, other equations are solved using the coarse grid to increase computational efficiency without loss of accuracy. Integration of equation (1) over a typical control volume results in an equation of the form:

$$a_P\phi_P = \sum_{\substack{N,S,E\\W,F,B}} a_i\phi_i + S_\phi \mathcal{V}_P \qquad (2)$$

Equation (2) describes the dependent variables in the control volumes. The summation extends over all neighbor computational cells and the value S_ϕ defines the source of ϕ in the volume (Patankar, 1980). The coefficients (a_P, a_E, a_W, etc.) depend on flow rates across the volume faces ($\rho_e u_e A_e$, $\rho_w u_w A_w$, etc.) and on diffusion conductances ($\Gamma_e A_e/\Delta x$, $\Gamma_n A_n/\Delta y$, etc.). All control volumes in the enclosures are described by equation (2), resulting in a system of N algebraic equations with N unknowns which can be solved for the transported quantity, ϕ, throughout the computational domain.

Nomenclature

a = coefficient of algebraic form of finite difference equation
A = pre-exponential factor
A = area, m^2
C = "universal" constant
d = diameter, m
E = activation energy, J $kgmol^{-1}$
F = strength of convection, kg $m^{-2}s^{-1}$
F_{x_i} = body force component, kg $m^{-2}s^{-2}$
G = total incident energy, J $m^{-2}s^{-1}$
h = heat transfer coefficient, J $s^{-1}m^{-2}K^{-1}$
h = enthalpy, J kg^{-1}
I = radiation intensity, J $m^{-2}s^{-1}\Omega^{-1}$
k = kinetic energy of turbulence, m^2s^{-2}
K = kinetic rate coefficient, s^{-1}
M = molecular weight, kg $kgmol^{-1}$
m = mass fraction
N = number of species
P = probability density function (PDF), phase function
P = pressure, Nm^{-2}
q = heat flux, J $m^{-2}s^{-1}$
r = stoichiometric oxidant-to-fuel ratio
r_{c1} = constant = 4.0
r_{c2} = constant = 0.5
R = reaction rate coefficient, kg $s^{-1}m^{-2}(N\ m^{-2})^{-1}$
R = gas constant, J $kgmol^{-1}K^{-1}$
S_ϕ = source term, ϕ-units kg $m^{-3}s^{-1}$
s = direction of radiation
S_{sw} = coal swelling coefficient = d_p/d_p^0
T = temperature, K
u_i = component of velocity (u_1, u_2, u_3), m s^{-1}
$\mathcal{V}$ = volume, m^{-3}
$\dot{w}$ = reaction rate, kg $m^{-3}s^{-1}$
x_i = coordinate direction (x_1, x_2, x_3), m
X_s = solid fraction = $\sum_i \tilde{m}_{pmr,\,i}$
α = volatile coefficient
β = extinction coefficient, m^{-1}
Γ = diffusion coefficient, kg $m^{-1}s^{-1}$

Table 1 Conservation equation parameters for equation (1)

Conservation of	ϕ	Γ_ϕ	S_ϕ
mass	1	0	0
x_1 momentum	$\tilde{u}_1$	μ_{eff}	$F_{x_1} + S_{x_1}$
x_2 momentum	$\tilde{u}_2$	μ_{eff}	$F_{x_2} + S_{x_2}$
x_3 momentum	$\tilde{u}_3$	μ_{eff}	$F_{x_3} + S_{x_3}$
kinetic energy	k	$\mu_{\text{eff}}/\sigma_k$	$G - \bar{\rho}\epsilon$
dissipation	ϵ	$\mu_{\text{eff}}/\sigma_\epsilon$	$\frac{\epsilon}{k}(C_1 G - C_2 \bar{\rho}\epsilon)$
initial particle mass	$\tilde{m}_{pm}$	$\mu_{\text{eff}}/\sigma_{pm}$	0
remaining coal	$\tilde{m}_{rc}$	$\mu_{\text{eff}}/\sigma_{rc}$	$\bar{S}_{rc}$
particle mass remaining	$\tilde{m}_{\text{pmr}}$	$\mu_{\text{eff}}/\sigma_{\text{pmr}}$	$\bar{S}_{\text{pmr}}$
fuel mixture fraction	$\tilde{m}_f$	$\mu_{\text{eff}}/\sigma_f$	$\bar{S}_f$
fuel remaining	$\tilde{m}_{fr}$	$\mu_{\text{eff}}/\sigma_{fr}$	$\bar{S}_{fr} = \bar{S}_f - \min(R_1, R_2, R_3)$
enthalpy	$\tilde{h}_m$	$\mu_{\text{eff}}/\sigma_h$	$\bar{S}_h$
carbon monoxide	$\tilde{\sigma}_{\text{CO}}$	$\mu_{\text{eff}}/\sigma_{\text{CO}}$	$\bar{S}_{\text{CO}} = y \cdot \min(R_1, R_2, R_3) - \bar{S}^k_{\text{CO}}$

$$G = 2\left(\frac{\partial \tilde{u}_i}{\partial x_i}\right)^2 + \left(\frac{\partial \tilde{u}_i}{\partial x_j} + \frac{\partial \tilde{u}_j}{\partial x_i}\right)^2_{i \neq j}$$

$$S_{x_i} = -\frac{\partial \bar{p}}{\partial x_i} + \frac{\partial}{\partial x_j}\mu_{\text{eff}}\frac{\partial \tilde{u}_j}{\partial x_i}$$

Table 2 Empirical constants for mixture equations (Launder and Spalding, 1972)

C_μ	C_1	C_2	σ_k	σ_ϵ	σ_{pm}	σ_{rc}	σ_{pmr}	σ_f	σ_{fr}	σ_h	σ_{CO}
0.09	1.44	1.92	1.0	1.21	0.9	0.9	0.9	0.9	0.9	0.9	0.9

Flow Field Analysis

Flow Field. In writing equation (1) for momentum, we have assumed a Favre average form of the three-dimensional, incompressible flow equations. Table 1 lists the values of ϕ, Γ_ϕ, and S_ϕ, while Table 2 lists the modeling constants. The effective diffusion coefficient can be represented by

$$\mu_{\text{eff}} = \mu_l + \mu_t \tag{3}$$

where μ_l and μ_t are the laminar and turbulent viscosities, respectively. Particles are assumed to follow the flow path lines. By invoking this no-slip assumption between the gas and particle phases, considerable simplification in the analysis results. The solution of these equations represents a mixture velocity distribution, which is characterized by a mean mixture density $\bar{\rho}$ defined as follows:

$$\frac{1}{\bar{\rho}} = \frac{1 - X_s}{\bar{\rho}_g} + \frac{X_s}{\rho_p} \tag{4}$$

Turbulence. Following recommendations by Launder and Spalding (1974), the turbulent viscosity is expressed as

$$\mu_t = \bar{\rho} C_\mu \frac{k^2}{\epsilon} \tag{5}$$

using the standard k–ϵ model (Jones and Launder, 1972). Values of ϕ, Γ_ϕ, and S_ϕ are listed in Table 1, while the modeling constants are listed in Table 2. This model has been widely applied, although it suffers from some drawbacks, such as

Nomenclature (cont.)

ϵ = dissipation rate of turbulent energy, $m^2 s^{-3}$
ϵ = emissivity
κ = absorption coefficient, m^{-1}
μ = dynamic viscosity, kg $m^{-1} s^{-1}$
$\bar{\rho}$ = mean mixture density, kg m^{-3}
σ = scattering coefficient, m^{-1}
σ_i = concentration of ith species, kgmol/kg
$\tilde{\sigma}$ = Boltzmann constant, J s^{-1} m^{-2} K^{-4}
ϕ = general transport parameter

Subscripts

B = back cell
b = back
c = coal
ch = char, or chemical
e = east
E = east cell
eff = effective
F = front cell
f = front, or mixture fraction
fr = fuel remaining
fu = fuel
g = gas, or coal size group
h = enthalpy
i = gas species index, or summation index
k = turbulent kinetic energy
l = laminar
m = mixture
n = north
N = north cell
ox = oxidant
P = center cell
p = particle
ph = physical
pm = particle mass
pmr = particle mass remaining
pr = products
rc = raw coal
s = south, solid, or species
S = south cell
t = turbulence
w = west, or wall value
W = west cell
ϵ = dissipation rate
μ = viscosity
ϕ = general variable

Superscripts

ch = char oxidation
d = devolatilization
$\sim$ = Favre mean
- = Reynolds mean
0 = initial condition
k = kinematic reduction of CO
+ = incoming radiant flux

underprediction of the sizes of wakes and recirculation zones (Pope, 1976; Gosman et al., 1979; Jones and Whitelaw, 1982). Additionally, the model does not account for the effect of combustion on turbulence or the effect of particles on turbulence. Even with these drawbacks, this model is useful because reasonable accuracy can be obtained and, unlike other models, solutions are computationally efficient for practical problems.

Heterogeneous and Homogeneous Chemistry

In pulverized coal combustion, solid fuel and inlet air mix and react upon entering the combustor. Particle flow is modeled in an Eulerian reference frame using the particle mass concentration $\tilde{m}_{pm}$ in equation (1). The continuous distribution of coal particle sizes is segmented into a number of discrete, uniform-diameter size groups. A conservation equation is solved for each particle size group.

Coal devolatilization and subsequent char oxidation processes are characterized by a total fuel evolution rate. The first stage of fuel evolution represents the devolatilization and char formation processes

$$\text{Coal} \xrightarrow[i=1,\,2]{K_i^d} \text{Fuel} + \text{Char} \tag{6}$$

Thus a conservation equation is solved for the mass of remaining coal $\tilde{m}_{rc}$ for each particle size group. The second stage of fuel evolution represents the rate of char weight loss

$$\text{Char} \xrightarrow{K^{ch}} \text{Fuel} + \text{Ash} \tag{7}$$

An approximation is made by which the char is converted to gaseous fuel before it reacts to form products. A conservation equation is solved for the particle mass remaining $\tilde{m}_{\text{pmr}}$, which includes both coal and char, for each particle size group.

The fuel is assumed to have the same elemental composition as the ash-free coal and is represented by a mixture of gases (CH_4, C, CO_2, H_2O, SO_2, and N_2). Combustion of the fuel is characterized by a two-step process. In the first step, fuel is assumed to react with oxygen to form carbon monoxide and other products as

$$\text{Fuel} + \text{Oxidant} \rightarrow y\text{CO} + z\text{H}_2\text{O} + \ldots \tag{8}$$

where y and z can be determined from an elemental balance. The second step involves kinetically controlled reduction in the quantity of carbon monoxide by the reaction:

$$\text{CO} + \text{Oxidant} \rightarrow \text{CO}_2 + \ldots \tag{9}$$

The reaction in equation (8) is modeled with the fast chemistry assumption as described by Bilger (1980). Thus when fuel and oxidant mix, they are assumed to react instantaneously and form products. Therefore there can be only one of the following mixtures: fuel and products, oxidant and products, or products alone. The fast chemistry assumption reduces the first stage of combustion to a single, irreversible global reaction of the form

$$1 \text{ kg fuel} + r \text{ kg oxidant} \rightarrow (1+r) \text{ kg products} \tag{10}$$

Bilger (1980) and others have shown that species conservation equations can be reduced to a single conservation equation for the fuel, the oxidant, and the products. Diffusion rates are assumed equal, and the reaction rates are related as follows:

$$\dot{w}_{fu} = \frac{\dot{w}_{ox}}{r} = -\frac{\dot{w}_{pr}}{1+r} \tag{11}$$

Transport of the fuel can then be modeled by a conservation equation for the fuel mixture fraction $\tilde{m}_f$. However, equation (1) is linear in $\tilde{m}_f$, and the fuel mixture fraction is simply determined from the relationship:

$$\tilde{m}_f = \tilde{m}_{pm} - \tilde{m}_{\text{pmr}} \tag{12}$$

where the distribution of $\tilde{m}_{pm}$ and $\tilde{m}_{\text{pmr}}$ is already known.

The reaction described in equation (8) is modeled by a conservation equation for the fuel remaining $\tilde{m}_{fr}$. The method proposed by Magnussen and Hjertager (1976) is used. This model is formulated by using the fast chemistry assumption and by further assuming that the rate of combustion is controlled by the rate of turbulent mixing.

The reaction described in equation (9) is modeled by a conservation equation for the average carbon monoxide concentration $\tilde{\sigma}_{\text{CO}}$. Since the time scale of turbulence is much greater than the time scale of chemistry, the CO reaction rate is also controlled by the rate of turbulent mixing. A transport equation describing the average carbon monoxide concentration is found by averaging the instantaneous equation over a probability density function to account for turbulence.

Subsequently, average species concentrations for O_2, CO_2, H_2O, N_2, and fuel species are calculated as follows:

$$\tilde{\sigma}_i = \tilde{m}_{fr}\sigma_{f,i} + \tilde{m}_{ox}\sigma_{ox,i} + \tilde{m}_{pr}\sigma_{pr,i} \tag{13}$$

where $\tilde{m}_{fr}$ and $\tilde{m}_{ox}$ are the amount of fuel and oxidant remaining and $\tilde{m}_{pr}$ is the amount of products. Values of $\tilde{m}_{ox}$, $\tilde{m}_{pr}$, and $\sigma_{pr,i}$ are calculated by conservation of mass and species as defined in equations (8) and (9).

The following sections describe the conservation equations and their source terms for heterogeneous and homogeneous chemistry.

Particle Mass. A conservation equation for $\tilde{m}_{pm}$ is solved for each particle size. Tables 1 and 2 list the values of ϕ, Γ_ϕ, S_ϕ, and modeling constants, respectively. Sources for $\tilde{m}_{pm}$ occur at inlet ports and are zero otherwise.

Remaining Coal. A conservation equation for $\tilde{m}_{rc}$ is solved for each particle size. As the coal loses volatile matter and is converted to char, the kinetic rates of reaction are assumed first order (Ubhayakar et al., 1975) in the mass of coal remaining. The kinetic rate is written in Arrhenius form

$$K_i^d = \tilde{m}_{rc} A_i e^{-E_i/R\tilde{T}} \tag{14}$$

The total coal conversion rate is expressed in terms of two simultaneous reactions using the rate constants proposed by Ubhayakar et al. (1975) or Kobayashi et al. (1976). Finally the source term for equation (1) is written as

$$\bar{S}_{rc} = -\bar{\rho} \sum_{i=1}^{2} K_i^d \tag{15}$$

Particle Mass Remaining. A conservation equation for $\tilde{m}_{\text{pmr}}$ is solved for each particle size group. Particle mass is reduced when fuel is evolved by devolatilization and char oxidation. The source term for this transport equation can be expressed

$$\bar{S}_{\text{pmr}} = -\bar{\rho}(K^d + K^{ch}) \tag{16}$$

The rate of devolatilization can be written as

$$K^d = \sum_{i=1}^{2} \alpha_i K_i^d \tag{17}$$

where α_i is the asymptotic volatile yield and K^d has been defined before. The effective char oxidation rate is estimated assuming that char particles burn with constant diameter. The char oxidation rate is calculated following the work of Baum and Street (1971):

$$K^{ch} = \tilde{m}_{pm}\tilde{\sigma}_{O_2} P M_m R S_{sw}^2/(\rho_p^0 d_p^0) \tag{18}$$

where S_{sw} is the swelling coefficient. The rate coefficient R is a function of the kinetic rate of the chemical reaction and the physical diffusion rate of the oxidizer to the surface of the particle as written

$$R = \frac{1}{1/R_{ch} + 1/R_{ph}} \tag{19}$$

Fuel Remaining. A conservation equation is solved for $\tilde{m}_{fr}$ with the source of fuel remaining given in the form

$$\bar{S}_{fr} = \bar{S}_f - \min(R_1, R_2, R_3) \tag{20}$$

The first term on the right side of the equation is the increase in fuel from the devolatilization and char oxidation, while the second term is the decrease in fuel from combustion.

The source of fuel is calculated for each discrete size group of coal particles and is accumulated over the entire particle size distribution. This source of fuel is expressed as

$$\bar{S}_f = \tilde{\rho} \sum_{i}^{N_g} (K_i^d + K_i^{ch}) \tag{21}$$

Because the chemical reactions in most cases are very fast (compared with the rate of turbulent mixing), the rate of combustion will be determined by the rate of mixing on a molecular scale of the fuel and oxygen eddies. Accordingly, the fuel and oxygen appear as fluctuating intermittent quantities, and there will be a relationship between the fluctuations and the mean concentration of the species. Consequently, the rate of dissipation can be expressed by a mean concentration of the reacting species.

In fuel-lean regions, the oxygen concentration is high, the fuel concentration is low (fuel is mostly intermittent), and the rate of combustion can be written as

$$R_1 = -\tilde{\rho} r_{c1} \tilde{m}_{fr} \frac{\epsilon}{k} \tag{22}$$

where r_{c1} is a constant that may depend on the flame structure and the rate of reaction between fuel and oxidant; $\tilde{m}_{fr}$ is the amount of fuel remaining; ϵ is the rate of dissipation of the turbulent kinetic energy; and k is the turbulent kinetic energy.

In fuel-rich regions, the fuel concentration is high, the oxidant concentration is low (oxidant is mostly intermittent), and the rate of combustion can be expressed as:

$$R_2 = -\tilde{\rho} r_{c1} \frac{\tilde{m}_{ox}}{r} \frac{\epsilon}{k} \tag{23}$$

where $\tilde{m}_{ox}$ is the amount of oxidant remaining, and r is the stoichiometric oxidant to burn 1 kg of fuel.

In premixed flames, oxidant and fuel can exist in the same eddy. These eddies will be separated by eddies containing hot products. The rate of combustion will be determined by local fire spread. The dissipation of the hot eddies must be modeled when the concentration of hot combustion products is low. This gives rise to the rate which follows as

$$R_3 = -\tilde{\rho} r_{c1} \cdot r_{c2} \frac{\tilde{m}_{pr}}{1+r} \frac{\epsilon}{k} \tag{24}$$

where r_{c2} is a constant, and $\tilde{m}_{pr}$ is the local concentration of the products.

The three reaction rates are applicable to premixed and nonpremixed flames. The minimum rate is controlling and determines the local rate of combustion.

Kinetic Reduction of Carbon Monoxide. A conservation equation for the average concentration of carbon monoxide is found by averaging the instantaneous conservation equation over a probability density function (PDF). This averaging process has been described by Bilger (1980).

$$\tilde{\phi} = \int_0^{1-X_s} \phi(m_f) P(m_f) dm_f \tag{25}$$

where ϕ is the intensive fluid property, $P(m_f)$ is a Favre probability density function that accounts for the turbulent mixing of fuel and oxidant. Averaging an instantaneous transport equation with equation (25) gives rise to equation (1) and values of ϕ, Γ_ϕ, and S_ϕ listed in Tables 1 and 2. The difficulty is computing the source term $\bar{S}^k_{CO}$ in the equation:

$$\bar{S}_{CO} = y \min(R_1, R_2, R_3) - \bar{S}^k_{CO} \tag{26}$$

The first term on the right side represents the production of CO from the combustion of the fuel, defined in equation (8). The second term is the kinetic reduction of CO, defined by equation (9). The instantaneous value S^k_{CO} is actually a function of both the mixture fraction and the enthalpy. However, we have chosen to express the fluctuations solely in terms of m_f, which reduces S^k_{CO} to a function of m_f alone.

The mean fuel fraction $\tilde{m}_f$, and mean fuel remaining $\tilde{m}_{fr}$, must match the values from the modeled conservation equations. Mathematically the following relations are satisfied:

$$\tilde{m}_f = \int_0^{1-X_s} m_f P(m_f) dm_f \tag{27}$$

$$\tilde{m}_{fr} = \int_0^{1-X_s} m_{fr} P(m_f) dm_f \tag{28}$$

A two-parameter PDF was chosen. Shape parameters for the PDF using equations (27) and (28) were found with a Newton–Raphson iteration. A triangular PDF was chosen instead of a Gaussian distribution (Bilger, 1980) because it is mathematically efficient and was shown to be accurate in numerical sensitivity studies.

Once the shape of the PDF is known from equations (27) and (28), an average value $\bar{S}^k_{CO}$ can be determined from the global reaction proposed by Howard (see Howard et al., 1972). The instantaneous source term for the kinetic reduction of CO can be written

$$S^k_{CO} = -\rho^2 A \sigma_{CO} (\sigma_{H_2O} \sigma_{O_2})^{1/2} \exp(-E/RT) \tag{29}$$

Equation (29) can be used to determine the Reynolds average source term for the conservation equation.

Energy

Smith and Smoot (1980) have defined an overall energy equation for the gas–particle mixture. The equation is listed in Table 1 and was derived subject to the assumptions:

- particle and gas phase temperatures are equal
- kinetic energy, viscous dissipation, gas compressibility, and the effect of gravity are neglected.

The conservation equation for enthalpy is solved using inlet enthalpies defined for the incoming fuel and oxidant streams. Wall losses or gains affect the enthalpy equation as a source or sink of energy, and can be written

$$q = h A (\bar{T} - T_w) \tag{30}$$

The wall temperature is determined for each control surface from a balance of energy

$$\epsilon(q^+ - \bar{\sigma} T_w^4) + h(\bar{T} - T_w) + q_{loss} = 0 \tag{31}$$

The first term is the net radiation absorbed by the wall, the second term is the convected energy to the wall, and the last term is the losses through the wall, estimated using a wall flux calculated from a thermal resistance between the surface and an ambient temperature. Volumetric sources of enthalpy arise

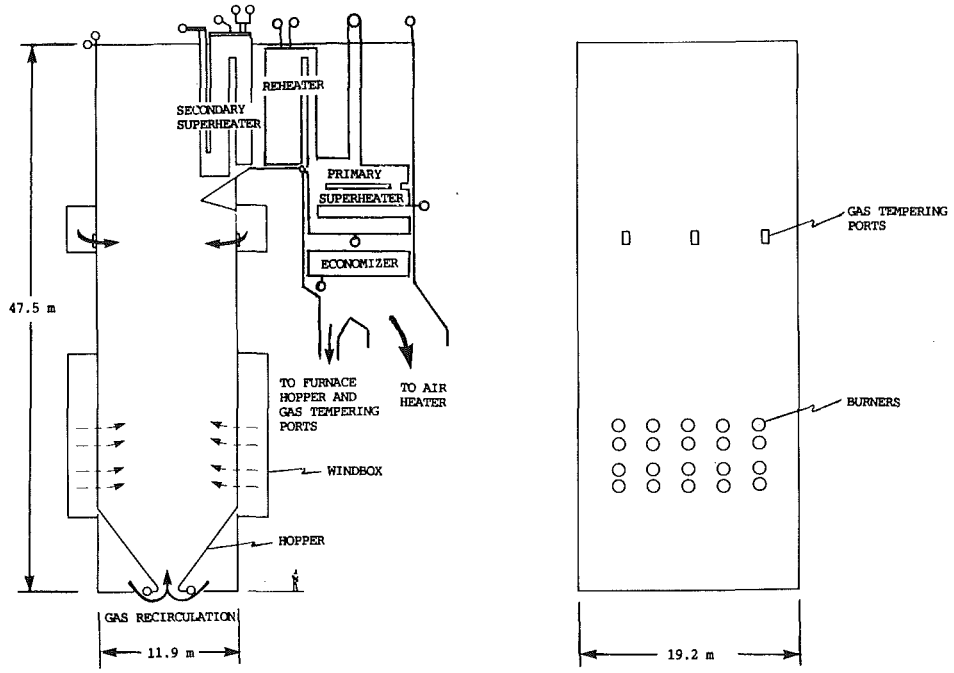

Fig. 2 560 MW universal pressure utility boiler

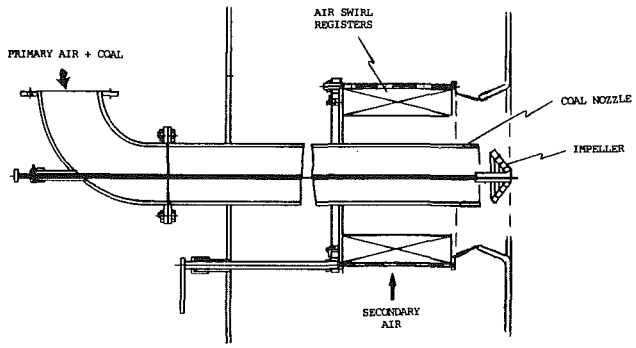

Fig. 3 Circular-type pulverized coal burner

from energy deposited in a volume by radiation according to the following equation:

$$\tilde{S}_h = \kappa(G - 4\tilde{\sigma}\bar{T}^4) \tag{32}$$

Once the mixture enthalpy is known, the Reynolds mean temperature of the mixture can be determined implicitly from the equation

$$\tilde{h}_m = X_s\, h_c + (1 - X_s) \sum_i^{N_S} \tilde{\sigma}_i M_i h_i \tag{33}$$

using Newton–Raphson iteration and relationships for enthalpy as a function of temperature.

Radiation Heat Transfer. In combustion chambers, radiative heat transfer comprises an important mode of heat transfer. We apply the discrete transfer method proposed by Shah (1979). The discrete transfer method uses one form of the radiative transport equation (Chandrasekar, 1950)

$$\frac{dI}{ds} = -\beta I + \kappa \frac{\tilde{\sigma}\bar{T}^4}{\pi} + \frac{\sigma}{4\pi} \int_{\Omega = 4\pi} I \, d\Omega \tag{34}$$

This equation assumes the particles scatter isotropically. While this assumption is somewhat questionable, it admits solutions which compare favorably with data. Other studies will be needed to assess the full impact on the model, however.

The method has many of the features of the Monte Carlo method (Gibb, 1977) but is not hampered by the stochastic errors commonly exhibited by that method. A fixed number of rays are emitted from each control surface. The ray is computationally followed and the radiant intensity is attenuated until another surface is struck; then the ray is terminated. As the rays are traced, the total incident energy is cataloged in each cell. Total energy deposited in each volume is accumulated for all rays penetrating a volume and can be written as shown in equation (32). Total radiant flux incident on each surface is accumulated for all rays striking a surface. Solutions are iterative and can be improved by increasing the number of rays emitted from each surface.

The radiative transport equation requires absorption and scattering coefficients for the particle–gas mixture. Van De Hulst (1957) discusses calculation of these coefficients for a particle mixture. In each computational cell the amount of each particle type is estimated and coefficients are computed using Mie theory (Van De Hulst, 1957; Dave, 1969) with refractive indices of coal, char, ash, and soot (Wessel, 1985). The absorption coefficients for the gas mixture are found using Edwards' wide-band model (Edwards, 1976).

Model Application

Pulverized-coal combustion was investigated for a 560-MW universal pressure utility boiler. The configuration of the furnace is shown in Fig. 2. The dry ash furnace is opposed-wall fired with 20 circular-type pulverized-coal burners on each firing wall arranged in an array, 4 burners high by 5 burners wide. A burner, depicted in Fig. 3, contains a central straight-tube "nozzle," 0.406 m in diameter, through which a mixture of pulverized coal and air is discharged into the furnace at the burner throat. Secondary air (main combustion air) flows from the windbox through air swirl registers (in a clockwise direction) and enters the furnace through an annulus formed by the coal nozzle and the burner throat (1.04 m in diameter). An impeller at the end of each coal nozzle deflects the coal into the swirling secondary airstream near the burner throat where combustion begins. Pulverized coal is supplied to the burners by ball and race type counterrotating pulverizers. At full load, a high volatile bituminous coal is supplied at a rate

Table 3 Pulverized coal characteristics

Ultimate analysis		Particle size distribution	
Moisture	6.0 percent	Diameter	Percent of total mass
Carbon	63.2	75 -300μm	13.9
Hydrogen	4.1	26.5- 75.0	18.6
Nitrogen	1.0	9.4- 26.5	29.5
Sulfur	3.5	4.7- 9.4	21.9
Ash	17.0	0.4- 4.7	16.1
Oxygen	5.2		100.0
	100.0		

Higher heating value: 2.695×10^7 J/kg.

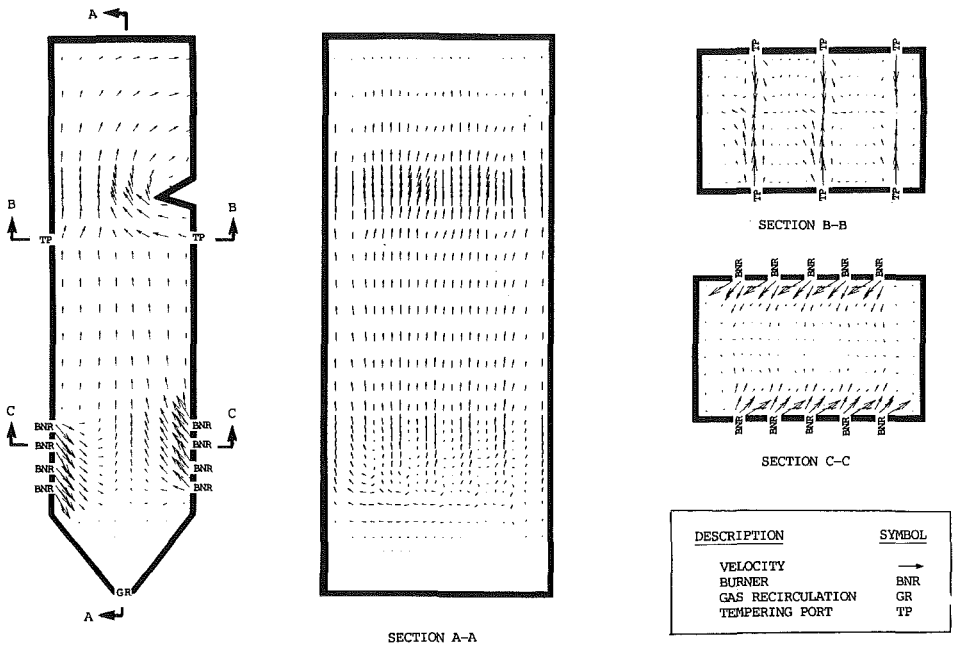

Fig. 4 Flow patterns at furnace centerline planes, gas tempering ports, and burners

of 54.18 kg/s with 17.5 percent excess air. The characteristics of the pulverized coal are shown in Table 3.

Flue gas recirculation is sometimes used in boiler designs for steam temperature control. In the present design, flue gas is extracted from the economizer outlet and is introduced directly into the furnace hopper or upper flame zone to modify furnace heat absorption and/or gas outlet temperature. At full load, the furnace operates with 10.08 kg/s of flue gas recirculation through the furnace hopper and 110.88 kg/s of flue gas recirculation through the gas tempering ports.

The furnace is enclosed by rows of vertically oriented, water-cooled tubes in a membrane wall construction. Water at supercritical pressure is circulated sequentially through all the heated surfaces: the membrane walls and convection pass elements. Thin layers of ash deposits (estimated average thickness—1.9 mm) exist on all internal surfaces of the enclosure during operation. At full load, the boiler produces 495 kg/s of steam at 817 K and 26.37 MPa.

Furnace performance was evaluated at full load conditions. Five particle groups were used to represent the coal particle size distribution. Rate constants by Ubhayaker (1975) were used to simulate coal devolatilization. A swelling coefficient of 2.0 and a surface area factor of 0.10 were used for char oxidation. The thermal boundary conditions at the furnace walls were modeled assuming a wall emittance of 0.8, an average convective heat transfer coefficient of 11.6 W/m^2 K, and a thermal conductance of 300 W/m^2 K to represent the slag layer (1.9 mm), tube metal (4.8 mm), and internal convective heat transfer. The supercritical water within the membrane walls was assumed at an average temperature of 700 K. The FURMO model was used to predict the isothermal flow patterns, furnace heat transfer, and species concentrations within the furnace.

Velocity vectors predicted by the model are shown in Fig. 4 at several planes within the furnace. The arrows indicate the direction of the flow in the plane and the lengths of the arrows are directly proportional to the magnitude of the velocity. The flow enters through the burners, furnace hopper, and gas tempering ports. Inlet velocity vectors at the burners are not perpendicular to the wall due to the swirling flow. The gas flow is relatively quiescent in the furnace hopper, has uniform upward velocity over the furnace cross section above the burners, and is mildly disturbed by the penetration of the tempering flue gas in the upper furnace. The flow bends around the nose of the furnace and exits the furnace through the secondary superheater tube bank. The complex three-dimensional flow patterns exhibited in these results demonstrate that numerical flow modeling provides valuable detailed information for combustion and heat transfer calculations. It is impractical and unlikely that enough experimental data could be collected to provide the detailed information required for combustion modeling.

Model predictions of temperature distribution at furnace centerline planes are shown in Fig. 5. Combustion causes gas temperature to increase from a mean inlet value of 517 K at the burner throat to a maximum temperature exceeding 2000 K at the center of the furnace. Radiant heat loss from the flue gas to the furnace walls causes temperatures to decrease as the

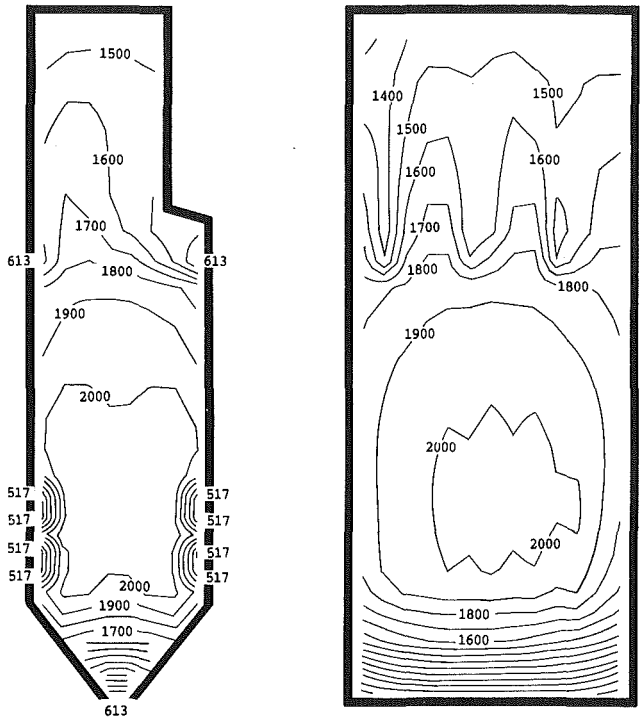

Fig. 5 Gas temperature at furnace centerline planes (contour lines in intervals of 100 K)

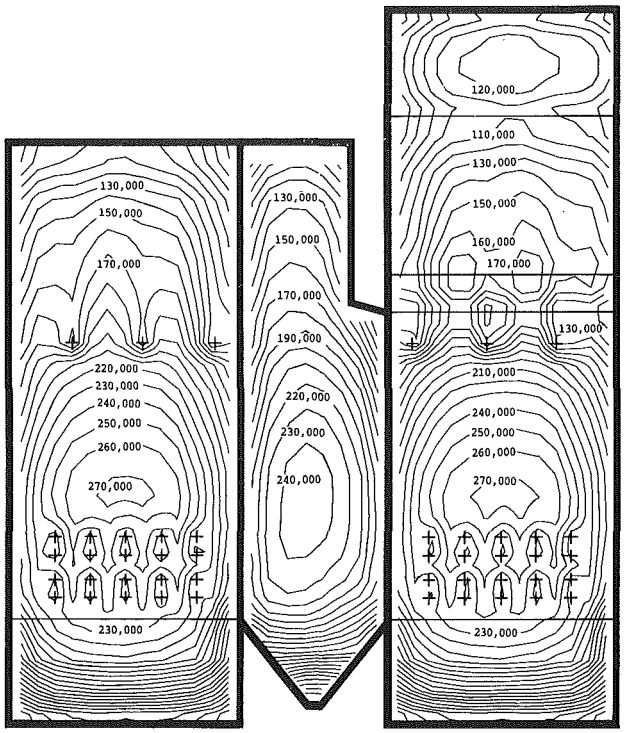

Fig. 7 Heat flux on furnace walls (contour lines in intervals of 10,000 W/m^2)

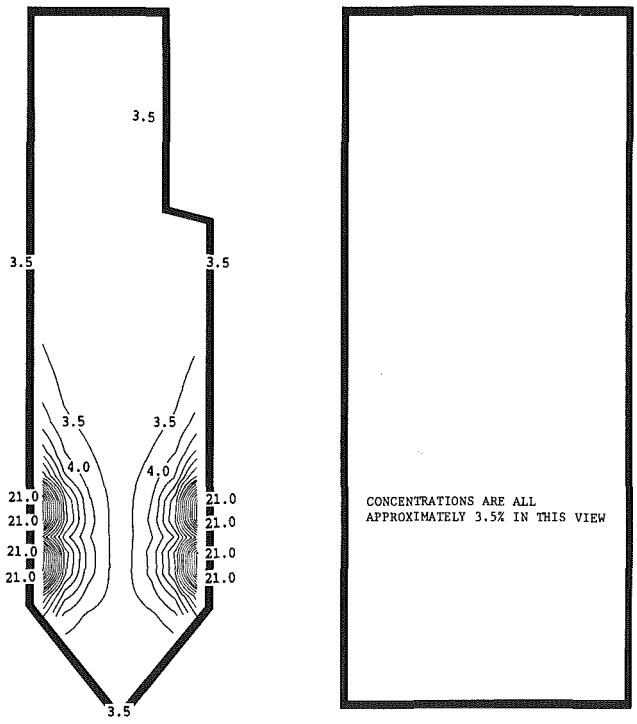

Fig. 6 Oxygen concentration at furnace centerline planes (contour lines in intervals of 0.5 percent molar concentration on a moisture-free basis)

gas flows upward within the furnace. Additional cooling occurs as the tempering flue gas enters the upper furnace at 613 K and mixes with the hotter combustion gases, thus producing depressions in the front-view, centerline temperature distribution. The mixture exits the furnace at a mean temperature of 1501 K. The furnace exit gas temperature that is typically observed for this furnace is 1520 K.

Predictions of species concentrations include oxygen, nitrogen, carbon dioxide, carbon monoxide, water vapor, fuel species, and particulate: coal, char, and ash. Nearly all of the fuel species are consumed within 1 or 2 m of the burner throats due to the rapid mixing of the fuel and swirling air effected by the circular burners. Carbon monoxide reaches a maximum of 2600 ppm near the burner throat and rapidly decreases to a few parts per million outside the flame. The char burns at a slower rate, and is not consumed until it reaches the center of the furnace. The combustion pattern is illustrated by the distribution of oxygen concentrations shown in Fig. 6. Oxygen concentrations are 21 percent at the burner throats and rapidly decrease to 3.5 percent after complete combustion of the fuel. The steepest gradients in oxygen concentration are near the burners where the fuel volatile species are more rapidly consumed. The distribution of carbon dioxide is approximately the reverse of the oxygen concentration: zero at the burner throats increasing to 14 percent after complete combustion of the fuel.

Results also include predictions of surface temperature and heat flux. The distribution of heat flux on furnace walls is shown in Fig. 7. The maximum heat flux is approximately 270,000 W/m^2 on the front and back walls of the furnace. Heat flux decreases toward the corners of the furnace and decreases toward the upper furnace because of the cooling of the combustion gases. The effect of gas tempering on the local heat transfer is apparent from the depressions in the local heat flux patterns on the front and back walls of the upper furnace.

Modeling results such as these are useful for evaluating a number of aspects of furnace performance. Flow patterns can be used to optimize furnace shape and size to provide sufficient residence time for combustion. Heat transfer results such as heat flux and temperature distributions can be useful for evaluating furnace heat transfer efficiency and can be helpful in identifying potential slagging/fouling problems on membrane walls or convection-pass elements. Species concentrations are useful for evaluating combustion efficiency, and are

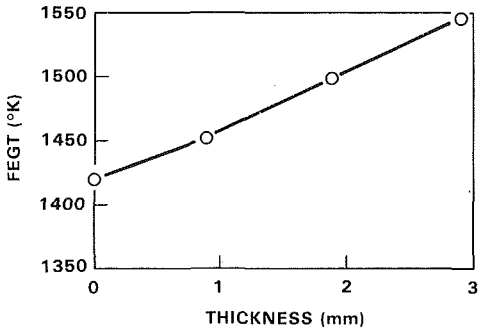

Fig. 8 The effect of slag layer thickness on FEGT

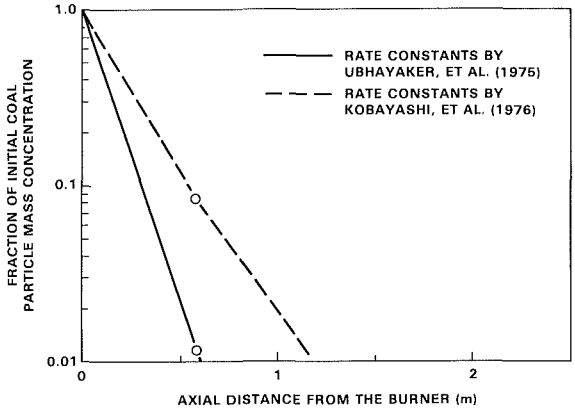

Fig. 9 The effect of devolatilization rate on the concentration of coal near the burner

necessary for predicting pollutant emission levels (NO_x and SO_2) and potential corrosion problems.

Model Sensitivity. The sensitivity of the model was investigated for several important parameters: slag layer thickness, particle size distribution, devolatilization rate parameters and char oxidation rate parameters. The effects were quantified in terms of heat transfer and combustion performance.

Slag layer thickness varies with the length of operation of the plant and varies locally with the soot-blowing (cleaning) cycle. Figure 8 shows the effects of a uniform slag layer thickness on furnace exit gas temperature (FEGT). Slag layers on the walls of the furnace have a significant impact on FEGT due to their low thermal conductance and insulating effect on surface heat transfer. The relationship between slag layer thickness and FEGT is nearly linear for thin layers. If slagging is overestimated and actual FEGT is too low, then superheated steam temperatures may be lower than desired. If slagging is underestimated and actual FEGT is too high, then heat exchanger fouling problems can develop downstream from the furnace. The importance of designing a furnace with an appropriate FEGT emphasizes the need to characterize accurately slagging conditions when evaluating furnace heat transfer performance.

The particle size distribution of pulverized coal may change during the life of the furnace due to abrasive wear of the pulverizers or variations in coal grindability. The mass mean diameter (MMD) is 33.3 μm for the coal particle size distribution shown in Table 3. When MMD is decreased to 25.6 μm, combustion is affected by a 30 percent increase in char oxidation rate, with an insignificant effect on flame length and major species concentrations. Another effect of reduced particle size distribution is a 0.8 percent decrease in heat transfer to the

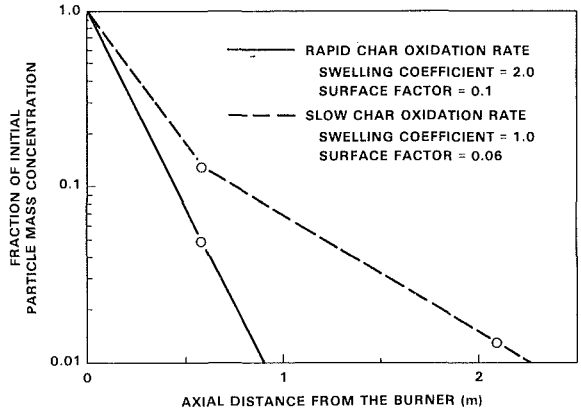

Fig. 10 The effect of char oxidation rate on the concentration of particles near the burner

walls of the furnace. The decrease in coal particle size produces a proportional decrease in ash particle size due to assumptions in the model. Small ash particles increase the radiative scattering and absorption coefficients in the furnace. For ash particles, the effects of scattering dominate the radiative transfer and the net result is a decrease in wall radiative heat transfer effecting a 5 K increase in FEGT.

Combustion properties of coal are major uncertainty in furnace predictions because they vary significantly with coal type and because there are various methods for measuring and analyzing coal combustion rate data. Figure 9 shows the effect of a change in devolatilization rate on the distribution of coal remaining. Predictions are shown for two cases; one case with rate constants by Ubhayaker et al. (1975) and the other case with rate constants by Kobayashi et al. (1976). With Kobayashi's rates the particle burnout is slower, thus increasing the concentrations of coal particles near the burners. Figure 10 shows the effect of a 75 to 85 percent decrease in char oxidation rate on the distribution of particle mass remaining. The reduction in char rate increases the concentration of particle mass near the burners. Therefore, the effects of devolatilization and char oxidation characteristics are important for near flame predictions of particle species concentrations. The changes in particle species affect the distribution of gas species near the flame, the length of the flame and the radiative properties of the particle–gas mixture. For the utility scale furnace these parametric changes do not have a significant effect on the overall furnace combustion efficiency, although the burner region is significantly affected.

Conclusions

The numerical furnace model (FURMO) is an advanced method for analyzing steady-state, three-dimensional, pulverized-fuel combustion. The model simulates the major aspects of pulverized coal combustion necessary for a comprehensive understanding and evaluation of furnace performance. The model is practical because its multidimensional capabilities give it the flexibility to handle many industrial-like geometries. It is realistic because detailed flow patterns are calculated, and it fully integrates the major processes of combustion, including heterogeneous and homogeneous chemical reaction and heat transfer.

While this model is still in the initial stages of validation, the model has already enhanced our understanding of the complex combustion processes and is a valuable engineering tool for assessing the major parameters for furnace design. Ongoing validation studies at B&W will identify areas where additional research is required.

References

1 Abou Ellail, M. M. M., Gosman, A. D., Lockwood, F. C., and Megahed, I. E. A., "Description and Validation of a Three-Dimensional Procedure for Combustion Chamber Flows," AIAA *J. Energy*, 1978.

2 Baum, M., and Street, P., "Predicting the Combustion and Behavior of Coal Particles," *Combustion Science and Technology*, Vol. 3, 1971, pp. 231-243.

3 Bilger, R. W., in: *Turbulent Reacting Flows—Turbulent Flows With Non-Premixed Reactants*, P. A. Libby and F. A. Williams, eds., Springer-Verlag, New York, 1980.

4 Chandrasekar, S., *Radiative Transfer*, Clarendon Press, Oxford, 1950.

5 Dave, F. J., "Subroutine for Computing the Parameters of Electromagnetic Radiation Scattered by Spheres," 360 D-17, 4.007, IBM Corporation, 1969.

6 Edwards, D. K., "Molecular Gas Band Radiation," *Advances in Heat Transfer*, Vol. 12, 1976, pp. 115-193.

7 Field, M. A., Gill, D. W., Morgan, B. B., and Hawksley, P. G., *Combustion of Pulverized Coal*, British Coal Utilization Research Association (BCURA), Leatherhead, 1967.

8 Fiveland, W. A., Cornelius, D. K., and Oberjohn, W. J., "COMO: A Numerical Model for Predicting Furnace Performance in Axisymmetric Geometries," ASME Paper No. 84-HT-103, 1984.

9 Gibb, J., "Furnace and High Temperature Heat Transfer," Intensive Course Lecture Notes, Central Electricity Generating Board, Research Division, Southampton, United Kingdom, 1977.

10 Gibson, M. M., and Morgan, B. B., "Mathematical Models of Combustion of Solid Particles in a Turbulent Stream With Recirculation," *J. Inst. Fuel*, Vol. 43, 1970, pp. 517-523.

11 Gosman, A. D., Pun, W. M., Runchal, A. K., Spalding, D. B., and Wolfshtein, M. W., *Heat and Mass Transfer in Recirculating Flows*, Academic Press, New York, 1969.

12 Gosman, A. D., Lockwood, F. C., and Salooja, A. P., *The Prediction of Cylindrical Furnaces Gaseous Fueled With Premixed and Diffusion Burners*, 17th Symposium (International) on Combustion, The Combustion Institute, 1978.

13 Howard, J. B., Williams, G. C., and Fine, D. H., "Kinetics of Carbon Monoxide in Postflame Gases," *Proceedings of the 14th International Symposium on Combustion*, The Combustion Institute, 1972.

14 Jones, W. P., and Launder, B. E., "The Prediction of Laminarisation With a Two Equation Turbulence Model," *Int. J. Heat Mass Transfer*, Vol. 15, 1972, p. 301.

15 Jones, W. P., and Whitelaw, J., "Calculation Methods for Reacting Turbulent Flows: A Review," *Combustion and Flame*, Vol. 48, 1982, pp. 1-26.

16 Kobayashi, H. J., Howard, J. B., and Sarofim, A. F., "Coal Devolatilization at High Temperatures," *Sixteenth Symposium (International) on Combustion*, The Combustion Institute, 1976, pp. 411-425.

17 Launder, B. E., and Spalding, D. B., *Mathematical Models of Turbulence*, Academic Press, London, 1972.

18 Launder, B. E., and Spalding, D. B., "The Numerical Computation of Turbulent Flows," *Computer Methods in Applied Mechanics and Engineering*, Vol. 3, 1974.

19 Lockwood, F. C., Salooja, A. P., and Syed, S. A., "A Prediction Method for Coal-Fired Furnaces," *Combustion and Flame*, Vol. 38, 1980, pp. 1-15.

20 Magnussen, B., and Hjertager, B., "On Mathematical Modeling of Turbulent Combustion With Special Emphasis on Soot Formation and Combustion," *16th Symposium on Combustion*, The Combustion Institute, 1976.

21 Mitchell, R. E., Sarofim, A. F., and Clomburg, L. A., "Experimental and Numerical Investigation of Combined Laminar Diffusion Flames," *Combustion and Flame*, Vol. 37, 1980, pp. 227-244.

22 Patankar, S. V., *Numerical Heat Transfer and Fluid Flow*, Hemisphere Publishing, New York, 1980.

23 Pope, S. B., "The Calculation of Flows Behind Bluff Bodies With and Without Combustion," PhD Thesis, University of London, London, United Kingdom, 1976.

24 Richter, W., and Fleischhans, G., "Theoretical Study of the Effect of Fuel, Burner, and Furnace Parameters on the Behavior of Enclosed Non-Swirling Anthracite PF Flames," International Flame Research Foundation Report F 24/ga/12, 1976.

25 Shah, N. G., "New Method of Computation of Radiation Heat Transfer in Combustion Chambers," PhD Thesis, Department of Mechanical Engineering, Imperial College of Science and Technology, University of London, London, United Kingdom, 1979.

26 Smith, P. J., and Smoot, L. D., "User's Manual for a Computer Program for Two-Dimensional Coal Gasification and Combustion (PCGC-2)," Draft Report, DOE Contract DE-AC21-80MC14380, Brigham Young University, Provo, UT, 1982.

27 Smith, P. J., and Smoot, L. D., "Modeling Pulverized Coal Reaction Processes," in: *Pulverized Coal Combustion and Gasification*, L. D. Smoot and D. T. Pratt, eds., Plenum Press, New York, 1979.

28 Ubhayakar, S. K., Stickler, D. B., Von Rosenburg, C. W., and Gannon, R. E., "Rapid Devolatilization of Pulverized Coal in Hot Combustion Gases," *16th International Symposium on Combustion*, The Combustion Institute, 1975.

29 Van De Hulst, H. C., *Light Scattering by Small Particles*, Wiley, New York, 1957.

30 Wessel, R. A., "Effective Radiative Properties for Particle-Gas Mixtures," in: *Heat Transfer in Fire and Combustion Systems*, HTD-Vol. 45, ASME, New York, 1985, p. 239.

F. Ito
Tokyo Electric Power Co., Inc.

K. Kuwabara
Central Research Institute of Electric Power Industry.

M. Miyazaki
Toshiba Corporation.

Y. Fukui
Hitachi, Ltd.

Y. Takeda
Mitsubishi Heavy Industries, Ltd.

Improved 12 Percent Cr Rotor Forgings for Advanced Steam Turbines

For future advanced steam turbines of 4500 psi and 1100°F, a high-temperature rotor is one of the most important components to be developed. We estimated that the usable temperature limit of existing 12Cr steel was approximately 1075°F, and then developed improved 12Cr steels. Prototype rotors were made from three types of developed steels, and were put to various evaluation tests. All three steels had creep-rupture strength exceeding that of existing 12Cr steels and were satisfactory in quality and in the other mechanical properties.

Introduction

Although efficiency was improved remarkably up to 1968, the maximum steam conditions for fossil-fired power plants in Japan have been limited to 3500 psi/1000°F for main steam and 1050°F for reheat steam for the last 18 years. However, the oil shock and subsequent higher fuel cost caused us to re-evaluate the existing steam conditions. As a result, the improvement in power plant efficiency by further increasing the steam conditions is today's new target. Therefore, the power plant research and development for advanced steam conditions are being carried out all over the world. In Japan, the construction of power plants of 700 MW/4500 psi/1050°F double reheat, which is the first step toward advanced steam conditions, is just around the corner [1]. Furthermore, research and development for more advanced steam conditions such as 4500 psi/1100°F and 5000 psi/1200°F are also being carried out [2, 3].

Technical difficulties and development technology were reviewed to produce a unit with advanced steam conditions by focusing on a steam temperature of 1100°F. As a result, it was found that the use of ferritic steels for major components, such as rotor and casing, gave economic and technical advantage to this unit.

Therefore, we have selected 4500 psi/1100°F as our targeted steam conditions, and subsequently we have planned to develop and then to verify rotor forging steels that could be used for key parts of the turbine.

Target Properties of 1100°F Rotor Forgings

With respect to turbine rotor forging, up to now, many strenuous efforts have been made to improve its chemical composition, quality, and homogeneity [4]. 1 percent Cr–1 1/4 percent Mo–1/4 percent V (CrMoV) steel has widely been used for high-temperature rotors for 1000°F and 1050°F turbines. In Japan, we have had much experience and success in the application of CrMoV steel for turbine rotors operating at a temperature of 1050°F.

Based on the application experience and history of CrMoV steel rotor forging at a temperature of 1050°F, we have studied the mechanical, metallurgical, and physical properties of CrMoV steel rotor forging so as to establish the target value of the creep rupture strength required for 1100°F turbine rotors. As a result, we found that the 10^5 hr creep rupture strength is 98 MPa (14 ksi) at 1050°F. Therefore, the creep rupture strength to be applied for 1100°F turbine rotor steels is specified as 98 MPa or higher at 10^5 hr.

On the other hand, there are steam turbine rotor forgings whose creep rupture strength is higher than that of CrMoV steel. Examples of these are 12CrMoVNbN steel [5] developed in the US and 12CrMoVTaN steel [6] developed in Japan. These 12Cr steel forgings were found to be satisfactory in 500–1000 MW class turbine rotors. To obtain the critical service temperature of conventional 12Cr steel rotor forgings, and to determine the target values for the characteristics, such as strength, of the new steel to be used for 1100°F turbine rotors, we closely investigated the physical, metallurgical, and mechanical properties of conventional 12Cr steel rotor forgings. With respect to the creep rupture strength of conventional 12Cr steel rotor forgings, we found that the temperature at which the creep rupture strength of these materials is about 98 MPa at 10^5 hr is 1075°F on average (shown in Fig. 3). From this, we concluded that the critical service temperature of the conventional 12Cr steel rotor forgings is 1075°F.

Therefore, forging steel of which the creep rupture strength is higher than that of conventional 12Cr steel rotor forgings is required for manufacture of 1100°F class turbines. We specified that the targeted creep rupture strength should be 98 MPa or higher at 10^5 hr and 1100°F.

Contributed by the Power Division and presented at the Joint ASME/IEEE Power Generation Conference, Portland, Oregon, October 19–23, 1986. Manuscript received by the Power Division March 16, 1987. Paper No. 86-JPGC-Pwr-3.

Moreover, Japanese turbine manufacturers have been engaged in the development of advanced 12Cr steels that can be used for 1100°F turbines. It was considered highly possible that these materials could attain the properties targeted for 1100°F turbine rotors. Considering the maximum-sized IP turbine rotors of 1000 MW class units for practical application, we decided to produce three sample forgings with a drum of 1.2 m (47.2 in.) diameter to investigate and evaluate the properties, producibility, and quality in greater detail. Table 1 shows our targeted properties for the 1100°F turbine rotor.

Manufacturing and Evaluation Test Programs for Sample Forgings

Tables 2 and 3 show the chemical compositions and manufacturing processes for the three sample rotor forgings. Three kinds of advanced 9 ~ 12 percent Cr steels are provided with the following characteristics:

Steel A: Steel of which the creep rupture strength is improved by reducing the carbon content, increasing the Ni and Mo contents as compared with conventional 12Cr steel, adding W, and further increasing the austenitizing temperature by 25°C (45°F) above the temperature of 1050°C (1922°F) applied for conventional 12Cr steel.

Steel B: Steel of which the creep rupture strength is improved by reducing the carbon content and increasing the Ni content as compared with Steel A, and adding 1 percent W. The austenitizing temperature applied is 1050°C.

Steel C: Steel of which the creep rupture strength is improved by reducing the carbon content as compared with conventional 12Cr steel, containing 9 percent Cr and 1.8 percent Mo, and further increasing the austenitizing temperature by up to 1085°C (1985°F).

Table 1 Target properties of improved 12Cr steel rotor forgings for 1100°F turbines

Items	Target Properties
Creep rupture strength	higher than 98 MPa (14.2 ksi) at 10^5 hr and 1100°F. In addition, notch strengthened
Embrittlement	no significant change in long-terms aging (10^5 hr) at 1100°F
Other mechanical properties	equivalent or superior to those of conventional 12Cr steel
Metallurgical properties	normal uniformity in micro-, macro-structure and no significant segregation

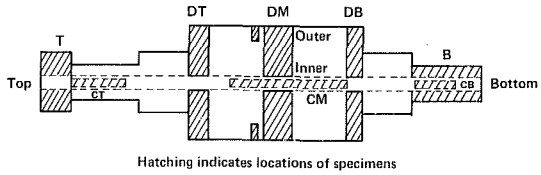

Hatching indicates locations of specimens

Fig. 1 Section and evaluated locations

The three rotors were melted and refined by electric furnace, and then both steels A and B were produced by the VCD process. Steel C was produced by the ESR process. The ingot weight of steel A and B was 70 metric tons each, and that of steel C was 40 metric tons.

Then, the rotors were manufactured and inspected by the same processes as those used for conventional rotor forgings. The finished dimensions of the three sample forgings were 1.2 m (47.2 in.) diameter, 1.8 m (70.9 in.) body length, and 4.5 m (177 in.) total length. Center core of 75 mm (3 in.) diameter was trepanned as a sample from each forging. These rotors were high-quality products that satisfied all the specified requirements for chemical analysis, mechanical tests, magnetic particle inspection for all surfaces, high-sensitivity ultrasonic inspection from periphery and center bore, sulfur-print check, and hardness test at every stage of the manufacturing proceses specified for the rotors.

Figure 1 shows the locations evaluated for the three sample forgings. Test blocks were cut from the sample forgings at the eight locations. Various kinds of tests at the locations indicated in Table 4 were carried out in three laboratories under the same test conditions.

Evaluation Test Results for Sample Rotor Forgings

Chemical Analysis. As indicated in Table 2, the chemical composition of each sample forging was homogeneous throughout the forgings. No significant segregation was found in any elements of the sample forgings.

Sulfur Print and Macrostructure. The three sample forgings were investigated for their sulfur print and macrostructure at the five sectional areas, but no sulfur segregation or abnormal macrostructure was found. In addition, there was no difference between forgings produced by the VCD process and by the ESR process.

Microstructure and Grain Size. The microstructures of the three sample forgings were all homogeneous martensitic structures at the various locations. No significant delta-ferrite was found. This was because the Cr equivalent value[1] of each ad-

[1] Cr equivalent (percent) = Cr + 6Si + 4Mo + 1.5W + 11V + 5Nb − 40C − 30N − 2Mn − 4Ni − 2Co.

Table 2 Chemical composition of sample forgings

	Steel A			Steel B			Steel C		
	Specification	Ladle	Check	Specification	Ladle	Check	Specification	After ESR	Check
C	0.13∿0.16	0.15	0.14∿0.16	0.12∿0.15	0.14	0.13∿0.14	0.12∿0.16	0.14	0.14∿0.15
Si	0.07 max.	0.03	0.04	0.10 max.	0.03	0.03∿0.04	0.10 max.	0.04	0.04∿0.06
Mn	0.40∿0.70	0.59	0.52∿0.56	0.40∿0.60	0.52	0.50∿0.52	0.40∿0.60	0.47	0.46∿0.48
P	0.015 max	0.008	0.004∿0.008	0.015 max.	0.009	0.008∿0.009	0.015 max.	0.012	0.012
S	0.010 max	0.003	0.004∿0.006	0.010 max.	0.0024	0.003	0.010 max.	0.005	0.003∿0.006
Ni	0.40∿0.70	0.63	0.62∿0.69	0.70∿1.20	0.73	0.71∿0.73	0.40∿0.80	0.58	0.58∿0.59
Cr	10.0∿11.0	10.38	10.00∿10.41	10.0∿11.0	10.36	10.31∿10.49	8.5 ∿9.5	9.34	9.23∿9.34
Mo	1.15∿1.35	1.21	1.15∿1.23	1.00∿1.20	1.05	1.05∿1.07	1.60∿1.90	1.68	1.68∿1.70
V	0.15∿0.25	0.19	0.15∿0.16	0.15∿0.25	0.21	0.21	0.12∿0.20	0.17	0.17∿0.18
Nb	0.04∿0.07	0.045	0.04∿0.06	0.06∿0.08	0.07	0.06∿0.07	0.04∿0.08	0.062	0.054∿0.061
W	0.25∿0.35	0.34	0.34∿0.35	0.80∿1.20	1.06	1.00∿1.05	-	-	-
N	0.03∿0.07	0.0458	0.046∿0.052	0.04∿0.06	0.0414	0.046∿0.051	0.02∿0.06	0.042	0.041∿0.043

Check analysis was carried out at eleven positions shown in Table 4.

vanced steel meet the specified value (below 10). The grain size of each sample forging was homogeneous and fine as indicated in Table 5.

Tensile and Charpy Impact Properties. Table 5 shows the tensile properties of the three sample forgings. The strengths of the three sample forgings at the surface and the center were nearly equal to each other. Their ductility was also satisfactory.

Furthermore, they gave satisfactory Charpy impact energy at all locations. The fracture appearance transition temperature (FATT) at body locations gave an excellent value equivalent to or higher than that of conventional steel. No difference was found between the surface and the center locations.

High-Cycle Fatigue Strength. Table 5 shows the high-cycle fatigue strength test results, and indicates that the high-cycle fatigue strengths of forgings A, B, and C are higher than those of conventional 12Cr steel.

Low-Cycle Fatigue Strength. As shown in Fig. 2, the low-cycle fatigue strengths of these forgings at 600°C (1112°F) were equivalent to those of conventional 12Cr steel.

Fatigue Crack Growth Rate. The fatigue crack growth rates of the three sample forgings were equivalent to each other and similar to those of conventional 12Cr steel.

Creep Rupture Properties. Figures 3 and 4 show the creep rupture strength and rupture ductility of the three sample forgings. They clearly indicate that each sample forging sufficiently attain the specified values of strength higher than 98 MPa at 1100°F and 10^5 hr. Their rupture ductility was satisfactory, the values being nearly equal to each other and remaining constant with the time in elongation and reduction of area during 9400 hr to date.

Table 3 Manufacturing processes and conditions of sample forgings

Items	Steel A	Steel B	Steel C
Steel making	VCD	VCD	ESR
Ingot weight	70 tons	70 tons	40 tons
Heat treatment			
quench	1075°C x 32 hrs Oil quench	1050°C x 33 hrs Oil quench	1085°C x 31 hrs Oil quench
temper	570°C x 31 hrs FC 660°C x 46 hrs FC	570°C x 33 hrs FC 660°C x 49 hrs FC	550°C x 32 hrs FC 665°C x 44 hrs FC

Table 4 Evaluation test matrix for improved 12Cr steel sample rotor forgings

Test items \ Locations / Positions / Directions	Center Core			Prolong		Drum									
	CT	CM	CB	T	B	DT			DM				DB		
	C	C	C	O	O	O	I		O		I		O	I	
	L	L	L	L	L	R	L	T	R	T	L	T	R	L	T
Chemical composition, sulphur print, macro- and micro- structure (grain size), tensile properties, charpy impact	○	○	○	○	○	○	○	○	○	○	○	○	○	○	○
Impact transition temperature (FATT)									○		○	○			
Creep rupture		○							○			○			
Tensile (high temperature), low cycle fatigue (600°C), fracture toughness									○			○			
High cycle fatigue (20°C), notch rupture, creep									○						
Long time aging (600°C), physical properties									○		○				
Step cool											○				
Fatigue crack growth												○			

Location CT, CM, CB, T, B, DT, DM and DB: shown in Fig. 1
Position C: Center core, O: Outer side, I: Inner side
Direction L: Longitudinal, R: Radial, T: Tangential

○: carried out

Table 5 Evaluation test results

Test Items		Steel A Whole Average	Steel A Location DM(O)	Steel A Location CM	Steel B Whole Average	Steel B Location DM(O)	Steel B Location CM	Steel C Whole Average	Steel C Location DM(O)	Steel C Location CM
Tensile properties	0.02% yield strength (MPa)	700	705	704	719	719	719	670	652	659
	Tensile strength (MPa)	915	916	927	926	927	930	894	878	885
	Elongation (%)	18.7	18.8	17.9	19.3	19.5	18.8	18.7	19.6	18.7
	Reduction of area (%)	55.5	56.2	53.7	58.2	63.5	55.9	58.9	60.6	56.1
Charpy impact energy (J)		30.4	24.5	36.9	25.5	23.5	27.5	35.3	28.4	38.5
	FATT (°C)	46	52	37	55	59	48	51	48	45
High cycle fatigue strength (MPa)		451	-	-	471	-	-	471	-	-
Embrittlement properties		Location DM(I)	Location DM(O)	Location DM(I)	Location DM(I)	Location DM(O)	Location DM(I)	Location DM(I)	Location DM(O)	Location DM(I)
	FATT as received (°C)	42	51	40	49	59	49	55	49	54
	FATT after step cool (°C)	38	-	-	46	-	-	53	-	-
	FATT after 3000 hrs aging at 600°	-	58	52	-	64	57	-	60	56
Grain size		2.7 4.0	-	-	3.9 5.1	-	-	3.6 4.9	-	-

The notch rupture strength of the three sample forgings was much higher than that of the smooth specimen. Therefore it is likely at present that there exists no potential trouble related to notch weakness.

It is necessary to perform much longer time tests and to evaluate the material properties with different chemical compositions, manufacturing processes, and heat treatments.

Creep Strength. The creep test was carried out at temperatures of 600°C and 630°C (1166°F). The test results obtained using the Larson–Miller parameter indicate that the strength is higher than that of conventional 12Cr steel.

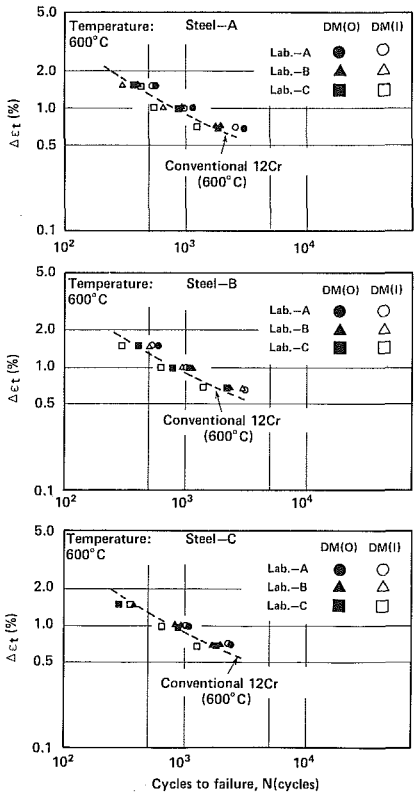

Fig. 2 Low-cycle fatigue properties of sample forgings

Step Cool Test. No significant effect on the FATT of three sample forgings after a step cool treatment[2] was found.

Long Time Aging. The FATT was measured after the sample forgings were aged for the period of 3000 hr up to the present at a temperature of 600°C. As shown in Table 5, no significant embrittlement was found for any of the three forgings. Much longer time tests are also necessary to evaluate the metallurgical stability.

Fracture Toughness. The fracture toughness of the three sample forgings was satisfactory at the surfaces and the centers, exceeding that of the conventional 12Cr steel.

Producibility and Quality. Regarding producibility, it was confirmed that the three steels could be produced without specific trouble in the same manufacturing process as that used for conventional 12Cr steel, and it was also found that the quality levels of the three sample forgings were as satisfactory as in the case of conventional 12Cr steel.

The metallurgical and mechanical properties of the three sample forgings at every location were homogeneous and sufficiently met their specifications according to every inspection test.

Furthermore, the qualities of steels A and B, which were produced by the VCD process, and the quality of steel C, produced by the ESR process, were satisfactory with regard to metallurgical properties. Within the scope of these evaluation tests, no significant differences between the two manufacturing processes were found. It is essential to define precisely the characteristics and the differences between the different steel processes from the other technical and also economical points of view.

Summary

The three different examples of advanced 12Cr rotor were developed in order to produce a large-sized steam turbine unit with the advanced steam temperature of 1100°F. The full-sized sample rotor forgings of the three examples were pro-

[2]Step cool: 595°C × 1hFC → 535°C + 15hFC → 525°C × 24hFC → 495°C × 48hFC → 475°C × 72hFC → 300°C AC

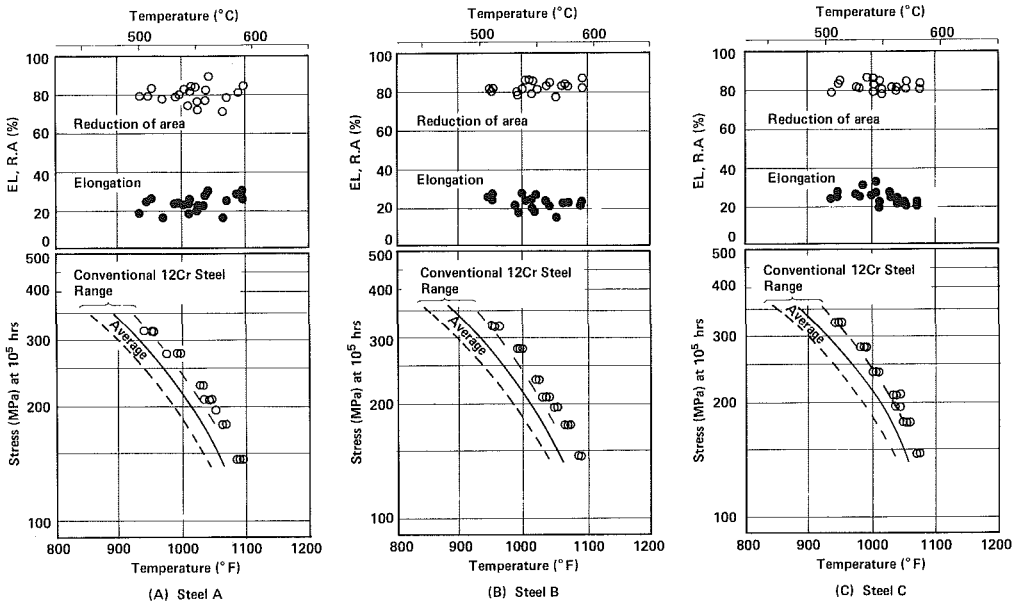

Fig. 3 Creep rupture strength for body surface DM(0) of sample forgings

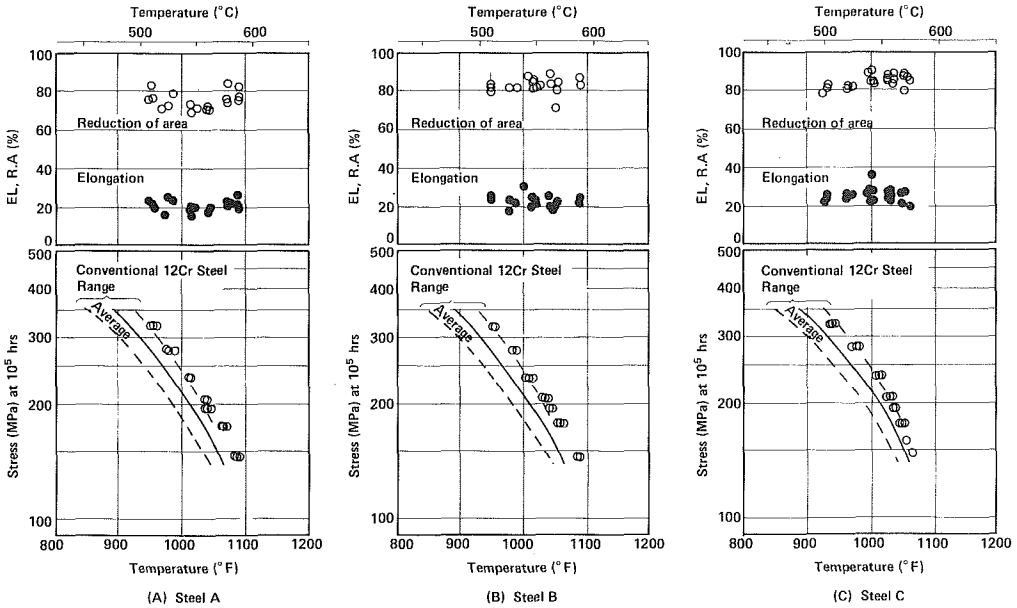

Fig. 4 Creep rupture strength for body center (CM) of sample forgings

duced to evaluate their soundness from the standpoints of producibility, metallurgy, and mechanical properties.

As stated above, we have succeeded in producing three advanced 12Cr steels that can be used for 1100°F steam turbines in rotor forgings through our study. The fact that advanced 12Cr steels can be used for 1100°F steam turbine without any trouble is quite encouraging to us, as we are making every possible effort to permit development of 1100°F steam turbines. Furthermore, application of the newly developed 12Cr steel makes it possible to design 1100°F turbines free from the lowered thermal efficiency caused by the design requirement of cooling the rotor to compensate for the lack of high temperature strength. We firmly believe that we have solved one of the greatest problems standing in the way of manufacture of 1100°F turbines.

References

1 Akiba, M., Ikeda, T., and Aizawa, K., "The Design of a 700 MW Steam Turbine With Advanced Steam Conditions," American Power Conference, Apr. 1985.

2 "Engineering Assessment of an Advanced Pulverized-Coal Power Plant," EPRI-CS2555.

3 Suzuki, Takao, "The Development of Coal Fired Power Unit With Ultra High Performance in Japan," EPRI Fossil Plant Heat Rate Improvement Workshop," Aug. 26–28, 1981.

4 Curran, R. M., Newhouse, D. L., and Newman, J. C., "The Development of Improved Rotor Forgings for Modern Large Steam Turbines," ASME Paper No. 82-JPGC-Pwr-25, 1982.

5 Newhouse, D. L., Boyle, C. J., and Curran, R. M., "A Modified 12-percent Chromium Steel for Large High-Temperature Steam Turbine Rotors," ASTM 68th Annual Meeting, June 1985.

6 Kawai, M., Kawaguchi, K., Yoshida, H., Kanazawa, E., and Mito, S., "Mechanical Properties of 12% Cr Steel Forging for Large Steam Turbine," *Journal of the Iron and Steel Institute of Japan*, Vol. 64, No. 1, 1978.

Centrispun High Alloy Steel Castings for Gas Turbine Applications

P. G. Nixon
Firth Vickers Foundry Ltd.,
Sheffield, United Kingdom

Extensive use has been made by the gas turbine industry of centrispun castings of certain highly alloyed heat resisting steels. The paper outlines the main features of the centrispinning process and discusses the advantages that one could expect, not only in mechanical properties, but also in cost and the casting to shape in refractory molds. Results of mechanical tests on sections cut from representative castings are given and show the high order of the tensile strength to be expected.

Introduction

As the name implies, the essential feature of the centrispinning process, or the centrifugal casting process, consists of subjecting molten metal to centrifugal pressure created in a rapidly rotating mold in such a manner that the metal is directed to take up the shape of the mold into which it is being poured. All the extraneous nonmetallic material, being less dense than steel, is retained at the bore surface together with the microporosity formed by the directional solidification. This is subsequently removed by machining to give a sound casting.

The centrispinning process itself is not new and goes back to the early 19th Century when the first British patents were published. The first commercial applications were in the 1920s when cast iron water pipes were developed, followed shortly by automobile liners and piston ring pots.

It did not take long for the aircraft industry to realize that the cleanliness and convenience of this process would lend itself readily to many aircraft applications. Shortly before the second world war, Firth Vickers Foundry became involved in the development of centrifugal castings for the production of special alloy cylinder sleeves for the Bristol Hercules and Centaurus sleeve valve engines, and over 3 million of these were produced by F. V. F.

Since that time, development has continued into the production of vertical and horizontal die castings from 6 in. o/d to 60 in. o/d, and over the last 30 years the technique for centrishaped castings has been perfected by casting into refractory molds to give diameters up to 120 in. o/d and 10,000 lb cast weight.

Process Plant

Normally, two distinct types of centrifugal casting machines are in daily use:

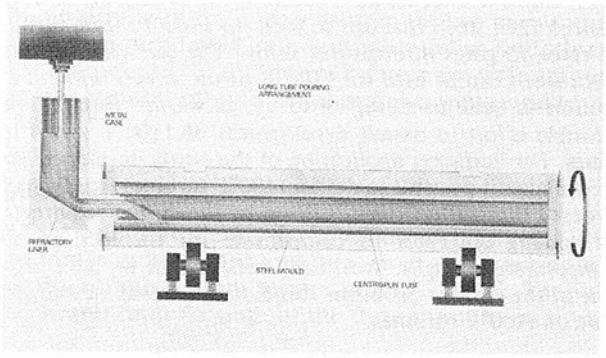

Fig. 1 Horizontal spinning machine/casting operation

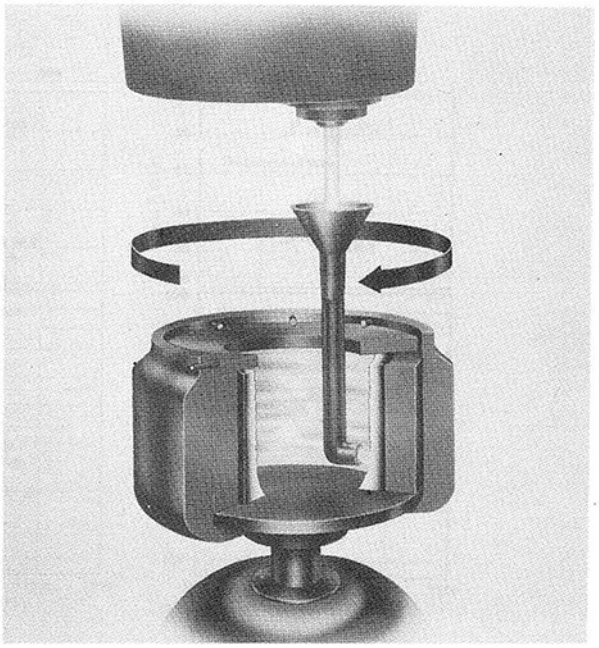

Fig. 2 Vertical spinning machine/casting operation

Contributed by the Gas Turbine Division of THE AMERICAN SOCIETY OF MECHANICAL ENGINEERS and presented at the 32nd International Gas Turbine Conference and Exhibit, Anaheim, California, May 31–June 4, 1987. Manuscript received at ASME Headquarters February 19, 1987. Paper No. 87-GT-206.

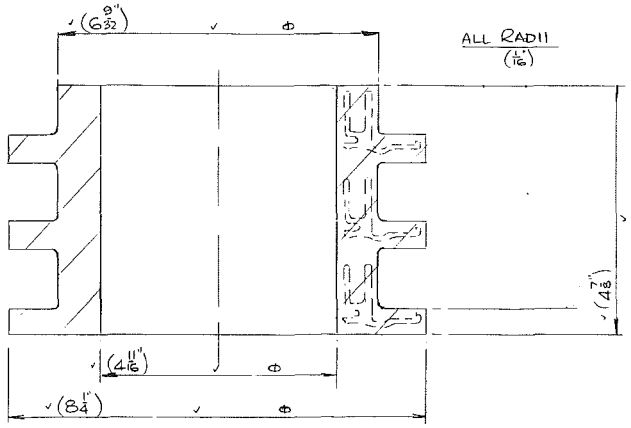

Fig. 3 Possibility of producing finished parts from short or long centrispun tubes

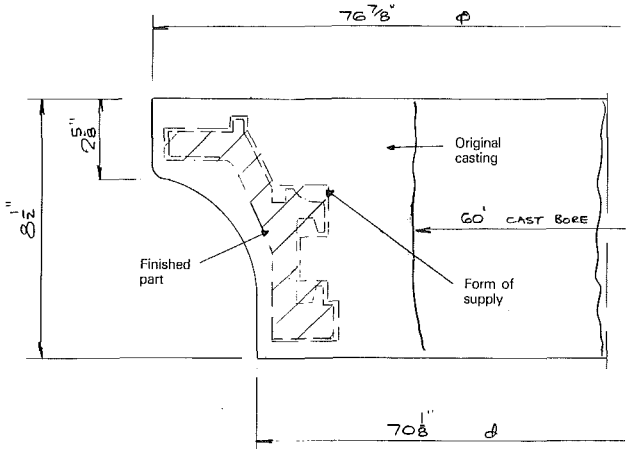

Fig. 4 Possibility of producing finished part from large vertical shaped casting

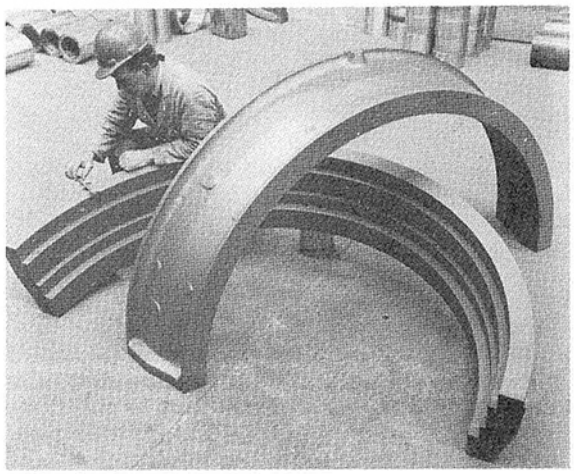

Fig. 5 Measurement of a split outer casing—material VIKRO 155

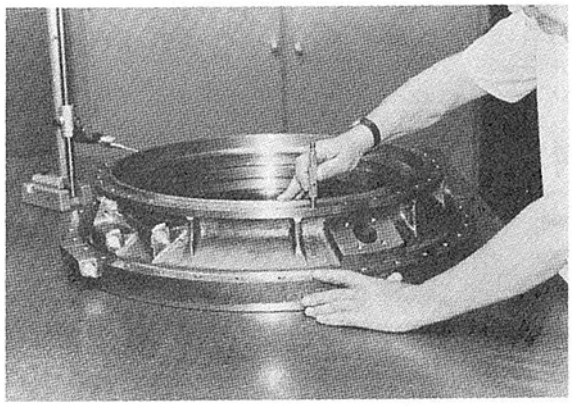

Fig. 6 Centrispun casting showing shaped outer cast profile—material HR Crown Max

(*i*) axis of rotation horizontal (Fig. 1)
(*ii*) axis of rotation vertical (Fig. 2)

Which type of process to use for a particular casting is generally governed by the shape of the casting itself. In general, one can say if the diameter is greater than the length, it should be made vertically, and for a length greater than the diameter, then horizontally is the answer. Obviously, this is only a general rule and the methods engineer has his own "built-in" computer made up over many years of experience to decide which method will be used for a certain job.

As the names of the process imply, in the horizontal method of casting the die is rotating in a horizontal position on twin rolls and the metal is introduced through an open end plate in one end of the die and moves along the die giving a casting of uniform thickness along its length.

In the vertical process, the die is spinning at a lower G force than with the horizontal process and the metal enters through an open top lid, by means of an inclined tundish, which ejects the metal onto the wall of the die at a tangent, in the direction the die is rotating.

Having decided on the method to use, it is then a matter of deciding the various parameters that govern the production of a sound casting and one that will give dimensions suitable to produce the finished part.

(*i*) Horizontal. If the horizontal method is chosen, then the choice of dimension is limited. The outside diameter of the casting will decide the metal die to be used and this outside diameter is calculated from the finished diameter of the casting to be supplied, with an allowance given for surface roughness contraction and the refractory coating thickness inside the die.

The internal diameter is calculated again from the diameter required by the customer, with an allowance made for the unsound material in the bore, peculiar to this process. From these dimensions, a calculation is made of the amount of metal required to produce the casting and, by the use of accurate digital scales situated above the ladle, this exact amount of metal is poured into the die.

(*ii*) Vertical. The choice of how to produce a casting by the vertical process is a little more complicated, as there are two methods available to us:

(*a*) metal die molds
(*b*) refractory-shaped molds

Metal mold dies are usually of relatively simple shape, as to produce a shaped o/d on a casting would mean a shaped bore in the die. This is obviously an expensive proposition as regards tooling costs and is only warranted when large production runs are expected or schedules of the same part over a number of years.

Figure 3 shows how we can produce shaped machined parts from a parallel-sided casting.

Similarly, from a large 76 in. diameter casting, weighing over 2000 lb in the as-cast condition, the profile shown in Fig. 4 can be produced with a delivered weight of 500 lb.

The decision on whether to produce a shaped casting for a particular part is not always easy and is often decided by the dies available. With this process, we have all the costs incurred in producing a conventional sand casting with regards to patterns, molding, drying, etc. This process is used widely at F.

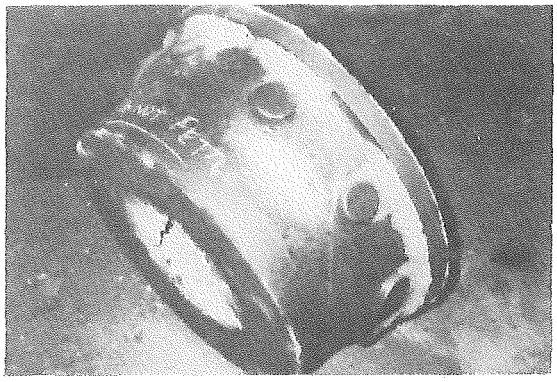

Fig. 7 Centrispun casting produced from refractory-shaped mold—as cast—material FV507

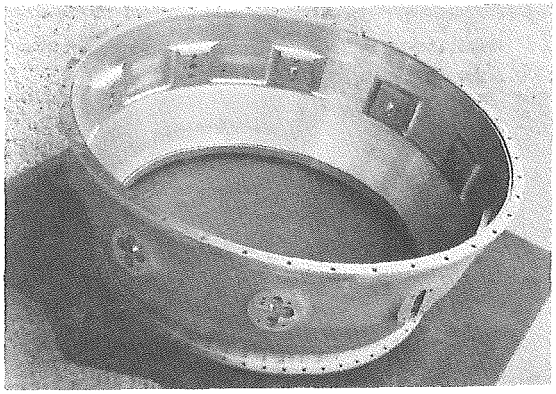

Fig. 8 Casting shown in Fig. 7 after final machining—material FV507

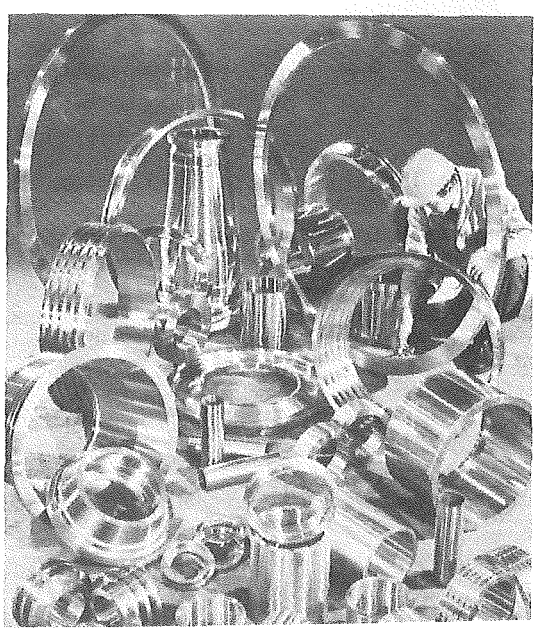

Fig. 9 A collection of machined centrispun components

V. F. for the production of large outer casings having top, bottom, and splitting flanges, and also any casting in which a profiled as-cast outer face is acceptable on the finished part, and where weight is not too important. A typical split outer casing is shown in Fig. 5. Other examples of shaped centrifugal castings are shown in Figs. 6–8.

It is quite easy to see, particularly with Fig. 5, how a shaped outer diameter on a centrispun casting can save a large amount of expense in machining and grinding to size. A photograph showing a collection of finished machined parts is shown in Fig. 9.

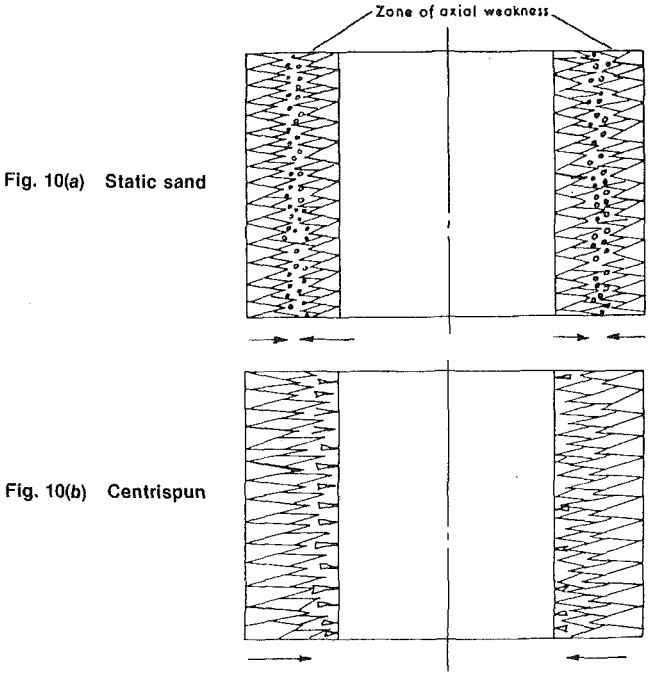

Fig. 10(a) Static sand

Fig. 10(b) Centrispun

Fig. 10 Solidification pattern in centrispun and static sand casting

Progressive Solidification

Having looked briefly at the methods that can be used to produce centrispun castings, we can now look at the reason why centrispun castings show a distinct advantage over static castings. The main reason for the advantage is the progressive solidification that takes place with both the die and refractory method of spinning. Solidification commences at the inner wall of the die, whether it be metal or refractory, and progresses radially from the outer edge of the casting to the axis of rotation. Foreign bodies and lighter inclusions are directed toward the bore initially by the centrifugal force and then by progressive solidification of the metal.

Figure 10 shows clearly the effect this has on the structure of the casting. Columnar grains grow continually from the outer wall to the bore giving an inner narrow zone of unsound material, which is subsequently machined away. With conventional sand casting, cooling proceeds from two faces with the formation of columnar grains meeting toward the center of the casting. All the unsoundness due to shrinkage, tears, inclusions, etc., remains in the middle of the casting and this either stays in the finished part or is subsequently ground out and needs expensive weld repair.

We can say, in general, that a metal die centrifugal casting will meet ASTM E446 Class I radiography and a refractory shape centrispun casting should fall within Class II, and, in most circumstances, would meet Class I.

Quality Control

Every process, whether it be in a forge, rolling mill, or casting shop, needs a good degree of shop floor control and the centrifugal casting process is no exception to this rule.

Control starts in the first instance with the metal itself being melted to produce the casting. The charge for the melt is selectively controlled with both economy and quality in mind. All our castings undergo extensive machining operation, which, at the end of the operation, may give over 70 percent returns in turnings. All these turnings are good quality material and,

after chipping and degreasing, are returned to the furnace for re-use in another melt. In order to use these turnings, it is essential to segregate the materials. We produce over 100 different materials, and this, in itself, needs good housework within the foundry grounds to avoid contamination.

The next operation is in preparation of the die. A well-prepared die is absolutely essential in producing a casting with no lapped surfaces, cracks, hot tears, etc. The dies are sprayed with a refractory slurry after first being preheated to 400°C in a hot stove. This slurry serves the purpose of both helping the metal flow along the die, and also preventing fusion onto the die.

Similarly, the refractory molds need the correct mix of refractories, accurate pattern control, molding, etc.

We have already said that the metal weight is calculated from the dimensions of the casting to be produced, and this is controlled accurately by digital crane scales. It must be appreciated that if too much metal is poured into the casting, this is all excess to requirements and must be machined out to produce the finished part. Machining is expensive and, therefore, accurate control is essential. Insufficient metal into the die would give an unsound casting, as there would not be enough metal in the bore to satisfy the feeding requirements. The bore size is calculated accurately to allow for unsound material to be removed in machining.

Once the casting has been withdrawn from the die, it is then immediately stamped with its own unique cast number, material, and machine on which it was cast. These numbers remain on the part throughout its life and into the customers'

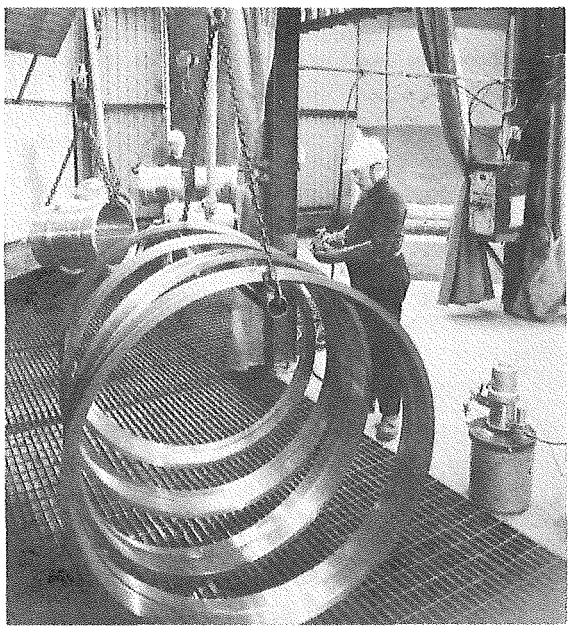

Fig. 11 Machined castings undergoing fluorescent dye penetrant inspection

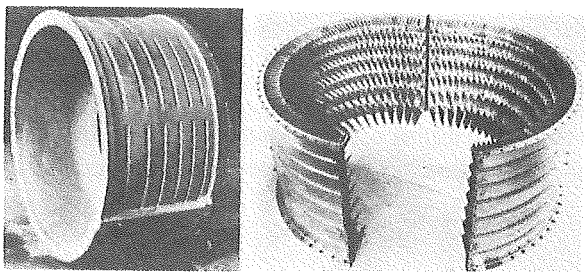

Fig. 12 Compressor casing: (*a*) as cast; (*b*) finished; machined, assembled, and bladed

Table 1 Materials for use in gas turbine application

Material Designation	C	Si	Mn	Cr	Ni	Mo	Co	Other Elements		
FI	.08 max	1.0 max	1.0 max	11.5/ 13.5	0.50 max	0.15 max				
FG	0.15/ 0.30	1.0 max	1.0 max	11.5/ 14.0	1.5 max					
FV13/4	0.06 max	1.0 max	1.0 max	11.5/ 14.0	3.5/ 4.5	0.40/ 1.0				
FV507	0.08/ 0.18	1.0 max	0.5/ 1.25	10.0/ 12.5	1.5 max	0.5/ 1.0		V 0.10/0.50	Cb 0.20/0.60	
FV681	0.10/ 0.15	0.50 max	0.4/ 0.9	10.5/ 12.5	2.5/ 3.5	1.5/ 2.0	1.0/ 2.0	V 0.25/0.45	Cb 0.3 max	N_2 0.020/0.045
FV M152	0.10/ 0.17	0.30 max	0.5/ 0.9	11.0/ 12.75	2.0/ 3.0	1.5/ 2.0		V 0.25/0.40	N_2 0.01/0.05	
FCB	0.16 max	0.5/ 2.0	2.0 max	17.0/ 20.0	7.0/ 12.0	0.6 max		V 0.1 max	Cb 8xC 1.5 max	
HRC1	0.25 max	0.5/ 1.5	1.5 max	21.0/ 25.0	10.0/ 13.0			W 1.0 max		
HRC MAX	0.10/ 0.25	1.2/ 2.0	1.0 max	21.0/ 25.0	10.0/ 12.0	1.0 max		V 0.2 max	Cb 0.3 max	W 2.7/3.5
VIKRO 7	0.08/ 0.15	1.0 max	1.0 max	18.0 21.0	Bal		5.0 max	Ti 0.2/0.6	Fe 5.0 max	
VIKRO 80	0.03/ 0.10	1.0 max	1.0 max	18.0/ 21.0	Bal		2.0 max	Ti 1.8/2.7	Al 0.5/1.8	Fe 5.0 max
VIKRO 9	0.10 max	1.5 max	1.0 max	18.0/ 21.0	Bal		15.0/ 21.0	Ti 1.8/3.0	Al 0.8/2.0	Fe 5.0 max.
VIKRO 20	0.05/ 0.15	1.0 max	1.0 max	20.5/ 23.0	Bal	8.0/ 10.0	0.5/ 2.5	W 0.2/1.0	Fe 17.0/20.0	
VIKRO 155	0.20 max	1.0 max	1.0/ 2.0	20.0/ 22.5	19.0/ 21.0	2.5/ 3.5	18.5/ 21.0	Cb 0.75/1.25	N_2 0.10/0.2	W 2.0/3.0
VIKRO 242	0.27/ 0.40	0.2/ 0.45	0.2/ 0.5	18.0/ 23.0	Bal	9.5/ 11.0	9.0/ 11.0	Cb 0.25 max	W 0.2 max	
VIKRO 263	0.04/ 0.08	0.4 max	0.6 max	19.0/ 21.0	Bal	5.6/ 6.1	18.5/ 21.0	Cb 0.25 max	Ti 1.9/2.4	Al 0.3/0.6
VIKRO 718	0.10 max	0.35 max	0.35 max	17.0/ 21.0	50/55	2.8/ 3.3	1.0 max	Cb 4.75/5.5	Ti 0.65/1.15	Al 0.4/0.8
VIKRO 3501	0.45/ 0.55	0.30 max	0.30 max	0.6/ 0.9	27.5/ 28.5	0.8/ 1.2	13.0/ 15.0	V 0.4/0.6		

works. If machining removed the identification marks, the casting is restamped before removal from the machine.

A cast identity card accompanies the casting along its route informing everyone of the heat treatment, cast and machine sizes, weights, dies to be used, spinning speeds, etc. The respective personnel at each stage of completion sign the card to verify the operation has been carried out.

The problem of spinning speed is all important. If the correct speed is not used, then the casting will more than likely be unsound, because the G force has been insufficient to force the deleterious inclusions, etc., to the bore of the casting. This casting speed is calculated by the formula

$$X\,G = 0.0000143\,DN2$$

where G is centrifugal force; D is internal diameter; N = rpm.

In long die tube production, it is necessary to aim for G forces on the order of 150–200, but this figure can be reduced drastically for the longer vertical spinnings and still give satisfactory structures and suitable properties.

Inspection

(i) Dye Penetrant. Foundry inspection segregates scrap castings before any work is done on them, but the essential final inspection is all important.

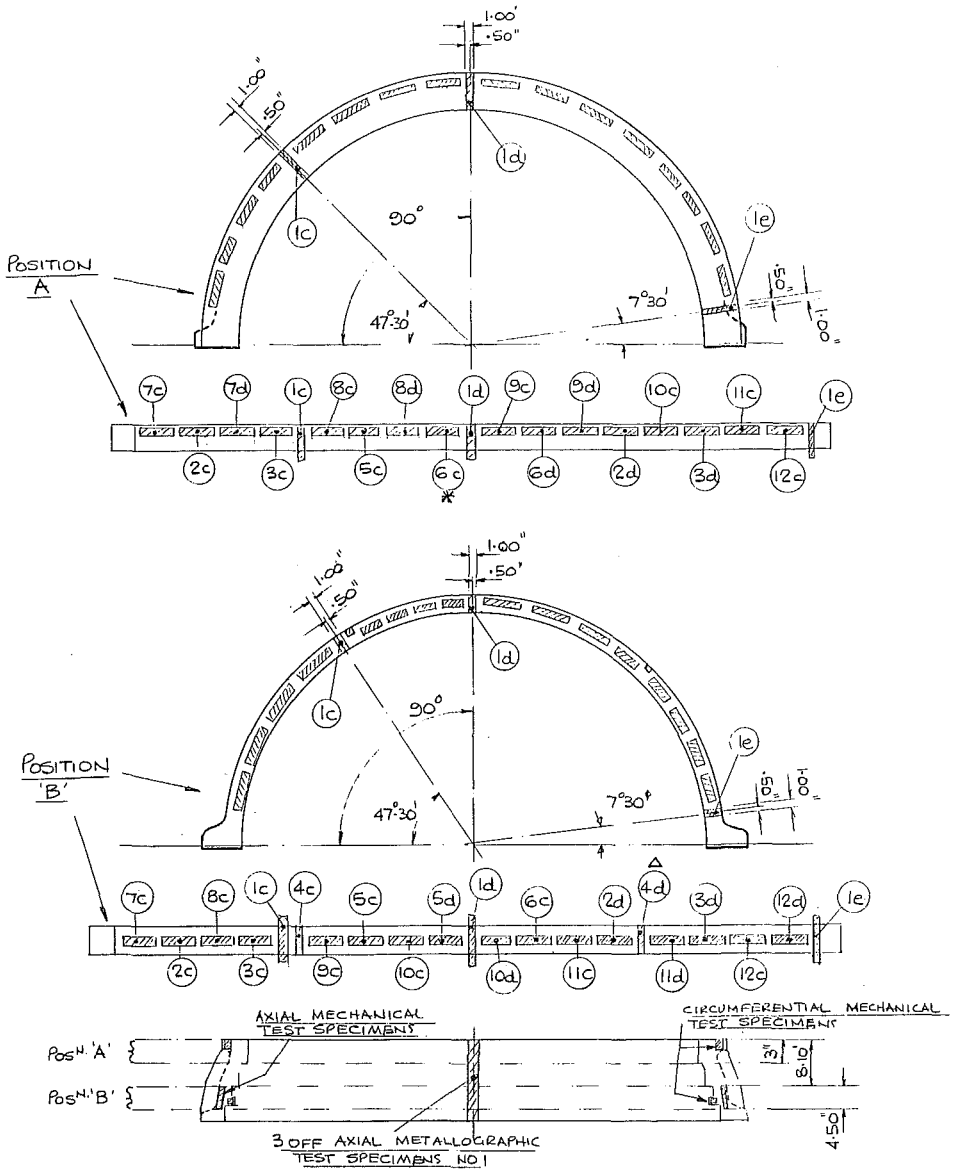

SPECIMEN NO	ORIENTATION	TEST	SPECIMEN SIZE	NO. OFF
1	AXIAL	METALLOGRAPHIC	1" THICK SLICE FULL LENGTH OF CASTING	3
2	CIRCUMFERENTIAL	TENSILE - ROOM TEMP.	1"x 1"x 4"	2 FROM 'A' & 2 FROM 'B'
3	CIRCUMFERENTIAL	TENSILE - 1000°F	1"x 1"x 4"	2 FROM 'A' & 2 FROM 'B'
4	AXIAL	TENSILE - 1000°F	3/4"x 3/4"x 4"	2 FROM 'B'
5	CIRCUMFERENTIAL	RUPTURE - SMOOTH BAR - 1000°F - 66 KSI	1"x 1" x 4"	1 FROM 'A' & 2 FROM 'B'
6	CIRCUMFERENTIAL	RUPTURE - NOTCHED BAR - 1000°F - 66 KSI	1"x 1"x 4"	2 FROM 'A' & 1 FROM 'B'
7	CIRCUMFERENTIAL	LOW CYCLE FATIGUE - 400°F - 90 KSI	1" x 1" x 6"	2 FROM 'A' & 1 FROM 'B'
8	CIRCUMFERENTIAL	LOW CYCLE FATIGUE - 400°F - 100 KSI	1" x 1" x 6"	2 FROM A & 1 FROM 'B'
9	CIRCUMFERENTIAL	LOW CYCLE FATIGUE - 400°F - 120 KSI	1"x 1" x 6"	2 FROM 'A' & 1 FROM 'B'
10	CIRCUMFERENTIAL	LOW CYCLE FATIGUE - 1000°F - 45 KSI	1"x 1" x 6"	1 FROM 'A' & 2 FROM 'B'
11	CIRCUMFERENTIAL	LOW CYCLE FATIGUE - 1000°F - 66 KSI	1" x 1" x 6"	1 FROM 'A' & 2 FROM 'B'
12	CIRCUMFERENTIAL	LOW CYCLE FATIGUE - 1000°F - 85 KSI	1" x 1" x 6"	1 FROM A & 2 FROM B

NOTE:- AXIAL METALLOGRAPHIC SPECIMENS (NO. 1 - 3 OFF) MUST BE OBTAINED BEFORE CASTING IS CUT UP TO OBTAIN MECHANICAL TEST SPECIMENS

SPECIMENS TO BE MARKED TO INDICATE POSITION FROM WHICH IT HAS BEEN OBTAINED EG. AGc (*), B4d (Δ) ETC.

Fig. 13 Cut-up tests on FV507 centrispun outer casing

All castings for the gas turbine industry are subject to surface dye inspection as a matter of routine, but is usually a mandatory requirement by the customer.

F. V. F. was the first to be approved to Defence Standard 0524 and needs to meet the stringent requirements of the various ministries of aircraft production, supply, aviation technology, and defense.

The older established method of red dye checking was found to be too insensitive to inspect aircraft quality castings adequately, and a semi-automatic fluorescent dye line was installed in its place in collaboration with Rolls Royce. This dye line is in the shape of a horseshoe and can take castings up to 120 in. diameter and is made up of seven stations (Fig. 11).

Table 2 Mechanical properties of materials to be used in the gas turbine industry

Material Designation	Heat Treatment (°F)	0.2% Proof Stress k.s.i.	0.2% Proof Stress MPa	Ultimate Tensile Strength k.s.i.	Ultimate Tensile Strength MPa	% El.
FI	1925 AC/1775 AC/1380 AC	53	370	78	540	15
FG	1925 AC/1775 AC/1170 AC	67	465	123	850	10
FV507	2150 AC/1250 AC	107	740	134	924	8
FV13/4	1925 AC/1100 AC/1100 AC	90	620	112	770	12
FV681	1925 AC/1200 AC/1200 AC	107	740	135	930	8
FV M152	2000 OQ/1050 OQ/1025 AC	120	825	150	1035	13
FCB	1925 AC	35	240	70	480	22
HRC1	1925 AC	29	200	78	540	40
HRC MAX	2025 AC	32	220	71	490	20
VIKRO 7	1925 AC	33	230	94	650	30
VIKRO 80	1950 AC/1550 AC/1300 AC	85	590	142	980	8
VIKRO 9	1950 AC		TO ANALYSIS ONLY			
VIKRO 20	2150 AC	30	205	67	465	25
VIKRO 155	2150 AC	40	280	80	550	20
VIKRO 242	AS CAST		TO ANALYSIS ONLY			
VIKRO 263	2100 AC/1475 AC	62	420	90	620	12
VIKRO 718	2000 AC/1750 AC/1325 FC TO 1100 AC	109	750	124	855	5
VIKRO 3501	2150 OQ	58	400	87	600	20

At final inspection, the presence of any defects is noted and compared with the stringent requirements laid down by the various inspectorate bodies, which, for the aircraft industry, are as near to perfection as makes little difference.

***(ii)* Radiography.** A high proportion of the castings produced are subjected to radiographic examination, in particular the critical aircraft parts.

Many of the aircraft castings currently being supplied have been made over many years and have been produced in hundreds and sometimes thousands. On these parts, because of the consistently good quality over the years, customers have relaxed radiography from 100 to 10 percent and, in some cases, even removed radiography completely from the supplied casting.

Problems do exist in the standards put down for the various parts. The only meaningful standards are, of course, for this type of work, E446. This standard, however, is for static sand castings and not for centrispun castings, and, although customers quote these standards on drawings, they must work to their own "built-in" standards using the ASTM charts purely as a guide.

Materials

The materials supplied to the gas turbine industry are fairly widespread and vary from the simple 13 percent chromium steels to the more exotic Multimets and Nimonic alloys.

Table 1 gives a list of the bulk of the materials supplied. Although several of the alloys fall into British Standards re-

Table 3

MECHANICAL PROPERTIES ON CASING (EXAMPLE 1) FV507

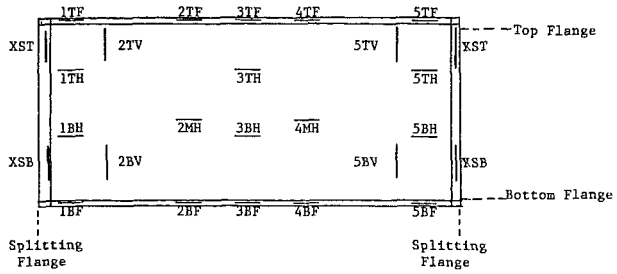

POSITION	0.1% PROOF STRESS k.s.i.	0.1% PROOF STRESS MPa	ULTIMATE TENSILE STRENGTH k.s.i.	ULTIMATE TENSILE STRENGTH MPa	% El.
1TF	125	862	137	945	14
2TF	125	862	138	951	12
3TF	126	869	139	959	11
4TF	129	890	138	951	8
5TF	126	869	139	959	9
1BF	130	896	138	951	14
2BF	127	875	141	972	16
3BF	129	890	142	979	15
4BF	131	903	141	972	14
5BF	127	875	141	972	15
1TH	130	896	138	951	12
3TH	126	869	141	972	9
5TH	129	890	138	951	13
1BH	127	875	138	951	8
3BH	129	890	140	965	13
5BH	125	862	140	965	11
2MH	126	869	139	959	13
4MH	125	862	138	951	15
2TV	127	875	138	951	9
5TV	124	855	141	972	13
2BV	127	875	139	959	15
5BV	123	848	140	965	15
XST	119	820	138	951	12
XSB	126	869	138	951	15
YST	118	814	137	945	15
YSB	124	855	137	945	16

Table 4 Mechanical properties on casing (Example 2)—FV507

ROOM TEMPERATURE TENSILE

POSITION	0.1% PROOF STRESS k.s.i.	MPa	0.2% PROOF STRESS k.s.i.	MPa	ULTIMATE TENSILE STRENGTH k.s.i.	MPa	% El.	% R/A
Spec'n	–	–	107	740	126	870	5	10
2C-A	115	793	119	820	138	950	13	34
2C-B	110	758	114	786	133	917	7	11
2D-A	116	800	119	820	138	950	13	34
2D-B	108	744	113	780	131	900	8	15

TENSILE TEST AT ELEVATED TEMPERATURE 1000°F (538°C)

3C-A	75	517	80	550	91	627	15	48
3C-B	73	503	78	540	87	600	17	49
3D-A	75	517	80	550	90	620	14	48
3D-B	71	490	75	520	87	600	14	42
4C-B	72	500	77	530	88	607	14	45
4D-B	75	517	79	545	91	627	13	39

STRESS TO RUPTURE 66000 p.s.i. AT 1000°F (538°C)

TYPE OF TEST	POSITION	LIFE (hours)
Notched test	6C-A	1176 unbroken
"	6C-B	" "
"	6D-A	" "
Unnotched test	5C-A	263 broken
"	5C-B	68 "
"	5D-B	140 "

LOW CYCLE FATIGUE

POSITION	TEMPERATURE °F	ALTERNATING STRESS (k.s.i.)	CYCLES TO COMPLETE FAILURE
A7C	400	90	11,400
A7D	"	90	9,253
B7C	"	90	2,850
A8C	"	100	6,560
A8D	"	100	3,875
A8C	"	100	2,240
A9C	"	120	4,010
A9D	"	120	4,600
B9C	"	120	1,015
A10C	1000	45	18,682
B10C	"	45	12,591
B10D	"	45	27,623 (unbroken)
A11C	"	65	14,646
B11C	"	65	13,854
B11D	"	65	7,998
A12C	"	85	4,065
B12C	"	85	4,910
B12D	"	85	2,588

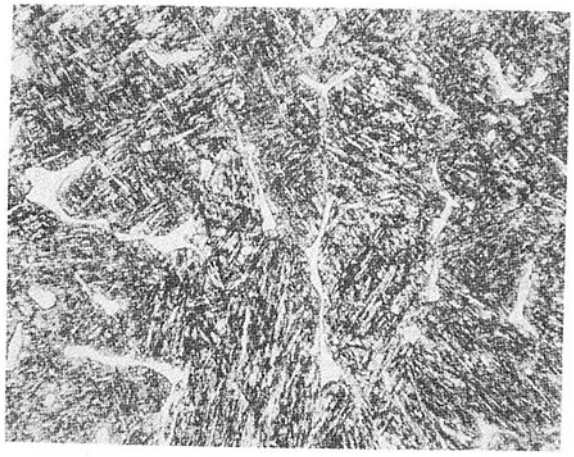

Fig. 14 Microstructure of FV507

Fig. 16 Microsection across haz of weld shown in Fig. 15

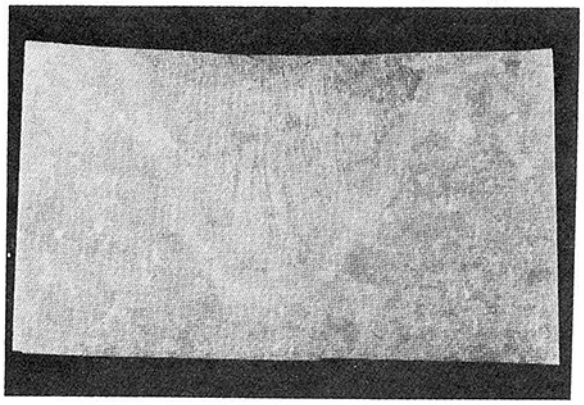

Fig. 15 Macrosection across welded FV507

quirements, the gas turbine industry will put its own specification to the alloys and possibly give tighter control to the analysis or mechanical properties and, in some cases, to both.

It is not the intention of this report to discuss at length all the mechanical and physical properties obtained on all the alloys mentioned, but to take two or three of the materials and discuss these in general.

The straight 13 percent Cr martensitic steels are known to people in all types of industry, and are not restricted to the gas turbine industry alone. The alloy based on 13 percent Cr, however, FV507, is, and has been used solely in the gas turbine industry for over 30 years. The alloy has become known for the good creep resisting properties that it possesses, up to 700°C. These properties are obtained by the strict control of the minor elements in the material, not only individually, but

Table 5

	C	Si	Mn	S	P	Cr	Ni	Mo	V	Nb	N_2	H_2
Specimen	0.08/ 0.18	1.0 max	1.25 max	0.040 max	0.040 max	10.5/ 12.5	1.5 max	0.5/ 1.0	0.10/ 0.30	0.20/ 0.60	0.01/ 0.05	3 ppm max
Sample J	0.10	0.78	0.60	0.013	0.029	11.16	0.61	0.77	0.16	0.33	0.047	3.0
P	0.105	0.74	0.65	0.014	0.030	11.12	0.61	0.77	0.16	0.36	0.043	0.9
G	0.10	0.76	0.60	0.013	0.027	11.09	0.60	0.77	0.16	0.31	0.046	2.9

Table 6

Cast No.	0.2 percent P.S., N/mm^2	u.t.s., N/mm^2	Percent El.	Percent *R/A*	Charpy impact *J*	Percent Cr equivalent
B2554	911	1087	13	37	43-44-43	3.4
AA6352	988	1189	15	56	57-58-47	5.1
AA6816	1019	1190	15	56	43-49-50	5.4
Spec. min.	825	1035	13	30	41	6.0 max

also collectively. FV507 is, by far, the most popular alloy used for this type of work in the U.K.

Table 2 shows the room temperature tensile values imposed on the alloy as a minimum, these being taken from centrispun test pots from the same heat. Over the years, however, many cut-up tests have been done on production castings to prove the overall consistency of the component.

Example 1. In the first example, we see a compressor casing (Fig. 12), which has been sectioned both circumferentially and axially to give 36 tensile tests. The results of these tests can be seen in Table 3 and it is quite clear that the properties obtained in both directions are uniform. If similar tests were performed on a forging, one might expect a difference due to the direction of forging.

Example 2. In the second example, a more extensive test program was carried out including tensile tests, fatigue tests, creep/stress rupture, microexamination, and welders tests.

These tests were carried out on a refractory spun casting similar to that shown in Fig. 5, which had the following dimensions:

78 in./72 in. × 71 in./64 in. × 14.1/2 in.

A sketch showing the position from which the specimens were taken and the type of test is shown in Fig. 13.

It can be seen from the values shown in Table 4 that the room temperature tensile values were all within the specification that was agreed upon for the casting. It was clear at this stage that the properties were a little lower at the larger diameter end of the casting than at the opposite end. Similar results were also obtained on the stress to rupture and fatigue tests. Various modifications were made to the molding parameter for subsequent castings, in an effort to increase the properties, even though they were still satisfactory in total to the customer.

Three full slices were taken through the casting and macrosections prepared through these and 10 microsections selected areas by the customer produced. The difference between the microstructures was negligible showing 7–8 percent ferrite in a martensitic matrix (Fig. 14). Extensive welding was not to be expected, but it would have been foolish to consider scrapping the casting due to some minor defects being present, and, for this reason, a groove was ground out of a further slice taken from the casting and filled with Metrode FV507 matching rod. After doing dye penetrant checks to prove the soundness of the weld, a section was prepared through the piece for microexamination and hardness checks. A macrosection can be seen in Fig. 15 and a microsection through the heat-affected zone in Fig. 16. A hardness traverse after retempering across and into the weld gave values of 260–311 BHN.

Table 7 Mechanical tests on centri-die cast shroud rings; HR Crown Max

(a) Section through 34" diameter Shroud Ring

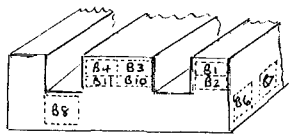

(b) Section through 30" diameter Shroud Ring

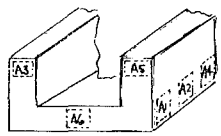

TEST PIECE	POSITION	YIELD POINT k.s.i.	YIELD POINT MPa	ULTIMATE TENSILE k.s.i.	ULTIMATE TENSILE MPa	% El.	% R/A
B1	C	48	331	80	551	44	52
B2	C	47	324	79	545	44	47
B3	C	43	296	80	551	44	47
B4	C	44	303	81	558	46	49
B8	C	46	317	80	551	43	47
B10	C	48	331	82	565	44	52
B11	C	46	317	81	558	44	47
B6	L	49	338	81	558	42	47
B7	L	48	331	83	572	36	52
A3	C	46	317	85	586	46	47
A5	C	46	317	85	586	40	41
A6	C	48	331	84	579	37	41
A1	L	47	324	84	579	40	44
A2	L	46	317	85	586	40	38
A4	L	48	331	85	586	35	44

C = circumferential L = longitudinal

Finally, an analysis check was done from three areas of the casting and the results are seen in Table 5. These are only two examples of many cut-up tests that have been done to prove the soundness and uniformity of parts produced by the centrispinning process in FV507. The two castings were vastly different in weight and section size and this is shown, as one might expect, in the uniformity of the properties.

Other tests carried out on castings in most materials produced by the centri-die technique show complete uniformity in both tensile and elongation values, and it would be a waste of paper recording the values in this report, due to the monotonous repetition.

Although no cut-up tests have been done on M152 material, tests have been taken from the ends of three separate castings made to the following dimensions:

28.1/4 in. o/d × 21 in. i/d × 90 in. long

A 12 in. piece was removed from one end of the casting, with the results shown in Table 6.

Components produced from austenitic steels are put into service in the solution annealed condition and experience has

shown that, provided the analysis of the material conforms to reasonable limits of specification requirements, the resultant mechanical properties are both regular and uniform. Mechanical tests were carried out on two shroud rings of 34 in. diameter and 30 in. diameter, respectively, both being on the order of 2 in. machined wall thickness and 8 in. long. The positions of the test pieces taken and the results can be seen in Table 7.

To show the further consistency in the mechanical properties, a complete ring 22.1/4 in. × 16.1/4 in. × 8 in. long was taken at random. The ring was sectioned longitudinally and one half heat treated at 1100°C before cutting and the other half tested in the as-cast condition. Twenty tensile test pieces of 0.564 in. diameter were obtained from the heat-treated portion and twelve taken from the untreated portion. The mean figures obtained are given in Table 8.

Although many tonnes of high nickel alloy castings have been produced, it has not been customer practice to have cut-up tests done, presumably due to the cost of the material. The values obtained on the separately cast test pots have always been sufficient proof as to the strength of the casting in question. Most of the high nickel alloys have wrought equivalents that, due to the hot work done during forging, rolling, etc., produce mechanical properties slightly higher than their cast equivalents. It must be remembered, however, that the directional properties of the wrought materials can result in their having no better properties than their cast equivalent as the component is only as strong as its weakest value.

Foundries are not always aware of the final properties on some of these alloys, as they are supplied in the annealed condition to analysis only, and it is the manufacturers who give vacuum heat treatments to bring out the precipitation effects of the material.

All the high nickel alloys are not easily castable and, even though centrispinning helps in reducing the mass of material in the casting and the problems associated with weighty castings, even this process is restricted with some of the more difficult alloys.

Table 8

	Yield point ksi (N/mm^2)	Maximum stress ksi (N/mm^2)	El. percent	*R/A* percent
20 tests—1100°C treated	43 (296)	79 (544)	39.2	35.1
12 tests—as-cast condition	44 (300)	80 (551)	40.3	37.9

All high nickel alloys are prone to segregation and, therefore, in thick sections over 4 in. wall thickness, one might expect difficulties with a secondary shrinkage formation within the wall of the material. The advantage with centrispinning, however, is that the supplier initially machines the unsound material from the bore and any evidence of secondary shrinkage would be found at this stage, which means there is no danger of the customer being supplied with an unsound casting, as it would be scrapped at this stage. The more complex the nature of the nickel base alloy, then the more susceptible are the castings to internal shrinkage. For this reason, even though VIKRO 718 is listed as a producible material, the presence of 5 percent columbium leads to the formation of laves phase on cooling and also the problems with internal shrinkage. The foundry would look at each job in isolation to decide whether it is a casting feasibility. Simple thin-walled shapes are no problem, but when the finished part has varying section size along its length, it is necessary to thicken the wall and this causes the problems of shrinkage mentioned above.

The choice of material is, of course, governed by the temperature range in which the part will work in conjunction with the mechanical properties required at that temperature. Inevitably the customer tells the foundry which alloy he requires, as only he is familiar with the stresses and temperatures the parts will meet in service.

The alloy VIKRO 155 (20 Ni/20 Cr/20 Co) is an example of the type of complex alloy that can be produced by the centrispun process. Castings made in this material are cast to size and shape on the outside diameter and weight up to 4 tons (Fig. 5).

Properties are obtained on an integral cast test piece attached to the top flange of the casting and typical properties from a recent batch after 2150°F water-quenched heat treatment are as shown in Table 9.

Summary of the Advantages to Be Expected From Centrispun Castings

This report started off by discussing the process of centrispinning, and explaining that all exogenous material and shrinkage cavities formed in the bore and that this material is subsequently machined away to give a completely sound casting to the customer for final machining. It must be clear, therefore, that, although the process is referred to as a casting process, one must never compare it with a static method of production and that the soundness of the part is one of the chief advantages of the process, leaving it comparable to a forging without any of the extensive forming operations required to produce that forging.

Table 9 Mechanical properties obtained on integral cast test rings from casting—VIKRO 155

CAST No.	0.2% PROOF STRESS k.s.i.	MPa	ULTIMATE TENSILE STRENGTH k.s.i.	MPa	% El.	% R/A	STRESS TO RUPTURE 180 MPa AT 730°C (1350°F)
AA7241							
Small flange	45	310	95	655	38	37	113 broken 113 unbroken
Large flange	44	303	89	613	34	46	72 broken 72 unbroken
AA7444							
Small flange	45	310	99	682	48	49	144 broken 144 unbroken
Large flange	48	331	91	627	31	36	124 broken 124 unbroken
AA7491							
Small flange	46	317	94	650	38	37	93 broken 93 unbroken
Large flange	44	303	94	650	41	42	103 broken 103 unbroken

The fact that the unsound material is centrifuged to the bore results in the casting being acceptable in most instances to Class I radiography. The standard has now become so high and acceptable in the gas turbine industry that 100 percent radiography for a casting in the supplied condition has now been disregarded and castings are generally supplied on 10 percent radiography on established parts. The customer carries out 100 percent radiography on the finished part, but the reject level has been so low that the radiography in the earlier stages and the cost involved has ruled it out.

It has been explained that the directional solidification, which occurs from the outside of the casting toward the bore, removes the possibility of planes of weakness and, together with the fine grains produced, gives mechanical properties in both longitudinal and radial directions of a uniform nature. This gives a distinct advantage over, first of all, static castings that contain porosity, planes of weakness, and coarser grains, and also forgings that show directional properties. Many cut-up tests have been carried out to prove the validity of this statement.

In the centrispinning process, it is also possible to cast shapes on the outside diameter which, in any other process, would involve expensive machining operations. We have seen in Fig. 5 that, for an alloy that is very expensive solely on the alloy content, savings can be made by cast lugs, etc., on the o/d. The cost of removing metal from a solid outside diameter to form the intricately shaped bosses, and also the waste of this removed material, is exceedingly high. Only the centrispun process can provide this additional cost saving. The turnings can be recycled in the melting process, and one can see that, with over 100 alloys being produced, the "housekeeping" needed to segregate these turnings must be of the highest order.

We have mentioned that shapes can be incorporated into the casting design, but we must not forget the different materials themselves that can be cast. Some materials, due to their alloy content, become increasingly difficult to hot work and it is here that the casting often shows an advantage. Elements can be added within reason to improve the mechanical properties, wear resistance, etc., to the casting, which, if added to an ingot in the first instance would make that ingot very difficult to hot work.

The flexibility and time factor is another all-important advantage. It is possible, by this process, for the customer to order "1 offs" knowing, at the same time, that the delivery time will only be a few weeks. Comparative processes of producing the same item would need requirements for several pieces and 6 months delivery time. The customer cannot afford to wait this length of time, as the "1 offs" are usually the result of a manufacturing mistake and the engine is part assembled. The time factor is critical as the work must continue.

Matching electrodes are always available for these alloys, and, providing procedure/qualification tests have been completed, small repairs can be undertaken if, which happens in only a small percentage of the castings produced, a defect is found.

To summarize, therefore, centrifugally cast products offer soundness, strength, and flexibility and have proved totally satisfactory over many years in service to render them comparable and often better than parts made by other methods of manufacture.

Field Evaluation of Gas Turbine Protective Coatings

A. McMinn
Southwest Research Institute,
San Antonio, TX 78284

R. Viswanathan

C. L. Knauf

Electric Power Research Institute,
Palo Alto, CA 94303

The hot corrosion resistance of several protective coatings that had been applied to MAR-M-509 nozzle guide vanes and exposed in a utility gas turbine has been evaluated. The coatings included basic aluminide, rhodium-aluminide, platinum-rhodium-aluminide, and palladium-aluminide diffusion coatings, and cobalt-chromium-aluminum-yttrium (CoCrAlY) and ceramic overlay coatings. A combination of metallographic examination of vane cross sections and energy dispersive X-ray analysis (EDS) was employed in the evaluation. The results showed that none of the coatings was totally resistant to corrosive attack. The CoCrAlY and platinum-rhodium-aluminide coatings exhibited the greatest resistance to hot corrosion. The CoCrAlY coated vanes were, however, susceptible to thermal fatigue cracking. Except for the poor performance of the palladium-aluminide coating, the precious metal aluminides offered the best protection against corrosion. Hot isostatically pressing coatings was not found to be beneficial, and in one case appeared detrimental.

Introduction

Blades and vanes in industrial combustion turbines are subject to hot corrosion, which is a form of accelerated oxidation induced by certain impurities in the combustion gases. The most common form of hot corrosion in turbines burning distillate and residual fuels is due to the deposition of alkali sulfates on the metal surface. To combat the problem, coatings have been in extensive use over the last decade. Although turbine manufacturers and coating vendors base their recommendations on in-house evaluations of coatings, results of these evaluations are often proprietary and therefore unavailable to electric utilities. Although some evaluations have been documented in the literature [1-3], the field performance of the many various commercially available coatings in different environments has not been adequately documented. Consequently, utilities are unable to make independent decisions regarding the type of coatings that will best serve their specific needs, economically and reliably. To overcome this situation, the Electric Power Research Institute (EPRI) has sponsored a number of projects over the years for relative evaluation of various commercial coatings, in both the laboratory and in the field. The present paper describes the results from a recent evaluation of several coatings tested in an FT4 turbine by the Long Island Lighting Company (LILCO).

Field Testing

Selection of coatings for this "rainbow" test program was based on vendor offerings and not on a systematically laid-out plan. A list of the coatings evaluated is provided in Table 1. The coatings evaluated include basic aluminide, rhodium-aluminide (Rh-aluminide), platinum-rhodium-aluminide (Pt-Rh-aluminide), and palladium-aluminide (Pd-aluminide) diffusion coatings, and CoCrAlY and ceramic overlay coatings. Full details of the coating compositions, processing, and quality control procedures were not available, since in many cases the coating suppliers regarded this information as proprietary. Thus, the initial condition of the coatings was not known. However, the CoCrAlY coating evaluated had a nominal composition of Co-21Cr-12Al-0.3Y and had been applied by physical vapor deposition. Details of the composition of the ceramic thermal barrier coating were not available, although the supplier did indicate that a low-pressure plasma spray (LPPS) process had been used for some vanes and a high-pressure plasma spray (HPPS) process had been used for other vanes. The precious metal aluminides had been applied by electroplating followed by pack aluminizing. The Pd-aluminide was an experimental coating. Two of the coatings (basic aluminide and Rh-aluminide) were also evaluated after hot isostatically pressing (HIP) the vane after coating.

The various coatings were applied to cast cobalt-based MAR-M-509 nozzle guide vanes which had a nominal composition of:

	Co	Cr	Ni	W	Ta	Ti	Zr	C
Wt. percent	55	23.5	10	7	3.5	0.2	0.5	0.6

The vanes had been re-airfoiled prior to coating so that the coatings would be applied to new base metal. The coated vanes were installed in a Pratt and Whitney FT4 engine owned by LILCO and situated in Holtsville. The vanes, which were coated in sets of six or seven, were arranged so that a set with a given coating would cover the area in front of one burner can. The fuel utilized was No. 2 grade home heating oil with the following maximum levels of contaminants recorded at some time during the test period. The high manganese level cor-

Contributed by the Gas Turbine Division for publication in the JOURNAL OF ENGINEERING FOR GAS TURBINES AND POWER. Manuscript received by the Gas Turbine Division January 14, 1986.

responds to a period when a manganese-base smoke suppressant was used.

Sulfur	0.25 percent
Lead	0.32 ppm
Sodium	0.45 ppm
Calcium	0.62 ppm
Potassium	0.50 ppm
Manganese	223 ppm

The vanes, which were placed in service in Nov. 1979, were exposed for a total of 812 hr with two intermediate visual inspections made by LILCO personnel. The turbine was used as a peaking unit and therefore saw cyclic operation. In Aug. 1981, after 500 fired hr of operation, six of the seven vanes coated with the ceramic overlay coating appeared to have leading edge damage. In Apr. 1983, after a total of 655 fired hr of operation, it was found that three of the CoCrAlY coated vanes were cracked. They were removed and replaced with refurbished Pt–Rh–aluminide coated vanes.

Laboratory Evaluation Procedures

All of the vanes received from LILCO were visually examined and a representative vane from each coating group was selected for detailed metallography. Typical surface deposits were removed from both the convex and concave sides of vanes and these were identified using standard X-ray diffraction techniques. A Siemens D-500 X-ray diffractometer and Cu K_α radiation were used, and the diffracted X-ray intensity was measured continuously.

The selected vanes from each group were cut transversely at three locations to obtain three complete cross sections of the vane airfoil. The locations selected were 6.3 mm from the outer shroud, midspan, and 6.3 mm from the platform. Each section was then further cut into three pieces to enable standard metallographic mounts to be made. The samples were nickel plated to provide good edge retention and to retain oxide scales and deposits. They were then mounted in a hard, low-shrinkage molding compound and polished.

The samples were metallographically examined and the corrosive degradation of the coatings was characterized with respect to type, severity, and uniformity of attack. For each section, 30 measurements of remnant coating thickness were made around the complete airfoil. The degree of base metal attack and the presence of internal sulfidation was also characterized.

Selected samples were examined in the scanning electron microscope (SEM). Energy dispersive X-ray analysis (EDS) was performed to identify elements in the scale, coating and substrate, and elemental mapping was used to determine the distribution of the elements detected.

Results

Visual Examination Results. Visual examination of the vanes revealed no evidence of extreme corrosive attack of the base metal. However, the severity of attack of the coatings did vary. Coatings that visually appeared in good condition included the Pt–Rh–aluminide and the Rh–aluminide. The coating that showed the worst degree of attack was the aluminide/ceramic coating with the Pd–aluminide and basic aluminide coatings exhibiting intermediate degrees of attack. The CoCrAlY coating showed little sign of corrosive degradation, but this group of vanes exhibited extensive thermal fatigue cracking.

Within a given group of vanes there did not appear to be any significant variation in corrosive attack as a function of the position in the turbine. Corrosive attack apeared to be limited to the leading edge and concave surfaces of the vanes, and apart from the ceramic coated vanes, the convex surfaces were generally unattacked. The corrosive attack took the form of pitting or roughening of the vane surface, although blistering and spallation was observed, especially for the ceramic-coated vanes.

Convex surfaces of the vanes were frequently covered with a matte purplish-black deposit, indicating the presence of $CoSO_4$. Brown and shiny black deposits were also observed. A brown, granular deposit and a blotchy, black deposit were generally observed on the concave surfaces of vanes. These deposits were mainly located in the center section of the vane. The amount of deposit varied from vane to vane, but there was no correlation with the position in the turbine.

Large thermal fatigue cracks, 13–60 mm in length, were observed in three of the vanes coated with CoCrAlY and one of the vanes coated with Pd-aluminide. These cracks were always located toward the midsection on the concave side of the vane. In addition, single small cracks less than 10 mm long were observed at the trailing edges of vanes close to the outer shroud. Every coating had suffered this type of cracking.

Deposit Analysis. X-ray diffraction only identified compounds associated with the smoke suppressants used. In particular, the convex side deposit was identified to be primarily α-Fe_2O_3 (hematite), which originated from the iron-based smoke suppressant. However, unaccounted diffraction lines indicated that the deposit was a mixture of substances, although it was not possible to identify accurately the other substances. EDS analysis of the deposit carried on in the SEM revealed the presence of Ca, Mn, and Zn.

An EDS analysis of the concave surface deposit revealed the presence of Ca, Si, Fe, and S together with trace amounts of K, Mn, Zn, Al, Ti, and Ni. The Ca, S, Fe, K, and Mn were known to be fuel contaminants. The source of the Si was believed to be from ingested sand particles in the intake air, since the LILCO Holtsville plant is located close to the sea, although the inlet air was filtered. The source of the Zn, Ti, and Ni is unkown, although both Ni and Ti are constituents of the MAR-M-509 and could have resulted from vane corrosion. It is also possible that these elements were present because of corrosion/erosion of components in the turbine compressor or combustor.

Metallography and Electron Microprobe Analysis. The integrity of the coatings and degree of corrosive degradation were determined over the complete airfoil surface for the three transverse sections studied. Corrosive attack was always found to be worse on the leading edge and concave surfaces of the vanes. The location of worst coating degradation was generally either toward the outer shroud or lower platform locations, that is, in the cooler zones of the vane airfoil. Detailed optical and scanning electron micrographs showing coating degradation and substrate attack, and detailed measurements of remnant coating thickness are presented elsewhere [4]. The salient features observed from metallographic examination are summarized in Table 1. Some of the significant observations pertaining to each coating are described below.

Basic Aluminide. The convex side of the vane exhibited shallow uniform attack as shown in Fig. 1(*a*). A uniform scale, identified to be rich in Al and Cr by EDS analysis (presumably Al_2O_3 + Cr_2O_3), was present on the surface. There was also evidence of the presence of small amounts of sulfur in the scale. The coating was still largely intact and contained CoAl and Cr-rich refractory phases. At the interface between the coating and the metal substrate, a continuous network of small voids was present. The voids were believed to be "Kirkendall" voids arising from interdiffusion of Co and Al across the interface.

Close to the leading edge, where corrosion was much more severe, the coating was frequently found to be completely destroyed, allowing direct attack of the metal substrate. This

Table 1 Summary of metallographic observations and relative ranking of coatings

Coating	Location of Worst Degradation	Remarks	Maximum Thickness of Coating, μm	Ranking*
CoCrAlY	Outer Shroud‡	Coating protective and uniform. Isolated penetration of coating with shallow attack elsewhere. No substrate attack.	56	1
Pt-Rh-Aluminide	Lower‡‡ Platform	Thinning of coating in areas but no evidence of advancing corrosion fronts. Only isolated penetration of coating. No substrate attack. Voids observed in coating.	102	1
Rh-Aluminide	Lower Platform	Coating completely penetrated over regions of outer shroud and lower platform sections; elsewhere coating still protective. Corrosion of coating fairly shallow and localized. Shallow attack of substrate.	64	2
Rh-Aluminide (HIPed)	Outer Shroud	As above but with more uniform coating degradation.	74	2
Aluminide/ Ceramic (HPPS)	All locations similar	Coating locally penetrated. Fairly uniform attack of outer ceramic layer. Inner aluminide layer of uniform thickness and still protective. Little substrate attack.	216	3
Aluminide	All locations similar	Uniform coating attack. Complete penetration in localized areas. Coating thinned in areas. Some substrate attack.	48	4
Aluminide (HIPed)	Outer Shroud Mid-Span	Coating completely removed from leading edge at outer shroud and mid-span locations. Attack of substrate. Elsewhere uniform attack of coating, but still protective.	48	5
Aluminide/ Ceramic (LPPS)	Outer Shroud	Coating completed removed over much of leading edge. Elsewhere coating still protective, although some corrosion of ceramic layer. Debonding of ceramic and aluminide layers. Attack of substrate.	483	5
Pd-Aluminide	Lower Platform	Coating completely penetrated at lower platform location. Uniform corrosion front and substrate attack. Coating debonded on concave side. Coating thinned on convex side but still protective, with little evidence of advancing corrosion front.	173	5

* Ranking 1 denotes best performance; 5 denotes the worst performance.
‡ Refers to the airfoil location 6.3 mm from the outer shroud.
‡‡ Refers to the airfoil location 6.3 mm from the lower platform.

is illustrated in Fig. 1(*b*). There is no evidence of the coating in the figure. A scale of corrosion products was found to be present directly on the substrate, with small fingerlike penetrations due to preferential attack of substrate carbides. At high magnification, the scale was found to consist of two layers. The inner layer consisted primarily of Cr (presumably Cr_2O_3), while the outer layer contained Al, Cr, Co, Ni, and some sulfur indicating that the coating had been destroyed by corrosion and not by spalling. There was no evidence of sulfur penetration into the substrate.

The pattern of corrosion in the HIPed basic aluminide coating was very similar to that described earlier for the non-HIPed aluminide, but the severity of the corrosion was considerably greater. Once again, the severe corrosion on the leading edge/concave side resembled that shown in Fig. 1(*b*), while the less severe corrosion on the convex side resembled that shown in Fig. 1(*a*). On the concave side, the base metal was attacked to a depth of 55 μm compared to only 25 μm in

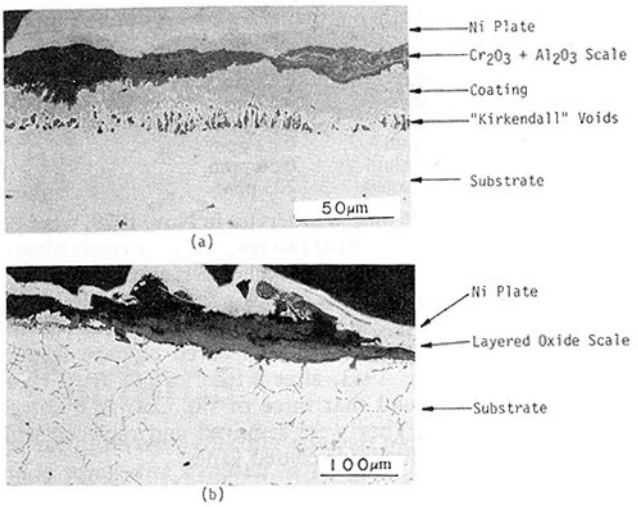

Fig. 1 Optical micrographs of basic aluminide coating illustrating: (*a*) uniform attack; (*b*) substrate attack, where coating has been dislodged either by spalling or corrosion

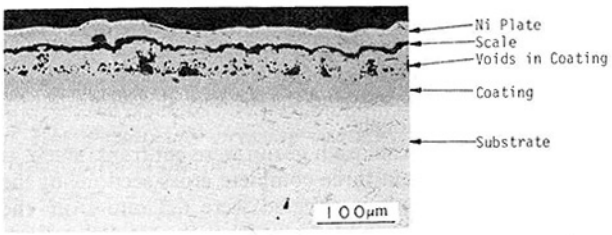

Fig. 2 Typical appearance of Pt-Rh-aluminide coating showing absence of corrosive attack and coating voids

the case of the non-HIPed coating. Interestingly no interfacial voids were found at any location.

Precious Metal Aluminides. Among the various aluminide coatings, the Pt-Rh-aluminide exhibited the best performance. Overall, the coating was very protective, and complete corrosive penetration had only occurred in isolated locations. Substrate attack had not occurred at any location. The coating was covered by a very thin scale with little evidence of corrosion deposits. The typical condition of the coating on the convex and concave sides of the vane is illustrated in Fig. 2. It was found that in some areas, the coating was locally thinned without any evidence of corrosive attack. The only concern with this coating was that it contained voids, sometimes as large as 75 μm in diameter in the outer regions of the coating. The effect of these voids on the integrity of the coating is not known. No Kirkendall-type voids were present at the interface between the coating and the substrate.

The most inferior performance was exhibited by the Pd-aluminide coating. Once again, the concave side was more severely attacked than the convex side. Features observed on the concave side included complete destruction of the coating, severe substrate attack due to corrosion, presence of voids in the outer layers of the coating as well as at the coating-metal interface, and debonding of the coating-metal interface by linkup of the voids. These features are illustrated in Figs. 3(*a*) and 3(*b*). Changes in the substrate caused by the hot corrosion included both the precipitation of a light grey phase, as well as void formation. EDS analysis revealed that high sulfur levels were associated with the phase immediately adjacent to the voids, but only for the deepest voids, that is, the voids at the front of the advancing corrosion front. The light grey phase observed in the substrate was found to be rich in Cr and depleted in Co, compared to the substrate. However, no sulfur

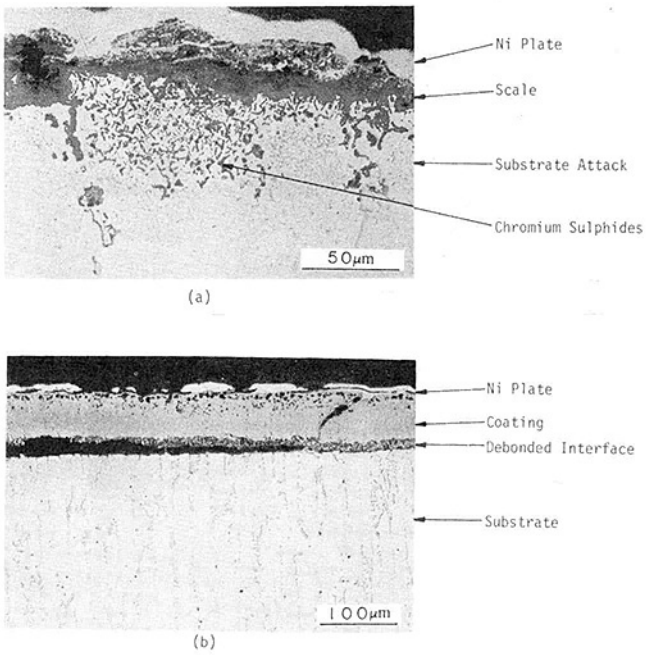

Fig. 3 Optical micrographs illustrating various features associated with degradation of vane coated with Pd-aluminide

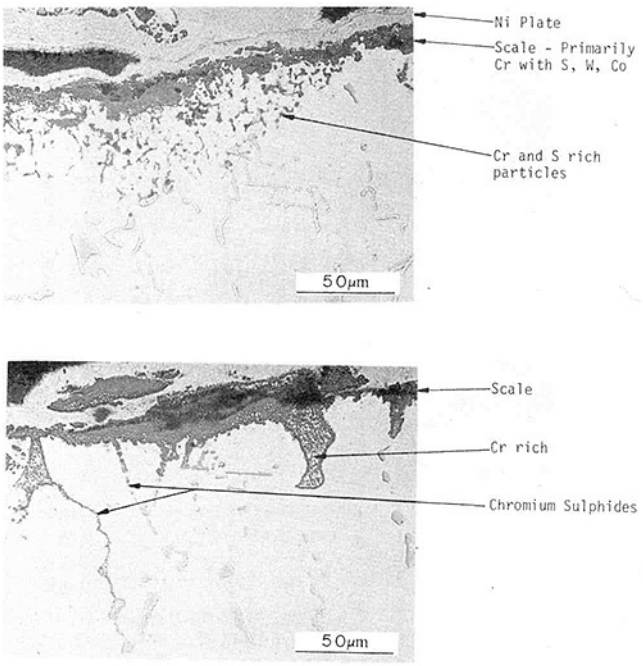

Fig. 4 Types of substrate attack observed on vane coated with Rh-aluminide

was detected which indicated that the phase was not a chromium sulfide, but was probably Cr_2O_3 or possibly a chromium nitride.

The performance of the Rh-aluminide coatings was intermediate between that of the Pt-Rh-aluminide and the Pd-aluminide. The worst corrosive attack of the coating had occurred on the concave side of the leading edge toward the lower platform location. In these areas, the coating had been completely penetrated and some attack of the substrate had occurred (Fig. 4). Elsewhere on the concave side of the vane, the coating was still protective, but localized corrosive attack was evident. On the convex side, only shallow corrosive degradation was observed, similar in appearance to Fig. 1(*a*). For the non-HIPed coating, voids were found to be present at the coating substrate interface, as well as in the center of the coating. No voids were observed for the HIPed coating.

Analysis of the scale by EDS showed Rh, Al, and S in the outer layers and Co, Cr, Ni, and W in the inner layers. The scale composition indicated that destruction of the scale was due to corrosion and not due to spalling. Compared to the basic aluminide coating, this coating seemed more brittle and contained many fine spanwise cracks running parallel to the surface of the vane, which appeared to cause some spallation of the coating, with resultant thinning. At no location, however, was there evidence of total loss of coating due to spalling alone.

CoCrAlY. The CoCrAlY coating was found to be very protective and had suffered little corrosive attack. A typical view of the coating as observed at most of the locations examined is shown in Fig. 5. There were a few isolated locations on the leading edge (concave side) where corrosion of the coating had almost penetrated the coating, but there was no evidence of substrate attack even at these locations.

The results of EDS analyses of the coating and the scale formed on this coating showed that the coating consisted of Co, Cr, Al, Ni, and W, but no Y was detected. The Ni and W had probably diffused into the coating from the substrate during service. The scale formed on the coating consisted primarily of Al, which indicated that it was Al_2O_3. A small amount of S was detected in the scale.

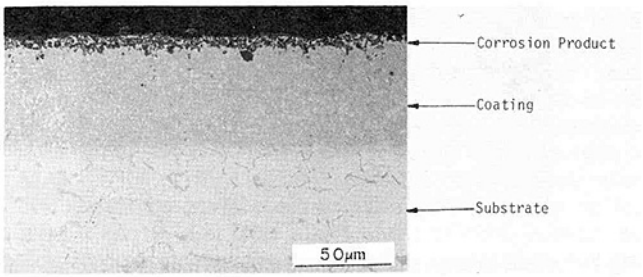

Fig. 5 Typical appearance of CoCrAlY coating

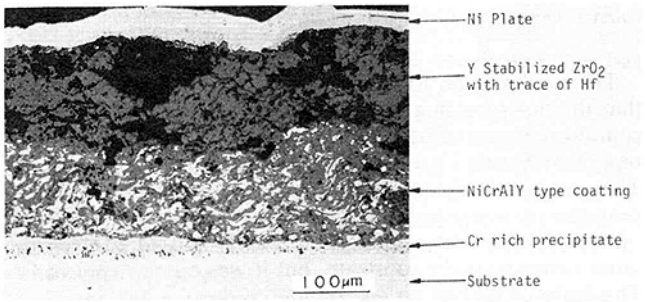

Fig. 6 Low-pressure plasma spray ceramic/aluminide coating

Aluminide/Ceramic. An optical micrograph of the low-pressure plasma spray (LPPS) coating is shown in Fig. 6. The coating consisted of a bond coat, with a ceramic layer on top. The bond coat contained small pores and was denser than the ceramic layer which contained large pores. Large pores were also observed at the interface between the two coatings. On the concave side of the vane, a third layer was observed between the bond coat and substrate. This layer appeared to be a diffusion aluminide coating, and it contained small voids in the interdiffusional zone. This layer was generally very thin in comparison to the LPPS bond coating and ceramic coating. The origin of this inner layer is unknown, although it may be the result of a postcoating thermal treatment or the result of the service exposure.

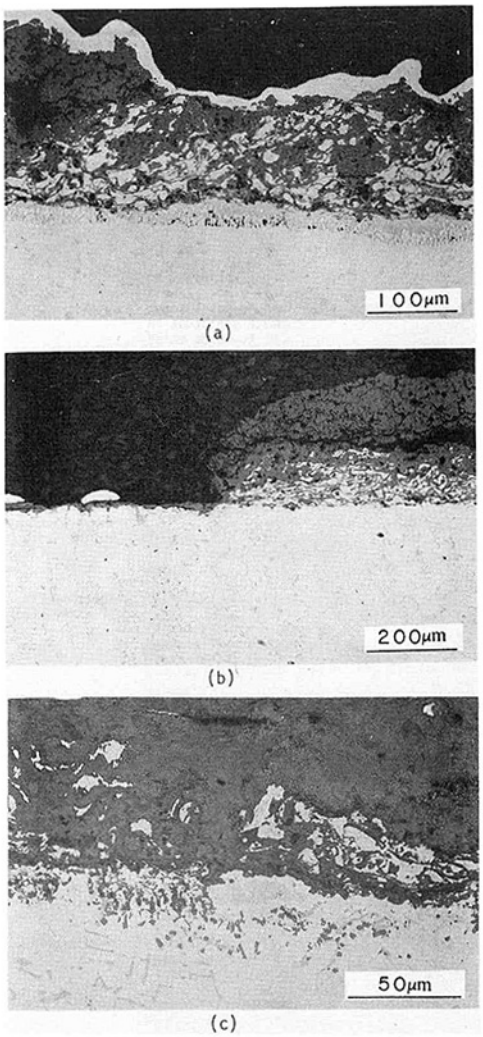

Fig. 7 Optical mircographs illustrating different modes of degradation of LPPS ceramic/aluminide coating: (*a*) debonding of ceramic layer accompanied by corrosion of NiCrAlY bond coating; (*b*) debonding of ceramic and NiCrAlY layers; (*c*) corrosion of entire coating followed by substrate attack

The results of an EDS analysis of the three layers showed that the outer coating was a yttria-stabilized zirconia, which contained a trace of hafnium. The bond coating was found to be rich in Ni and Cr and also contained some of the ceramic. This coating also contained Al, but no Co, and it would appear that it was not basic aluminide, but was an NiCrAlY overlay coating. The inner layer was found to contain the same elements as the substrate, but it was much richer in Cr. This layer contained no Al.

The most severe degradation of this coating had occurred on the concave side. Three basic modes of coating degradation were observed as illustrated in Fig. 7. These modes were (*a*) debonding of the ceramic layer accompanied by corrosion of the NiCrAlY bond coat; (*b*) debonding of both ceramic and the bond coat; and (*c*) corrosion of entire coating accompanied by attack of the substrate. The primary reason for coating degradation appeared to be debonding of the coating rather than overall corrosive attack. In general, on the convex side of the vane, the bond coat gave protection to the substrate even though much of the ceramic had disappeared.

An example of the high-pressure plasma spray (HPPS) coating is shown in Fig. 8. Three layers were observed: an outer porous ceramic layer, an intermediate porous coating, and an inner layer typical of a diffusion aluminide. Based on EDS analysis, the ceramic outer layer appeared to be zirconia,

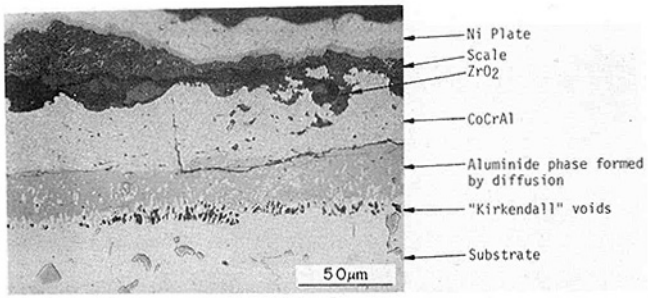

Fig. 8 High-pressure plasma spray ceramic/aluminide coating

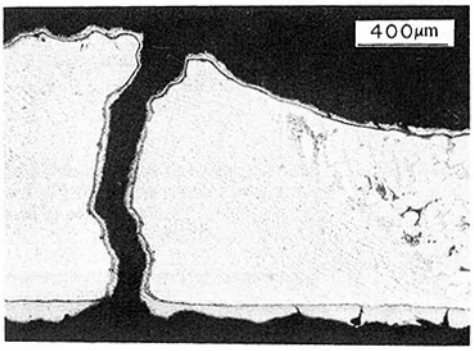

Fig. 9 Optical micrograph of section through trailing edge crack

and the absence of yttrium indicated that it was not stabilized by yttria. The intermediate layer appeared to be CoCr aluminide, and the inner layer appeared to be a basic aluminide formed by inward diffusion of Al. As expected, this layer contained elements found in the substrate, typically Ni and W. It is not known whether this inner aluminide was part of the original coating or whether it was the result of service exposure.

In comparison to the LPPS coating and ceramic, the HPPS coating and ceramic had withstood the corrosive degradation better. In general, most of the ceramic coating was missing and the intermediate HPPS coating had been attacked to varying degrees, but the inner aluminide coating was unattacked and protective. There were areas however where all the coating had been removed. Generally, where there was no protective coating, the substrate had suffered very little attack.

Cracks were frequently seen between the intermediate and inner layers (Fig. 8). These may have been caused by differential thermal expansion between the layers, but it would appear that while the outer and intermediate layers may spall off, the inner layer would remain to protect the substrate. This was different from the LPPS bond coat and ceramic, which was seen to debond at the coating/substrate interface, leaving the substrate unprotected.

Examination of Cracked Vanes. As stated earlier, three of the vanes coated with CoCrAlY and one of the vanes coated with Pd-aluminide contained single large (13-60 mm) cracks located toward the midsection on the concave side of the vane. The cracks had propagated completely through the airfoil section (approximately 1.8 mm thick) to the inside surface. The cracks however were much longer in the coating than in the substrate, and were obviously propagating from the outside surface inward.

Examination of the fracture surfaces of the large cracks by SEM revealed that the cracks were completely covered in a fine oxide, which completely obliterated details of the fracture morphology. This oxide proved to be very tenacious and attempts to remove it by chemical cleaning were unsuccessful. Thus, it was not possible to identify the mechanism of crack-

ing, although cracks in these components are normally considered to be thermal fatigue cracks.

Small trailing edge cracks were also observed in the airfoil of a number of vanes, independent of the coating utilized. Two of these vanes were also examined. A metallographic section through one of these cracks is shown in Fig. 9. It is seen that the crack had occurred in a region of the vane where the microstructure was different to the normal structure of α-matrix and Chinese-script carbides. The crack had occurred in a fine dendritic structure where the dendritic boundaries were delineated by carbides. The crack surfaces were covered with a thin layer of coating indicating that the crack existed prior to coating.

Discussion

The objective of this coating evaluation was primarily to compare the hot corrosion resistance of various coatings and to rank them. It was found that none of the coatings was totally corrosion resistant, since even the best coating was unprotective in small localized areas where complete coating penetration had occurred. Ranking the coatings based on their overall corrosion resistance gives the results shown in Table 1. The coatings have been ranked in groups, since the differences in performance between coatings in the same group were indistinguishable. This ranking is partly based on the extensive measurements reported in [4]. In arriving at this ranking, numerous indices of coating degradation, which could not be quantified precisely, had to be considered. Important among these were the depth of coating attack, the number of locations at which coating had been attacked, the depth of substrate attack, and the extent of debonding of the coating. These indices of corrosion do not always go hand in hand. For instance, some coatings showed a few localized areas of attack, while others were subject to uniform degradation on a much broader front. In some instances, corrosion of the coating was accompanied by substrate attack, while in other instances no substrate attack could be observed despite the total destruction of the coating. Frequently, the coatings were found to be debonded from the substrate over a large area, but still remained intact. Such debonding was presumably the result of cyclic operation and was not strictly a measure of corrosion performance. Some of the coatings contained large pores and other defects, which had no apparent influence on coating performance at this time, although their detrimental effect could become manifest with further operation. Coating thicknesses were frequently nonuniform due to poor quality control and hence the extent of degradation with respect to the original coating thickness could not be assessed. Since the initial thickness of each coating was different, direct comparisons of their performance could not be made. In view of these considerations, no single index of corrosion could be utilized quantitatively. The ranking of coatings was therefore based on overall observations, tempered with the investigator's judgment.

Undoubtedly, the CoCrAlY coating was found to be the best, based solely on its excellent corrosion resistance. However, three of the CoCrAlY vanes had to be replaced after 655 hr of operation because of large thermal fatigue cracks on their concave surfaces. Therefore, if a coating is being chosen for its total integrity, the CoCrAlY coating would be excluded and the Pt-Rh-aluminide coating would be the best choice. If the CoCrAlY coating is excluded, then it is seen that as a group, the precious metal aluminides offered the best protection, excepting the poor performance of the experimental Pd-aluminide coating. The high-pressure plasma spray ceramic coating was given an intermediate ranking, because its underlying aluminide coating essentially remained protective, even though much of the overlying ceramic layer had been removed.

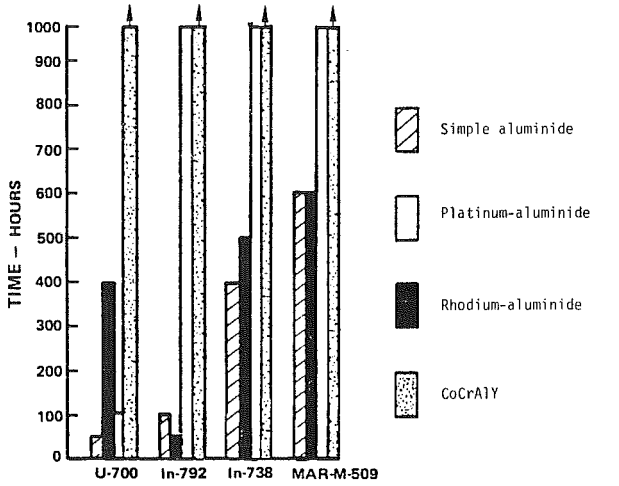

Fig. 10 Summary of sulfidation behavior for coatings tested by United Technologies Corporation at 982°C [5]

Results of this study indicate that hot isostatically pressing (HIP) the coatings after application had no real beneficial effect. The HIPed Rh-aluminide coating was only very slightly better than the non-HIPed Rh-aluminide, and in the case of the basic aluminides, the HIPed coating was markedly worse than the non-HIPed coating.

In spite of the subjective judgment associated with ranking the coatings, it is heartening to note that results of this field evaluation are completely in agreement with earlier results from laboratory tests [5]. The laboratory tests had been performed to evaluate basic aluminide, precious metal aluminides, and CoCrAlY coatings applied to MAR-M-509, IN-738, IN-792, and U-700 substrate alloys. Hot corrosion tests in Na_2SO_4 were conducted at 982°C for up to 1000 hr. MAR-M-509 performed the best of the four substrate alloys evaluated, whichever coating was applied, as may be seen from Fig. 10. For this alloy, the CoCrAlY coating was superior in protecting the substrate from sulfidation, followed by the Pt-aluminide, and then jointly by the Rh-aluminide and basic aluminide, respectively. Almost exactly the same coating ranking was found in the present evaluation under actual service conditions. The main difference was that in service the Rh-aluminide coating performed better than the basic aluminide coating.

In another study, United Technologies Corporation examined Rh-aluminide coated MAR-M-509 nozzle guide vanes that had been exposed for up to 500 hr in a similar FT4 engine at the LILCO Holtsville plant [6]. It was found that this coating offered excellent corrosion protection, with localized attack and penetration only occurring along the leading edge and concave surface.

Thus, these studies and others [7–9] have shown that Pt-aluminide and Rh-aluminide offer good protection to Co-based and Ni-based superalloys. The precious metal aluminides were developed in the mid-1970s and have been in successful use since. In a Pt-aluminide, the Pt is present in solid solution or as a $PtAl_2$ phase near the surface. The Pt apparently improves the corrosion resistance of the coating by increasing the activity of the aluminum in the coating, enabling a very protective and adherent Al_2O_3 scale to form on the surface. The Pt-Rh-aluminide studied in this program was obtained by electroplating Rh and then Pt, and then aluminizing, which apparently produces a Pt-rich outer layer and an Rh-rich inner layer adjacent to the substrate material [8].

It has been shown that not all the previous metal aluminides offer optimum protection, since the performance of the Pd-aluminide was poor. Part of the problem with the Pd-aluminide coating was the debonding at the

substrate/coating interface. However, the general corrosive attack of the Pd-aluminide coating was still more severe than the Rh-, and Pt-Rh-aluminides. The reason that the Pd-aluminide was poor in comparison to the other precious metal aluminides may be because of its thickness. The Pd-aluminide had a maximum thickness of 170 μm, compared to 100 μm for the other precious metal aluminides. Aluminide coatings on Co-based superalloys consist of an outer layer of β-CoAl, and an inner layer of refractory elements in a solid solution of α-Co [10-12]. As Al diffuses inward and forms CoAl, the solubility of the elements in the Co matrix changes, and some are rejected to form additional phases, such as metallic Cr and W, carbides, and σ phases such as CoCr. EDS analyses performed in this program indicated that the coatings consisted of a protective CoAl phase and a Cr-rich intermetallic at the substrate/coating interface. Thus, the thicker the aluminide coating formed, the greater the amount of Co that is effectively extracted from the substrate to form the CoAl, and therefore the greater the opportunity to form a continuous layer of refractory phases and carbides at the substrate/coating interface. This is bad for coating integrity since this zone can crack and cause debonding at the interface. The debonding of the Pd-aluminide is thus considered to be a result of its larger thickness.

Diffusion aluminide coatings offer protection to the underlying substrate by forming a tenacious, continuous Al_2O_3 scale on the surface, which is impervious to diffusion of oxygen. As the CoAl coating loses aluminum due to repeated spallation, Al_2O_3 can no longer form as the sole oxide. Since diffusion coatings formed on MAR-M-509 also contain Co and Cr, there is thus a tendency to form a protective Cr_2O_3 scale which is beneficial for hot corrosion resistance since it is much less reactive than Al_2O_3 to sodium sulfate. However, Cr_2O_3 is not as protective as Al_2O_3 for oxidation resistance, since its rate of growth is greater than for Al_2O_3, and all other things being equal, it is preferred that the protective oxide increase in thickness at the lowest possible rate [13].

EDS analyses of the scales formed on the diffusion aluminide and CoCrAlY coatings evaluated revealed that when most of the coating was still present, then the scale was rich in Al, that is, a predominantly Al_2O_3 scale. In cases where corrosive attack had removed the protective coating, then the scales were found to be Cr-rich, and based on previous work of other investigators [14-16], were likely to be Cr_2O_3. Previous work has shown that in the absence of salt, both Co-20 percent Cr and Co-25 percent Cr form a protective Cr_2O_3 layer. For the 20 percent Cr alloys, this develops below an initially formed CoO and $CoCr_2O_4$ spinel layer, and for the 25 percent Cr alloy, the cobalt-containing oxides are absent. MAR-M-509, with a nominal Cr content of 23.5 percent, falls between the behavior of these two alloys, but since Co was identified in the EDS analyses from the scale, this indicated that some cobalt-containing oxides were formed. The layered scale formed on the basic aluminide coating showed an outer scale rich in Al and Cr (Al_2O_3 and Cr_2O_3), and an inner Cr-rich coating (Cr_2O_3) which had formed by apparent oxidation of the substrate. This indicated that the outer scale was no longer protective and was ineffective in preventing the diffusion of oxygen to react with the substrate.

The voids seen in the interdiffusional zone between the substrate and coating form because the substrate is richer in Co and poorer in Al than the coating. Co diffuses into the coating and Al into the substrate, setting up conditions ideal for Kirkendall void formation at the coating-substrate interface. The thicker the coating, the greater the reservoir of Al, and therefore the greater the diffusion of Co, with the resultant number of voids being greater. This is believed to be one of the causes of the poorer performance of the Pd-aluminide coating studied in this program.

Since Kirkendall porosity is a result of interdiffusion, then it is possible that the voids can form during coating or during service, although the latter is normally assumed to be the case. However, the basic aluminide and Rh-aluminide coatings were found to have far fewer interdiffusional zone voids in their HIPed condition, compared to their non-HIPed condition. This implies that hot isostatically pressing the coatings had closed up the voids, but also implies that the voids were present after coating. Alternatively, hot isostatically pressing the coatings at high temperature and pressure caused interdiffusion of Al and Co between the coating and substrate, reducing the tendency to form Kirkendall voids during subsequent service conditions.

The CoCrAlY coating evaluated in this study had the nominal composition Co-21 Cr-12 Al-0.3 Y. In view of the low-Cr and high-Al content, this coating would normally be expected to be suitable for "Type I" hot corrosion encountered at temperatures above 1400°F. In the range of 1200-1400°F, a layered attack known as "Type II" hot corrosion characterized by severe pitting occurs. To protect against the Type II corrosion, the conventional wisdom is to use a coating with high-Cr/Al ratio. As part of the EPRI Research Project 1344-1, an optimized CoCrAlY with the composition Co-35 Cr-8 Al-0.5 Y was developed to resist both types of hot corrosion [17]. The coating was applied to MAR-M-509 vanes and tested in a FT4 engine using No. 2 distillate fuel at the Oakland Station of Pacific Gas & Electric Company. For comparison, some vanes coated with a Co-22 Cr-12 Al-0.5 Y commercial coating were also tested. After about 750 hr of cyclic duty, most of the vanes coated with both types of CoCrAlY were found to contain cracks. This prior experience reinforces the finding of the present study and indicate a general vulnerability of the CoCrAlY type coating to thermal fatigue under cyclic operation.

As part of another EPRI Research Project 2465-1, a variety of coatings (including several CoCrAlY compositions) are being field tested in a Solar-Centaur machine operating as a base load unit, but having a hisotry of severe hot corrosion [18]. When the results from this study become available, they will provide a valuable comparison between the performance of the coatings in steady-state versus in cyclic operation.

The observation that hot corrosion and degradation of coatings had occurred in the case of all eight commercial coatings, after only 812 hr of exposure, is surprising. Neither the fuel analysis nor the analysis of the deposits found on the vanes are indicative of an abnormally severe corrosive environment. It seems reasonable to surmise that the cyclic duty seen by this "peaking" machine may have partly contributed to early scale breakdown and penetration of the coating by sulfur and oxygen. The severity of the cycling is evidenced by the large thermal fatigue cracks found in the vanes coated with CoCrAlY. This result brings out the need for taking turbine operation modes into account when selecting appropriate coatings.

The performance of the ceramic coatings in this study was poor, especially in the case of the LPPS coating, which also lost its protective NiCoAlY bond coat. In the case of the HPPS coating, although the ceramic spalled, the bond coat remained protective. Similar experience with the stability of thermal barrier coatings has been observed [19-20], and work is ongoing to develop improved coatings. This work has shown that two new thermal barrier coating systems, Ca_2SiO_4/Ni-16.2 Cr-5.6 Al-0.6 Y and ZrO_2-8 Y_2O_3/Ni-16.4 Cr-5.1 Al-0.15Y have better corrosion resistance compared to the standard ZrO_2-12 Y_2O_3/Ni-16 Cr6 Al-0.6Y coating [19]. Since the ceramic coatings evaluated in this program came from the early generation of thermal barrier coatings, it is unlikely that they would be considered today as candidate coatings for nozzle guide vanes.

Finally, a word of caution would be appropriate, concerning the use of results reported here in selecting coatings for

field application. A total of only eight coatings were evaluated. Selection of the coatings was strictly based on vendor offerings and not based on a systematically laid-out plan. Details of the coating processes, quality control procedures exercised, initial condition of the coatings, and operational history of the turbine were not known. Under these circumstances, the present study should be recognized as being limited in scope and the conclusions from the study should not be generalized. It is particularly important to realize that the performance of coatings can be specific to the corrosive environment, temperature (Type I versus Type II) and turbine operation (base load versus cycling). It is hoped that additional field evaluations such as those being carried out under EPRI RP2465-1 and others being planned will eventually enable utilities to select coatings more intelligently for specific application.

Summary

Evaluation of eight coatings applied to MAR-M-509 vanes and exposed to hot corrosion in a FT4 engine for 812 hr has been completed. Results show that none of the coatings was totally resistant, since even the most protective coating had degraded in localized areas. Based on corrosion resistance alone, the CoCrAlY and Pt-Rh-aluminide were found to be the best coatings. However, the CoCrAlY vanes had proved susceptible to thermal fatigue cracking. As a group, the precious metal aluminides offered the best protection, with the exception of Pd-aluminide coating. Hot isostatically pressing both basic aluminide and Rh-aluminide coatings after application appeared to have no real beneficial effect on hot corrosion resistance, and in the case of the basic aluminide appeared detrimental. The tendency of some of the coatings to debond at the coating-substrate interface and spall, and the tendency for thermal fatigue cracking in CoCrAlY coated vanes, clearly show that cyclic operation can have a profound effect on the performance of coatings. Turbine operation (base load versus cycling) must therefore be taken into consideration in selecting coatings.

References

1 Davis, F. N., and Grinnell, C. E., "Engine Experience of Turbine Rotor Blade Materials and Coatings," ASME Paper No. 82-GT-244, 1982.

2 Spengler, C. J., Scheiser, S. T., and Barksdale, D. C., "Microstructural Characterization of Service Exposed CoCrAlY Overlay Coating," in: *High-Temperature Protective Coatings*, S. C. Singhal, ed., TMS-AIME, Mar. 1983, pp. 189-200.

3 Lindblad, N. R., Schilling, W. F., Aeschbacher, H. J., and Knoll, W. H., "Gas Turbine Bucket Corrosion Protection Development," ASME Paper No. 79-GT-47, 1979.

4 McMinn, A., "Evaluation of Protective Coatings for Hot Components of Combustion Turbines," EPRI Final Report No. AP-4194, Project 2388-3, Aug. 1985.

5 Krasij, M., Barnum, B. M., and Kemp, F. S., "Parameter Monitoring for Corrosion Control of Utility Gas Turbines," EPRI Annual Report, AP-1369, Project 643-1, Mar. 1980.

6 Krasij, M., Barnum, B. M., and Kemp, F. S., "Parameter Monitoring for Corrosion Control of Utility Gas Turbines," EPRI Final Report, AP-2737, Project 643-1, Dec. 1982.

7 McCarron, R. L., and Brobst, R. P., "Corrosion of Turbine Materials Exposed to the Effluent of an Experiment PFBC," *Materials Performance*, Vol. 24, Jan. 1985, pp. 32-38.

8 Durst, C., Davis, A., Marijnissen, G., and Pichoir, R., "Recent Approaches to the Development of Corrosion Resistant Coatings," in: *High Temperature Alloys for Gas Turbines 1982*, R. Brunetaud et al., eds., Reidel Publishing Co., Holland, 1982, pp. 53-86.

9 Malik, M., Morbioli, R., and Huber, P., "The Corrosion Resistance of Protective Coatings," in: *High Temperature Alloys for Gas Turbines 1982*, R. Brunetaud et al., eds., Reidel Publishing Co., Holland, 1982, pp. 87-98.

10 Sims, C. T., "Cobalt-Base Alloys," in: *The Superalloys*, C. T. Sims and W. C. Hagel, eds., Wiley, New York, 1972, pp. 145-174.

11 Chatterji, D., DeVries, R. C., and Romeo, G., "Protection of Superalloys for Turbine Application," *Advances in Corrosion Science and Technology*, Vol. 6, M. G. Fontana and R. W. Staehle, eds., Plenum Press, New York, 1976, pp. 1-87.

12 Lindblad, N. R., "A Review of the Behavior of Aluminide-Coated Superalloys," *Oxidation of Metals*, Vol. 1, No. 1, 1969, pp. 143-170.

13 Goward, G. W., "Current Research on the Surface Protection of Superalloys for Gas Turbine Engines," *J. of Metals*, Oct. 1970, pp. 31-39.

14 Nagarajan, V., Stringer, J., and Whittle, D. P., "The Hot Corrosion of Cobalt-Base Alloys in a Modified Dean's Rig—I. Co-Cr, Co-Cr-Ta, and Co-Cr-Ti Alloys," *Corrosion Science*, Vol. 22, No. 5, 1982, pp. 407-427.

15 Stringer, J., and Whittle, D. P., "Hot Corrosion of Cobalt-Based Alloys," in: *Deposition and Corrosion in Gas Turbines*, A. B. Hart and A. J. B. Cutler, eds., Wiley, New York, 1973, pp. 197-209.

16 Beltran, A. M., "The Oxidation and Hot-Corrosion Resistance of Cobalt-Base Superalloys," *Cobalt*, No. 46, Mar. 1970, pp. 3-14.

17 Kemp, F. S., and Krasij, M., "Protective Coatings for Utility Gas Turbines," EPRI Final Report, AP-2929, Project 1344-1, Mar. 1983.

18 Kubarych, K. G., "Evaluation of Performance of Gas Turbine Blade Coatings," EPRI RP 2388-1, Draft Final Report, Sept. 1984.

19 Hodge, P. E., Stecura, S., Gedwill, M. A., Zaplatynsky, I., and Levine, S. R., "Thermal Barrier Coatings: Burner Rig Hot Corrosion Test Results," *J. of Matls. for Energy Systems*, Vol. 1, Mar. 1980, pp. 47-58.

20 Singhal, S. C., and Bratton, R. J., "Stability of a ZrO_2 (Y_2O_3) Thermal Barrier Coating in Turbine Fuel With Contaminants," ASME JOURNAL OF ENGINEERING FOR POWER, Vol. 102, Oct. 1980, pp. 770-775.

Pack Cementation Coatings for Superalloys: a Review of History, Theory, and Practice

G. W. Goward

L. W. Cannon

Turbine Components Corporation,
Branford, CT 06405

Nickel and cobalt-base superalloy blades and vanes in the hot sections of all gas turbines are coated to enhance resistance to hot corrosion. Pack cementation aluminizing, invented in 1911, is the most widely used coating process. Corrosion resistance of aluminide coatings can be increased by modification with chromium, platinum, or silicon. Chromium diffusion coatings can be used at lower temperatures. Formation and degradation mechanisms are reasonably well understood and large-scale manufacturing processes for these coatings are gradually being automated. Pack cementation and related diffusion coatings serve well for most aircraft engine applications. The trend for industrial and marine engines is more toward the use of overlay coatings because of the greater ease of designing these to meet a wide variety of corrosion conditions.

Introduction

Nickel and cobalt-base superalloy vanes and blades in the hot sections of all types of gas turbines are coated to enhance their resistance to hot corrosion. The most widely used coatings are those based on the intermetallic compound NiAl (CoAl on cobalt-base alloys) formed by interaction of superalloy surfaces with aluminum. Almost all such coatings are manufactured by pack cementation processes involving heating the parts in contact with a powder mixture of aluminum or an aluminum alloy, a chemical transfer agent, usually a chloride or fluoride salt, and an inert diluent such as aluminum oxide (alumina).

In a related process, termed "gas phase" or "out-of-contact," parts are held out of contact with the aluminizing source to preclude plugging of small holes and cooling passages with coating powder. Such processes also facilitate the coating of complex cooling passages in blades and vanes difficult or impossible to coat by pack cementation.

To enhance resistance to certain types of hot corrosion, aluminide coatings can be modified to contain elements such as chromium, platinum, and silicon.

For some relatively low-temperature gas turbine applications, e.g., < 870°C (1600°F), chromide or chromium-rich diffusion coatings can be used to protect against certain types of hot corrosion. In addition, low-alloy steels can be chromized to protect against aqueous corrosion and high-temperature oxidation and corrosion.

This paper will present a short history of the development and applications of these types of pack cementation coating, a summary of what is known about coating formation mechanisms, a brief review of manufacturing processes, some practical applications of contemporary pack and related coatings, and some expectations for further development and use of such coatings.

Historical

The first public descriptions of pack cementation aluminizing were by Van Aller in a U.S. patent [1] filed in 1911 and in 1914 in a technical paper by Allison and Hawkins of the General Electric Research Laboratory [2]. The process consisted of embedding pieces of copper or iron to be coated in a powder mixture of aluminum, sal ammoniac (ammonium chloride), and an inert filler, and heating the assembly at 450°C (842°F) for two hours. The inert filler first used was graphite. After removal from the powder, the pieces were further heat treated at 700 to 800°C (1292 to 1472°F). Later, Gilson, at the same laboratory, patented the use of a mix consisting of aluminum, a chloride, and aluminum oxide for coating ("calorizing") metals, specifically copper and iron, to render them "inoxidizable" [3].

Initial applications of aluminizing were coating of iron wire or ribbon heating elements and of copper for use in power plant steam condenser tubes. These early workers correctly attributed the enhanced oxidation resistance to the selective formation of protective alumina scales at elevated temperatures in air.

Ruder [4] summarized applications of aluminizing in 1915; these included coating steels for furnace fixtures and nickel for use as combustion screens.

The General Electric process was licensed to a British Company[1] for further development. Additional development and

Contributed by the Gas Turbine Division of THE AMERICAN SOCIETY OF MECHANICAL ENGINEERS and presented at the 32nd International Gas Turbine Conference and Exhibit, Anaheim, California, May 31–June 4, 1987. Manuscript received at ASME Headquarters February 4, 1987. Paper No. 87-GT-50.

[1] Calorizing Corporation of Great Britain, Ltd., Dumbuck Works, Glasgow Road, Dumbarton, United Kingdom.

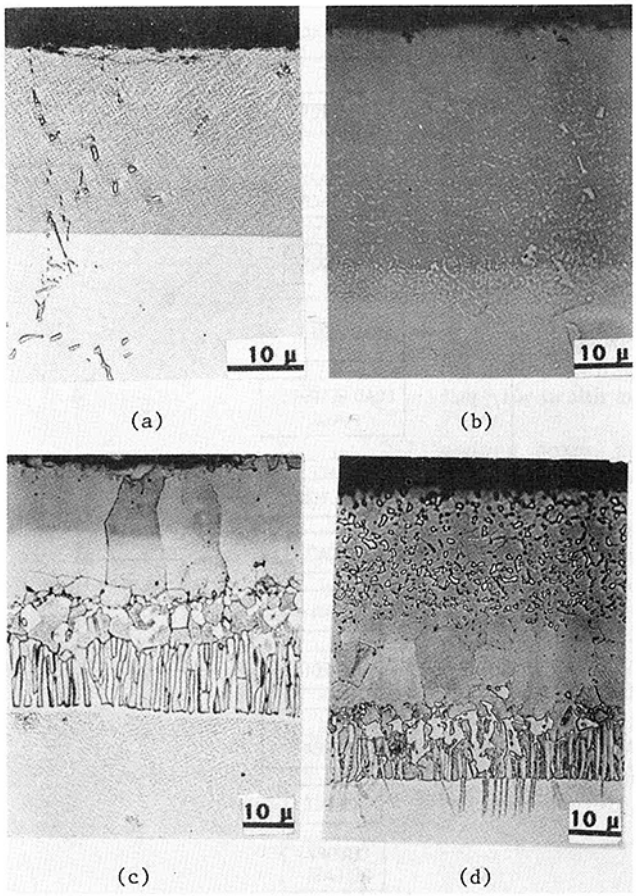

Fig. 1 Microstructures of aluminide coatings: (*a*) inward diffusion based on Ni_2Al_3; (*b*) inward diffusion based on NiAl; (*c*) outward diffusion based on NiAl; (*d*) NiAl coating from (*a*) after heat treatment

uses of the process up until the first practical use of pack cementation aluminizing of gas turbine vane airfoils in 1957 [5] is not well documented.

Turbine blades may have been first aluminized by hot dip processes for Allison [6] and Curtiss Wright engines in about 1952. Other early applications of aluminide coatings on nickel alloy turbine blades were by slurry–fusion methods [7] but since about 1970 the majority of such coatings has been applied by pack cementation and the more recently developed, related out-of-contact processes [8, 9]. Complex internal cooling passages are coated by forced flow gas phase aluminizing [10, 11] and by vacuum pulsed aluminizing [12].

Kelley [13] described his invention of pack cementation chromizing of steels, the properties of the coated steels, and applications of these in 1923. Resistance to corrosion in aqueous media was the most important property described and one of the first uses was the improvement in surface stability of steam turbine buckets. In 1953, Gibson patented aluminizing of chromized steels with aluminum paints and heat treatment to further improve high-temperature oxidation resistance [14].

A comprehensive review of chromide coatings on steel was published by Samuel and Lockington in 1951–1952 [15] and another by Drewett in 1969 [16]. The origins of use of chromide coatings on gas turbine blades and vanes is obscure but they were probably first used in Europe for protection of industrial turbine blades from hot corrosion. Schneider et al. [17] and Bürgel [18] describe the use of chromide coatings on nickel alloy blades beginning in the early 1960s.

During the 1970s the major new developments in the field of pack cementation aluminide coatings have been modifications of such coatings with chromium [19], platinum [20], and to a lesser extent, silicon. It is estimated that greater than 90 percent of all coated turbine airfoils are coated by pack cementation processes. Out-of-contact coating of blades and vanes is gaining in use at the expense of pack cementation, not only for coating of internal cooling passages, but as an overall more versatile and cost effective process.

Theory

Formation Mechanisms. As is usual for such technology, practical processes and applications substantially preceded the development of formation and degradation mechanisms of pack cementation aluminide and related coatings. The classic studies of diffusion in nickel–aluminum by Janssen and Rieck [21, 22] and investigations of aluminide coatings on nickel-base superalloys by Goward and Boone [23] provided rational diffusion mechanisms involved in the formation of so-called inward and outward diffusion coatings. Important work by Levine and Caves [24] and Seigle and co-workers on diffusion in the nickel–aluminum system and thermodynamics and kinetics of the pack aluminizing has now provided a firm theoretical base for further technological progress. For example, Seigle and Shankar [25] demonstrated that diffusion of nickel predominates in nickel-rich NiAl, nickel and aluminum diffusion are equal at about 51 atom percent aluminum, and aluminum diffusion increasingly predominates with increasing aluminum content of the compound.

The latter work leads to the conclusion that inward and outward diffusion aluminide coatings [23] define the extremes of structure and that intermediate structures should exist. Figure 1 illustrates this by showing (*a*) an extreme inward structure based on Ni_2Al_3, (*b*) an intermediate structure involving predominant aluminum diffusion in NiAl but with some nickel diffusion, and (*c*) an ouward diffusion structure formed by predominant nickel diffusion. The coating based on Ni_2Al_3 is not practically useful and must be subjected to further heat treatment to convert it to the NiAl based coating shown in Fig. 1(*d*).

There has been little basic work on formation of chromide coatings on nickel and cobalt superalloys. The coatings are commonly made by both pack cementation and out-of-contact processes. Typical structures derived from sources containing chromium powder, ammonium chloride, and alumina are shown in Fig. 2. The coatings consist principally of chromium in solution in gamma nickel. The pack cementation coating has discontinuous alpha chromium on its surface. The gamma prime phase normally present in the nickel alloy has been removed by partial transfer of aluminum from the alloy to the coating source. The dark inclusions are aluminum oxide formed by internal oxidation caused by the oxygen potential sustained by the chromium–chromium oxide system. This can be prevented by adding appropriate amounts of aluminum to the chromium source mix [19, 26].

Most chromium-modified aluminide coatings have little difference in microstructure compared to simple aluminides. Those formed by chromizing, followed by inward diffusion aluminizing and then heat treatment to form beta (NiAl), contain the chromium enrichment in the form of alpha chromium particles in the outer layer of the coating [19, 27]. Conversely if aluminizing is of the outward diffusion type, the chromium will remain near the original surface of the alloy, that is, in the diffusion zone of the coating [9, 27] and will be present in the top layer only to the extent of its solubility, approximately 2 to 5 percent, in NiAl.

It has been generally understood that simultaneous deposition of aluminum and chromium by pack cementation is difficult, if not impossible [28]. Marijnissen, however, has devised a process that approximates such co-deposition [29], but the microstructures which result are unique in that they con-

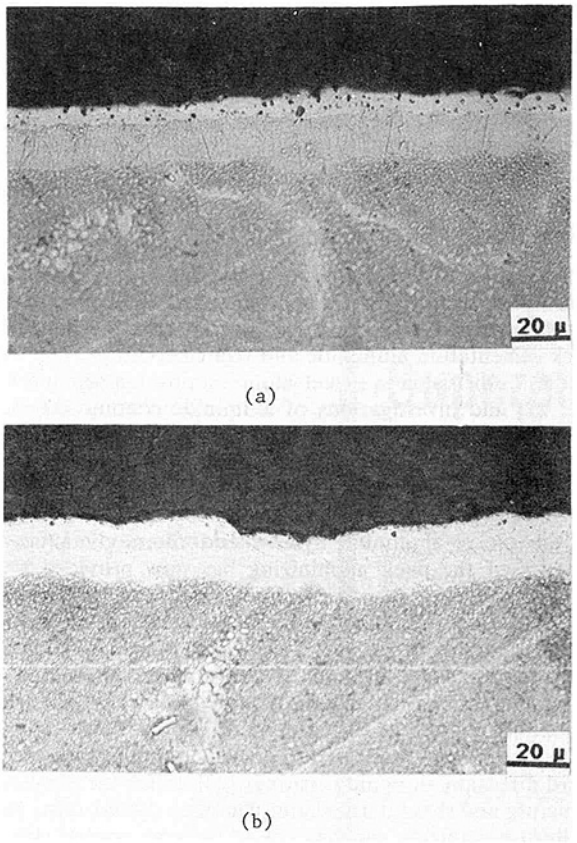

Fig. 2 Chromium diffusion coatings formed: (*a*) by pack cementation, and (*b*) by out-of-contact with the coating source

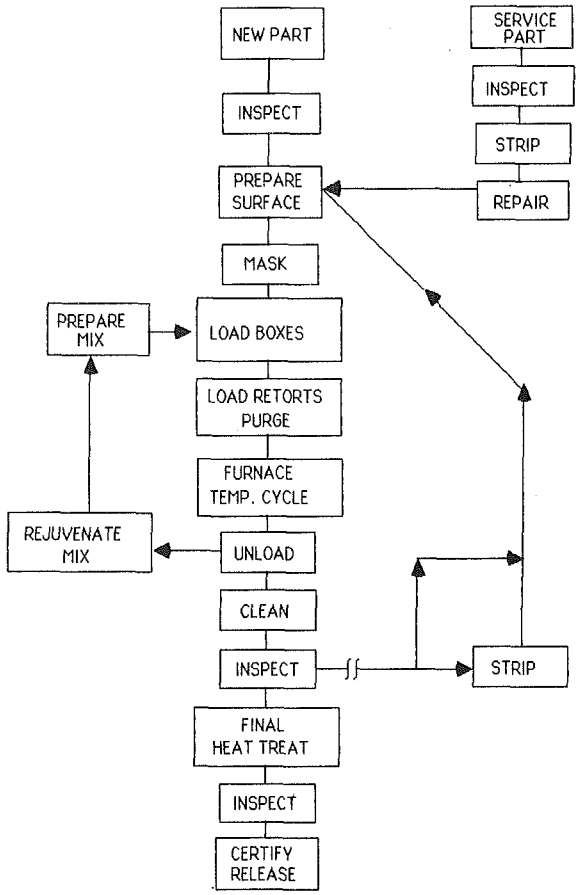

Fig. 3 Flow diagram for typical pack cementation process

tain discrete layers of chromium and NiAl. It is difficult, therefore, to characterize the coatings as belonging to the normal class of aluminide coatings.

Formation mechanisms of platinum modified aluminide coatings, made by plating of platinum followed by aluminizing are not yet well understood. Some progress has been made [30] but much more work is required to build an effective technology base for these coatings.

Degradation Mechanisms. A complete review of the large amount of work on coating degradation mechanisms is beyond the scope of this paper. In brief summary, the coatings degrade by high-temperature oxidation, high-temperature (Type 1) and low-temperature (Type 2) hot corrosion [31], interdiffusion with the substrate alloy, and thermal fatigue cracking.

A most important factor in coating function is the adherence of the protective aluminum oxide scale under cyclic operation of the turbine. This adherence is aided by the presence of oxygen active elements, which for diffusion coatings, can currently only be derived from the substrate alloy. Hafnium, added to the alloys for grain boundary strengthening, serendipitously serves this function for diffusion coatings. The mechamisms by which oxide adherence is achieved have been extensively studied but are not yet fully understood [32].

The presence of chromium improves resistance to both types of hot corrosion. The mechanisms of this improvement are not yet fully understood.

The presence of platinum as $PtAl_2$ dispersed in NiAl improves resistance to Type 1 hot corrosion but not that for Type 2 which is induced by SO_3 and V_2O_5 in sulfate deposits [18, 33]. If the coating consists of continuous $PtAl_2$ in its outer layer, it also has good resistance to Type 2 hot corrosion [34], but this layer is very brittle and may not be mechanically satisfactory.

The presence of silicon enhances resistance to high-temperature oxidation [35] possibly by aiding in the formation and adherence of the alumina scale. Resistance to Type 2 acidic fluxing is also improved by silicon [35]; this may be related to the insolubility of silica and silicates in acidic corrodents.

Degradation by interdiffusion between aluminide coatings and nickel superalloy substrates becomes significant above about 982°C (1800°F). Contrary to popular conception, the mechanism involves nickel diffusion from the alloy into the coating [23] and not significant diffusion of aluminum into the substrate alloy. Fleetwood [36] demonstrated that high concentrations of refractory elements, such as tungsten, in superalloys tended to inhibit aluminide coating-substrate interdiffusion. This might be interpreted as the result of lower nickel activity in such highly alloyed systems.

Repeated thermal cycling can initiate cracks in aluminide coatings either by brittle fracture when strains peak below the brittle-ductile transition temperature (1200–1400°F, 649–760°C) or by ductile failure when strains peak above these temperatures [37]. Such cracks may be temporarily blunted by oxidation in the interdiffusion zone, but will eventually propagate into the substrate, and require component removal. Coating structure, e.g., inward versus outward diffusion types, should influence thermal fatigue properties of diffusion aluminide coatings but no definitive studies of such effects have been published in the open literature.

Manufacturing Processes

A flow diagram for a typical production scale pack cemen-

tation process is shown in Fig. 3. Comments on some of the more important parts of the process follow.

- Visual and flow inspections of cooled airfoils provide one of the last opportunities to determine if external and internal surfaces are suitable for the intended purposes of the parts.
- Surface preparation by grit blasting and/or vibratory finishing provides a clean surface for coating and a finish consistent with aerodynamic design intent.
- Masking with mechanical, oxide barrier, or chemically reactive masks prevents coating of critical surfaces such as blade roots. Sequencing of coating before final machining avoids costly masking.
- Preparation of pack mixes requires large-scale powder handling equipment designed for effective mixing, storage, and dispensing. Closed systems are necessary for health and safety reasons.
- Loading parts with pack mix into coating boxes, and loading boxes onto racking and into retorts is a labor intensive process. Automation is developing only very slowly.
- Furnaces with appropriate temperature capability and uniformity and associated gas handling and environmental control systems are the most costly part of the plant. Furnace operation and gas purging are amenable to automation which provides integrated quality control.
- Unloading, removal of masks, and cleaning are labor intensive operations. Mix rejuvenation and recycling are amenable to automation.
- The most widely accepted final inspection involves destructive metallography of representative samples to assure that the coatings meet thickness and microstructural requirements.

Practical Applications

For aircraft gas turbine blades and vanes fabricated from moderately hot corrosion resistant alloys, e.g., 12 to 15 percent chromium, simple aluminide coatings of the inward and outward diffusion type provide adequate protection for many engines currently in service. When alloys are more corrosion prone, e.g., 7 to 10 percent chromium, it is prudent to modify the aluminide coating by chromizing before aluminizing. Aluminizing should be of the inward type to locate the chromium in the outer layer of the coating where is more effective [38]. Addition of chromium is the least costly modification but for more severe Type 1 hot corrosion resulting from extended exposure to marine environments, modification of the aluminide coating with platinum can prove to be the most cost effective solution [39].

If the design philosophy is such that more expensive alloy structures, such as single crystals, are used to their maximum temperature capabilities to improve fuel efficiency, then contemporary diffusion coatings may not meet design requirements for oxidation and/or thermal fatigue resistance. For these situations, the more expensive MCrAlY (M = Ni, Co) coatings applied by electron beam evaporation or low-pressure plasma spraying are the only remaining choice.

The situation for ground or marine-based gas turbines is more complex because of the wide variability of local environments with respect to air contaminants (salts, industrial pollutants, sulfur oxides) and fuel properties (salts, sulfur, vanadium). Bürgel [18] has recently summarized experience with several kinds of coatings in ground based engines. In the lower metal temperature range, approximately 740°C (1364°F), where Type 2 corrosion predominates, pack cementation chromide coatings proved to be best compared to silicides (Elcoat 360), platinum aluminides (LDC 2) and advanced overlay nickel-chromium-silicon and MCrAlY coatings [40]. Grünling [41] has reported that while the chromide coatings give reasonable service up to about 800°C (1472°F), better coatings are required 50 to 100°C (90 to 180°F) above that temperature. Pack cementation silicides showed good corrosion resistance but were prone to failure by cracking and spalling. To utilize silicon more effectively, a plasma sprayed nickel-chromium-silicon coating was developed. This coating is serviceable for reasonable periods of time in the 800 to 850°C (1427 to 1562°F) temperature range.

Bürgel [18] also described tests of a platinum aluminide diffusion coating (RT 22) on Inco 738 blades and vanes. The life of this coating on blades at metal temperatures of about 840°C (1472°F) was satisfactory, but severe Type 2 attack occurred on vanes cooled to metal temperatures of about 750°C (1382°F) and below. Schilling [42] reported the same behavior in a turbine fired with high-sulfur natural gas while running at "very low firing temperatures."

Harry [43] has reported generally satisfactory results with platinum aluminide coatings in marine propulsion applications but has also observed more rapid degradation at lower metal temperatures.

All of these observations confirm the results of Wu and Rahmel [33] who found that the $PtAl_2$ dispersed phase type of coating had poor resistance to acidic (SO_3) sodium sulfate.

Bürgel [18] also reported that the RT 22 coating showed significant cracking on Inco 738 vanes after only 5000 hr of service.

Bürgel concludes, and these authors concur, that while certain types of aluminide coatings are useful in industrial gas turbines, they lack the compositional flexibilitiy required to meet the many different demands of this class of engines. The trend for these applications will be away from pack cementation coatings and toward MCrAl-based compositions with chromium and aluminum varied, and silicon, hafnium, and perhaps platinum [44] added to adjust to specific environments.

Future development activity in pack cementation and related coatings, primarily for aircraft engines, will focus on more efficient, automated processing and means to incorporate appropriate additions of beneficial elements, such as silicon, hafnium, and other oxygen active elements. Combination of pack cementation with other processes, such as plasma spraying, will also receive increasing attention [45].

References

1 Van Aller, T., "Treatment of Metals," U.S. Patent No. 1,155,974.

2 Allison, H. B. C., and Hawkins, L. A. "Calorizing: A Protective Treatment for Metal," *General Electric Review*, Vol. 17, 1914, pp. 947–951.

3 Gilson, E. G., "Process of Treating Metals," U.S. Patent No. 1,091,057.

4 Ruder, W. E., "Calorizing Metals," *Trans. Amer. Electrochem. Soc.*, Vol. 21, 1915, pp. 253–261.

5 Seelig, R. P., and Steuber, R. J., "High Temperature Resistant Coatings for Superalloys," *High Temp.-High Press.*, Vol. 10, 1978, pp. 207–213.

6 Nichols, E. S., Burger, J. A., and Hanink, D. K., *Mech. Eng.*, Mar. 1965, pp. 52–56.

7 Joseph, A. D., "Applying Protective Coating From Powdered Material Utilizing High Temperature and Low Pressure," U.S. Patent No. 3,102,044.

8 Parzuchowski, R. S., "Gas Phase Deposition of Aluminum on Nickel Alloys," *Thin Solid Films*, Vol. 45, 1977, pp. 349–355.

9 Gaujè, G. and Morbioli, R., "Vapor Phase Aluminizing to Protect Turbine Airfoils," *High Temperature Protective Coatings*, S. C. Singhal, ed., The Metallurgical Society of AIME, Atlanta, GA, Mar. 1983, pp. 13–26.

10 Parzuchowski, R. S., and Benden, R. S., "Gas Phase Deposition of Aluminum Using a Complex Aluminum Halide of an Alkali Metal or an Alkaline Earth Metal," U.S. Patent No. 4,132,816.

11 Parzuchowski, R. S., and Benden, R. S., "Apparatus for Gas Phase Deposition of Coatings," U.S. Patent No. 4,148,275.

12 Restall, J. E., et al., "A Process for Protecting Gas Turbine Blade Cooling Passages Against Degradation," *Superalloys 1980*, J. K. Tien et al., eds., American Society for Metals, Seven Springs, PA, Sept. 1980, pp. 405–411.

13 Kelley, F. D., "Chromizing," *Trans. Amer. Electrochem. Soc.*, Vol. 43, 1923, pp. 351–370.

14 Gibson, T., "Surface Treatment of Metals," U.S. Patent No. 2,809,127.

15 Samuel, R. L., and Lockington, M. A., "The Protection of Metallic Surfaces by Chromium Diffusion," *Metal Treatment and Drop Forging*, Vol. 18, 1951, pp. 354–359, 407–414, 440–444, 495–506, 543–548; Vol. 19, 1952, pp. 27–32, 81–85.

16 Drewett, R., "Diffusion Coatings for the Protection of Iron and Steel," *Anti-Corrosion Methods and Materials*, Vol. 16, 1951, pp. 543-548.

17 Schneider, R., Bauer, R., and Grünling, H. W., "Corrosion and Failure Mechanisms of Coatings for Gas Turbine Applications," *Thin Solid Films*, Vol. 54, 1978, pp. 359-367.

18 Bürgel, R., "Coating Service Experience With Industrial Gas Turbines," *Matls. Sci. and Tech.*, Vol. 2, 1986, pp. 302-308.

19 Brill-Edwards, H. W., "Method for Coating Heat Resistant Alloys," U.S. Patent No. 3,801,353.

20 Lehnardt, G., and Meinhardt, H., "A New Protective Coating for Nickel Alloys," *Electrodeposition and Surface Treatment*, Vol. 1, 1972, pp. 189-193.

21 Janssen, M. M. P., and Rieck, G. D., "Reaction Diffusion and Kirkendall Effect in the Nickel-Aluminum System," *Trans. TMS of AIME*, Vol. 239, 1967, pp. 1372-1385.

22 Janssen, M. M. P., "Diffusion in the Nickel-Rich Part of the Nickel-Aluminum System at 1000 to 1300°C: Ni_3Al Layer Growth, Diffusion Coefficients, and Interface Concentrations," *Met. Trans.*, Vol. 4, 1973, pp. 1623-1633.

23 Goward, G. W., and Boone, D. H., "Mechanisms of Formation of Diffusion Aluminide Coatings on Nickel-Base Superalloys," *Oxid. of Metals*, Vol. 3, 1971, pp. 475-495.

24 Levine, S. R., and Caves, R. M., "Thermodynamics and Kinetics of Pack Aluminide Coating Formation on IN-100," *J. Electrochem Soc.*, Vol. 121, 1974, pp. 1051-1064.

25 Shankar, S., and Seigle, L. L., "Interdiffusion and Intrinsic Diffusion in the NiAl Phase of the Nickel-Aluminum System," *Met. Trans. A*, Vol. 9A, 1978, pp. 1468-1476.

26 Baldi, A. L., "Protecting Metals," U.S. Patent No. 4,308,160.

27 Godlewska, E., and Godlewski, K., "Chromaluminizing of Nickel and Its Alloys," *Oxid. of Metals*, Vol. 22, 1984, pp. 117-131.

28 Walsh, P. N., "Chemical Aspects of Pack Cementation," *Proceedings of the Fourth International Conference on Chemical Vapor Deposition*, G. F. Wakefield and J. M. Blocher, Jr., eds., The Electrochemical Society, Princeton, NJ, 1983, pp. 147-168.

29 Marijnissen, G. H., "Co-deposition of Chromium and Aluminum During a Pack Process," *High Temperature Protective Coatings*, S. S. Singhal, ed., TMS of AIME, Atlanta, GA, Mar. 1983, pp. 27-35.

30 Streiff, R., Boone, D. H., and Purvis, L. J., "Structure of Platinum Modified Aluminide Coatings," *Surface Engineering*, R. Kossowski and S. S. Singhal, eds., NATO ASI Series, Martinus Nijhoff, Les Arcs, France, July 1983, pp. 469-480.

31 Goward, G. W., "Low Temperature Hot Corrosion in Gas Turbines: A Review of Causes and Coatings Therefor," ASME JOURNAL OF ENGINEERING FOR GAS TURBINES AND POWER, Vol. 108, 1986, pp. 421-425.

32 Smeggil, J. G., Funkenbusch, A. W., and Bornstein, N. S., "A Relationship Between Indigenous Impurity Elements and Protective Oxide Scale Adherence Characteristics," *Met. Trans. A*, Vol. 17A, 1986, pp. 923-932.

33 Wu, W. T., Rahmel, A., and Schorr, M., "Role of Platinum in the Sodium Sulfate Induced Hot Corrossion of Aluminum Diffusion Coatings," *Oxid. of Metals*, Vol. 22, 1984, pp. 59-81.

34 Barkalow, R. H., and Pettit, F. S., "Degradation of Coating Alloys in a Marine Environment," Report FR-10225, U.S. Navy Contract N0-00173-75-C-0146, June 1978.

35 Bauer, R., and Grünling, H. W., "The Role of Silicon in Corrosion Resistant High Temperature Coatings," *Thin Solid Films*, Vol. 95, 1982, pp. 3-20.

36 Fleetwood, M. J., "Influence of Nickel-Base Alloy Composition on the Behavior of Protective Aluminide Coatings," *J. Inst. of Metals*, Vol. 98, 1970, pp. 1-7.

37 Schneider, K., and Grünling, H. W., "Mechanical Aspects of High Temperature Coatings," *Thin Solid Films*, Vol. 107, 1983, pp. 395-416.

38 Godlewski, K., and Godlewska, E., "Effect of Chromium on the Protective Properties of Aluminide Coatings," *Oxid. of Metals*, Vol. 26, 1986, pp. 125-138.

39 Cocking, J. L., Johnston, G. R., and Richards, P. C., "Protecting Gas Turbine Components; The Relative Durability of a Conventional and Platinum Modified Aluminide Coating," *Materials and Design*, Vol. 6, 1985, pp. 224-229.

40 Diblon, R., and Keienburg, K. H., "Refurbishing Gas Turbine Blades, Technical and Economic Aspects," ASME Paper No. 85-GT-181.

41 Grünling, H. W., and Schneider, K., "Coatings in Industrial Gas Turbines: Experience and Further Requirements," *Thin Solid Films*, Vol. 84, 1981, pp. 1-15.

42 Schilling, W. F., "Low Pressure Plasma Sprayed Coatings for Industrial Gas Turbines," *NATO Advanced Workshop on Coatings for Heat Engines*, I. Kvernes, ed., Acquafredda di Maratea, Italy, Aprl 1984.

43 Harry, J. F. V., "Marine Applications," *Matls. Sci. and Tech.*, Vol. 2, 1986, pp. 295-301.

44 Grisik, J. J., Miner, R. G., and Wortman, D. J., "Performance of Second Generation Coatings in Marine Service," *Thin Solid Films*, Vol. 73, 1980, pp. 397-406.

45 Restall, J. E., and Wood, M. I., "Alternate Processes and Treatments," *Matls. Sci. and Tech.*, Vol. 2, 1986, pp. 225-231.